Accreting Compact Objects in Technicolor: Multiwavelength Characterization of High Mass X-ray Binaries in the Local Group

Margaret Lazzarini

A dissertation
submitted in partial fulfillment of the
requirements for the degree of

Doctor of Philosophy

University of Washington

2021

Reading Committee:

Benjamin Williams, Chair

Julianne Dalcanton

Ann Hornschemeier Cardiff

Eric Bellm

Program Authorized to Offer Degree:
Astronomy

University of Washington

Abstract

Accreting Compact Objects in Technicolor: Multiwavelength Characterization of High Mass X-ray Binaries in the Local Group

Margaret Lazzarini

Chair of the Supervisory Committee:
Professor Benjamin Williams
Astronomy

High mass X-ray binaries (HMXBS) are systems that contain a compact object (neutron star or black hole) that accretes mass from a massive stellar companion. HMXBs are highly observable due to their bright X-ray luminosities, making them an observational window into the complex process of massive binary stellar evolution. In this thesis I present work I have completed over the past six years to measure the population demographics of HMXBs in Local Group galaxies M31 and the Small Magellanic Cloud (SMC) and the spatially resolved recent star formation history (SFH) of M33. In M31, I used observations from the *Hubble Space Telescope (HST)*, the *Chandra X-ray Observatory*, and the *Nuclear Spectroscopic Telescope Array (NuSTAR)* to characterize the population of HMXBs in that galaxy and measure the overall HMXB production rate. In the SMC, I used *NuSTAR* observations to characterize the accreting compact objects in the detected HMXB systems. In M33 I use multi-band photometry to measure the spatially resolved recent SFH of M33 using color-magnitude diagram fitting. I discuss the results of my work in M31 and the SMC in the context of massive binary stellar evolution and previous studies of HMXB populations in the context of their host galaxies. For the spatially resolved recent SFH of M33, I discuss our measurements and their implications for the timescale of M33's large-scale morphological evolution.

TABLE OF CONTENTS

Page

LIST OF FIGURES

LIST OF TABLES

ACKNOWLEDGMENTS

The work presented in this thesis is the culmination of the past six years in graduate school. None of the work presented here would have been possible without the incredible mentorship, support, and encouragement I have received from my family, friends, and collaborators along the way.

I would first like to thank the mentors who have guided me throughout my graduate school career. I would like to thank my advisor, Ben Williams, who has been an incredible mentor and support for me throughout my time in graduate school. He has consistently provided encouragement when I need to push through a difficult part of a project, excitement when things are going well, and hands on guidance when I needed it. Thank you to Ann Hornschemeier Cardiff. You took me on as an intern when I came to GSFC and have provided me with so much continued support and connected me with so many collaborators and opportunities. Thank you to Julianne Dalcanton for your collaboration, insightful feedback, and support throughout my graduate career. Thank you to Eric Bellm for your support and agreeing to serve on my committee. Thank you to my GSR, Jessica Thompson.

I have been so lucky to join such a rich community of graduate students at the University of Washington. I want to especially thank Iryna Butsky for your friendship and support through it all. Thank you to my office mates Hannah Bish and Dave Fleming, I'm sorry we couldn't close out grad school physically in the same office but thank you for the scientific discussions, life chats, and the foosball games. Thanks to the rest of my grad cohort Trevor Dorn-Wallenstein, Spencer Wallace, and Matt Wilde, for your support and friendship. Thank you to Nicole Sanchez for being a great friend and colleague, I loved teaching Pre-MAP and Protostars with you. Thank you to Meredith Durbin for such great collaboration. And thank you to the rest of the graduate community, you

have all made my time at UW incredibly special.

Thank you to the X-ray galaxies group at Goddard Space Flight Center for your mentorship and collaboration.

I would like to thank my family. Thank you to my extended family including cousins who have housed me, lived with me, and supported me so much throughout my time in the Northwest. Thank you to my parents Martha McInnes and Albert Lazzarini for their support and encouragement. Thank you to my brothers Alessandro, Christian, and Thomas Lazzarini and to my wonderful sisters-in-law Grace and Melissa for their constant support and friendship.

Lastly, I want to thank my husband, Paul Orland, for his constant support throughout graduate school. He has always supported me and believed in me, sometimes more than I have believed in myself.“You heard it here first!”

DEDICATION

To Paul and Melba

Chapter 1

INTRODUCTION

Stars in massive binary stellar systems have some phases of evolution that are extremely complex. Knowledge of the demographics of accreting binary stars is critical to understanding these phases. This thesis focuses on multi-wavelength observations of nearby galaxies, which are used to gather population demographics of high mass X-ray binary (HMXB) populations. Similar to population demographics in humans, population demographics of HMXBs describe the fraction of systems of different ages that belong to different groups. Specifically, the population demographics of HMXBs refer to the ages of the systems, the fraction of HMXB systems with black hole or neutron star compact objects, and the physical properties of the companion stars including spectral type, mass, temperature, and radius. This demographic information can then be compared directly with theoretical models of binary stellar evolution in order to constrain some of the more complex phases of massive binary stellar evolution.

X-ray binaries (XRBs) are systems in which a compact object accretes material from a stellar companion. High mass X-ray binaries (HMXBs) are systems in which the companion star is a massive star ($M > 8 M_{\odot}$) that will eventually become a black hole or neutron star itself. The HMXB phase is one phase in the complex process of massive binary stellar evolution that may result in the formation of binary compact objects that, if they merge within a Hubble time, can produce observable gravitational wave radiation (e.g.; Tauris & van den Heuvel, 2006). Previous studies have tied the population of XRBs to host galaxy properties including the galaxy's total stellar mass (e.g.; Lehmer et al., 2010), star formation rate (SFR; e.g.; Ranalli et al., 2003; Gilfanov et al., 2004; Antoniou et al., 2010; Mineo et al., 2012; Antoniou & Zezas, 2016; Lehmer et al., 2019), and metallicity (e.g.; Basu-Zych et al., 2013, 2016; Brorby et al., 2016). XRBs are also thought to be a likely contributor to the heating of the primordial Intergalactic Medium (IGM), out of which the first galaxies formed, because at redshifts beyond $z \sim 6$, HMXBs outshine active galactic nuclei (AGN) as the dominant source of X-ray photons in the universe (e.g. Mesinger et al., 2014; Madau & Fragos, 2017; Greig & Mesinger, 2018).

Massive stars play an outsize role in their host galaxies. They inject energy, ionizing photons, and chemical enrichment into the interstellar medium (e.g. Dalgarno & McCray, 1972; Oey, 1999). Most massive stars form in binary or higher order multiple star systems, with the binary fraction

and number of stellar companions increasing with the mass of the primary star (e,g. Sana et al., 2012; Moe & Di Stefano, 2017). Upwards of 60% of massive stellar binaries form in systems that are close enough (orbital periods between 2 and 5000 days) to interact during their lifetimes (Moe & Di Stefano, 2017). This interaction is characterized by mass transfer between the stars in close separation binaries, which generally begins before the supernova of the primary star. This exchange of mass results in many of the complex phases of massive binary stellar evolution including Roche lobe overflow (RLOF), the X-ray binary phase, common envelope evolution, and stellar mergers (e.g. Sana et al., 2012; Tauris et al., 2017).

More attention has been paid to massive binary stellar evolution since the first detection of gravitational wave radiation from the merger of two black holes by LIGO in 2015 (Abbott et al., 2016). The masses of the merging black holes raised questions about our understanding of isolated binary stellar evolution. The progenitors of binary compact object mergers observed with gravitational waves are difficult to model. There are multiple proposed formation channels including binary stellar evolution, which would include the HMXB phase (e.g.; Podsiadlowski et al., 2004; Belczynski et al., 2008; Ivanova et al., 2013; Belczynski et al., 2016; Eldridge & Stanway, 2016; Mapelli & Giacobbo, 2018). Dynamical evolution in dense environments including globular clusters is also thought to contribute to the observed population of binary compact object mergers, and might contribute more heavily to the most massive binary black holes yet observed (e.g.; Portegies Zwart & McMillan, 2000; Rodriguez & Loeb, 2018; Antonini & Gieles, 2020). Determining the fraction of binary compact object mergers that formed via each channel requires reducing uncertainty in the production rates for each formation pathway. The HMXB population demographics discussed in this thesis are important for reducing uncertainties in models of massive binary stellar evolution.

Before delving into the reasoning for studying HMXB populations in nearby galaxies and the reason for studying them at various wavelengths, I will provide a brief overview of massive binary stellar evolution and a broad picture of our understanding of HMXB systems.

1.1 Massive Binary Stellar Evolution

Massive stars – those with masses greater than $8M_\odot$ – will go on to form black holes or neutron stars at the ends of their lives. Due to their mass, these are the only stars that pass through all nuclear fusion stages. Depending on their mass, these stars will end their lives as red supergiants ($8M_\odot \lesssim M \lesssim 25M_\odot$) or Wolf Rayet stars ($25M_\odot \lesssim M \lesssim 120M_\odot$). The cause of this divergence in the life trajectory for massive stars is the rate of mass loss from the star via stellar winds (Lamers & Levesque, 2017).

As stated earlier in this introductory section, interaction with a binary companion is the rule rather than the exception for massive stars. For most of these massive stellar binaries, mass transfer commences before the primary star reaches supernova (Kiminki & Kobulnicky, 2012; Sana et al., 2012; Sota et al., 2014). In most cases, this pre-SN mass transfer occurs via Roche Lobe overflow (RLOF), wherein the primary star expands beyond its Roche Lobe, resulting in mass transfer to the less massive secondary star in the binary system. The mass loss rates via RLOF can be significant, resulting in a nearly total loss of the Hydrogen rich outer envelope of the primary star (Podsiadlowski et al., 1992). This significant mass transfer results in a transfer of angular momentum from the primary (mass donor) to the secondary star in the system, resulting in a significant spin-up of the secondary star (e.g. de Mink et al., 2013). Depending on the amount of "spin-up", the mass gainer can start to spin at near critical rotational speeds, turning it into a Be star, depending on its spectral class. Be stars have equatorial decretion disks, which are caused by their extreme rotation. They are distinguishable observationally by the strong Hydrogen emission lines from the disk (Porter & Rivinius, 2003). The orbital separation of the binary also increases as a result of the mass transfer.

If this mass transfer becomes unstable, the binary can enter a common envelope phase, in which both stars are are inside of the primary star's Hydrogen envelope. During the common envelope phase, friction causes the two stars to inspiral. This can result in a stellar merger if the energy loss via inspiraling is not enough to expel the common envelope. However, if the energy transfer via friction during inspiral is great enough to eject the common envelope, the binary survives the

common envelope phase with a much closer orbital separation than before. This close separation is thought to be necessary to generate double compact objects that are close enough to merge during a Hubble time. The common envelope phase can occur at different phases of massive binary stellar evolution, both before and after the primary star supernova (Podsiadlowski et al., 1992; Glebbeek et al., 2013; Ivanova et al., 2013; Tauris et al., 2017).

Most X-ray binary progenitors have undergone significant mass transfer, resulting in a nearly stripped primary star before the first SN. Without significant mass transfer, the binary system is more likely to be disrupted during the primary star's supernova (Tauris et al., 2017). After the primary star's supernova, it becomes a compact object, either a black hole or neutron star depending on its mass. The binary system can now enter the X-ray binary phase depending on the separation and mass accretion rate from the secondary star onto the compact object.

1.2 High Mass X-ray Binaries

High mass X-ray binaries are systems in which a compact object accretes material from a massive stellar companion. The low mass counterpart of HMXBs, have a low mass companion star. In this thesis, I focus on HMXBs for two main reasons: 1. They are the likely progenitors to binary compact objects that may merge to produce gravitational wave radiation and 2. the companion stars in these systems are luminous enough to be identified and characterized in extragalactic environments.

The two major classes of HMXBs are defined by the type of the companion star: supergiant HMXBs (sgHMXBs) and Be HMXBs (BeHMXBs). There are 114 HMXB systems known in the Galaxy, of which sgHMXBs comprise roughly 30% and BeHMXBs comprise about 50%, with the rest of the systems comprised of a combination of giant, main sequence, and unknown companion types (Liu et al., 2006; Walter et al., 2015). The INTEGRAL telescope led to the discovery of many of the Galactic sgHMXBs, which were previously obscured by the plane of the Milky Way. The Magellanic Clouds host 121 HMXBs, of which all but possibly two are known to be BeHMXBs (Maravelias et al., 2014; Haberl & Sturm, 2016).

SgHMXBs can be futher subdivided based on their accretion mechanism: sgHMXBs that are

powered via wind fed accretion and those powered via RLOF. Wind powered sgHMXBs are often referred to as classical sgHMXBs. Material from the stellar winds of the secondary are accreted onto the compact object, causing bright X-ray luminosities during outbursts. In RLOF powered sgHMXB, the secondary star over fills its Roche Lobe, allowing material to be accreted onto the compact object. These systems tend to be less luminous than wind fed sgHMXBs, but they are more persistent sources (e.g. Chaty, 2013).

BeHMXBs almost exclusively host accreting neutron stars (Coe, 2000; Liu et al., 2006; Chaty, 2013; Casares et al., 2014; Haberl & Sturm, 2016). Only one known BeHMXB system is powered by an accreting black hole (Casares et al., 2014). This lack of observed black hole BeHMXBs could be a result of binary evolution, with black hole BeHMXBs having a lower probability of surviving common envelope evolution (Zhang et al., 2004; Belczynski & Ziolkowski, 2009). It has also been proposed that the lack of black hole BeHMXBs could be an observational effect. Efficient disk truncation in these systems would result in long quiescent states, making them difficult to observe (Zhang et al., 2004; Casares et al., 2014). In systems where pulsations have not been detected, when spectroscopic observations are available, they almost always confirm a neutron star companion. Mass measurements via radial velocity spectroscopy are required to confirm the presence of a black hole companion (Casares et al., 2014).

In BeHMXB systems, the companion star is a Be star, which is rapidly rotating and has an equatorial circumstellar disk. The Be stars in BeHMXB systems have spectral types of O9$-$B2V, which correspond to stellar masses of roughly 8$-$22 $M_{\odot}$ (Portegies Zwart, 1995; McBride et al., 2008; Chaty, 2013). Stars with masses outside of this mass range are thought to be either ejected from the binary during the SN event (for M$<$ 8$M_{\odot}$) while more massive stars become supergiants rather than Be stars. Spectroscopy is required to confirm a Be companion star, because they are characterized by strong Hα emission lines from the circumstellar disk (e.g. Coe, 2000). In Chapter 7 I will discuss future plans to obtain spectroscopy (and for the brightest sources, time resolved spectroscopy) to confirm the spectral types for HMXB companion stars in M31 and M33 and potentially determine orbital periods and accretor masses for these systems.

BeHMXB systems are highly variable X-ray sources. They can exhibit both Type I and Type

II outbursts. Type I X-ray outbursts are moderate intensity outbursts ($L_X \sim 10^{36} - 10^{37}$ erg s^{-1}) which occur close to the time of periastron of the neutron star. Type II outbursts are brighter ($L_X > 10^{37}$ erg s^{-1}) and are a result of reformation and dissipation of the accretion disk or large scale perturbations of the disk. The exact accretion mechanism depends on the geometry of the system. In BeHMXB systems where the compact object is on a highly eccentric orbit, it will accrete material at each periastron passage and the system will show periodic Type I X-ray outbursts. In systems where the compact object is on a less eccentric orbit, the compact object will not pass close enough to the Be star's decretion disk to show periodic Type I outbursts. The system will instead show less frequent, but brighter, Type II outbursts (Okazaki & Negueruela, 2001; Casares et al., 2014).

1.3 Multiwavelength Observations of HMXBs

Nearby galaxies are the ideal location to study populations of high mass X-ray binaries with the goal of gathering their population demographic information. Local group galaxies M31 and M33 are close enough for us to resolve their stellar populations, they can be observed in relatively few telescope pointings, and they do not have the distance uncertainties and absorption issues that plague Galactic studies. A full population of HMXBs can be observed at the same distance. These nearby galaxies can bridge between studies of more distant galaxies and more detailed studies of individual systems in the Milky Way. Studies of more distant galaxies have connected the integrated X-ray emission from their XRB populations with galaxy-wide properties including stellar mass, star formation rate, and metallicity (e.g. Lehmer et al., 2010; Basu-Zych et al., 2013, 2016; Brorby et al., 2016; Lehmer et al., 2019). These empirical relations are key for modeling XRB populations and including XRB feedback and X-ray emission from galaxies in cosmological simulations. More detailed studies of XRBs in our own galaxy have allowed us to model and understand the mechanism of accretion and X-ray emission in these systems (e.g. Shakura & Sunyaev, 1973; Davidson & Ostriker, 1973; White et al., 1983; Joss & Rappaport, 1984; Okazaki & Negueruela, 2001; Done et al., 2007).

To identify HMXB systems and and study their accreting compact objects, we must turn to

observations at X-ray wavelengths. In this thesis, I focus on observations made with two space-based X-ray telescopes: the *Chandra* X-ray Observatory and the *Nuclear Spectroscopic Telescope Array (NuSTAR)*.

The *Chandra* telescope, which was launched in 1999, is one of NASA's "Great Observatories". It has the capability of sub-arcsecond imaging, spectrometric imaging, and dispersive spectroscopy in the energy range of 0.08−10 keV (Weisskopf et al., 2000; O'Dell et al., 2010). *Chandra* is a powerful tool for studying XRBs in nearby galaxies because of its high angular resolution. The sub-arcsecond imaging allows us to pair X-ray images with optical images of the same area to identify the optical counterpart to the X-ray source, which would be the companion star in HMXB systems (e.g. Williams et al., 2014a, 2018). As described in Section 1.2, HMXB systems are grouped mostly on the properties of their companion stars, making this identification of the companion star crucial for understanding these systems and using their observed properties to constrain our understanding of massive binary stellar evolution.

Launched in 2012, *NuSTAR* is a focusing high energy X-ray telescope that operates from 3 to 79 keV (Harrison et al., 2013). While the angular resolution of *NuSTAR* is much worse (the full width half maximum of the PSF core is $18''$) than that of Chandra, the hard X-ray coverage of *NuSTAR* makes it an invaluable tool for studying accreting compact objects. Spectral differences between accreting neutron stars and black holes at hard X-ray wavelengths (E>10 keV) can be exploited to distinguish between types, and even accretion states, of compact objects for whole populations of X-ray binaries observed with *NuSTAR* (e.g. Wik et al., 2014; Yukita et al., 2016; Vulic et al., 2018; Lazzarini et al., 2018, 2019). Along with the companion star, characterizing the compact object in HMXB systems is critical for constraining our models of massive binary stellar evolution.

To study the companion star to the accreting compact object and an HMXB's parent stellar population, we must turn to longer wavelengths (near infrared, optical, near ultraviolet) where main sequence and evolved stars emit most of their light. Resolved stellar populations, observations in which individual stars can be resolved, are critical for identifying and characterizing the companion star to the compact object and tying the HMXB to its parent stellar population. Resolved stellar

populations can be used to measure the star formation history, a measurement of the star formation rate over time, in different spatial bins across the galaxy. This spatially resolved star formation history can then be used to measure the ages of HMXB systems and the overall HMXB production rate of the galaxy.

Much of the pioneering work pairing X-ray and optical observations of extragalactic HMXB populations has been done in the Small and Large Magellanic Clouds. Due to their proximity, the stellar populations of these galaxies can be resolved from the ground, allowing for the identification of the companion stars in HMXB systems and the creation of spatially resolved star formation history maps. X-ray observations from *Chandra* were paired with ground-based observations to identify HXMB companion stars in the Small and Large Magallanic Clouds (Antoniou et al., 2010; Antoniou & Zezas, 2016). These observations were paired with spatially resolved star formation history maps (Harris & Zaritsky, 2004) to determine the dominant ages of the HMXB populations in these galaxies and calculate an HMXB production rate (Antoniou et al., 2019).

Combining observations taken in multiple wavelength regimes gives us a fuller picture of HMXB systems – allowing us to characterize both the accreting compact object, its stellar companion, and the system's parent stellar population. With these observations, we can determine the HMXB production rate for an individual galaxy and characterize the HMXB population demographics including the X-ray luminosity of each system, its likely age, the physical properties of the companion (mass, temperature, radius, etc.), and compact object type for all or a subset of HMXB systems, depending on the coverage of different wavelength observations. These population demographics can then be compared directly with model populations produced with binary population synthesis, which will be discussed in the future work portion of Chapter 7.

I have spent the past six years reducing X-ray observations from *Chandra* and *NuSTAR*, identifying and characterizing HMXB companion stars, and classifying compact objects using their *NuSTAR* colors and luminosities. While my first few years were spent deep in the world of data processing pipelines, code-debugging, cross matching source catalogs, and more, I feel like I have finally started to see the forest from the trees. These observations are powerful, and the exquisite observations I have been able to use for my thesis are providing us our first look at a full population

of extragalactic HMXBs in this much detail. I am excited to continue working in this field after I graduate. I plan to do a similarly detailed characterization of the HMXB population in M33, get more detailed spectroscopic observations of HMXB companion stars in M31 and M33, and use all of the population demographic constraints to make some of the first measurements of parameters describing key phases of massive binary evolution that have been made with these types of observations. This work will deepen our understanding of massive binary stellar evolution, help us understand how many binary compact object mergers we are observing with gravitational waves formed via isolated binary stellar evolution, and provide strong orthogonal constraints to these parameters, which have previously only been constrained using observed gravitational wave merger rates.

1.4 Outline of Thesis

In the rest of this thesis, I will discuss observations and characterization of the HMXB populations of M31 and the Small Magellanic Cloud. I will also discuss work using optical observations of M33 to measure its spatially resolved recent star formation history. Finally, I will summarize previous chapters and discuss future work which will use the HMXB characterization in this thesis along with some future work to constrain theoretical models of massive binary stellar evolution.

1.4.1 Chapter 2 Summary

In Chapter 2, I will present results from the *Chandra*-PHAT survey. The *Chandra*-PHAT survey covered roughly one third of the star forming disk of M31, using seven pointings from the *Chandra* X-ray Observatory. The survey was designed to overlap with the Panchromatic *Hubble* Andromeda Treasury (PHAT), a deep survey that covered one third of the star forming disk of M31 in six photometric bands from near infrared to near ultraviolet wavelengths. The *Chandra*-PHAT survey produced an X-ray source catalog with roughly 300 sources, of which about 60 were identified as potential HMXBs due to their point source optical counterparts. The *Chandra*-PHAT source catalog provides the X-ray data used in my analysis in Chapters 3 and 4, which involve multi-wavelength analysis of these sources. In Chapter 2 I present the observations, how optical

counterparts were identified, and preliminary analysis to identify high quality HMXB candidates and determine their ages.

1.4.2 Chapter 3 Summary

In Chapter 3 I present analysis on a sample of 15 HMXB candidates in M31 for which overlapping *Chandra*, *Hubble*, and *NuSTAR* observations are available. With these overlapping observations we are able to infer the compact object type, spectral type of the companion star, and age of the system. The hard X-ray colors and luminosities from *NuSTAR* permit the tentative classification of the accreting compact object by comparing with Galactic XRBs of known compact object type. We describe comparisons between the compact object types and optical counterparts of the sources in our sample. We also determine the likely spectral type for the companion stars by performing spectral energy distribution (SED) fitting using the photometry for the companion stars from the PHAT survey. We use the spatially resolved recent star formation history of M31 to determine ages for individual systems and present the age distribution for sources in our sample.

1.4.3 Chapter 4 Summary

In Chapter 4 I present multi-wavelength characterization of the 57 HMXB candidates identified with observations from the *Chandra*-PHAT survey. These are X-ray sources that were observed by *Chandra* that had point source optical counterparts in the PHAT imaging. We fit the SEDs for the HMXB optical counterparts using the Bayesian Extinction and Stellar Tool (BEAST) and use the best fit luminosity, effective temperature, and radius to determine the most likely spectral type. We then combine these best fit values with local star formation histories, dust maps of M31, published X-ray spectral fits from *XMM-Newton*, infrared colors from PHAT, and hardness ratios from the *Chandra*-PHAT catalog to determine our best sample of HMXB candidates. We then use this best sample to determine the age distribution of HMXBs in M31 and the HMXB production rate, both as a function of time and over the last 50 and 80 Myr.

1.4.4 Chapter 5 Summary

In Chapter 5 I present results from the Small Magellanic Cloud (SMC) NuSTAR Legacy Survey, a set of deep (1 Ms) observations of three fields along the bar of the Small Magellanic Cloud. These fields were chosen for their young stellar and accreting binary populations. We detected 10 sources above a 3σ significance level in the full $4-25$ keV band and obtained upper limits for an additional 40 sources. We reached a 3σ limiting luminosity in the $4-25$ keV band of $\sim 10^{35}$erg s^{-1}, allowing us to probe fainter X-ray binary populations than has been possible with other extragalactic *NuSTAR* surveys. We used hard X-ray colors and luminosities to constrain the compact objet type, exploiting the spectral differences between accreting black holes and neutron stars at E$>$10 keV. Several of our sources demonstrate variability consistent with previously observed behavior. We confirmed pulsations for seven pulsars in our 3σ sample. We present the first detection of pulsations from Be-XRB SXP 305 (CXO J005215.4$-$73191), with an X-ray pulse period of 305.69 $\pm$ 0.16 s and a likely orbital period of $\sim$1160$-$1180 days. Bright sources ($\gtrsim 5 \times 10^{36}$ erg s^{-1}) in our sample have compact object classifications consistent with their previously reported types in the literature. Lower luminosity ($\lesssim 5 \times 10^{36}$ erg s^{-1}) sources have X-ray colors and luminosities consistent with multiple classifications. We raise questions about possible spectral differences at low luminosity between SMC pulsars and the Galactic pulsars used to create the diagnostic diagrams.

1.4.5 Chapter 6 Summary

In Chapter 6 I present the spatially resolved recent star formation history of M33, which was measured using optical images taken with the Hubble Space Telescope as part of the Panchromatic Hubble Andromeda Treasury: Triangulum Extension Region (PHATTER) survey. We fit color magnitude diagrams in approximately 2000 regions that measure 100 pc by 100 pc. There are significant fluctuations in the SFH on small spatial scales but there are also galaxy wide fluctuations in the SFR that we measure back to about 500 Gyr ago. We observe morphological evolution of M33. Most notably, we observe the emergence of a more flocculant spiral structure around 80 Myr ago, before which the structure of M33 is dominated by two spiral arms. We also observe a bar

in the center of M33, which dominates at ages older than about 80 Myr ago. Finally, we find that the mean SFR over the last 100 Myr in within the PHATTER footprint in M33 is 0.33 ± 0.02 $M_{\odot}$ yr^{-1} . We measure a current SFR within the PHATTER footprint of M33 (over the last 10 Myr) of 0.21 ± 0.03 $M_{\odot}$ yr^{-1} . This SFR is slightly higher than previous measurements from broadband estimates, when scaled up to account for the fraction of the D25 area covered by the PHATTER survey footprint.

1.4.6 Chapter 7 Summary

In Chapter 7 I present a summary of major findings from this thesis and present some ongoing and future work. The overall goal of my future work is to perform detailed statistical fitting of the observed and theoretical populations to obtain a measurement of the common envelope efficiency and supernova kick magnitudes for the HMXB populations in M31, M33, and the SMC. I will use theoretical simulations of binary stellar populations, binary population synthesis (BPS) to create and evolve massive binary stellar populations for comparison with our observed populations in M31, M33, and the SMC. I plan to characterize the HMXB population in M33 using a similar approach to Chapter 4 using the new PHATTER photometry and star formation history maps from Chapter 6. Additionally, I plan to obtain spectroscopy that I can use to confirm stellar spectral types of companion stars that were fit with photometry using the BEAST. For companion stars that are bright enough, I also plan to obtain time resolved spectroscopy to determine orbital periods, as these can also be compared directly with the theoretical binary populations produced via BPS.

Chapter 2

COMPARING *CHANDRA* AND *HUBBLE* IN THE NORTHERN DISK OF M31

Portions of this chapter were originally published in collaboration with Benjamin F. Williams, Paul P. Plucinsky, Manami Sasaki, Vallia Antoniou, Neven Vulic, Michael Eracleous, Knox S. Long, Breanna Binder, Julianne Dalcanton, Alexia R. Lewis, and Daniel Weisz in the November 2018 edition of the Astrophysical Journal (Williams et al., 2018, The Astrophysical Journal Supplement Series, Vol. 239, 13; 2018 © American Astronomical Society, DOI: 10.3847/1538-4365/aae37d), and are reproduced below with the permission of the American Astronomical Society.

2.1 Introduction

X-ray sources probe the most exotic forms of matter in the universe. Those outside of active galactic nuclei, such as X-ray binaries (XRBs) and supernova remnants (SNRs), can only be detected in nearby galaxies. Chandra and XMM-Newton can resolve hundreds of individual stellar-mass X-ray sources in Local Group galaxies, but outside of the Magellanic Clouds, the identification of counterparts for these stellar mass X-ray sources has been hampered by low spatial resolution X-ray data, difficulty separating background galaxies from stars in optical imaging, and stellar crowding.

Over the past decade, our ability to identify high-quality counterpart candidates for X-ray sources outside of the Galaxy and Magellanic Clouds has improved greatly due to the combination of high spatial resolution X-ray imaging with Chandra and resolved stellar photometry with the Hubble Space Telescope (HST). Populations of OB star and background galaxy counterpart candidates have been classified out to distances of 3 Mpc, in particular, M31 (770 kpc; Williams et al., 2005b,c,a; Hatzidimitriou et al., 2006; Williams et al., 2014a), NGC 300 (2 Mpc; Binder et al., 2012), NGC 2403 (3 Mpc; Binder et al., 2015), and NGC 404 (3 Mpc; Binder et al., 2013).

As the nearest massive spiral, M31 has been observed extensively in X-rays. Building on early surveys with the Einstein observatory (van Speybroeck et al., 1979) and ROSAT (Supper et al., 1997, 2001), XMM-Newton has mapped the entire interior of the D_{25} isophotal contour (Pietsch et al., 2005; Stiele et al., 2011, hereafter S11), and Chandra has observed the inner disk with the HRC (Williams et al., 2004a), mapped portions of the disk with ACIS (Di Stefano et al., 2004; Vulic et al., 2016), and monitored the bulge and nuclear regions for over a decade (Kong et al.,

2002; Kaaret, 2002; Garcia et al., 2010; Li et al., 2011). These surveys have detected dozens of transient X-ray sources, and thousands of persistent sources.

Most of the known X-ray sources are unidentified, but many are consistent with emission originating from background active galactic nuclei (AGNs). Others are clearly matched to bright Milky Way foreground stars. However, the most interesting sources are those that may truly be in M31. Pietsch et al. (2005) and S11 provided hundreds of source classifications based on variability and hardness ratios, and they identify dozens of SNRs and XRB candidates based on cross-matching with bright stars and star clusters from ground-based imaging and catalogs. With all of this work, only two strong high mass X-ray binary (HMXB) candidates were seen (sources 1579 and 1716 in S11), potentially because of the difficulties of identifying stellar counterparts in the crowded M31 with the spatial resolution available in these data. By comparing the XMM-Newton catalogs and ground-based photometry, Williams et al. (2014a) obtained spectra of dozens of optical counterpart candidates in the M31 field, finding few, if any HMXBs. Most of their spectra showed the counterparts to be background AGN, even though they were targeted to be blue point sources in ground based imaging.

While all of this work has significantly advanced our knowledge of M31's X-ray source populations, at this point it remains unclear what fraction of the known X-ray sources actually belong to M31 and which of the sources are background galaxies being viewed through M31. It is also unclear what the nature of most M31 sources is.

The very recent HST survey of the northern half of M31, the Panchromatic Hubble Andromeda Treasury (PHAT; Dalcanton et al., 2012; Williams et al., 2014b), offers an opportunity to remedy this situation. PHAT is the largest HST mosaic ever assembled, covering a large fraction of the northern M31 disk in 6 HST filters from the near ultraviolet to the near infrared, supplying photometry for over 100 million stars. The high-resolution imaging provides the opportunity to find high-quality counterpart candidates for background galaxies and HMXBs. The resolved photometry allows us to determine the physical characteristics of the stellar populations surrounding the X-ray sources.

In addition to allowing us to optically identify background galaxies, we expect the PHAT (Dal-

canton et al., 2012; Williams et al., 2014b) footprint to contain $\gtrsim$ 20 HMXBs. Measurements of the star formation rate in M31 (Williams, 2003; Lewis et al., 2015) are $\sim$0.3 $M_\odot$ yr^{-1} in the PHAT footprint. The scaling relation between SFR and HMXBs (Grimm et al., 2003) implies $\sim$20 HMXBs with $L_X > 10^{36}$ erg s^{-1} should be associated with that amount of star formation, and the scaling relation in the Magellanic Clouds (Antoniou et al., 2010) suggests $\sim$100 Be-XRBs. Only a fraction of these ($\sim$20) are expected to have high X-ray luminosities, usually associated with accretion disk systems (i.e., fed by Roche-lobe overflow). Combining the catalogs of Binder et al. (2015) with the optical catalogs from the ANGST program (Dalcanton et al., 2009) suggests a scaling relation between the number of OB stars with $M_V < -1$ and the number of bright HMXBs ($L_X > 10^{36}$ erg s^{-1}). There are $\sim 8\times10^4$ such stars ($m_{f475w} < 23.55$, $m_{f475w} - m_{f814w} < 0.5$) in the PHAT footprint, which implies $\sim$30 bright HMXBs. Finally, the summed spectra of sources with $L_X \sim (5\text{–}10)\times10^{35}$ ergs s^{-1} has a photon index consistent with neutron star HMXBs (see Figure 6 of Shaw Greening et al., 2009), consistent with this estimate.

So, where are the bright HMXBs in M31? Perhaps they are being missed due to stellar crowding in the M31 disk. To better localize the X-ray sources, we have undertaken a Chandra survey covering much of the PHAT survey area. We designed our survey to provide the largest number of precise positions for the least amount of *Chandra* time. Our final observations achieved a $0.35-8$ keV depth of 3×10^{-15} erg cm^{-2} s^{-1} (assuming a power-law spectrum with an index of 1.7 and N_H=7×10^{20} cm^{-2} (as in, e.g., S11), which corresponds to $\sim 3\times10^{35}$ erg s^{-1} at the distance of M31 (770 kpc, McConnachie et al., 2005). This depth should allow us to detect dozens of HMXBs and provide a reliable test of the predicted numbers.

Low-mass X-ray binaries (LMXBs) are not as simple to identify, even with *HST* imaging, as their optical counterparts are too faint to be distinguished. However, based on the stellar mass maps from PHAT (Williams et al., 2017), there are $\sim 2\times10^{10}$ $M_\odot$ in the region covered by our X-ray data, suggesting a LMXB population with $L_X > 3\times10^{35}$ erg s^{-1} of $\sim$100 according to the LMXB X-ray luminosity function (XLF) from Lehmer et al. (2014). By identifying a large fraction of the other sources, we can test this prediction for consistency.

By combining Chandra positions with HST imaging, we simultaneously limit the number of

potential counterpart candidates, identify the most likely counterpart to the X-ray source based on HST photometry, and easily resolve many background galaxies, which we expect to dominate the X-ray catalog. For the best X-ray binary candidates, the same data set can be used to constrain the progenitor age, physical characteristics of the secondaries, and provide targets for follow-up optical spectroscopy to measure orbital periods. Ideally, time-resolved spectroscopy of the resulting catalog will ultimately provide clean age and orbital period distributions for a sample of M31 X-ray binaries, which can also be tied to the properties of their local stellar populations. Such a sample will provide quantitative tests for predictions of HMXB production from binary evolution models.

In this chapter, we present our initial catalog, counterpart candidates, and measure the age distribution of HMXB candidates. In Section 2, we describe the observations of our Chandra survey of the PHAT region, as well as our data reduction technique for measuring the X-ray sources and aligning the Chandra data to PHAT directly. In Section 3, we present our Chandra catalog, cross-matched with the XMM-Newton catalog of S11. We include the most likely optical counterparts in cases where a likely counterpart is present in the HST data. In Section 4, we describe some of the most interesting counterpart candidates, including the best HMXB candidates, and in Section 5 we summarize our work.

2.2 Observations and Reductions

In October of 2015, we observed the PHAT footprint with Chandra with 7 pointings. The footprints are overlaid on a GALEX NUV image of M31, along with the corresponding HST coverage, in Figure 2.1. Using the S11 catalog, we found that by obtaining 25 counts for each 5×10^{-15} erg cm^{-2} s^{-1} source, we would achieve excellent efficiency in measuring positions, and we would detect fainter sources (down to a faint limit of $\sim10^{-15}$ erg cm^{-2} s^{-1}) near the field centers. Therefore, at each pointing we observed for about 50 ks in VF mode. These 7 observations are summarized in Table 2.1.

2.2.1 X-ray Photometry

We processed these observations independently using CIAO 4.7 with CALDB version 4.6.7 (Fruscione et al., 2006). We first generated exposure maps and images of the counts covering the full detector with 0.492″ pixel resolution using the task *fluximage*. We made corresponding maps of the point spread function using *mkpsfmap*. These were put through the task *wavdetect* using the default parameters, and searching on scales of 1, 2, 3, 8, and 16. The output source regions were then overplotted on the images and inspected by eye to assure that no obvious sources were missed and that all sources appeared to correspond to true overdensities of counts. At the same time, we ensured that sources appearing in multiple observations were noted so that they would appear in our catalog only once, but their measurements in each observation were kept separate to assess variability and position uncertainty. This process resulted in a total of 373 unique detected sources.

Once we had measured the source positions using the initial Chandra astrometric solution that came with the data products, we used the ACIS-Extract (Broos et al., 2010) package (version 4994, 2016-09-22) to measure the positions and photometry at all of these locations in the data. We ran ACIS-Extract iteratively, including the task `fit_positions`, to ensure that the software converged on the position of each source on the ACIS-I detector. We looked at multiple possible source positions for each source ("data mean, correlation, and maximum-likelihood reconstruction") in each iteration, and we found that the data mean position both appeared most centered on the sources and converged reliably for all but the faintest, most off-axis sources. We show the impact of our iterative technique in Figure 2.2, where we compare the difference in the data mean positions of the sources between the first two iterations in one panel and the last two iterations in another panel. Source names were generated by ACIS-Extract from the input X-ray source positions.

While most sources were observed in only one observation, many were in overlapping regions, allowing multiple measurements. In these cases, the position and position error are from the best (most on-axis) measurement, as are all of the other values in our final catalog.

This process resulted in a limiting flux of 3×10^{-15} erg cm^{-2} s^{-1}.

2.2.2 *Alignment to PHAT*

The PHAT data have astrometric accuracy of ∼10 milliarcsec (Williams et al., 2014b), while typical raw Chandra data have a 90% accuracy of ∼800 milliarcsec[1]. To greatly improve the astrometry of the Chandra data, we aligned the initial source catalog to the PHAT imaging data using the optimized Chandra centroids. We visually inspected all positions on the PHAT imaging data, making note of which sources corresponded to a clear foreground star, star cluster, or bright background galaxy. Examples of these objects are shown in Figure 2.3. We then used the IRAF task *ccmap* to reset the astrometric solution of the *Chandra* data to force these positions to align with their counterparts in the PHAT catalog. The 26 sources used for alignment are provided in Table 2 of the online published paper version of this chapter so that it is clear which sources were forced to match the PHAT positions. All Chandra observations had at least 3 alignment sources, and the corrections were all $<1''$.

We fit the positions allowing for rotation, translation, and pixel scale adjustments. However, we checked that the solution recovered a pixel scale of $0.492''$ (the known Chandra plate scale). Since there is little chance that $0.492''$ in both the X and Y pixel direction would be the best-fit pixel scale if the matched sources were incorrect, our recovery of this pixel scale provided confirmation that the matched sources we used were correctly identified. For background galaxies, we assumed that the X-ray source corresponds to the center of the background galaxy. If the true positions of the X-ray sources were far off the galaxy center, the fit to the pixel grid would be poor (X and Y plate scales would not likely match). Smaller offsets from the center could go unnoticed, but they would contribute to the RMS scatter in the fit, which is included in the errors.

The RMS of the astrometric solution returned by *ccmap*, suggests that the *Chandra* sources are aligned to the PHAT imaging to a precision of better than $0.1''$ (see Table 2.1). We have used the position uncertainty formula of Kim et al. (2004) to calculate the positional uncertainty for the catalog, setting our floor term to the alignment uncertainty between *Chandra* and PHAT for each observation provided in Table 2.1.

---

[1] http://cxc.harvard.edu/cal/ASPECT/celmon/

2.2.3 *Counterpart Candidate Identification*

We plotted 1, 2 and 3 σ error circles for the Chandra X-ray sources on the PHAT mosaic images. These were plotted independently for each observation so that sources detected in multiple observations served as a consistency check on our positional alignment to PHAT, and counterpart candidate. We examined the X-ray image, color PHAT image, and UV-only PHAT image at each X-ray source location. We made a note of any interesting counterpart candidates, which included bright stars, blue stars, UV-bright stars, star clusters, or background galaxies.

When searching for point source counterparts, we made color-magnitude diagrams (CMDs) and color-color diagrams of the stars in the PHAT catalog within 3σ of the Chandra source position in F336W-F475W, F475W-F814W, and F110W-F160W. We inspected these diagrams to look for sources with colors that placed them off of the main CMD features of the survey, or on the upper-main sequence, where the optical counterparts of HMXBs would tend to reside. Because HMXBs have massive secondary stars, if the secondary dominates the optical light, they would reside on the main sequence in these CMDs; however, because the primary could have a bright accretion disk that may irradiate the secondary or produce emission lines, they could be pushed away from the stellar locus on such CMDs. Examples of these CMDs are shown in Figure 2.4, where we have plotted points for all sources in the error circle with measured F336W and F475W magnitudes and marked with a star the counterpart candidate we chose by eye. The color-color diagram of all of our final point source counterpart candidates is shown in Figure 2.5. Figure 2.4 shows an example of each category of point source counterpart candidate: those with upper-main sequence colors, those with unusual colors, and those not associated with a young population. The unusual colored source has a UV color (upper-left panel) that is typical of an upper-main sequence star, but its optical color is quite red, more like a red He-burning star or red supergiant. Such figures are available for all of the sources in the supplemental material available online [2], and point source counterpart candidates from the PHAT catalog are marked as in the Figure 2.4 example.

The selection of counterpart candidates was iterative. Two people searched the images and

[2] https://iopscience.iop.org/article/10.3847/1538-4365/aae37d

CMDs independently, compared notes, and re-examined the positions of sources where there was initial disagreement until the two lists converged on a set of candidates. Table 4 of the electronic version of Williams et al. (2018)[3] gives brief notes on the sources from this process. When the process was complete, each X-ray source either had one optical source that appeared to be a good candidate (bright star, star cluster, or blue star, UV-bright star, or background galaxy), or no such candidate. Objects with no such candidate could be either highly-extincted (e.g., embedded HMXB, or AGN behind M31 dust), or too faint in the optical to be detected (e.g., faint AGN or LMXB). While our error circles typically contained dozens or more M31 stars, these stars were nearly all similar to the red giant branch stars that are common throughout the galaxy. We chose only point source candidates that stood out as being brighter and bluer either in the UV or optical than the stars in the surrounding area of the field. The chances of such an object being within our rather small error circles by chance was relatively low. Objects of comparable colors and magnitudes have surface densities of $\sim 10^{-2}$ arcsec^{-2} in PHAT, and our error circles were typically $\lesssim 2$ arcsec^{-2}, leaving only about a 2% chance of false positives.

Resolved galaxies are difficult to find in an automated way, since they are faint and diffuse and are not properly detected or measured in point source optical catalogs of resolved stars such as that of Williams et al. (2014b). For example, we cross-correlated our by-eye background galaxies with those identified by the Andromeda Project (AP; Johnson et al., 2015), which was a crowd-sourcing project in which the public identified star clusters in the PHAT imaging data. As a secondary option, users could also mark background galaxies. They found thousands of relatively bright galaxies in the PHAT footprint visible in the F475W and F814W bands, 28 of which are in the 1σ error circles of X-ray sources in the full sample. However, we have found that many of the other 79 background galaxies that coincide with X-ray source positions are very faint and would likely be missed by those not looking for something specifically at these locations. Furthermore, many of these galaxies have most of their flux in the F160W band, likely because of high absorption in the optical through the M31 disk. AP limited their search to the F475W and F814W imaging, and

[3] https://iopscience.iop.org/article/10.3847/1538-4365/aae37d#apjsaae37dt4

therefore has likely missed many of these very red background galaxies.

Example images of background galaxy candidates are provided in Figure 2.6, and all such images are included in the supplemental data. Figure 2.4 presents an example finding chart from the PHAT data; the supplemental data include these for all of the sources in the catalog. These finders allow catalog users to assess for themselves the veracity of any chosen counterpart candidate.

2.2.4 Catalog Cross-Matching

We cross-correlated all of these sources with the most recent XMM-Newton catalog (S11) for simple consistency comparisons. This catalog has a limiting sensitivity of 10^{-15} erg s cm^{-2} in the 0.2-4.5 keV band. We matched all sources within 5″ of an XMM-Newton source to allow for the XMM-Newton PSF size. These matches are all included in our catalog. There were 311 S11 sources within our survey area. We matched 203 of the Chandra sources to 202 of the S11 sources (S11 1848 matched to both CXO J004648.19+420855.4 and CXO J004648.27+420851.1). To more directly compare our fluxes with previous data from XMM-Newton, we used WebPIMMS to determine conversion factors between ACIS-I count rates in our bands and the S11 0.2-4.5 keV band assuming a power-law spectrum with an index of 1.7 and N_H=7$\times$10^{20} cm^{-2}.

A large fraction of fainter the sources in this M31 field vary in brightness on long timescales such that they are not detected in all observations. While we found excellent overall agreement for the 203 matched sources, as shown in Figure 2.7, the scatter is sometimes beyond the uncertainties due to intrinsic variability of sources. Moreover, most of the fainter sources were only detected in one set of observations. There are 170 sources in our catalog that are not in S11, and 168 of these have 0.35-8 keV fluxes below 1.5$\times$10^{-14} erg cm^{-2} s^{-1} ($\sim$10^{36} erg s^{-1}). Many of these were likely fainter during the XMM-Newton observations, since the XMM-Newton observations were sensitive to sources of this brightness. In the other direction, there were 109 sources in the S11 catalog in our fields that were not detected by our observations, and 104 of these had 0.2-4.5 keV fluxes below 1.5$\times$10^{-14} erg cm^{-2} s^{-1}. The similar numbers suggest that variability on $\sim$10 year timescales (S11 observations were taken from 2000$-$2008) is the main cause for the differences. Such variability at the faint end is similar to that seen in a dedicated study of the variability of the

XLF in NGC 300 (Binder et al., 2017), where a large fraction of the sources below 4×10^{36} erg s^{-1} varied significantly between epochs. X-ray binaries and AGNs are known to vary on such long timescales (e.g., Mushotzky et al., 1993; McHardy et al., 2005; Kotze & Charles, 2012); however, the photon statistics on the flux measurements are severely limited for these faint sources in M31, making it difficult to quantify their variability. These detections are faint, and only put a lower-limit on their amplitude. It is possible that some of these sources could be truly transient, and change in brightness by more than a factor of 100. More detailed variability analysis of sources in this region detected by XMM will be provided in Sasaki et al. (2018, A&A, submitted), as their more sensitive observations allow for more precise measurements of the X-ray flux.

Two of the brightest sources not seen by both surveys are previously-designated transient outbursts. The brightest source in S11 that is not in our catalog was S11 1416, which had a 0.2-4.5 keV flux of 8.55×10^{-14} erg cm^{-2} s^{-1}, and was shown by them to be a known transient associated with a nova. The brightest source in our catalog that was not in S11 (CXO J004420.54+413702.3) was designated a transient source by Swift (Henze et al., 2015). This source had a 0.2-4.5 keV flux of 3.5×10^{-13} erg cm^{-2} s^{-1} in our observations. We found no clear optical counterpart candidate for this source inside of its very small error circle, suggesting it is a low-mass X-ray binary.

The only other bright source that does not appear in both catalogs is CXO J004427.13+412258.2, which does not appear in any previous X-ray catalog of M31. This source has a good point source counterpart candidate. In this case, the counterpart candidate is a bright red star, undetected in the UV. The PHAT photometry places it above the tip of the red giant branch, and it is in a region with a high star formation rate. This could be a potential supergiant X-ray binary, and would be of particular interest for spectroscopic follow-up.

2.3 Results

Our final source catalog columns are described in Table 2.2, and the values are provided in Table 4 of the electronic version of Williams et al. (2018)[4], including all of the X-ray measurements for

[4] https://iopscience.iop.org/article/10.3847/1538-4365/aae37d#apjsaae37dt4

each source found in our 7 observations, the mean extinction at that location in M31, a one letter code for our best optical counterpart candidate determination, and descriptions from the visual inspection of the PHAT images. We discuss the characteristics of the sources in detail below.

2.3.1 X-ray Properties

The main goal of this work was to provide exquisite astrometry for the X-ray sources. We did not acquire deep enough data for detailed spectral analysis of the sources. Much of this work is in a complementary XMM-Newton program (Sasaki et al., 2018). However, we did measure fluxes in many energy bands, allowing us to examine hardness ratios in the context of the counterpart candidate types. In Figure 2.8, we plot the hardness ratios of sources with >20 counts (0.35-8 keV, $\sim$1.2e-14 erg cm^{-2} s^{-1}) in our data, color-coding the points by the candidate type. We use fluxes in: S=0.35$-$1 keV, M=1$-$2 keV, and H=2$-$8 keV. We see the well-known separation of SNRs and foreground stars which are soft (Pietsch et al., 2005; Tüllmann et al., 2011), congregating at or below (M-S)/(H+M+S) values of -0.25; however, we also see that all of the hardest sources ((H-M)/(H+M+S) >0.8) with counterpart candidates are background galaxy candidates. While the uncertainties in these ratios, which are$\pm\sim$0.2, make it difficult to reliably separate source types in this crowded part of the diagram, this distribution hints that sources with very high (H-M)/(H+M+S) ratios may be more likely to be background galaxies. More sensitive observations would be necessary to confirm such a possibility.

2.3.2 Optical Counterpart Candidates

We found optical counterpart candidates from the PHAT data for 188 sources. These include 6 SNRs, 5 star clusters, 12 foreground stars, 107 resolved background galaxies, and 58 point sources. There were also 185 sources with no clear PHAT counterpart candidate. Below we discuss each of these source types in turn.

Supernova Remnants, Star Clusters, and Foreground Stars

The SNRs and foreground stars are relatively easy to distinguish in our survey due to their soft X-ray spectra, and their clear detections in radio (e.g., Braun, 1990; Kong et al., 2003; Williams et al., 2004b; Galvin & Filipovic, 2014) and/or narrow-band optical wavelengths (Lee & Lee, 2014, e.g.,).

Six previously-known SNRs were detected in our survey. Table 5 of the online published version of Williams et al. (2018) (linked at the beginning of this section) lists the catalog name of the detected SNRs, the S11 source ID #, if the remnant was detected in the radio or the optical, the Lee & Lee (2014) identification number if it exists, the counts in the 0.35-8.0 keV band, the absorption-corrected luminosity in the 0.35-8.0 keV band, if the source shows extent beyond that expected for a point source and if there is any evidence of hard emission (>2.0 keV). The source extraction region created by ACIS-Extract was examined and adjusted to be larger for these six objects if there was flux outside of the extraction region. As SNRs are not point sources, the measurements are much more reliable for these sources than those in the point source catalog.

Our survey was conducted with the ACIS-I array to maximize the field-of-view. Thus the sensitivity to soft sources such as SNRs is lower than with the S3 CCD on ACIS-S. However, the high angular resolution of the Chandra data enables a search for emission extended beyond that expected for a point source and a search for hard emission that might indicate the presence of a central compact object or pulsar wind nebula. Given that the detected counts range from ∼5 to 36, a spectral analysis is not feasible. However, the spatial distribution of the counts was examined for evidence of extended emission and the counts above 2.0 keV were examined for evidence of hard emission.

The sources CXO J004513.88+413615.7, CXO J004413.49+411954.1, and CXO J004451.06+412906.6 show evidence for extended emission, but given the limited number of counts it is difficult to estimate the size of the SNR in X-rays. A deeper observation close to on-axis would be required to characterize the spatial distribution as “shell-like” or “center-filled”.

Given that the detected counts range from ~ 14 to 83 counts, the luminosities were determined

by assuming an APEC model in XSPEC with a temperature of $\mathrm{kT} = 0.6\ \mathrm{keV}$, neutral hydrogen column density of N_H=$7.0 \times 10^{20}\ \mathrm{cm}^{-2}$, and solar abundances. We fit this model to the data with the only free parameter being the normalization. Two of the SNRs, CXO J004513.88+413615.7 and CXO J004451.06+412906.6, appear in more than one observation, such that the spectral data were combined from the two observations and weighted response files were created using specextract in CIAO. Of the six SNRs detected, only CXO J004451.06+412906.6 shows evidence for hard emission, there is a clear excess at high energies that can not be well fitted by an APEC model with $\mathrm{kT} = 0.6\ \mathrm{keV}$. Therefore a power-law component was added to the spectral model with a fixed index of $\Gamma = 2.0$ and a variable normalization. The hard counts appear to be centrally concentrated, whereas the soft counts appear around the periphery of the hard counts. A much deeper observation would be required to confirm this morphology. CXO J004451.06+412906.6 is a promising candidate for a central compact object and/or pulsar wind nebula.

The 5 star clusters were well known globular clusters. Two of our sources match to S11 sources that were globular cluster candidates in their survey, but do not appear as clusters in the PHAT data. Source 004343.00+412850.0, which matches to S11 source 1289, had a tentative S11 classification as a globular cluster, but the HST image shows a well-resolved background galaxy at the source location. Source 004353.65+411655.4, which matches to S11 source 1327 had a tentative S11 classification as a globular cluster, but the PHAT data shows no globular cluster at the X-ray source location. This source is particularly interesting as it is very bright in X-rays but has no outstanding optical source in the error circle. These traits may make this source an X-ray binary candidate.

The 12 foreground stars we detected have mostly been previously identified. These are easily seen from the ground as they appear very bright in the optical. Thirteen of the objects in our field matched to S11 are foreground stars. Eleven of the sources classified as foreground by S11 were independently matched to foreground stars by us. In 2 cases, sources that were classified as foreground stars in S11, were not classified as foreground stars by us. One of these (CXO J004541.06+412752.7) was outside of the PHAT footprint. The other
(CXO J004532.11+414527.4) is extended in the PHAT data, suggesting a background galaxy. In

one case, CXO J004604.55+414943.7, we see a foreground star, but S11 classified this object as a SNR candidate. The source is very far off axis, where the point spread function is $>8''$, so the position uncertainty is large and we cannot determine if the source is extended. The foreground star is just outside of the one-sigma position uncertainty, so this source classification is still quite uncertain.

One source was near a foreground star, but the small Chandra uncertainties show that it is unlikely to be associated. Source CXO J004427.13+412258.2 is just $1''$ away from of foreground star, but the star is clearly outside of our Chandra error circle, and the hardness ratio is harder than those of typical foreground stars. This source is a newly detected transient by our survey, and the PHAT data show a bright M31 star in the error circle, making it likely to be an X-ray binary in M31.

Background Galaxies

Figure 2.9 compares the 0.5-7 keV flux distribution of our galaxies (90% of the 0.35-8 keV flux) to the 0.5-7 keV flux distribution of the Luo et al. (2017) Chandra Deep Field catalog for fluxes $>3\times10^{-15}$ erg cm^{-2} s^{-1}. The distribution has been normalized so that both samples have a total of 1. The remarkable similarity suggests that our counterpart candidates are correct for these sources, and they are indeed background. Our high fraction of background galaxies (57% of our counterpart candidates) is consistent with statistical estimates for the background contamination in the M31 field. The 107 background galaxies we have identified can now be removed from studies attempting to obtain a cleaner sample of M31 X-ray sources. After removing the 188 sources with counterpart candidates from the sample, there are 185 sources without candidates. Based on scaling relations (e.g., Lehmer et al., 2014), we expect $\sim$100 LMXBs in this region based on the stellar mass. Thus, it is likely that about another hundred sources in our catalog are still unidentified background galaxies, which is also consistent with expectations from the Chandra Deep Field, as discussed below.

The by-eye search of the PHAT data identified resolved background galaxies for roughly half of the total number expected from deep field statistics. Because of the uncertain impact of the

presence of M31 on the detection of background sources, we can only make sensible estimates of the total number to expect as a consistency check. Based on the Chandra Deep Field (Luo et al., 2017), we expect about half of our survey area (roughly 0.2 deg^2) to be sensitive to background sources down to 0.35-8 keV fluxes of $\sim 3 \times 10^{-15}$ erg cm^{-2} s^{-1}. Luo et al. (2017) measured $\sim$1000 sources deg^{-2} down a 2-7 keV flux level of 10^{-15} erg cm^{-2} s^{-1}, suggesting that roughly 200 of the sources we detected are background galaxies. If there are another $\sim$90 background galaxies in our sample ($\sim$200-107), their host galaxies were too faint or too absorbed to be seen in the PHAT images. The A_V distribution of the source locations does not appear to have many areas of high extinction, so optical counterpart intrinsic faintness may be more to blame for non-detections than absorption. Some fraction of our point source candidates could also be AGN where the host galaxy was too faint in the optical for us to detect. In any case, the number of unidentified sources appears to be consistent with a combination of the expected number of LMXBs given the M31 stellar mass and the expected number of additional background galaxies from the Chandra Deep Field.

Among the large number of high-quality new galaxy candidates behind M31 we have found, one of our AGN had been previously identified by Williams et al. (2014a) as an HMXB candidate. In that study, spectra were obtained for blue sources detected in ground based images within the error circles of the XMM-Newton catalogs of M31. One of these was the strong S11 HMXB candidate 1716, which is our source CXO J004556.98+414832.0. The blue star was spectroscopically determined to be a high mass star in M31; however, in this case, the Chandra position and HST imaging reveals a red background galaxy at the position of the X-ray source, while the bright blue M31 star is about 2″ away from the Chandra position. Here is a case where the improved image quality revealed a complex location that was over-simplified with lower resolution X-ray and ground-based optical data.

Point Sources

In Table 2.3, we list the subset of sources with stellar counterpart candidates in the PHAT survey, along with the PHAT positions and photometry. Three of our sources (CXO J004537.84+414856.7, CXO J004537.67+415124.4, and CXO J004502.33+414943.1) contained both a UV point source

and a background galaxy in the Chandra error circle. In these cases, we made a note of the galaxy in the notes column; however, we take the UV emission as the strongest sign of the counterpart. Thus, these sources received "p" designations in the catalog, and we included these in our point source analysis. Figure 2.9 shows that the flux distribution of these sources differs from that of galaxies in that the point sources tend to be brighter, consistent with this sample is probing a separate population that contains a larger fraction of sources in M31.

The PHAT point source counterpart candidates mostly have non-standard colors. These colors made them stand out in the PHAT imaging allowing us to identify them as very good counterpart candidates because any contribution from an accretion disk or irradiation from the X-ray source may cause non-standard colors. As shown in Figure 2.5, some of the colors are consistent with the relatively flat spectral energy distributions expected for AGN, which argues against these objects belonging to M31. However, since these colors may also be due to a hot X-ray source in a binary system and these counterpart candidates are too optically bright to be low-mass X-ray binaries, we include all of these sources as potential high-mass X-ray binaries. We plot the X-ray fluxes vs. the optical (F475W) magnitudes of these sources in Figure 2.9, and the best HMXB candidates generally fall at lower X-ray fluxes than the other candidates.

For these PHAT point sources that were not clearly foreground stars (i.e. saturated sources with bright diffraction spikes), we studied the local stellar populations to shed light on their nature. In particular, we would expect HMXBs to reside in young regions. Thus, we used the star formation history results of Lewis et al. (2015) to constrain the age distribution of any co-located population of stars younger than 80 Myr. We then take the dominant age to be the most likely age of the HMXB system. Note that this is not the time since the binary began producing X-rays, but the time since the binary itself was formed. Source CXO J004339.06+412117.6 falls in the portion of the PHAT footprint that was considered too crowed to measure a reliable SFH, leaving 54 sources with local SFH measurements.

Using the local SFHs, we calculate an age probability distribution function. We limit the age as older ages can be significantly contaminated by unassociated stars, which could swamp the signal. In addition, neutron star and black hole primaries likely come from core-collapse SNe, which are

produced by stars in this age range. Thus, the main assumptions are that the source is an HMXB and that mass transfer onto the compact object began shortly after the compact object formed. We show a few examples of these star formation histories and age distributions in Figure 2.10.

HMXB ages, as inferred from their surrounding populations, provide sensitive tests of binary formation and evolution models. The theoretical work of Belczynski et al. (2008) shows the luminosity distribution to be sensitive to star formation history, and Linden et al. (2010) predict that higher metallicity populations of bright HMXBs will have a younger distribution than lower metallicity populations. These predictions have been qualitatively consistent with observations; for example, Antoniou et al. (2010) and Williams et al. (2013a) both find that HMXBs have preferred ages at $\sim$40-60 Myr, and Antoniou & Zezas (2016) find evidence for a younger HMXB population (6-25 Myr) in the higher metallicity Large Magellanic Cloud (LMC). In M31, we probe the highest metallicity (roughly solar; Venn et al., 2000; Gregersen et al., 2015) extragalactic HMXB sample yet, putting these predictions to an even stronger observational test. If HMXB ages are strongly influenced by metallicity then, since M31 generally has a higher metallicity than the LMC, we should see that in M31, HMXBs are very young (compared to the SMC and LMC).

From these stellar age distributions, we then calculated the stellar mass in each 0.1 dex wide age bin $<$80 Myr and divided it by the total amount of stellar mass $<$80 Myr old. This calculation provides the fraction of young stars in each bin, which is a proxy for the probability that the HMXB has that age. The result is a probability distribution function for the age of each HMXB candidate living in a population of stars with ages $<$80 Myr. These probabilities are provided in Table 2.4. If the counterpart is correct, then this result is our best estimate of the age of the progenitor of the compact object, and the X-ray source is likely an HMXB. In cases lacking a young population (denoted with a "c" in Table 2.3), the source is less likely to be an HMXB; however, the counterpart candidate is not ruled out, as it may be a background AGN with a very faint host, a more evolved lower-mass star, or a runaway massive star.

To investigate the age distribution of the HMXB candidates, we added the probability distributions together. Forty of the stellar candidates have a significant detection of a young ($<$80 Myr) population in the Lewis et al. (2015) maps. The sum of the probabilities provides an estimate of

the age distribution of our HMXB candidates. We show this distribution for the full sample of point source counterpart candidates, as well as our subsample of the best HMXB candidates in Figure 2.11. In each panel, the histogram shows the age distribution of the HMXB candidates, and the black lines show 50 draws of SFHs from random draws from the locations of X-ray sources associated with background galaxies in our catalog. We do not include LMXBs as a separate set of candidates here, as they are not distinguishable from undetected background galaxies in our data.

All random background galaxy locations show a higher probability of being older than 30 Myr than being younger. This result suggests that these slightly older populations spread over larger areas than the younger ones. There is a hint that the full point source counterpart sample has a higher fraction of areas with $\sim$20 Myr old populations than the control. If we are more conservative in our choice of candidates, choosing only candidates that looked particularly stellar or relatively blue in the PHAT images (marked with blue diamonds in Figure 2.5), we find the 8 marked with an 'a' in Table 2.3. Six of these have local SFH measurements, and all 6 are in regions with recent star formation. Their age distribution (right panel of Figure 2.11) has 2 ages: one at 15-20 Myr, and one at 40-50 Myr.

The 40-50 Myr peak is similar to that found for other samples of HMXB candidates in nearby galaxies, and may be attributable to the characteristic timescale for neutron star formation and B-star activity (Antoniou et al., 2010; Williams et al., 2013a). The 15-20 Myr peak is observed in the Large Magellanic Cloud (Antoniou & Zezas, 2016), and appears to coincide with a star formation episode 6-25 Myr ago. These results could be hinting that the star formation rate in M31 has been more continuous than in the much smaller SMC and LMC, allowing HMXBs to form at multiple ages, perhaps through multiple channels. Seeing both ages in M31 suggests that both formation timescales occur at high metallicity, which would point to differences between the Magellanic Cloud populations being more attributable to star formation history than to metallicity.

2.4 Conclusions

We have obtained *Chandra* imaging covering a large fraction of M31 with *Hubble Space Telescope* imaging obtained by the Panchromatic Hubble Andromeda Treasury (PHAT) survey. Combining

these data sets, we have produced a catalog of X-ray sources along with their most likely optical counterparts from HST. These optical counterpart candidate identifications allow background galaxies and high-mass X-ray binaries to be separated from other potential hard sources, such as low-mass X-ray binaries.

- We find that most counterpart candidates are resolved background galaxies, and that there are over 100 of these, which is consistent with the majority of X-ray sources in the M31 disk field being background contaminants if we assume a similar fraction of the sources with no counterpart candidate are undetected fainter background galaxies. This assumption is consistent both with the expected number of background galaxies estimated from the Chandra Deep Field and with the expected number of LMXBs estimated from the PHAT stellar mass.

- We find about a third of the point source counterpart candidates are not associated with any young stellar populations.

- The number of optical point source candidates (58) is larger than the expected number of bright HMXBs in this region, but it is similar to expectations if about half of the 40 candidates in regions with young stellar populations are indeed HMXBs.

- We find 8 of the point source counterpart candidates have colors typical of single stars, suggesting that many of the point sources in this sample are background galaxies. The number of good HMXB candidates is somewhat below the number expected from the star formation rate and number of OB stars in the region surveyed; however, some of the other point source candidates could be HMXBs with odd colors due to binarity. Further observations will be necessary to determine if M31 actually has as many bright HMXBs as predicted by scaling relations.

- We find that the age distribution of the young populations surrounding the point source counterpart candidates (including the 8 with typical star colors), is peaked at 15-20 Myr and 40-50 Myr in agreement with previous studies in other nearby galaxies (Antoniou et al., 2010;

Table 2.1. Chandra-PHAT Observations

ObsID	RA_NOM (deg)	DEC_NOM (deg)	ROLL_NOM (deg)	Date (YYYY-MM-DD)	Exptime (s)	RMS ($''$)
17008	11.06541197	41.38758162	181.58	2015-10-06	49141	0.08
17009	11.01739502	41.57751223	215.29	2015-10-26	49405	0.08
17010	11.24607031	41.53432975	202.70	2015-10-19	49423	0.07
17011	11.37564751	41.72352482	184.29	2015-10-08	49429	0.07
17012	11.19575165	41.86086452	196.22	2015-10-11	48440	0.05
17013	11.53451858	41.95795668	199.11	2015-10-17	44790	0.08
17014	11.58803371	42.15469119	180.22	2015-10-09	49139	0.08

Williams et al., 2013a; Antoniou & Zezas, 2016), but at higher metallicity, significantly impeding the searches for optical counterparts.

The production of this catalog was only the beginning of the Chandra-PHAT program. In Chapters 3 and 4 I present MCMC fits to the spectral energy distribution from the PHAT photometry of all of the sources within 3-σ of X-ray sources using the Bayesian Extinction and Stellar Tool (BEAST Gordon et al., 2016). These fits provide further confirmation of our original classifications presented here, and result in a few new classifications in cases where there were no obvious candidates in our CMDs or images. Furthermore, the SED fits allow us to provide physical parameters for the companion stars in these systems. In the future, follow-up spectroscopy of our optical point source candidates will help identify more HMXBs, type their secondaries, and measure orbital periods. In turn, we can use all of these measurements in addition to the local star formation histories to place new constraints on X-ray binary formation and evolution models by improving the statistics on their age and mass distributions which the models should reproduce.

.

Table 2.2. Chandra PHAT Catalog column names and descriptions

Column	Description
Src	Source number in this catalog
ObsID	Observation in which the source was measured
Catalog Name (CXO J)	Unique source identifier from coordinates. Prefix for all is CXO J.
RA	J2000 Right Ascension
DEC	J2000 Declination
σ [$''$]	X-ray position uncertainty in arcsec
Θ [$'$]	Off-axis angle in the Chandra observation in arcmin
Cts 0.35-8.0	Source Net Counts in the 0.35-8.0 keV band
Cts 0.35-1.0	Source Net Counts in the 0.35-2.0 keV band
Cts 0.5-8.0	Source Net Counts in the 0.5-8.0 keV band
Cts 0.5-1.0	Source Net Counts in the 0.5-1.0 keV band
Cts 1.0-2.0	Source Net Counts in the 1.0-2.0 keV band
Cts 2.0-4.0	Source Net Counts in the 2.0-4.0 keV band
Cts 2.0-8.0	Source Net Counts in the 2.0-8.0 keV band
Cts 4.0-8.0	Source Net Counts in the 4.0-8.0 keV band
Rate 0.35-8.0	ARF-corrected Count Rate in the 0.35-8.0 keV band
Rate 0.35-1.0	ARF-corrected Count Rate in the 0.35-2.0 keV band
Rate 0.5-8.0	ARF-corrected Count Rate in the 0.5-8.0 keV band
Rate 0.5-1.0	ARF-corrected Count Rate in the 0.5-1.0 keV band
Rate 1.0-2.0	ARF-corrected Count Rate in the 1.0-2.0 keV band
Rate 2.0-4.0	ARF-corrected Count Rate in the 2.0-4.0 keV band
Rate 2.0-8.0	ARF-corrected Count Rate in the 2.0-8.0 keV band
Rate 4.0-8.0	ARF-corrected Count Rate in the 4.0-8.0 keV band
PNS 0.35-8.0	The probability that no source was at this location in the 0.35-8.0 keV band
Flux 0.35-8.0	Energy flux (erg cm^{-2} s^{-1}) in the 0.35-8.0 keV band (Count Rate * 1.313E-11)
Flux 0.35-1.0	Energy flux (erg cm^{-2} s^{-1}) in the 0.35-1.0 keV band (Count Rate * 1.767E-11)
Flux 0.5-8.0	Energy flux (erg cm^{-2} s^{-1}) in the 0.5-8.0 keV band (Count Rate * 1.272E-11)
Flux 0.5-1.0	Energy flux (erg cm^{-2} s^{-1}) in the 0.5-1.0 keV band (Count Rate * 1.438E-10)
Flux 1.0-2.0	Energy flux (erg cm^{-2} s^{-1}) in the 1.0-2.0 keV band (Count Rate * 5.620E-12)
Flux 2.0-4.0	Energy flux (erg cm^{-2} s^{-1}) in the 2.0-4.0 keV band (Count Rate * 1.443E-11)
Flux 2.0-8.0	Energy flux (erg cm^{-2} s^{-1}) in the 2.0-8.0 keV band (Count Rate * 2.138E-11)
Flux 4.0-8.0	Energy flux (erg cm^{-2} s^{-1}) in the 4.0-8.0 keV band (Count Rate * 3.487E-11)
Flux 0.2-4.5	Energy Flux (erg cm^{-2} s^{-1}) in the 0.2-4.5 keV band (0.35-8.0 keV Count Rate * 9.416E-12)
XMM ID	Matched source identifier in S11
XMM Class	Source classification in S11
PHAT	Single letter PHAT counterpart code: n (none), g (galaxy), p (point/star), f (foreground), s (SNR), c (cluster)
A_V	Mean extinction from Dalcanton et al. (2015) maps
Notes	Notes from visual inspection of the PHAT images

Note. — Full electronic table with these columns available online at https://iopscience.iop.org/article/10.3847/1538-4365/aae37d (Table 4).

Table 2.3: PHAT Point Source Counterpart Candidate Multiwavelength Properties

Name (CXO J)	CXO R.A.	CXO Dec.	σ^b ($''$)	PHAT R.A.	PHAT Dec.	F275W	F336W	F475W	F814W	F110W	F160W	Flux 0.35-8.0
004339.06+412117.6^a	10.912737	41.354885	0.66	10.912961	41.354867	23.84	23.23	23.87	23.63	23.60	23.27	$4.9e-14^{+4e-15}_{-4e-15}$
004420.18+413408.2^a	11.084068	41.568957	0.55	11.084035	41.568901	21.60	21.59	22.58	22.19	21.89	21.67	$4.4e-15^{+1e-15}_{-1e-15}$
004445.88+413152.3^a	11.191148	41.531182	4.6	11.191047	41.531859	21.58	21.28	22.30	21.55	21.17	21.00	$6.2e-15^{+2e-15}_{-2e-15}$
004514.76+415034.5^a	11.311509	41.842926	0.77	11.311492	41.842875	18.94	19.17	20.57	20.49	99.999	99.999	$1e-14^{+2e-15}_{-2e-15}$
004536.13+414702.5^a	11.400529	41.784043	0.81	11.400650	41.784065	19.31	19.27	20.38	19.81	19.76	19.64	$3.2e-15^{+1e-15}_{-1e-15}$
004537.67+415124.4^a	11.406964	41.856792	2.3	11.407024	41.856355	20.60	20.46	21.64	21.08	20.95	20.82	$5.9e-15^{+2e-15}_{-2e-15}$
004637.22+421034.5^a	11.655092	42.176248	0.75	11.655076	42.176184	18.63	19.00	20.54	20.53	20.70	20.70	$3.1e-15^{+1e-15}_{-1e-15}$
004639.47+420649.2^a	11.664470	42.113665	0.89	11.664686	42.113558	23.70	23.69	24.33	24.24	25.71	25.50	$3.7e-15^{+1e-15}_{-1e-15}$
004350.76+412118.1^c	10.961516	41.355033	0.45	10.961508	41.355045	22.78	21.16	21.69	19.84	19.13	18.25	$4.4e-14^{+4e-15}_{-4e-15}$
004352.37+412222.8^c	10.968197	41.372997	0.9	10.968015	41.373104	24.50	23.10	23.30	21.90	21.43	20.83	$4.2e-15^{+2e-15}_{-1e-15}$
004356.78+413410.9^c	10.986584	41.569705	0.4	10.986615	41.569631	99.999	24.75	24.65	23.15	22.33	21.32	$4.1e-15^{+1e-15}_{-1e-15}$
004402.02+414028.8^c	11.008427	41.674679	1.1	11.008576	41.674590	22.10	21.10	22.13	20.69	20.05	19.36	$7.3e-15^{+2e-15}_{-2e-15}$
004404.55+413159.4^c	11.018958	41.533179	0.52	11.018864	41.533169	25.89	24.14	24.03	23.17	22.34	21.74	$3.9e-15^{+1e-15}_{-1e-15}$
004407.44+412460.0^c	11.031002	41.416662	0.64	11.031037	41.416678	24.86	23.06	20.93	17.31	16.20	15.49	$1.8e-15^{+1e-15}_{-7e-16}$
004437.96+414512.6^c	11.158149	41.753505	0.85	11.158152	41.753489	22.95	22.84	22.95	22.32	21.45	20.45	$1.8e-14^{+3e-15}_{-3e-15}$
004452.51+411710.7^c	11.218808	41.286303	1.2	11.218816	41.286414	23.15	19.75	20.88	19.83	19.42	18.48	$3.5e-14^{+4e-15}_{-4e-15}$
004454.75+411918.3^c	11.228112	41.321761	1.5	11.228090	41.321657	21.11	20.92	22.41	21.29	20.62	19.50	$1.2e-14^{+3e-15}_{-2e-15}$
004525.67+413158.2^c	11.356948	41.532845	1.1	11.356959	41.532850	23.26	22.47	22.56	21.04	20.25	19.47	$3.6e-15^{+1e-15}_{-1e-15}$
004542.25+420817.9^c	11.426039	42.138318	1.2	11.426153	42.138378	25.84	23.30	23.60	22.38	22.01	21.38	$1.1e-14^{+2e-15}_{-2e-15}$
004552.94+420234.0^c	11.470589	42.042780	0.86	11.470609	42.042771	26.52	23.84	23.67	22.14	21.32	20.48	$1.1e-14^{+2e-15}_{-2e-15}$
004558.04+420302.9^c	11.491829	42.050818	0.7	11.491873	42.050830	21.00	20.97	21.89	21.23	20.59	19.76	$3.1e-14^{+5e-15}_{-4e-15}$
004612.67+421027.8^c	11.552784	42.174382	0.39	11.552790	42.174390	24.12	22.55	23.08	21.31	20.76	20.09	$7.5e-15^{+2e-15}_{-2e-15}$
004640.59+415422.8^c	11.669118	41.906343	0.6	11.669103	41.906427	23.59	22.18	22.44	20.25	19.43	18.49	$5.5e-14^{+5e-15}_{-4e-15}$
004652.18+421505.8^c	11.717403	42.251599	2.1	11.716865	42.251591	22.42	22.03	23.15	21.75	21.38	20.19	$6.8e-15^{+2e-15}_{-2e-15}$
004703.82+420453.0^c	11.765906	42.081385	0.84	11.765933	42.081374	21.56	21.14	22.30	20.59	19.90	18.65	$7.6e-14^{+6e-15}_{-5e-15}$
004336.08+413320.4	10.900328	41.555683	0.87	10.900361	41.555726	23.67	22.16	21.87	20.37	19.50	18.82	$7.3e-15^{+2e-15}_{-1e-15}$
004357.54+413055.8	10.989765	41.515488	0.49	10.989700	41.515450	24.79	22.80	23.88	22.36	22.20	21.05	$1.2e-14^{+2e-15}_{-2e-15}$
004359.83+412435.6	10.999304	41.409889	0.68	10.999142	41.410006	25.81	23.47	23.59	21.95	21.50	20.89	$4.9e-15^{+2e-15}_{-1e-15}$
004412.04+413217.4	11.050183	41.538170	0.8	11.050257	41.538157	26.05	23.94	21.77	18.24	17.00	16.26	$4.1e-15^{+3e-15}_{-2e-15}$
004412.17+413148.4	11.050698	41.530100	0.36	11.050679	41.530036	22.34	21.30	21.77	20.28	19.97	19.42	$2.7e-14^{+3e-15}_{-3e-15}$

Name (CXO J)	CXO R.A.	CXO Dec.	σ^b ($''$)	PHAT R.A.	PHAT Dec.	F275W	F336W	F475W	F814W	F110W	F160W	Flux 0.35-8.0
004413.18+412911.4	11.054915	41.486508	0.89	11.054808	41.486368	26.49	24.06	99.999	21.33	20.66	19.91	$9.1e-15^{+2e-15}_{-2e-15}$
004422.57+414506.5	11.094057	41.751798	0.68	11.094097	41.751878	20.80	20.43	21.01	19.94	19.25	18.38	$8e-14^{+6e-15}_{-5e-15}$
004424.80+413201.4	11.103325	41.533731	0.41	11.103325	41.533695	25.50	24.87	24.13	21.43	19.95	19.11	$4.8e-14^{+4e-15}_{-4e-15}$
004425.73+412242.4	11.107221	41.378442	0.33	11.107175	41.378477	26.06	24.94	24.65	22.62	21.88	21.45	$1.5e-14^{+2e-15}_{-2e-15}$
004431.82+415217.2	11.132597	41.871441	0.55	11.132547	41.871387	22.27	21.44	21.90	20.49	20.10	19.83	$4.4e-15^{+2e-15}_{-1e-15}$
004448.13+412247.9	11.200545	41.379973	0.71	11.200584	41.380057	23.48	23.39	24.59	22.95	21.85	20.45	$1.8e-14^{+3e-15}_{-2e-15}$
004453.33+415159.5	11.222218	41.866543	0.34	11.222263	41.866515	25.05	23.09	23.19	21.22	20.47	19.85	$7.8e-15^{+2e-15}_{-1e-15}$
004455.72+415334.6	11.232187	41.892939	0.53	11.232176	41.892884	24.75	23.22	23.26	22.04	21.20	20.50	$4.1e-15^{+2e-15}_{-1e-15}$
004459.11+414005.1	11.246280	41.668081	0.9	11.246206	41.668054	26.14	22.74	22.06	20.70	19.94	19.32	$1.6e-14^{+3e-15}_{-2e-15}$
004500.89+414309.8	11.253707	41.719385	0.78	11.253848	41.719425	27.47	25.15	25.38	24.51	24.42	24.11	$9.7e-15^{+2e-15}_{-2e-15}$
004502.33+414943.1	11.259688	41.828654	0.61	11.259761	41.828766	24.07	23.46	23.44	22.74	22.66	22.48	$4.6e-15^{+1e-15}_{-1e-15}$
004510.96+414559.2	11.295681	41.766440	0.43	11.295651	41.766412	23.71	22.78	23.30	21.08	20.35	19.03	$3.2e-14^{+3e-15}_{-3e-15}$
004526.67+415631.0	11.361109	41.941936	1.4	11.361074	41.942056	23.01	22.34	22.74	21.05	20.62	19.46	$1.5e-14^{+3e-15}_{-3e-15}$
004527.88+413905.5	11.366179	41.651539	0.43	11.366180	41.651542	24.34	22.81	23.41	20.87	19.97	18.82	$3e-14^{+3e-15}_{-3e-15}$
004528.24+412943.9	11.367681	41.495538	0.42	11.367687	41.495535	19.76	19.20	20.23	19.01	18.53	17.75	$1.3e-13^{+7e-15}_{-6e-15}$
004537.84+414856.7	11.407660	41.815743	1.4	11.408020	41.815702	22.74	21.69	22.12	20.74	20.43	20.14	$3.9e-15^{+2e-15}_{-1e-15}$
004543.15+415519.4	11.429790	41.922042	1.4	11.429859	41.922029	22.14	21.40	21.80	20.24	19.72	19.36	$3.7e-15^{+2e-15}_{-1e-15}$
004550.83+415835.1	11.461787	41.976427	0.58	11.461834	41.976518	22.06	21.88	23.13	22.08	21.32	20.20	$5.5e-15^{+2e-15}_{-1e-15}$
004607.50+420855.7	11.531257	42.148817	0.41	11.531258	42.148852	27.37	24.31	24.98	23.27	22.69	21.88	$9.5e-15^{+2e-15}_{-2e-15}$
004611.38+415903.9	11.547414	41.984406	0.31	11.547478	41.984419	99.999	24.19	24.81	23.01	22.29	21.18	$2.1e-14^{+3e-15}_{-3e-15}$
004611.85+420827.9	11.549374	42.141082	0.28	11.549385	42.141077	99.999	24.77	23.50	20.70	19.21	18.31	$7.2e-14^{+5e-15}_{-5e-15}$
004613.49+415043.3	11.556209	41.845353	0.71	11.556171	41.845410	20.34	20.12	21.20	19.94	19.60	18.60	$3.9e-14^{+4e-15}_{-4e-15}$
004617.57+415913.6	11.573194	41.987108	0.42	11.573203	41.987150	22.54	21.65	22.85	21.55	21.03	20.48	$7.2e-15^{+2e-15}_{-1e-15}$
004630.46+421028.7	11.626900	42.174642	0.43	11.626948	42.174642	24.37	22.99	22.91	21.10	20.56	19.90	$5e-15^{+2e-15}_{-1e-15}$
004630.68+420947.0	11.627815	42.163055	0.39	11.627821	42.163064	25.10	24.55	26.15	24.02	22.66	21.45	$7.3e-15^{+2e-15}_{-2e-15}$
004648.19+420855.4	11.700785	42.148718	0.42	11.700789	42.148730	22.34	21.65	21.84	19.93	19.28	18.29	$5.7e-14^{+4e-15}_{-4e-15}$
004648.27+420851.1	11.701118	42.147536	0.55	11.701051	42.147534	22.75	21.88	22.35	20.76	20.32	19.24	$2.1e-14^{+3e-15}_{-3e-15}$

[a] Included in the "best candidate" sample. CXO J004339.06+412117.6 is considered such a candidate, but no SFH is available. [b] X-ray source position uncertainty. [c] No local young population detected.

Table 2.4. Best HMXB Candidate Age Probabilities: full table electronic only

Catalog Name	Low Age (Myr)[a]	High Age (Myr)	Prob.[b]	+err	−err
004425.73+412242.4	4.0	5.0	0.000	0.077	0.000
004425.73+412242.4	5.0	6.3	0.000	0.127	0.000
004425.73+412242.4	6.3	7.9	0.000	0.182	0.000
004425.73+412242.4	7.9	10.0	0.000	0.254	0.000
004425.73+412242.4	10.0	12.6	0.795	0.000	0.760
004425.73+412242.4	12.6	15.8	0.000	0.506	0.000
004425.73+412242.4	15.8	20.0	0.000	0.460	0.000
004425.73+412242.4	20.0	25.1	0.021	0.406	0.021
004425.73+412242.4	25.1	31.6	0.000	0.403	0.000
004425.73+412242.4	31.6	39.8	0.000	0.409	0.000
004425.73+412242.4	39.8	50.1	0.000	0.414	0.000
004425.73+412242.4	50.1	63.1	0.000	0.405	0.000
004425.73+412242.4	63.1	79.4	0.184	0.136	0.184
004448.13+412247.9	4.0	5.0	0.000	0.098	0.000
004448.13+412247.9	5.0	6.3	0.000	0.160	0.000
004448.13+412247.9	6.3	7.9	0.000	0.232	0.000
004448.13+412247.9	7.9	10.0	0.000	0.304	0.000
...	...	...	...	...	...

Note. — [a] Low and high ages refer to the edges of the age bin. For example, if low age is 4.0 and high age is 5.0, then the Prob. column refers to the probability that the HMXB candidate has an age between 4.0 and 5.0 Myr. [b] Probability that the HMXB system has an age in this interval. There are uncertainties on this probability, given by the +err and -err columns. Full electronic table available at https://iopscience.iop.org/article/10.3847/1538-4365/aae37d#apjsaae37dt4.

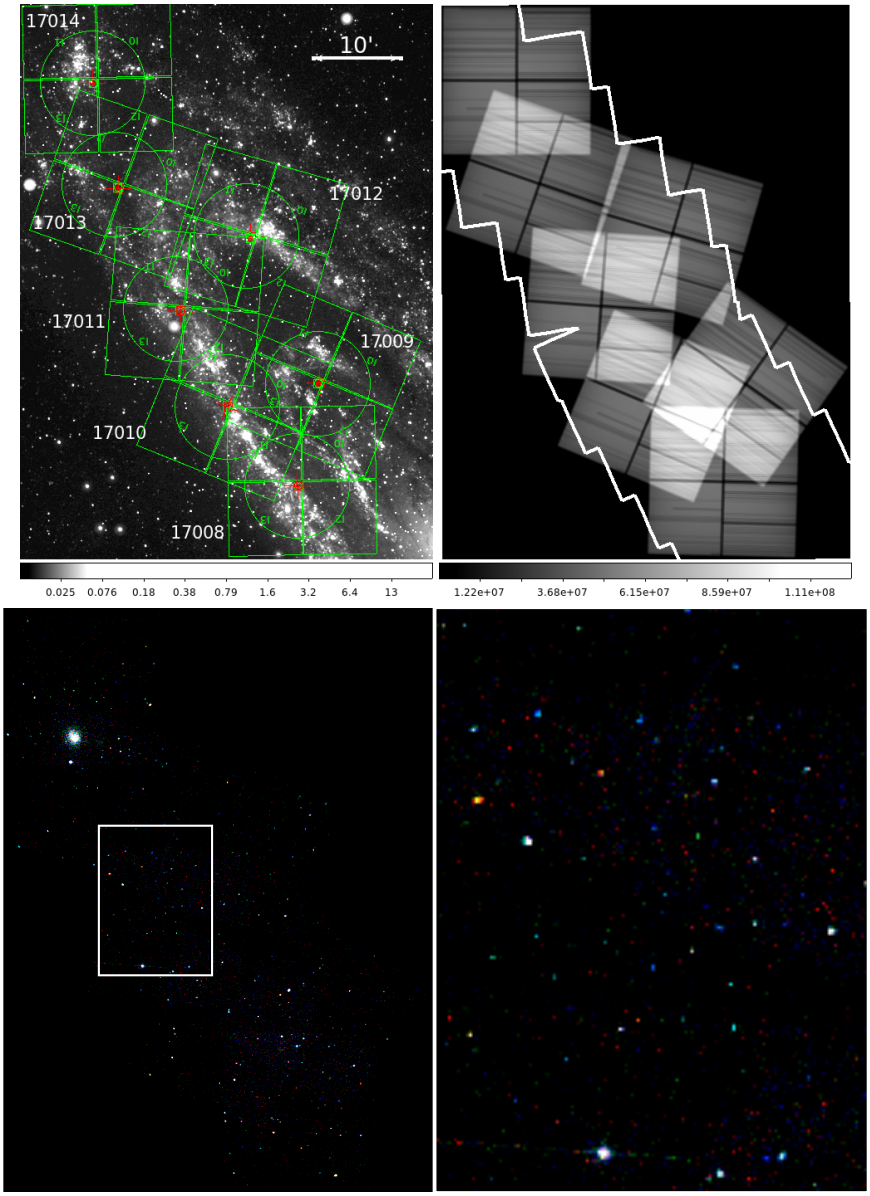

Figure 2.1 *Top left:* GALEX NUV image of M31 with our planned Chandra pointings overlaid. This image is oriented with North-up, East-left, and the inset scale bar is 10′. *Top right:* Exposure map of the Chandra survey as observed. The total coverage is 0.41 square degrees. The white polygon marks the PHAT footprint, and the overlap is 0.36 square degrees. *Bottom left:* Color mosaic of our Chandra data, where red is 0.3-1.0 keV, green is 1.0-2.0 keV, and blue is 2.0-8.0 keV. We include a zoomed in view of the region outlined in white in the bottom right panel of this figure. *Bottom right:* Zoomed in view of region outlined in white in bottom left image to show detail. ©AAS. Reproduced with permission from Williams et al. (2018).

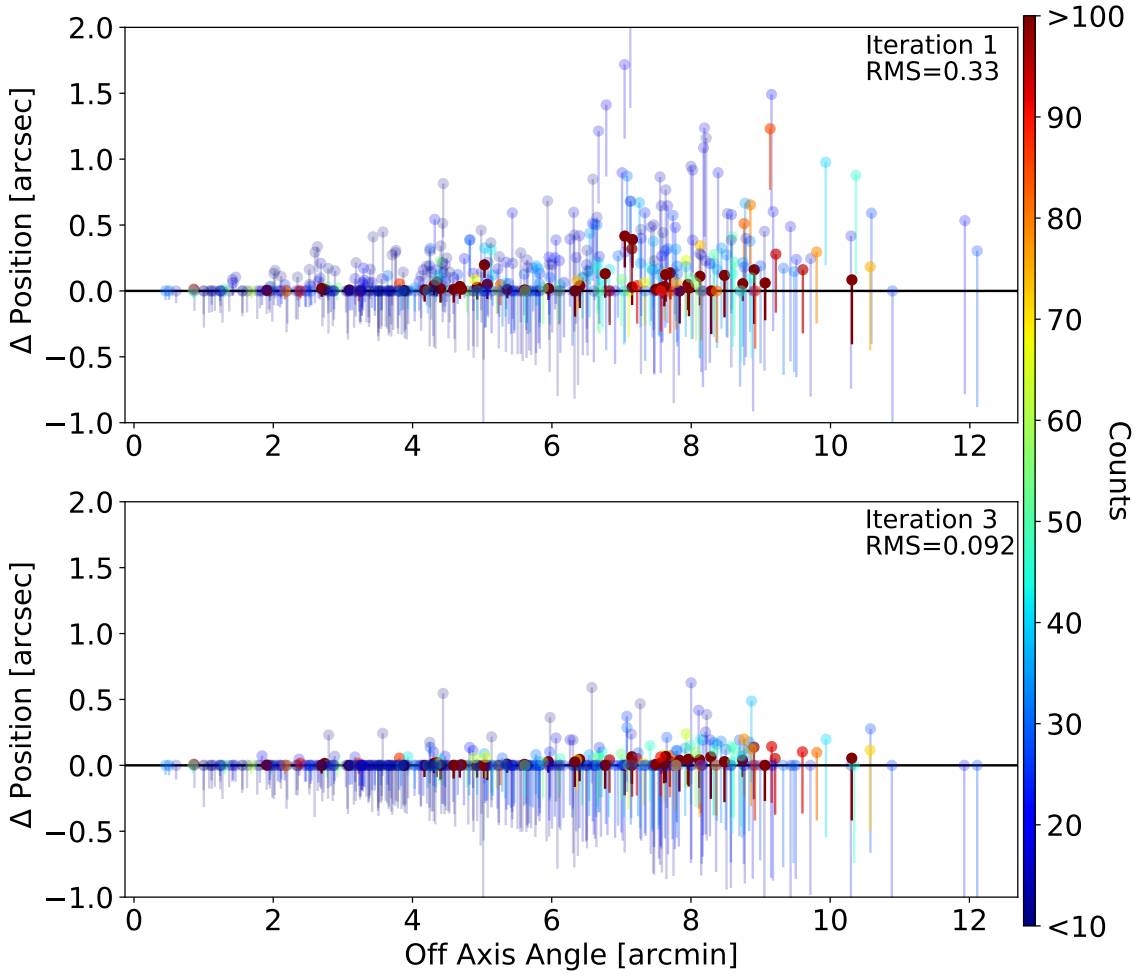

Figure 2.2 Results of our AE `fit_positions` iterations on the source positions. *Top:* Position offsets between the first run of `fit_positions` and the second. Point colors are coded by the number of counts (0.35-8.0 keV). *Bottom:* Same as *top*, but comparing our final run of `fit_positions` to the penultimate run. ©AAS. Reproduced with permission from Williams et al. (2018).

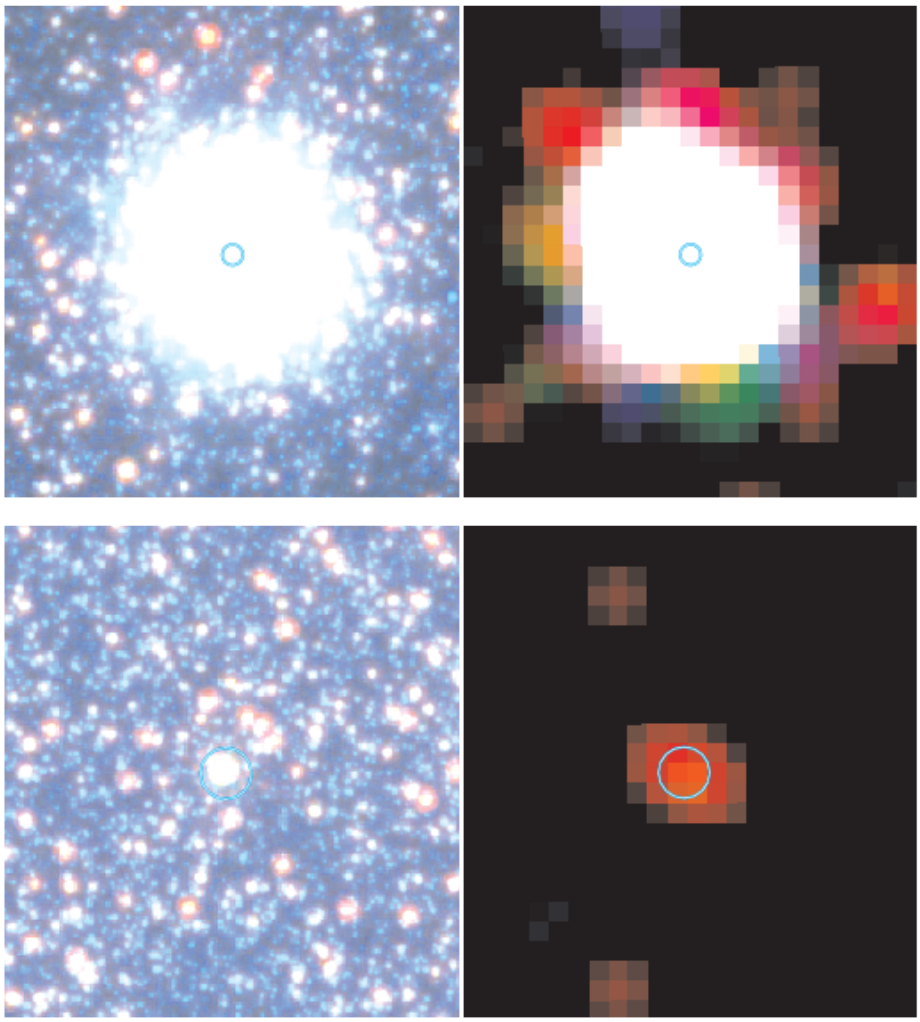

Figure 2.3 Examples of optical sources used to align our *Chandra* imaging to the PHAT imaging shown on $10'' \times 10''$ PHAT and Chandra images, oriented with north-up and east-left. *Top:* Source CXO J004429.57+412135.7 in observation 17008 clearly matches a star cluster. The left panel shows the PHAT image (red=F160W, green=F814W, blue=F475W), with the *Chandra* position (blue circle) marked. The right panel shows the same markings on the color *Chandra* image (red=0.35-1 keV, green=1-2 keV, blue=2-8 keV, all smoothed with a Gaussian kernel of radius 3 pixels). *Bottom* Source CXO J004407.44+412500.0 in observation 17008 is very soft and clearly matches a bright star in the PHAT image. Because it is so soft, that star is likely to be in the foreground, as bright XRBs typically have hard X-ray spectra. Panels show images and markings corresponding to the same bands and instruments as *top*.

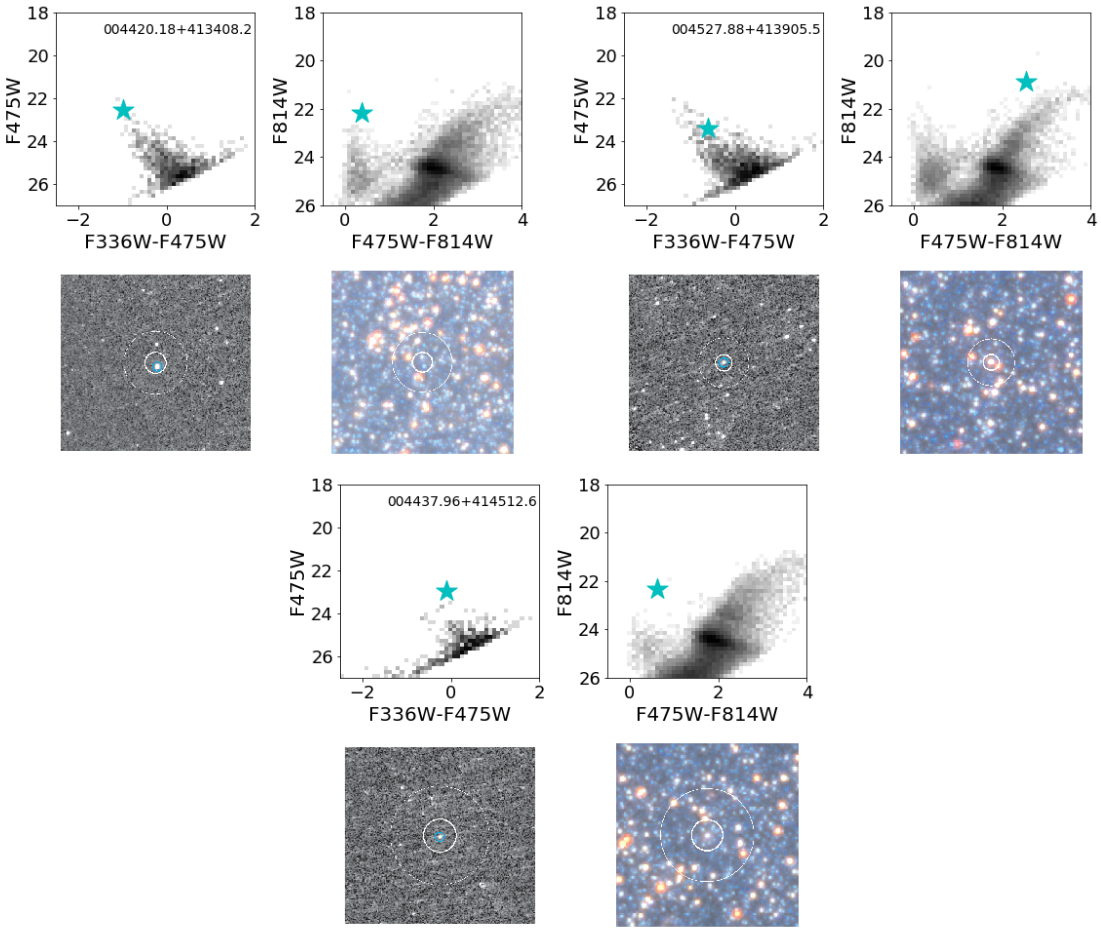

Figure 2.4 Examples of four panel figures showing the identification of optical counterpart candidates. Upper left is a high-quality HMXB candidate CXO J004420.18+413408.2. Upper right is a candidate with atypical colors, CXO J004527.88+413905.5. Lower center is a candidate in a region without any young stellar population, CXO J004437.96+414512.6. For each source, for example CXO J004527.88+413905.5, the four panels depict *Upper-left:* CMD in the near-UV (F336W-F475W) from the PHAT catalog of objects within 10″ of the position of Source CXO J004527.88+413905.5. Grayscale shows all stars in a 5″ circle surrounding the source location for context. Purple dots mark other sources within the error circle with measured F336W and F475W magnitudes. However, none of these examples contain any such sources. The blue star marks the position of the best counterpart candidate as it is UV-bright in addition to being spatially coincident with the position of the X-ray source. *Upper-right:* Same as Upper-left but for the optical (F475W-F814W) CMD. The object is much brighter and redder in the optical than a typical star, suggesting that the SED is being affected by the X-ray source (see Section 2.2.3). *Upper-right:* F336W PHAT image of a 10×10″ region surrounding the X-ray position. The 1-σ and 3-σ error circles are overplotted in heavy and light white circles, respectively. A single bright star is circled in blue. *Lower-center:* Color PHAT image of the same region (blue is F475W, green is F814W, and red is F160W). In addition to the spatial alignment, this object is an excellent counterpart candidate because of its atypical colors. ©AAS. Reproduced with permission from Williams et al. (2018).

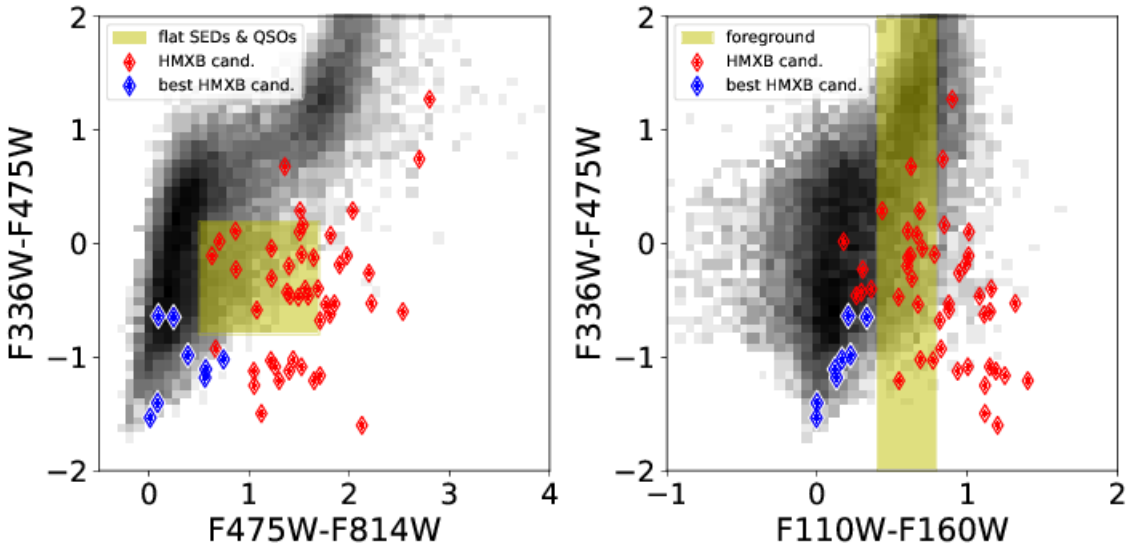

Figure 2.5 UV-optical and UV-IR color-color diagrams of the best stellar optical counterpart candidates. Other M31 stars near the X-ray sources (black points) follow a clear locus. The area of the plot where a flat spectrum or a QSO spectrum would fall is shaded yellow in the left panel, and the area where foreground stars would occupy is shaded yellow in the right panel. Many counterpart candidates fall redward of the stellar locus and in regions expected for sources with non stellar spectra, suggesting that they are not normal single stars, but either binaries in M31 or background galaxies. The counterpart candidates with the bluest colors, typical of young massive stars in M31, are plotted in blue. These 6 are our best HMXB candidates. ©AAS. Reproduced with permission from Williams et al. (2018).

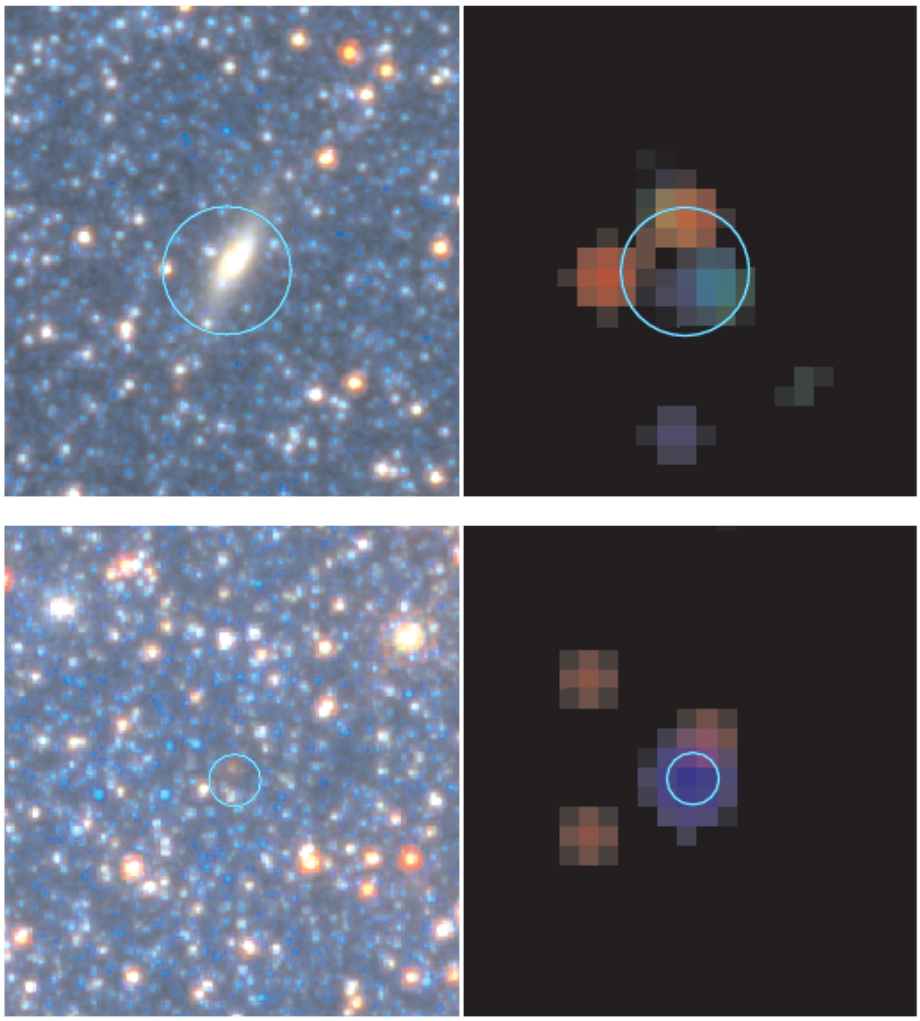

Figure 2.6 Same structure as the panels of Figure 2.3, but instead of alignment sources, these are examples of background galaxies found in the PHAT imaging after alignment. *Top:* Source CXO J004535.86+413322.8 in observation 17010 is clearly extended and red in the optical. The left panel shows the PHAT image (red=F160W, green=F814W, blue=F475W), with the *Chandra* 1-σ position error marked in blue. The right panel shows the same markings on the color *Chandra* image (red=0.35-1 keV, green=1-2 keV, blue=2-8 keV). The source is clearly extended and red in the optical. *Bottom* Source CXO J004437.52+415124.9 in observation 17012. Panels show images and markings corresponding to the same bands and instruments as *top*. Here the background galaxy near the top of the 1-σ position error is very faint and red, but distinct from the stars in the image.

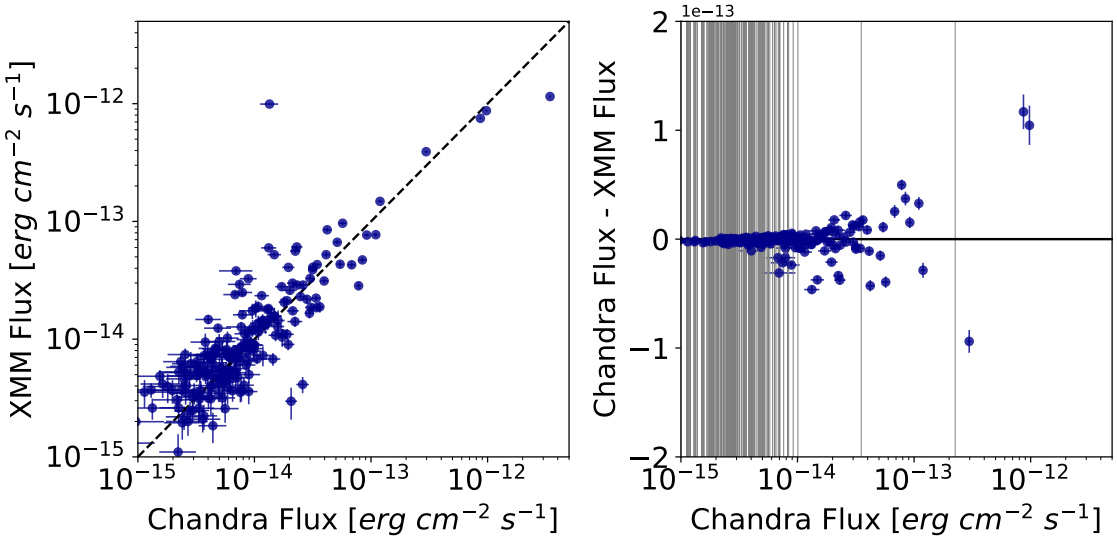

Figure 2.7 Comparison between Chandra and XMM-Newton 0.5-4.0 keV fluxes, using the cross-matching from our catalog, assuming a power law spectrum with slope 1.7 and N_H=7×10^{20} cm^{-2}. *Left:* Direct comparison of fluxes between measurements for all sources matched. *Right:* Residuals of all matched sources, with sources undetected by XMM-Newton marked with gray vertical lines. ©AAS. Reproduced with permission from Williams et al. (2018).

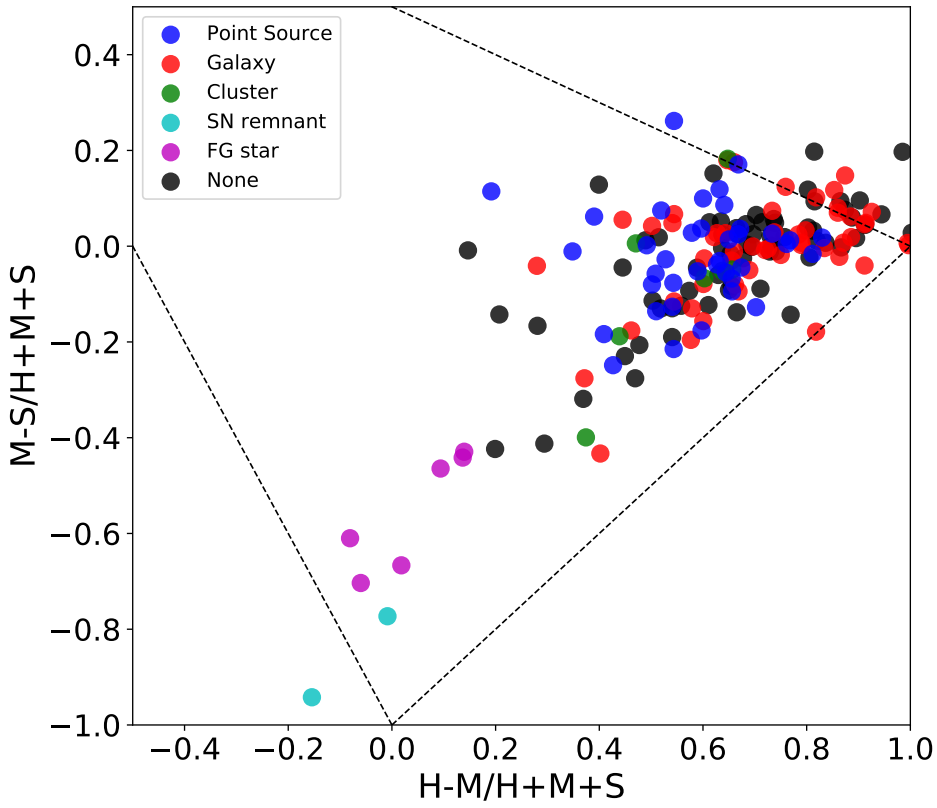

Figure 2.8 Hardness ratios for all sources with >20 counts. Bands are fluxes in: H=2-8 keV, M=1-2 keV, S=0.35-1 keV, and points are color-coded by their counterpart candidate type. The triangle marks the allowed region for positive counts in all bands. Many of the hardest sources show negative counts in the soft band due to uncertainties in the background level when zero counts are detected in the soft band. The area at the bottom of the plot is dominated by foreground stars and SNRs, and the area at the extreme right of the plot is dominated by background galaxies. ©AAS. Reproduced with permission from Williams et al. (2018).

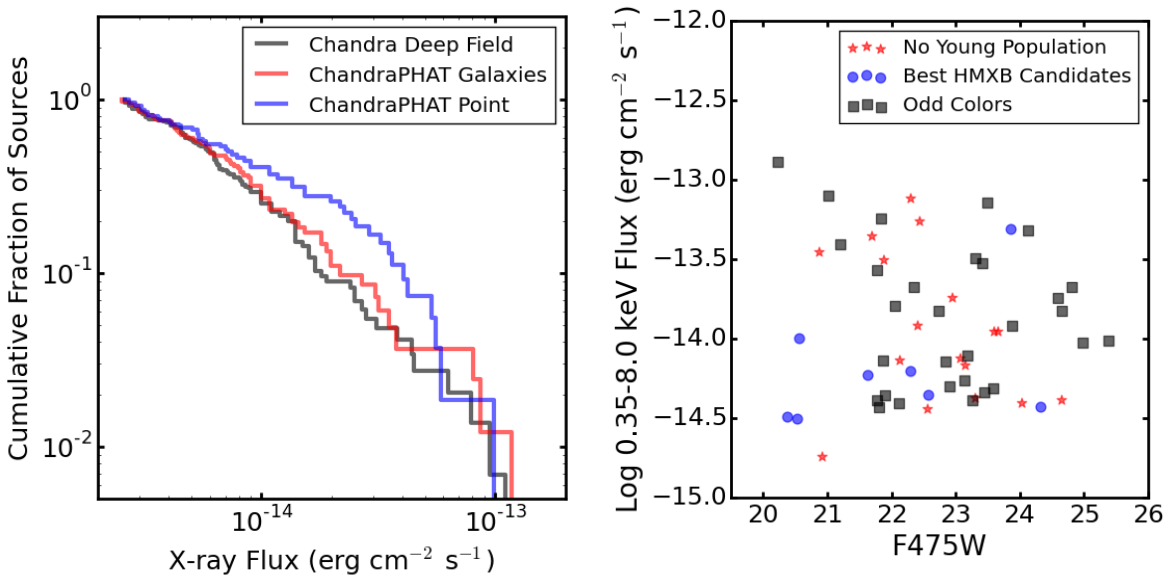

Figure 2.9 *Left:* The fractional cumulative 0.5-7.0 keV flux histograms for the Chandra Deep Field (CDF) (Luo et al., 2017), the 107 sources with background galaxy candidates in our sample, and the 58 sources with point source optical candidates in our sample. While the galaxies follow a very similar distribution to the CDF, the point sources do not, confirming that they represent a different population of sources. *Right:* The X-ray fluxes vs. F475W magnitudes of the point source counterpart candidates. The different point types correspond to the three tiers of counterpart candidates in Table 2.3. ©AAS. Reproduced with permission from Williams et al. (2018).

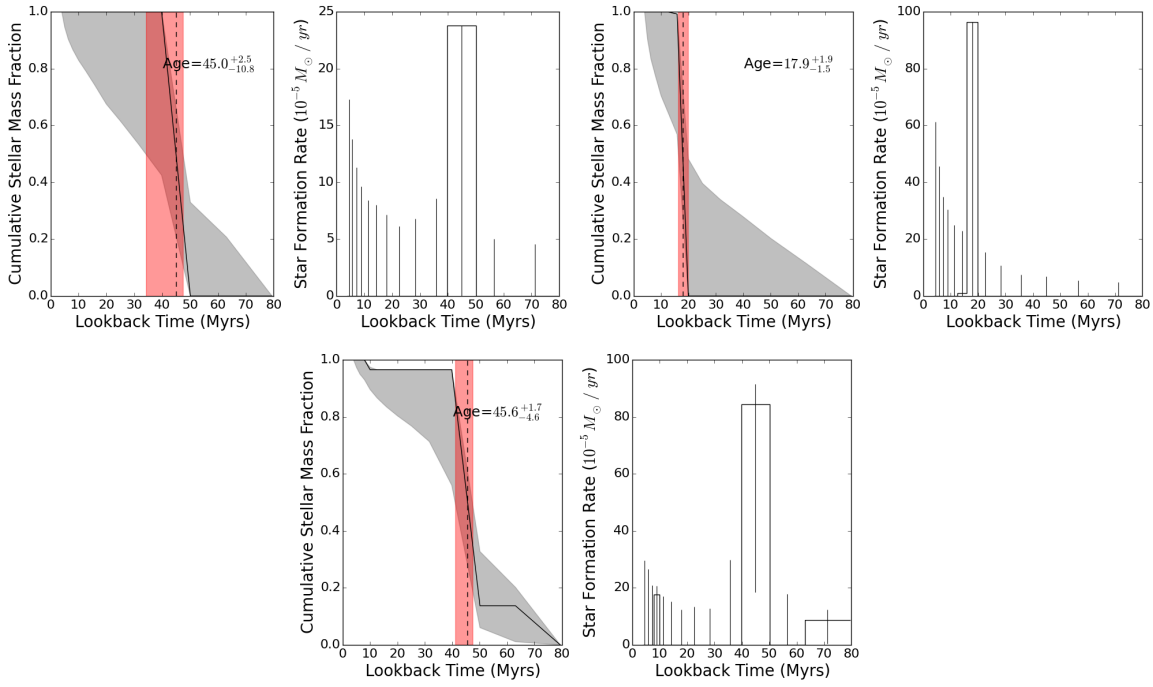

Figure 2.10 Age estimation of HMXB candidates. These ages refer to the time since the parent binary system formed, and do not probe how long the binary has been producing X-rays. *Top left:* CXO J004420.20+413407.4. *Top right:* CXO J004514.78+415034.2. *Bottom center:* CXO J004637.23+421033.7. *Left:* Cumulative stellar mass fraction as a function of age for all stars <80 Myr old. This fractional distribution is calculated from the rates and uncertainties in *right*, which shows the most recent 80 Myr of the Lewis et al. (2015) star formation history of the region where the HMXB is located. Dashed line shows the median age for the best fit distribution. The gray shading shows the 1σ uncertainty range, and the red shading shows the ages consistent with the median age within the uncertainties. ©AAS. Reproduced with permission from Williams et al. (2018).

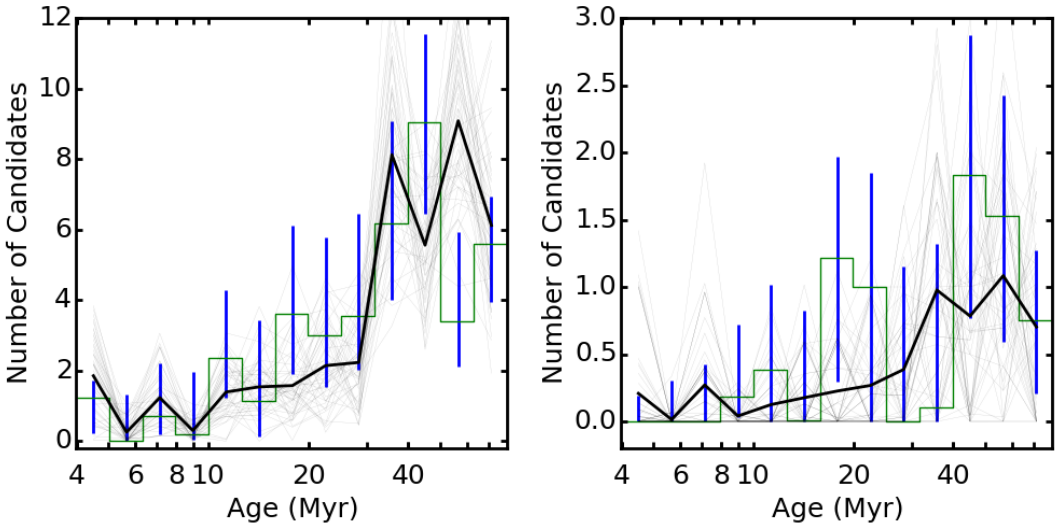

Figure 2.11 Sum of the probability distributions for a few sub-samples of the HMXB candidates. In each case, the green histogram with blue error bars shows the distribution (and uncertainty) of the candidates, the thin gray lines show the results of measuring the same distribution on equal-sized sets of SFHs taken from positions that do not include an HMXB candidate. The heavy black line shows the average of all of the thin gray lines. In short, the black lines show the effects of contamination (young stars that are unrelated to the presence of any HMXBs). *Left:* Distribution of all 58 point source candidates with SFH measurements, but only 40 are included because 17 did not reside in a region with recent star formation according to the PHAT data, and one did not have a PHAT SFH. *Right:* A sample of the 7 bluest stellar candidates with SFH measurements, which are our best HMXB candidates, all of which are in regions with recent star formation. ©AAS. Reproduced with permission from Williams et al. (2018).

Chapter 3

YOUNG ACCRETING COMPACT OBJECTS IN M31: THE COMBINED POWER OF NUSTAR, CHANDRA, AND HUBBLE

Portions of this chapter were originally published in collaboration with Ann E. Hornschemeier, Benjamin F. Williams, Daniel Wik, Neven Vulic, Mihoko Yukita, Andreas Zezas, Alexia R. Lewis, Meredith Durbin, Andrew Ptak, Arash Bodaghee, Bret D. Lehmer, Vallia Antoniou, and Thomas Maccarone in the July 2018 edition of the Astrophysical Journal (Lazzarini et al., 2018, ApJ*, Vol. 862, 28; 2018 © American Astronomical Society, DOI: 10.3847/1538-4357/aacb2a), and are reproduced below with the permission of the American Astronomical Society.*

3.1 Introduction

The production of extragalactic X-ray binaries (XRBs) is closely related to properties of the galaxies in which they form, such as the star formation rate (e.g. Ranalli et al., 2003; Gilfanov et al., 2004; Mineo et al., 2012), stellar mass (Lehmer et al., 2010), and metallicity (Basu-Zych et al., 2013; Brorby et al., 2016). Population studies of XRBs probe the production of these compact objects and their relationship to their host galaxy properties. However, the fundamental properties of XRBs, such as the compact object type and the physical properties of the donors, have remained difficult to determine given the limited information contained in the 0.5-10 keV energy range covered by soft X-ray telescopes such as *Chandra* and *XMM-Newton*. Broadening the observed energy range to include data from the near IR (*Hubble Space Telescope (HST)*) through hard X-rays (*NuSTAR*) allows us to determine the compact object type, the physical properties of the donors, and place constraints on the age of XRBs using star formation histories for their surrounding stellar populations.

Conducting a galaxy-wide study of high mass X-ray binaries (HMXBs) in connection to their star forming environments is challenging in the Milky Way due to distance uncertainties, but there has been some successful work in this area (Grimm et al., 2002). Additionally, Bodaghee et al. (2012) used the spatial correlation between HMXBs and OB associations in the Milky Way to determine ages of the systems. It is expected that 5-10 Myr elapses between the formation of a high mass star and the supernova, which forms the compact object in HMXBs (Schaller et al., 1992; Linden et al., 2010). Thus, an HMXB cannot migrate far from its birthplace, allowing its spatial correlation with an OB association to be used to constrain its age. Bodaghee et al. (2012)

determined the time from supernova through the HMXB phase (the "kinematic age") using the spatial correlation between HMXB candidates and OB associations. They found that most systems have kinematic ages of ~ 4 Myr.

Detailed studies of XRBs in extragalactic star forming environments have been done previously in the Small Magellanic Cloud (SMC), Large Magellanic Cloud (LMC), NGC 300, NGC 2403, and M33. In the SMC, B*e*/X-ray binaries are found in regions with star forming bursts 25-60 Myr ago (Antoniou et al., 2010). In the LMC, HMXBs are found in areas with considerably more recent star formation, between 6 and 25 Myr ago (Antoniou & Zezas, 2016). In NGC 300 and NGC 2403, HMXB candidates have been found in regions with surrounding stellar populations between 20 and 70 Myr old (Williams et al., 2013a) with a peak at 40-55 Myr, agreeing with ages in the SMC. In M33 a similar set of peaks is seen in the HMXB age distribution (Garofali et al., 2018). These ages suggest two potential formation channels: one that operates on the timescale of B-star evolution ($\sim$50 Myr) and the other that operates much more promptly.

To better connect the properties of the XRBs themselves to their parent populations, classifying the compact object in the system is critical. However, compact object characterization can be difficult because there are currently very limited methods available. If a low-mass XRB has an observed Type-I X-ray burst, its compact object may be classified as a neutron star (e.g., Lewin et al., 1993). Black holes can be classified as such if the mass of the compact object can be confirmed using the orbital period and mass of the companion (Orosz & Bailyn, 1997), but stellar companion orbits are not always available, especially for extragalactic XRBs.

The hard X-ray coverage of *NuSTAR* allows compact objects to be tentatively classified using their X-ray properties. With X-ray observations that cover the hard band (4-25 keV), compact objects can be classified as neutron stars or black holes based on a combination of their X-ray colors and luminosities (Zezas et al., in prep.; Zezas et al., 2014; Wik et al., 2014; Yukita et al., 2016). This can be done because neutron stars always have hard emission associated with matter accreting onto the surface, while black holes do not and are dominated by the disk emission properties (Maccarone et al., 2016). Thus, an XRB's hard X-ray colors distinguish between neutron star and black hole systems. Techniques involving hard X-rays are more indirect but are critical for expanding our tool

kit for classifying X-ray sources as black holes or neutron stars.

Andromeda (M31), the nearest spiral galaxy to the Milky Way, is one of the best systems for studying X-ray binary populations in the context of their star forming environments because of its proximity and the large number of multiwavelength data sets available. Observations with the sensitivity to detect faint point sources extend from near infrared wavelengths up to hard X-rays ($E \lesssim 50$ keV) (e.g., Williams et al., 2014b; Yukita et al., 2017; Maccarone et al., 2016; Vulic et al., 2014, 2016).

There has recently been a major improvement in the X-ray coverage of Andromeda owing to two powerful and deep surveys by *NuSTAR* and *Chandra*, both taken in 2015. *NuSTAR* observed an ~ 750 arcmin^2 area of M31 at a depth of $\sim$1.4 Ms (Wik et al., 2016a,b, 2018, in prep.). A *Chandra* Large Project survey covered ~ 1800 arcmin^2 to a depth of 50 ks (ChandraPHAT; Williams et al., 2018).

We pair these X-ray observations with existing near-infrared to ultraviolet observations from Hubble (PHAT; Dalcanton et al., 2012; Williams et al., 2014b) to study hard X-ray emitting compact objects and their optical counterparts in the context of their star forming environments. A total area of ~ 570 arcmin^2 is covered by all three telescopes. This area comprises approximately 6% of the D_{25} area of M31.

The maturity of the PHAT project means that invaluable secondary data products are available to characterize the star forming environments around X-ray sources. For example, Lewis et al. (2015) spatially mapped the recent star formation history of M31 and Gregersen et al. (2015) mapped the metallicity distribution. Both properties allow the X-ray binary population to be put in the context of its environment. The Bayesian Extinction and Stellar Tool (BEAST) by Gordon et al. (2016) can fit the spectral energy distribution (SED) of individual stars in the disk of M31. The BEAST code provides a powerful tool for understanding the physical characteristics of the companion star in an XRB. Additionally, M31 allows us to study XRB populations in their environments without the uncertainties in the distance to each system that plague such studies in the Milky Way.

In this chapter we use the multiwavelength coverage from *NuSTAR*, *Chandra*, and *HST* to

investigate the HMXB population in the northern disk of M31. In Section 3.2, we describe the three data sets used in this study: *NuSTAR* observations, two sets of *Chandra* observations, and reduced *HST* photometry and imaging from the PHAT survey. We describe the methods used to match sources between the three data sets in Section 3.3. In Section 3.4, we describe our results: how *NuSTAR* sources were classified using their X-ray colors and luminosities, how we determined ages for HMXB candidates using spatially resolved star formation histories, and the SED fitting used to determine spectral types for companion stars in HMXB candidates. In Section 3.5, we discuss our results in the context of previous studies and in Section 3.6, we provide a brief summary of our results.

We assume a Galactic column density, $N_H = 7 \times 10^{20}\ cm^{-2}$, and a photon index, $\Gamma = 1.7$ (Stiele et al., 2011), to convert count rates to absorbed energy flux. We assume a distance of 776 kpc to M31 (Dalcanton et al., 2012) for luminosity calculations.

3.2 Data

In this study we employ data from *NuSTAR*, *Chandra*, and *HST*. We now describe each data set in more detail below. For an overview of the area observed by each telescope, see Figure 3.1.

3.2.1 NuSTAR Data

NuSTAR source catalogs and source classifications come from Wik et al. (2016a,b, 2018, in prep.). Observations were taken between October and February 2015 covering the area outlined in green in Figure 3.1 with an average exposure time of 1.4 Ms and were reduced using the `nupipeline` software. Sources previously observed with *Chandra* were used for astrometric alignment. For detailed information on data reduction, source detection, and source classification please see Wik et al. (in preparation), which presents the entire *NuSTAR* M31 survey. The *NuSTAR* observations cover the nucleus and inner disk regions of M31 at an energy range of 4-25 keV using the 4-6 keV, 6-12 keV, and 12-25 keV energy bands. The completeness of the *NuSTAR* observations starts to fall off at a luminosity of $\sim 3 \times 10^{36}\ erg\ s^{-1}$ and reaches zero at $\sim 2 \times 10^{36}\ erg\ s^{-1}$.

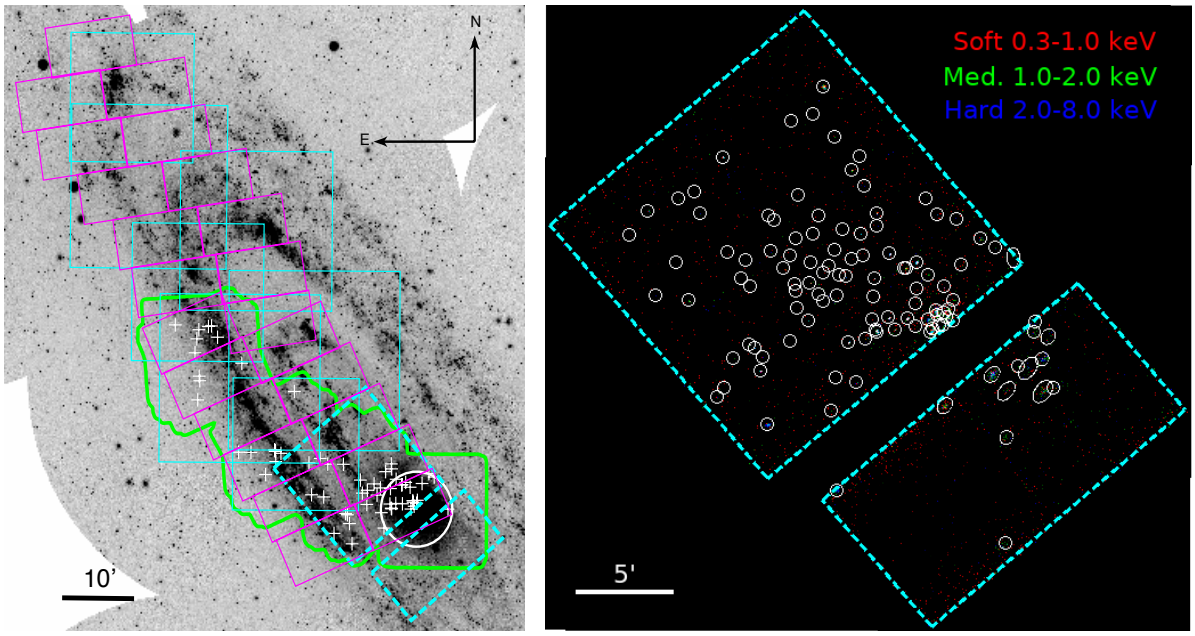

Figure 3.1 Near UV image of M31 from the Galaxy Evolution Explorer (GALEX) (left) (Gil de Paz et al., 2009a) and three color X-ray image of *Chandra* Field A (right), see Section 3.2.2 for more information on Field A data reduction. Magenta regions outline the area observed by PHAT. Green outlines the *NuSTAR* observed region and cyan outlines the area observed by *Chandra*, with solid lines indicating ChandraPHAT observations and dashed lines indicating Field A observations. In the UV image, the 64 sources observed by *NuSTAR* and *Chandra* that fall within the PHAT footprint are marked with white crosses and a 5′ circle outlines the densest inner bulge region of M31. In the X-ray image, all sources detected by wavdetect within Field A are marked with white ellipses (including sources that do not match to *NuSTAR* sources or are outside the PHAT footprint, and thus are not presented in our sample in Table 3.1). ©AAS. Reproduced with permission from Lazzarini et al. (2018).

3.2.2 Chandra Data

Chandra data used in this study are comprised of two data sets: the ChandraPHAT data, a *Chandra* Large Project survey by Williams et al. (2018), and one additional *Chandra* field (obsid 18046, P.I. Hornschemeier), hereby referenced as Field A, that was reduced for this chapter. The ChandraPHAT data set is comprised of 7 *Chandra* pointings, each with a depth of about 50 ks. The Field A data is made of one *Chandra* pointing with a depth of 25 ks. The ChandraPHAT observations were taken in October 2015 and the Field A observation was taken in August 2016. The completeness in the ChandraPHAT field starts to drop at a luminosity of $\sim 3 \times 10^{35}\ erg\ s^{-1}$ and reaches zero at $\sim 5 \times 10^{34}\ erg\ s^{-1}$. The completeness in Field A starts to drop at $\sim 7 \times 10^{35}\ erg\ s^{-1}$ and reaches zero at $\sim 1 \times 10^{35}\ erg\ s^{-1}$.

Field A is centered at (RA,Dec)=(00:43:29.30, +41:18:21.20) and was designed to overlap with *NuSTAR* Field A in the observations by Wik et al. (in preparation). For a detailed description of the data reduction for *Chandra* sources within the ChandraPHAT footprint, see Chapter 2, which is also published in Williams et al. (2018). Sections 3.2.2 and 3.2.2 contain a detailed description of the reduction of the *Chandra* Field A data, which follows the methodology in Chapter 2.

Source Detection

We generated the initial source list using the `wavdetect` tool of CIAO version 4.9 and CALDB version 4.7.7 (Fruscione et al., 2006). We produced the source image and exposure map using the CIAO command `fluximage` and created the PSF map using the CIAO tool `mkpsfmap` with the standard parameters, energy=1.4967 and ecf=0.393. We then ran `wavdetect` using the source image and PSF map to create a source list. The wavelet scales were set to 1.0, 2.0, 3.0, 8.0, and 16.0 pixels.

We ran ACIS extract (AE) version 2016sept22 (Broos et al., 2010) on the source list output from `wavdetect`. We followed Section 3.2 of the AE users guide to prepare the event files, aspect histogram file, aspect solution file, and mask file for AE source extraction. With the input source list from `wavdetect`, we extracted sources with energy limits of 0.35-8.0 keV. See Table

3.1 for the positions, off-axis angle, and net counts output by AE.

We iterated AE four times in order to obtain the most precise positions. The first AE run used the output positions from CIAO `wavdetect` as the initial positions. Each subsequent AE run used the data mean position output from the previous run as the initial positions, this was repeated until the input and output data mean positions converged (Figure 3.2).

Astrometric Alignment

Once we obtained precise positions for the *Chandra* sources with ACIS extract, we aligned the Field A observations to the PHAT data set (Dalcanton et al., 2012). *NuSTAR* data were previously aligned to the ChandraPHAT data by Wik et al. (in preparation).

We used 8 bright globular clusters that were detected at optical wavelengths by *HST* and X-ray wavelengths by *Chandra* for astrometric alignment. Clusters were identified by visual inspection of the PHAT imaging. First, we measured the centroids of the clusters using the `centroid_1dg` tool in the `photutils` (v0.4) Python package. To find the astrometric solution, we used the CIAO tool `wcs_match` that aligns the *Chandra* sources in a given image to the measured cluster positions from the PHAT images and outputs an astrometric solution. The parameters used in `wcs_match` were radius=5, residlim=0, residtype=0, and residfac=25 using the description in Vulic et al. (2016) as a guide. The CIAO tool `wcs_update` was used to updated the header of the *Chandra* images and update the RA and Dec of the measured source positions.

Positional errors were calculated using the net counts in the 0.35-8.0 keV band and the off axis angle using the formula in Hong et al. (2005), listed as Equation 5. Instead of using the $0.25''$ baseline error in that equation, we added the residuals from astrometric alignment to PHAT, which were $0.29''$ in RA and $0.03''$ in Dec.

We merged the Field A catalog prepared for this chapter with the ChandraPHAT catalog from Chapter 2 for source matching with the *NuSTAR* source catalog by Wik et al. (in preparation) and PHAT, detailed in Section 3.3.

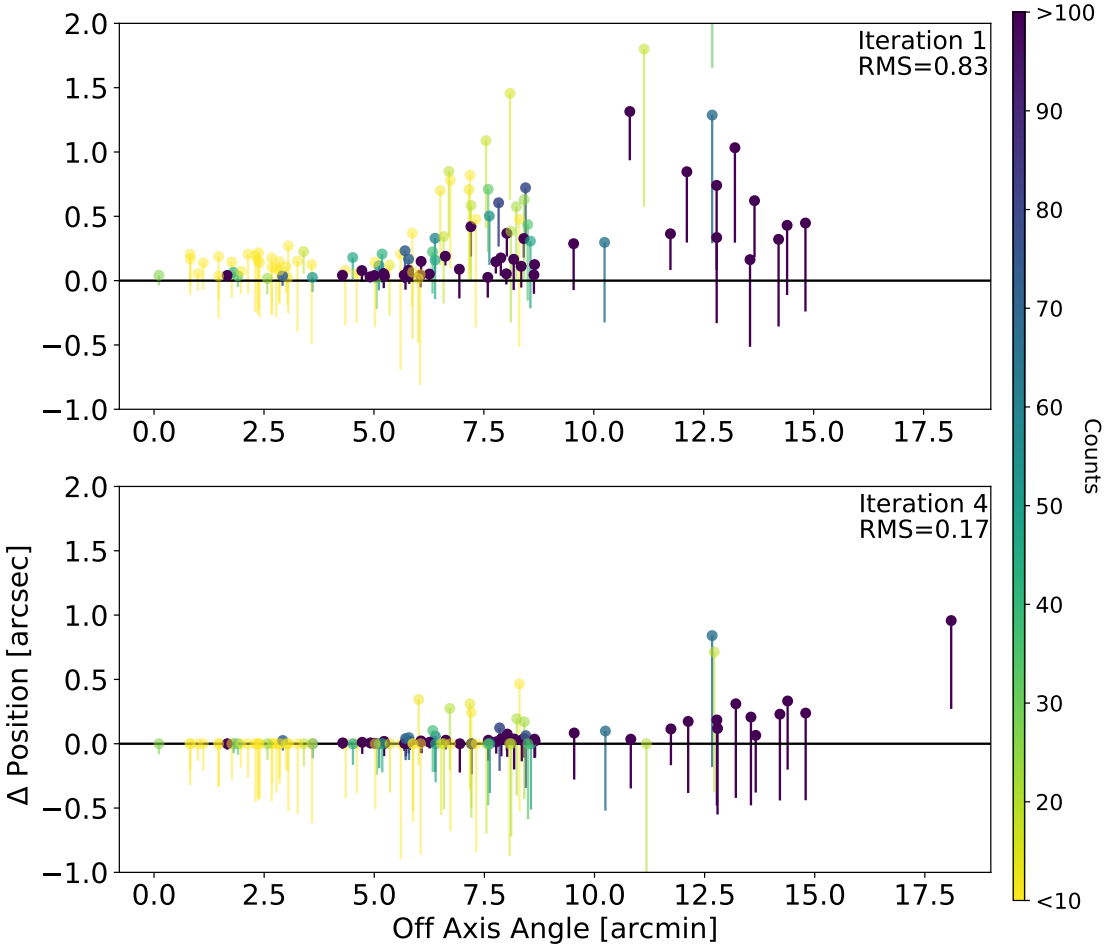

Figure 3.2 Results of ACIS extract iteration to improve *Chandra* source positions in Field A observations (see Section 3.2.2). The top panel shows the change in source position between the input source list from wavdetect and the output AE positions. The bottom panel shows the change between the input and output source positions for the fourth iteration of AE. Note that most of the sources with an off-axis angle $> 10'$ have more than 100 counts. These belong to the nucleus of M31, which is far off axis in the Field A observations and has a high source density. The source with an off axis angle of $\sim 17.5'$ in the bottom panel does not show in the top panel because it has a Δ position $> 2''$ between the input position from wavdetect and the output position from AE. ©AAS. Reproduced with permission from Lazzarini et al. (2018).

3.2.3 HST Data: Panchromatic Hubble Andromeda Treasury

The *HST* data come from the published Panchromatic *Hubble* Andromeda Treasury (PHAT) dataset (Dalcanton et al., 2012). The PHAT survey imaged roughly a third of the disk of M31 in six *HST* filters ranging from near infrared to ultraviolet wavelengths: F160W, F110W, F814W, F475W, F336W, and F275W (central λ = 1.150 μ, 1.545 μ, 8353 Å, 4750 Å, 3375 Å, 2750 Å). We use published photometry catalogs by Williams et al. (2014b) for optical counterpart analysis. PHAT observations were taken in 2010 and 2011. The PHAT data have a limiting F475W magnitude of ~ 28 in the outer disk, and ~ 25 in the more crowded inner disk region.

3.3 Source Matching Between Data Sets

We first matched *NuSTAR* sources to *Chandra* to find precise positions. We then used the *Chandra* positions to identify optical counterparts in the PHAT data.

3.3.1 Source Matching Between NuSTAR and Chandra

We identified 60 *NuSTAR* sources with positions inside the PHAT observed area that positionally match to *Chandra* sources. These 60 sources have 64 associated *Chandra*-detected X-ray sources. We cross-matched *NuSTAR* and *Chandra* sources within 10″ so we could use the more precise *Chandra* positions to identify optical counterparts.

We chose a 10″ match radius to account for the 9″ full width at half-maximum of the *NuSTAR* point spread function (PSF) and the $\sim$0.5″ mean *Chandra* positional errors for sources in our sample. We measured the *Chandra* exposure time at the position of each detected *NuSTAR* source to confirm that if a source was observed by both telescopes, there was a match.

In order to quantify the confidence level of these matches, we investigated the false match probability between *NuSTAR* and *Chandra*. To do this, we adjusted the *NuSTAR* source positions for the full 121-source *NuSTAR* M31 catalog (Wik et al., in preparation) by 10″ in both RA and Dec. We performed this adjustment four times, using all permutations of adding and subtracting 10″ from the RA and Dec of *NuSTAR* sources. We re-matched the *NuSTAR* and *Chandra* source

positions each time to see how many *Chandra* sources matched to the adjusted *NuSTAR* source positions. We found an average of 5 matches between the adjusted *NuSTAR* source positions and the *Chandra* source positions. Out of 121 *NuSTAR* sources, this equals a false match probability of 4.1%. This means that 2-3 of the *NuSTAR* sources in our sample could have false matches to *Chandra* sources.

We note that while our sample covers an area $\sim$ 75% of the *NuSTAR* total observed area, it only contains $\sim$ 50% of the *NuSTAR* sources in the full 121 source catalog. This is because our sample only contains sources observed with *NuSTAR*, *Chandra*, and *HST*, which excludes part of the bulge of M31, in an area with high *NuSTAR* source density.

There are five *NuSTAR* sources that are within the *Chandra* Field A footprint that were not detected by *Chandra*. Given that the *Chandra* Field A and *NuSTAR* observations were taken a year apart, we believe this discrepancy is due to variability.

There are three *NuSTAR* sources whose positions are compatible with multiple *Chandra* sources. This is not surprising as *NuSTAR* can blend *Chandra* sources together because of its large PSF. The PSF of *NuSTAR* has a core with a full width at half-maximum of $18''$ and a half-power diameter of $58''$ (Harrison et al., 2013). This is quite large compared to the *Chandra* PSF, which is $\sim 0.5''$ on-axis to $\sim 10''$ at the edge of the field (Williams et al., 2004a).

NuSTAR source 105 matched to three *Chandra* sources, and *NuSTAR* sources 70 and 57 matched to two *Chandra* sources. In these instances, we kept all *Chandra*-detected sources in our total list of 64 X-ray sources. When comparing *NuSTAR* classifications with optical counterpart types, we only used the optical counterpart associated with the *Chandra* source with the largest number of counts in the 0.35-8.0 keV band.

To further confirm associations between the *NuSTAR* and *Chandra* sources, we compared the flux of each match in the 4-8 keV energy range, as shown in Figure 3.3. We converted from count rates to fluxes for each telescope using the NASA High Energy Astrophysics Science Research Archive Center's (HEASARC) web-based Portable, Interactive Multi-Mission Simulator

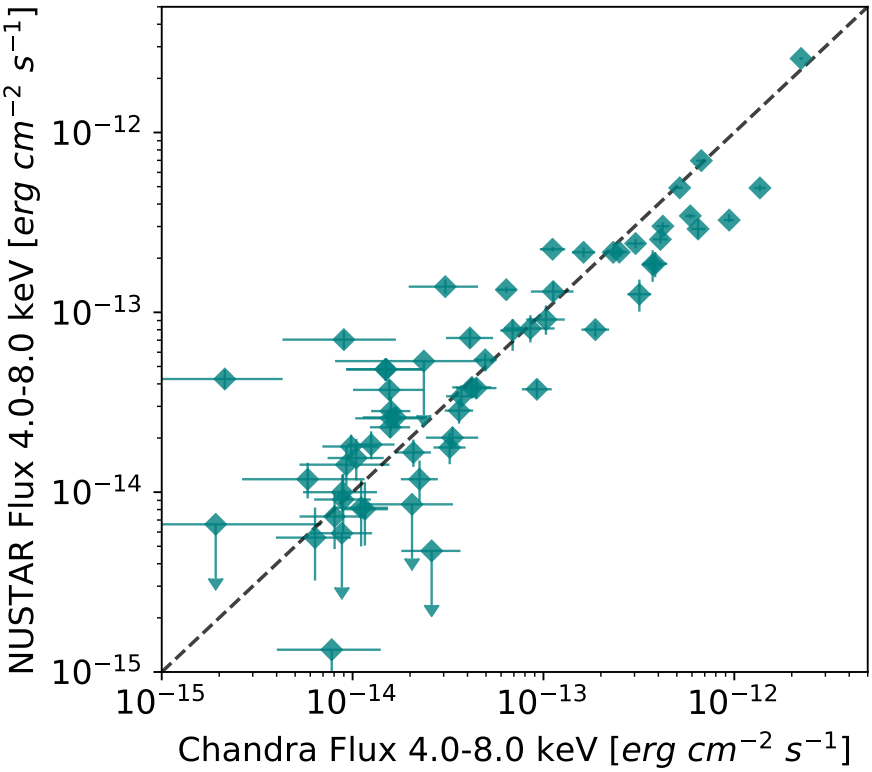

Figure 3.3 A comparison of *NuSTAR* and *Chandra* measured fluxes for 60 hard X-ray sources observed by both telescopes. Sources were matched positionally within 10″. ©AAS. Reproduced with permission from Lazzarini et al. (2018).

(WebPIMMS) tool.[1]

3.3.2 Identifying Optical Counterparts in PHAT

We determined optical counterparts to X-ray sources using a combination of positional matching, UV magnitude cuts, and visual inspection. We initially determined optical counterpart candidates by looking at both optical and UV images of the PHAT data within the 1-σ *Chandra* positional error circles of a hard X-ray source. This method allowed for initial detection of likely counterparts such

[1] https://heasarc.gsfc.nasa.gov/cgi-bin/Tools/w3pimms/w3pimms.pl

as background galaxies and globular clusters (e.g., Galleti et al., 2003). If a source had a clear point source in the UV F336W image within the 1-σ *Chandra* positional errors, it was noted as a point source counterpart candidate and its PHAT photometry was retrieved and is listed in Table 3.2.

We investigated the false match probability for the PHAT counterparts. The PHAT survey area is divided into 23 "bricks" (see Dalcanton et al. (2012) for description of brick boundaries). We calculated the source density of O/B stars in the PHAT survey in the bricks (9 bricks total) covered by *Chandra* and *NuSTAR* observations. We used only stars with good data in at least three of the HST photometric bands used by PHAT and an F336W magnitude of less than 23. Dividing the number of O/B stars by the total area of the 9 bricks gives a density of O/B stars per area. We then multiply this source density by the area of the average *Chandra* 1-σ error circle to determine the probability of finding an O/B star within the 1-σ error circle of an X-ray source. We find a false match probability of about 2%. Accounting for the 64 X-ray sources in our combined *NuSTAR-Chandra* sample within the PHAT footprint, we expect 1-2 false matches.

We used finding charts and color-magnitude diagrams (CMDs) to identify optical counterparts. Figure 3.4 shows a representative figure for source 004335.91+411433.4, an X-ray source with a point source optical counterpart. The optical counterpart is marked in the UV image (lower left) with a cyan circle and is visible as a very bright star in the 1-σ *Chandra* positional errors of the optical finder (lower right). The counterpart is also plotted on two color-magnitude diagrams (CMDs) in the top row of the figure as a cyan star. It falls along the massive end of the main sequence in both CMDs. Note that there are far fewer stars in the upper left CMD because there are not as many stars in the PHAT survey that have well-measured UV (F336W) magnitudes. The very populated region of the upper right CMD is the red giant branch, which is too faint in the UV to be detected in the PHAT data, so that feature is not as prominent in the UV CMD.

We looked for optical counterparts for the *NuSTAR-Chandra* sources, 64 of which are within the area of M31 observed by PHAT. We determined the following optical counterparts: 15 point sources, 13 globular clusters, and 8 background galaxies. The remaining 28 *NuSTAR-Chandra* sources do not have clear optical counterparts. Optical counterparts for all sources are listed in the last column of Table 3.1.

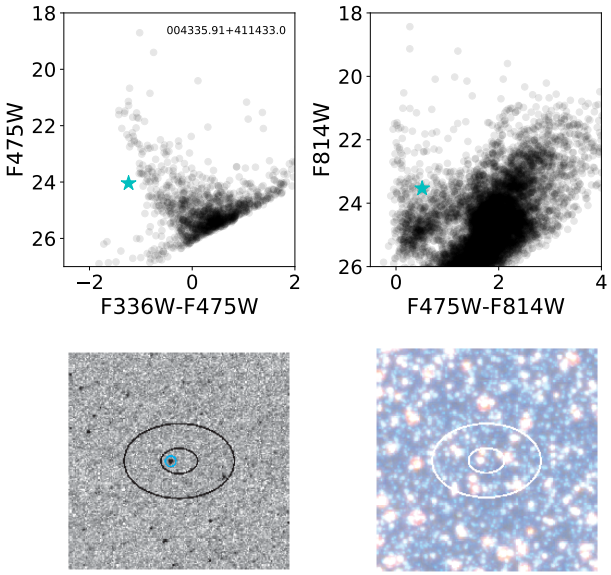

Figure 3.4 Color-magnitude diagrams (CMDs) (top) and finding charts (bottom) from the PHAT data set for the $10'' \times 10''$ region surrounding source 004335.91+411433.4. The top two panels show the UV and optical CMDs. The bottom two panels show a UV image in the F336W filter and an RGB optical image with the F160W filter as red, F814W as green, and F336W as blue. The plotted ellipses represent the 1- and 3-σ *Chandra* positional errors. The optical counterpart is identified in the UV finder (lower left) with a cyan circle and on the CMDs with a cyan star. The black points in the background represent other stars in the PHAT photometry catalog within $5''$ of the X-ray source position. ©AAS. Reproduced with permission from Lazzarini et al. (2018).

We expect to find 7-8 background AGN in our *NuSTAR* sample. Wik et al. (in preparation) identified *NuSTAR* sources with luminosities greater than $\sim 2 \times 10^{36}\ erg\ s^{-1}$, and used the published log(N)-log(S) relationship from Harrison et al. (2016) to calculate the expected contamination of background AGN. We scale this relation to the area of the *NuSTAR* field also covered by *Chandra* and *HST*. We identify 8 background galaxies using the PHAT imaging (listed in Table 3.1), which is consistent with this prediction, suggesting that all AGN with *NuSTAR* detections were visible in the optical PHAT data.

3.4 Results

3.4.1 NuSTAR Source Classification

Wik et al. (in preparation) classified the hard X-ray sources in this sample by comparing their X-ray colors and luminosities to those of Galactic XRBs with known compact object types. This method is presented in Zezas et al. (in preparation) and has previously been used to classify sources in NGC 253 (Wik et al., 2014).

Black-hole XRBs are known to exhibit different accretion states which are manifested by their different broad-band X-ray spectra (especially above 10 keV) and power-spectra (e.g., Remillard & McClintock, 2006; Done et al., 2004). The main differences between these spectral states are identified at energies above 8.0 keV, i.e. energies that can be probed with *NuSTAR*.

In order to develop a diagnostic tool that can be used to characterize *NuSTAR* observations of extragalactic XRBs, Zezas et al. (in preparation) used the extensive library of black-hole spectra of (Sobolewska et al., 2009). This library includes includes a set of 1772 Rossi-XTE - PCA observations of 6 Galactic black-hole X-ray binaries. These observations were performed during different accretion states, and in some cases they cover the complete evolution of a system during an outburst. Each spectrum was modeled with a Comptonized disk black-body model (Sobolewska et al., 2009). The state characterization was based on the spectral shape (see Sobolewska et al., 2009, for more details).

Based on this model and the *NuSTAR* response files, Zezas et al. (in preparation) simulated

NuSTAR observations and calculated the expected count-rates in different bands. Extensive tests showed that hardness ratios involving the 4.0-6.0 keV (soft), 6.0-12.0 keV (medium), 12.0-25.0 keV (hard), and 4.0-25.0 keV (full) bands give the optimal separation of spectral states, while maximizing the number of counts in each band. Luminosities and count rates of Galactic XRBs were scaled to the distance of M31 for comparison with XRBs in our sample.

We note that the highest energy of the *NuSTAR* data (25 keV) is well within the range of the RXTE-PCA spectra, ensuring high-quality input spectral models. Fig. 5.4 shows the locus of the different black-hole accretion states on the intensity-hardness ratio and hardness-ratio hardness-ratio diagrams (red, green, and blue correspond to the soft, intermediate, and hard accretion states respectively).

In these diagrams we also include accreting B*e*-XRB pulsars with available RXTE-PCA spectra (e.g., Reig, 2011) following the same procedure as for the black-hole X-ray binaries. Their intrinsically hard X-ray spectra clearly separate them even from the locus of the hard-state black hole X-ray binaries (Zezas et al., in preparation). Finally, we include spectra of Z-track neutron star Low-mass X-ray binaries (LMXBs).

Determining background AGN contamination is difficult as their hard X-ray colors and luminosities can be similar to those of compact objects in the disk of M31 (see e.g., Tozzi et al., 2006). While most background galaxies do not have *NuSTAR* classifications because they do not have enough counts in the hard (12-25 keV) band, they can occupy similar regions of the hardness ratio and hardness-intensity diagrams as compact objects in M31. Two sources that were determined to be background galaxies using PHAT imaging are plotted as black circles outlined in orange in Figure 5.4. This highlights the importance of incorporating data at optical wavelengths to remove these sources from our hard X-ray sample.

3.4.2 SED Fitting of Stellar Optical Counterparts

We obtained SED fits of 15 point source optical counterparts using the Bayesian Extinction And Stellar Tool (BEAST) (Gordon et al., 2016). The BEAST code fits the observed SED of an individual star in M31 with theoretical SEDs from the Padova stellar evolution models (Marigo

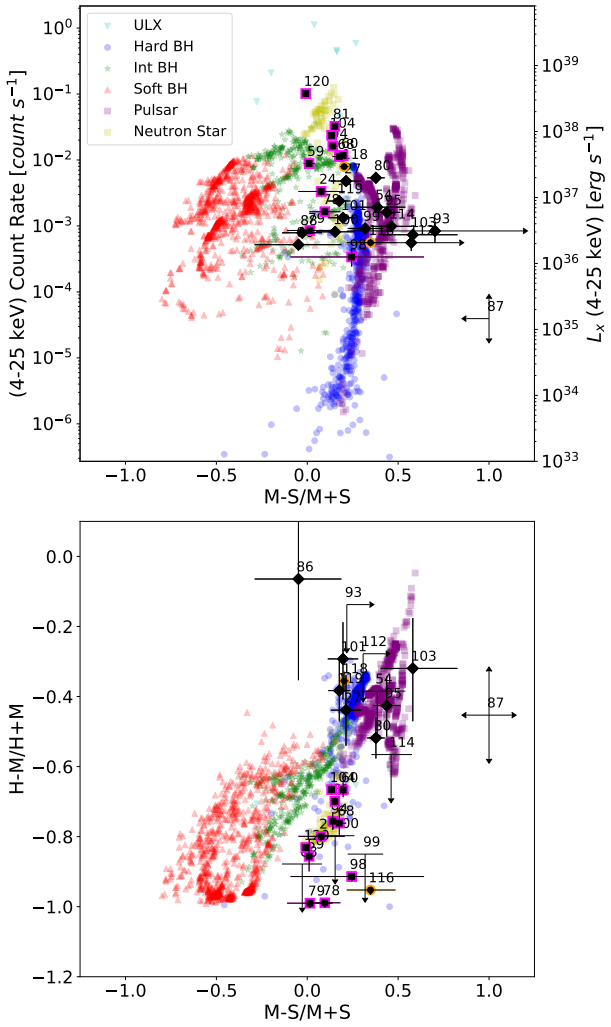

Figure 3.5 Hardness-intensity diagram and hardness ratio plots used to classify *NuSTAR* sources. These plots show sources classified as HMXB candidates as black diamonds. Circles outlined in orange are the two background galaxies with *NuSTAR* classifications that were identified using *HST* imaging, described further in Section 3.5.1. Squares outlined in magenta are globular clusters, which occupy the non-magnetized neutron star region of both diagrams (see Section 3.5.5 for further discussion of X-ray sources in clusters). The bands are defined as follows: soft (S=4-6 keV), medium (M=6-12 keV), and hard (H=12-25 keV). Sources are labeled by *NuSTAR* ID. Background colored sources represent modeled evolutionary tracks of Galactic X-ray binaries with known compact object types, adjusted for the distance of M31. *NuSTAR* data and source classifications for M31 sources from Wik et al. (in preparation). ©AAS. Reproduced with permission from Lazzarini et al. (2018).

et al., 2008) using a Bayesian statistical approach. The code assumes single-star evolution and that sources are in M31. Photometric bias and uncertainty are applied from artificial star tests performed on the data. The input for the BEAST code is the six-band photometry and artificial star tests of the star measured by the PHAT survey. The code uses upper limits as constraints. Output parameters include several primary and derived quantities. Primary fit outputs include initial stellar mass, $A(V)$ (dust extinction), and stellar metallicity. Derived quantities include luminosity, effective temperature, and stellar surface gravity. Output physical parameters for the 15 point source optical counterpart candidates in our sample are listed in Table 4.1.

As part of the fitting, χ^2 values are computed assuming multi-variate Gaussian uncertainties, either uncorrelated or correlated. The probability of a given model is proportional to χ^2, letting us use the χ^2 value as a relative assessment of the "goodness of fit".

In most HMXBs, the donor star is much brighter than the accretion disk at optical wavelengths, so the fits with low χ^2 values should be robust. The BEAST code is designed to fit individual stars, and so it will return a poor fit if a point source is not an individual star. Examples of systems that might return a poor fit include parts of a multiple star system, background AGN, companions in XRBs that have been irradiated by their associated X-ray source (Phillips & Podsiadlowski, 2002), stars contaminated with light from the compact object's accretion disk, chance superpositions of sources, or B*e* star donors with a red excess from the accretion disk relative to the underlying B star's spectrum.

Table 4.1 shows a clear division in χ^2 values: $\chi^2 \lesssim 12$ or $\chi^2 \gtrsim 50$. Examples of these two categories are shown in Figure 3.6. The lower χ^2 fit appears similar to a stellar SED model, while the high χ^2 appears to have a flat SED. Based on the clear division in fit quality as well as SED appearance, we decided that fits with $\chi^2 \lesssim 12$ likely have SEDs consistent with stars in M31 fits with higher χ^2 values do not. Thus, we did not determine a spectral type for sources with χ^2 values above ~ 12.

Table 4.1 lists the probable spectral type given the best-fit physical parameters. We determine masses, temperatures, and luminosities for 7 of the 15 point sources which are consistent with a B-type star, and therefore very strong HMXB candidates. B-type stellar classification was determined

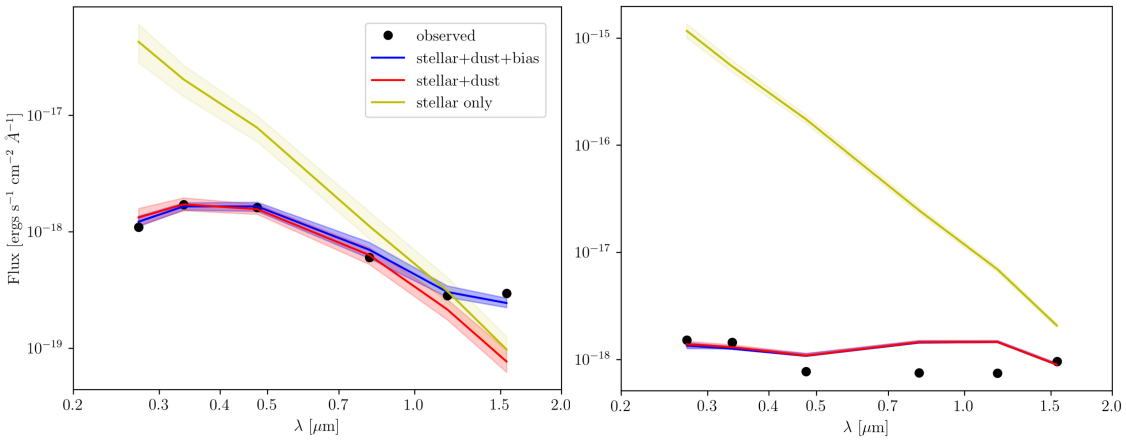

Figure 3.6 BEAST SED fits for the optical counterparts of two HMXB candidates, 004321.48+411556.9 (left) and 004448.13+412247.9 (right). The counterpart in the left panel has a robust fit and is most likely a B-type star. The counterpart in the right panel returns a poor fit. Black points show measured photometry for the optical counterparts from the PHAT dataset, listed in Table 3.2. The colored lines show the median fit $\pm 33\%$ errors of the three different models. Yellow shows the stellar-only model, red shows a stellar+dust model and blue shows a stellar+dust+bias model. The observational bias is determined using artificial star tests. ©AAS. Reproduced with permission from Lazzarini et al. (2018).

for $4 M_{\odot} \lesssim M \lesssim 17 M_{\odot}$ and $4.0\ K \lesssim log(T_{eff}) \lesssim 4.5\ K$ (e.g., Silaj et al., 2010). Figure 3.6 shows the SED fit for the optical counterpart to 004321.48+411556.9, an example of a good fit for a B-type star.

One optical counterpart (004249.22+411815.8) is classified as a possible red Helium burning star given its high luminosity, low temperature and low surface gravity. The hard X-ray source associated with this optical counterpart does not have a *NuSTAR* classification.

We do not rule sources out as HMXB candidates due to fits because a poor fit may be returned for stars that have been irradiated by their associated X-ray source or contaminated with light from their compact object's accretion disk, as discussed previously in this section. However, sources with good fits to stars in M31 may be stronger than those that do not.

We find two point sources that have relatively flat SEDs, noted in Table 4.1. Figure 3.6 illustrates the BEAST fit for the optical counterpart of one of these sources, 004448.13+412247.9. The

BEAST attempts to fit the point source as a hot star with a high A(V) (e.g., 4.6 magnitudes of extinction, as shown in Figure 3.6, compared to the 1.2 magnitudes of dust extinction shown for a star that has a robust fit to a B-type star) and still returns a poor fit. The other source that has an optical counterpart with a flat SED is 004316.11+411841.5. Such a flat SED may be indicative of a background AGN.

3.4.3 Star Formation Histories of HMXB Candidates

We used the spatially resolved recent star formation history (SFH) of M31 by Lewis et al. (2015) to determine likely ages of HMXB candidates in our sample. Lewis et al. (2015) inferred these SFHs using CMDs of 100 pc by 100 pc regions in the M31 disk.

We assume HMXBs contain secondary stars more massive than 7 $M_{\odot}$, which have lifetimes of 10 Myr. Thus we conservatively restrict our age distribution analysis to $<$ 60 Myr. The time resolution of the SFHs is log(time)=0.1 yr. Star formation histories are not available for regions too close to the bulge of M31 (in PHAT bricks 1 and 3) because crowding does not allow for accurate CMD fitting, and so not all HMXB candidates are included in our analysis. For that reason, 8 of the 15 HMXB candidates are used in the SFH analysis: 004335.91+411433.4, 004350.76+412118.1, 004404.75+412127.2, 004404.75+412127.2, 004425.73+412242.4, 004448.13+412247.9, 004518.38+413936.6, 004527.88+413905.5, and 004528.24+412943.9.

For each HMXB region containing an HMXB candidate, we calculated the total stellar mass formed in the past 60 Myr. For each time bin younger than 60 Myr, we calculated the fraction of the mass formed in that bin. This fraction gives the normalized probability that the given HMXB candidate formed in that time bin. We take the uncertainties in the SFH into account by sampling the SFH 1000 times and recalculating the age distribution. We take the 16th and 84th percentile in each time bin, to determine uncertainties. The number of HMXB candidates expected to form in each time bin is shown in Figure 3.7 in teal.

We then compare the probability distribution for regions with HMXB candidates to the rest of the M31 disk. We do this by randomly selecting 8 regions from a sample of $\sim$ 49 regions containing known background galaxies identified by Williams et al. (2018) in the PHAT bricks observed by

Chandra and *NuSTAR* and immediately adjacent. We use the SFH for regions around background galaxies because these should be randomly distributed throughout the disk and not correlated with the HMXB population. We perform this random selection 100 times and plot the average expected number of candidates in each time bin in black in Figure 3.7.

Using the sub-sample of 8 HMXB candidates with SFHs, we were able to determine that about 3 HMXBs in our sample have an age of ∼25-50 Myr, 2 are ∼10 Myr old, and 1 is ∼4 Myr old. Two of the HMXB candidates analyzed, 004350.76+412118.1 and 004404.75+412127.2, are found in regions without significant star formation in the last 60 Myr, making them weaker HMXB candidates.

The ages of candidates between 25 and 50 Myr are fairly consistent with random draws from the disk of M31. This indicates that the regions with these HMXB candidates do not appear to be a different age than the average population. The peak in star formation in regions surrounding HMXB candidates in the 10-12 Myr and 4 Myr time bins are more significant deviations from the overall SFH of M31, as demonstrated in Figure 3.7. These may be probing the prompt HMXB formation channel in M31.

3.5 Discussion

Our measurements allow many detailed comparisons of the X-ray sources in this region of M31. First, we can compare the optical and X-ray characteristics of the sources with counterparts. Next, we can compare those characteristics with the age distribution of the surrounding stellar populations as an additional consistency check, and finally we can consider the sources in globular clusters to look for X-ray characteristics unique to that specific subclass. We discuss all of these comparisons below.

3.5.1 Comparing NuSTAR and HST Source Classification

In Figure 3.8 we compare the classification of the compact object determined by *NuSTAR* colors with the type of the associated optical counterpart. Sources that fall within the "none" *NuSTAR* classification did not have enough counts in all three X-ray bands to be accurately classified.

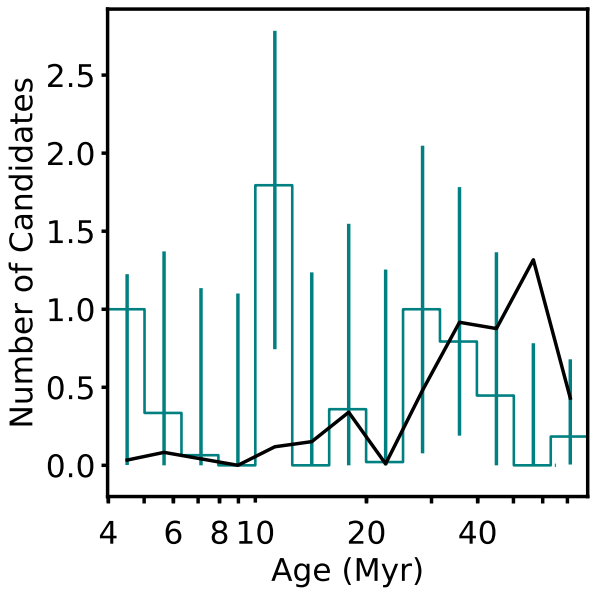

Figure 3.7 Histogram showing the number of HMXB candidates associated with each time bin based on their spatially resolved star formation histories from Lewis et al. (2015). The time bins are defined by the age resolution of the SFHs. The black line represents the average of 100 random samples of regions in M31 not associated with HMXB candidates, providing a reference for the overall SFH of M31. ©AAS. Reproduced with permission from Lazzarini et al. (2018).

Sources with the "none" optical counterpart classification did not have a clear optical counterpart in PHAT imaging.

Nine *NuSTAR* classified non-magnetized neutron stars in our sample are found within globular clusters, and we find no pulsars or hard state black holes in globular clusters. Roughly equal numbers of pulsars, non-magnetized neutron stars, and hard state black holes have point sources as optical counterparts. We also find that four pulsars in our sample are HMXB candidates with point source optical counterparts, while four have no optical counterpart. Pulsars without optical counterparts could be part of a low or intermediate mass X-ray binary system. This suggests that the pulsars in our sample are not preferentially in HMXB systems. When we compare the *NuSTAR* source classifications with the results of the BEAST SED fitting (summarized in Table 3.4), we notice that none of the HMXB candidates with classified hard state black holes have good SED fits to B-type stars.

It is important to note *NuSTAR* sources 57 and 70, which are each blends of two *Chandra* sources (see Section 3.3.1). In both cases, one *Chandra* source has a globular cluster optical counterpart and the other has no optical counterpart. Source 70 is classified as a non-magnetized neutron star, suggesting that the *Chandra* source associated with a globular cluster may dominate the light detected by *NuSTAR*. Source 57 is classified as an intermediate state black hole, which would be unusual associated with a globular cluster. We compared the 4-8 keV *Chandra* flux of the two *Chandra* sources that matched to *NuSTAR* source 70 and 57. The energy fluxes were consistent within errors, so we could not determine which source dominated the flux observed by *NuSTAR*. The *NuSTAR* source classification may be affected by the blend of the two *Chandra* sources, and thus additional investigation is needed to confirm if the source classification is a result of the blend.

We compare PHAT imaging with *NuSTAR* classifications to remove background AGN contamination from our sample. We find two cases where sources classified as compact objects in the disk of M31 were determined to be background galaxies using PHAT imaging. See Figure 3.9 for PHAT images used to identify these background galaxies. The apparent misclassification of these two sources does not affect the conclusions of this chapter, but illustrates the power and necessity

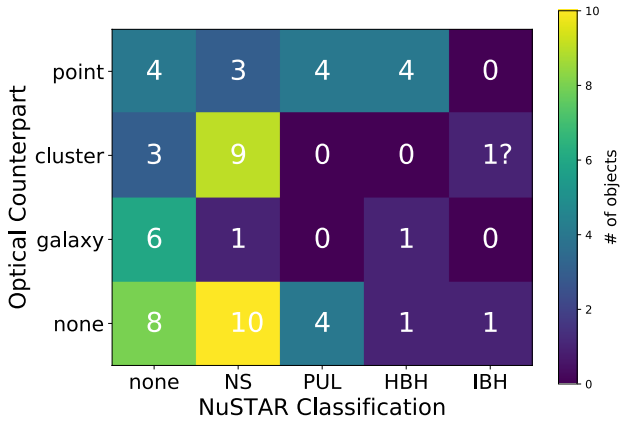

Figure 3.8 Comparing the *NuSTAR* X-ray classification and optical counterpart of sources observed with *NuSTAR*, *Chandra*, and PHAT. *NuSTAR* classifications are defined as follows: NS=non-magnetized neutron star, PUL=pulsar, HBH=hard-state black hole, IBH=intermediate-state black hole. For further discussion of the *NuSTAR* classified intermediate state black hole associated with a cluster, see Section 3.5.5. ©AAS. Reproduced with permission from Lazzarini et al. (2018).

of combining *NuSTAR* observations with *HST* data to eliminate background AGN contamination. These two sources are 004527.30+413254.1 (*NuSTAR* source 118, discussed in more detail in Section 3.5.5), which is classified as a hard state black hole, and 004530.61+413600.4 (*NuSTAR* source 116), which is classified as a non-magnetized neutron star. Both sources have resolved background galaxies as optical counterparts in the PHAT imaging.

3.5.2 Evaluation of HMXB Candidates

Table 3.4 summarizes our investigation of HMXB candidates, identified by selecting for hard X-ray sources spatially coincident with UV-bright point source optical counterparts. We evaluate whether a source is a likely HMXB using three methods: (1) SED fitting with the BEAST code to determine if a massive, young star appears to be the donor, (2) age estimation using spatially resolved SFHs, and (3) compact object classification using *NuSTAR* hard X-ray colors and luminosities.

We consider any hard X-ray source with a UV-bright point source optical counterpart an HMXB candidate, even if it does not satisfy all three criteria. For example, the optical counterpart could have a poor SED fit because of irradiation from the compact object or mass transfer, as discussed

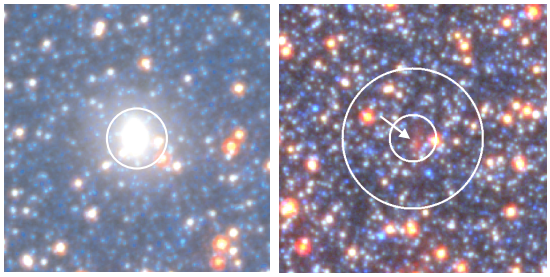

Figure 3.9 Images showing background galaxies associated with *NuSTAR* source 118 (left) and 116 (right). These color images were created with *HST* imaging from the PHAT survey and use the F160W filter as red, F814W as green, and F336W as blue. Images are 10″ on a side. White circles indicate the 1- and 3-σ *Chandra* positional errors. The 1-σ error is not visible on the image on the left as it lies on top of the bright galaxy. The galaxy on the left is bright, extended, and elliptical in shape. The galaxy on the right is much fainter. It is visible as a faint, red, extended source within the 1-σ error error circle, indicated with an arrow. For more discussion of background galaxies, see Section 3.5.1. ©AAS. Reproduced with permission from Lazzarini et al. (2018).

in Section 3.4.2. Additionally, not having a *NuSTAR* compact object classification does not rule out an HMXB candidate. Sources must have enough flux in all three *NuSTAR* bands to be classified, so a source could remain unclassified if it is too faint or there is too much absorption to be detected in all bands. We simply comment that having a *NuSTAR* compact object classification or good optical companion SED fit makes an HMXB a stronger candidate because we have more information about the system.

We find that HMXB candidate 004425.73+412242.4 satisfies all three criteria. It has a good SED fit indicating a B-type donor star and the SFH in the region around this source shows star formation bursts within the last 60 Myr. This source's *NuSTAR* colors and luminosities indicate it is likely a pulsar.

Three HMXB candidates in our sample, 004308.63+411248.4, 004321.08+411750.6, and 004339.06+412117.6 have optical counterparts that have good SED fits to B-type stars and have a *NuSTAR* classification of pulsar or non-magnetized neutron star. However, due to their location close to the bulge of M31, spatially resolved star formation histories are not available for the region surrounding these candidates.

Four HMXB candidates in our sample, 004448.13+412247.9, 004518.38+413936.6, 004527.88+413905.5, and 004528.24+412943.9 satisfy two of the three criteria listed in Table 3.4. All of these sources are found in regions with recent star formation but are either lacking a good SED fit to a B-type star or do not have a compact object classification from *NuSTAR*.

Four HMXB candidates in our sample have either a good SED fit for a B-type donor star (004249.22+411815.8 and 004321.48+411556.9) or *NuSTAR* classified compact object (004240.31+411845.6 and 004316.11+411841.5). These sources do not have SFHs available, due to their proximity to the bulge of M31.

Two HMXB candidates in our sample lack good SED fits to B-type companion stars and are found in regions with no significant star formation in the last 60 Myr. These sources are indicated as HMXB candidates because they have UV-bright point sources associated with a *NuSTAR*-detected hard X-ray source. Source 004350.76+412118.1 is classified as a non-magnetized neutron star and source 004404.75+412127.2 is classified as a hard state black hole. The lack of star formation and poor SED fits could indicate that these sources are background AGN. Thus, further multi-wavelength observations are needed.

3.5.3 Comparison With Other Hard X-ray Observations of M31

Three sources in our sample were investigated in detail by Stiele & Kong (2018) in a *NuSTAR* survey of the central region of M31. This study was designed to overlap with a previous *XMM-Newton* survey of M31 (Stiele et al., 2011). Stiele & Kong (2018) use hardness ratios, to classify four X-ray sources previously classified only as "hard" using *XMM-Newton* data as X-ray binaries. Two of these new XRB candidates are in our sample: *NuSTAR* sources 47 and 65. We classify these sources as non-magnetized neutron stars and find no optical counterpart, suggesting that they could be LMXBs because these types of stars would be too faint to be observed in the PHAT survey. Additionally, Stiele & Kong (2018) discuss several sources that are too hard to be located in the XRB area of their hardness ratio diagrams. One of these sources is in our sample (*NuSTAR* source 91) and is classified as a pulsar with no optical counterpart.

3.5.4 Ages of Stellar Populations Hosting HMXBs

The ages (20-50 Myr) of the regions surrounding most HMXB candidates in this study are consistent with the results seen in the Small Magellanic Cloud (SMC) (Antoniou et al., 2010). In the SMC, B*e*/X-ray binaries are the most numerous subclass of HMXBs, and are found in regions with star bursts that occurred between 25 and 60 Myr ago. In the LMC X-ray binaries were found associated with younger regions, between 6 and 25 Myr old (Antoniou & Zezas, 2016). The statistically significant increase in the number of HMXB candidates we found in M31 in regions with a star formation burst 10 Myr ago (Figure 3.7) aligns with the young ages found in the LMC.

We examined the 3 sources in regions with a strong peak in star formation rate in the 10 Myr bin, since this is a 1.5 σ deviation from the background population (as shown in Figure 3.7). The stellar population surrounding one source in particular, 004425.73+4122241.8, experienced almost all of its star formation in the 10 Myr time bin. This HMXB candidate has been classified as a pulsar with a B-type stellar companion, determined by its *NuSTAR* colors and BEAST SED fit. Two other sources are also located in regions with SFR peaks in this time bin: 004518.38+413936.6 and 004448.13+412247.9. Source 004518.38+413936.6 has an optical counterpart that is classified as a B-type star with no *NuSTAR* classification for the compact object. Source 004448.13+412247.9 is classified as a neutron star by *NuSTAR* but the BEAST SED fit quality is too low to determine the spectral type of the companion, but it is unlikely a single star in M31.

Source 004518.38+413936.6 (with a B-type stellar optical counterpart) is located in a region that also experienced significant star formation in the 4 Myr time bin. Note that connecting HMXB populations to stellar ages is important for constraining formation models of compact objects. Rappaport et al. (2005) and Justham & Schawinski (2012) predict that a time delay of 10 Myr (assuming instantaneous burst of star formation) or 200 Myr (continuous star formation) may be expected between the onset of star formation and the production of X-rays, depending on star formation history. XRB pulsars have been found with similar ages in the Magellanic Clouds. Li et al. (2016) found an X-ray pulsar with an O-type counterpart star in the SMC, suggesting the system is $\sim 5 - 6$ Myr old and Belczynski et al. (2008) find that XRB pulsars can form at ages

as young as ~ 5 Myr. HMXBs associated with very young stellar ages (10 Myr or less) but with B-star secondaries can place a particularly important constraint on initial mass ratios of HMXBs, as such an object must have had a much more massive companion with a lifetime short enough to have become the accreting compact object.

3.5.5 X-ray Sources in Clusters

Maccarone et al. (2016) investigated hard X-ray sources in globular clusters using combined *Swift*-*NuSTAR* spectroscopy. Our sample of 64 X-ray sources observed by *NuSTAR*, *Chandra*, and *HST* includes four of the five sources in that study. These sources are not HMXB candidates as they were found to be spatially coincident with globular clusters, not point sources. We find that three of these sources (*NuSTAR* sources 65, 104, and 120 in our sample) are classified as neutron stars and one (*NuSTAR* source 118) is classified as a hard state black hole.

We determine the hard state black hole has a background galaxy optical counterpart rather than a globular cluster, using its PHAT imaging. We also cross-reference the globular cluster and background galaxy catalogs published by the PHAT survey and find that this source is classified as a galaxy based on its morphology (Johnson et al., 2015).

This source was investigated in detail by Dorn-Wallenstein et al. (2017), who found that it has a spectroscopic redshift, which agrees with our classification as a background galaxy. This source highlights the importance of incorporating data at optical wavelengths to remove background AGN contamination.

We identify one, source (NuSTAR source 57) classified as an intermediate state black hole that may be associated with a globular cluster. Some caution is warranted in interpreting this source because it is associated with two separate Chandra sources, 004255.61+411834.8 and 004255.19+411835.7, and hence the NuSTAR spectrum is probably a superposition of two different source spectra. The former of the two Chandra sources has a globular cluster optical counterpart, while we do not see evidence for a globular cluster associated with the latter source.

The potential connection between the globular cluster and a black hole is intriguing. For quite some time, it was thought that the Spitzer (1969) instability would lead to mass segregation that

would, in turn, expel most or all stellar mass black holes from globular clusters (Kulkarni et al., 1993; Sigurdsson & Hernquist, 1993). The discoveries of strong candidate globular cluster black holes in external galaxies (e.g., Maccarone et al., 2007) and in the Milky Way (e.g., Strader et al., 2012; Chomiuk et al., 2013; Giesers et al., 2018) has helped motivate and support theoretical work which has shown that globular clusters may retain black holes (e.g., Mackey et al., 2008; Sippel & Hurley, 2013; Morscher et al., 2015).

The globular cluster G1 is of special interest as it has been suggested to contain an intermediate mass black hole (IMBH) on the basis of stellar dynamical evidence (Gebhardt et al., 2002; Baumgardt et al., 2003, for an alternative view). Its X-ray source is consistent with accretion from the putative IMBH (Pooley & Rappaport, 2006). It appeared as a detectable radio source in VLA data (Ulvestad et al., 2007), but later sensitive radio data found only deep upper limits (Miller-Jones et al., 2012), again providing an ambiguous determination of whether the cluster contains an IMBH. The IMBH classification is highly uncertain, as the X-ray observations are also consistent with emission from an LMXB (Kong et al., 2010; Miller-Jones et al., 2012). Potentially, deep *NuSTAR* imaging could provide some additional clues about this interesting globular cluster source as well.

Still, the total number of strong candidate black holes in globular clusters remains relatively small, especially at distances where the clusters' structural parameters are measurable, so *NuSTAR* source 57 in our sample merits follow-up work to further test the black hole hypothesis.

3.6 Conclusions

In this work we present 15 HMXB candidates: hard X-ray sources observed by *NuSTAR* and *Chandra* that are spatially associated with UV-bright point sources from the PHAT catalog.

We investigated the correlation between the *NuSTAR* determined compact object type and the optical counterpart determined with PHAT imaging. We find 9 *NuSTAR* classified non-magnetized neutron stars associated with star clusters, making this the strongest correlation in our sample, agreeing with the findings in Maccarone et al. (2016).

We did not find any pulsars or hard state black holes associated with star clusters. There did

not appear to be a preference for non-magnetized neutron stars, pulsars, or hard state black holes associated with UV-bright point source optical counterparts. None of the HMXB candidates in our sample with hard state black hole compact objects have a companion star with a good SED fit to a B-type star.

We also find an equal number of pulsars in HMXB and LMXB systems. For the pulsars, this may point towards an interesting result, however our source statistics are too small to tell; further observations are needed. However, either the pulsars are not HMXBs, and might have intermediate donor masses such as those found in other M31 pulsar systems (e.g., Esposito et al., 2016; Yukita et al., 2017) or perhaps their pulsar identifications are not as secure.

We determined likely ages for HMXB candidates using published SFHs. We find that 3 HMXBs in our sample are associated with stellar populations between 25 and 50 Myr old, and 2-3 HMXB candidates are associated with younger stellar populations: 1-2 are $\sim$10 Myr old, and 1 is $\sim$4 Myr old. These ages agree with findings in the Magellanic Clouds, M33, NGC 300, and NGC 2403. The ages we find in M31 and those found in other galaxies suggest two potential formation channels for HMXBs.

Beyond our results investigating individual X-ray sources, this study demonstrates the ability to study both the compact object and companion star in an XRB from the hard X-rays to the near infrared using *NuSTAR*, *Chandra*, and *HST*. In this work we were able to utilize classifications by Wik et al. (in preparation) of hard X-ray sources as neutron stars or black holes based on their X-ray colors and luminosities. Matching the *NuSTAR* sources to *Chandra* allowed us to determine the positions of these X-ray sources with increased accuracy, and thus find and classify their optical counterparts using the PHAT data set. This study is an exciting foray into the combination of hard X-ray and deep optical observations in nearby galaxies. Given the maturity of the PHAT data set, we are able to harness the data products created by the many scientists on the PHAT team to determine ages and spectral types.

Table 3.1: List of all *NuSTAR-Chandra* sources within the PHAT footprint. Optical counterparts to X-ray sources are listed in the *PHAT Cpt.* column: *g* = galaxy, *n* = no optical counterpart, *c* = cluster and *p* = point source. See Section 3.3.2 for further discussion of optical counterpart determination. Stiele ID and classifications from Stiele et al. (2011).

NuSTAR ID	*Chandra* Catalog Name	*Chandra* RA	*Chandra* Dec.	*Chandra* RA err [$''$]	*Chandra* Dec. err [$''$]	Theta $'$	*Chandra* Flux (0.35-8.0 keV) $\times 10^{-13}\ erg\ cm^{-2}\ s^{-1}$	Stiele ID	Stiele Class.	PHAT Cpt.
19	004220.96+411520.3	10.587329	41.255773	2.0	2.0	13.0	$4.2^{+0.4}_{-0.4}$	...	...	n
24	004231.27+411937.5	10.630292	41.327141	2.0	2.0	10.0	$1.9^{+0.3}_{-0.2}$	923	GlC	c
26	004235.20+412005.0	10.646687	41.334782	1.0	0.9	9.5	$3.4^{+0.3}_{-0.3}$	952	⟨hard⟩	n
27	004240.31+411845.3	10.667979	41.312682	2.0	1.0	8.6	$0.90^{+0.15}_{-0.14}$	972	⟨hard⟩	p
41	004243.81+411631.0	10.682538	41.275371	0.7	0.4	8.3	$13.0^{+0.7}_{-0.6}$	1005	⟨XRB⟩	n
43	004244.27+411607.6	10.684498	41.268868	0.7	0.4	8.4	$19.0^{+0.9}_{-0.9}$	1010	⟨XRB⟩	n
44	004246.19+411543.2	10.692552	41.262086	2.0	2.0	8.2	$0.76^{+0.25}_{-0.21}$	...	...	n
45	004246.97+411615.3	10.695737	41.271019	0.6	0.4	7.9	$13.0^{+0.6}_{-0.6}$	1023	⟨AGN⟩	n
46	004247.18+411628.0	10.696608	41.274542	0.6	0.3	7.8	$26.0^{+0.8}_{-0.8}$	1024	⟨XRB⟩	n
47	004248.56+411520.8	10.702332	41.255889	0.6	0.3	8.0	$51.0^{+1.0}_{-1.0}$	1036	⟨XRB⟩^{a}	n
54	004249.22+411815.5	10.70509	41.304395	0.8	0.5	6.9	$1.5^{+0.2}_{-0.1}$	1041	⟨hard⟩	p
55	004252.53+411854.0	10.718888	41.315082	0.5	0.2	6.3	$19.0^{+0.5}_{-0.5}$	1060	⟨XRB⟩	n
65	004254.93+411602.8	10.728903	41.267544	0.5	0.2	6.6	$16.0^{+0.5}_{-0.5}$	1075	⟨XRB⟩^{a}	n
57	004255.19+411835.4	10.729964	41.309922	0.7	0.5	5.8	$0.83^{+0.12}_{-0.10}$	1078	⟨hard⟩	n
57	004255.60+411834.5	10.731708	41.309676	0.7	0.4	5.7	$0.91^{+0.12}_{-0.11}$	1078	⟨hard⟩	c
59	004259.66+411918.9	10.748579	41.322021	0.4	0.2	4.9	$11.0^{+0.4}_{-0.4}$	1102	GlC	c
68	004259.88+411605.3	10.749525	41.268225	0.5	0.2	5.8	$10.0^{+0.4}_{-0.4}$	1103	GlC	c
70	004302.94+411522.2	10.762284	41.256263	0.5	0.2	5.8	$6.4^{+0.3}_{-0.3}$	1116	GlC	c
77	004303.03+412041.6	10.762621	41.344983	0.6	0.4	4.5	$0.50^{+0.09}_{-0.07}$	1115	⟨hard⟩	n
70	004303.23+411527.3	10.763472	41.257677	0.5	0.2	5.7	$13.0^{+0.4}_{-0.4}$	1116	GlC	n
78	004303.29+412121.5	10.763713	41.35607	0.5	0.2	4.7	$2.3^{+0.2}_{-0.2}$	1118	GlC	c
60	004303.87+411804.5	10.766124	41.301336	0.4	0.2	4.3	$6.0^{+0.3}_{-0.3}$	1122	GlC	c
71	004304.25+411600.7	10.767706	41.266967	0.7	0.5	5.2	$0.59^{+0.10}_{-0.09}$	1124	⟨GlC⟩	n
79	004307.51+412019.4	10.781315	41.338806	0.5	0.3	3.6	$0.58^{+0.09}_{-0.08}$	1137	⟨GlC⟩	c
80	004308.62+411248.0	10.785948	41.213448	0.8	0.5	7.2	$3.2^{+0.3}_{-0.3}$	1146	XRB	p
81	004310.62+411451.0	10.794248	41.247599	0.4	0.2	5.2	$23.0^{+0.6}_{-0.6}$	1157	GlC	c
82	004311.37+411809.3	10.797389	41.302675	0.5	0.2	2.9	$0.78^{+0.10}_{-0.09}$	1160	⟨hard⟩	n
85	004313.88+411711.5	10.807835	41.286615	0.7	0.5	3.0	$0.13^{+0.05}_{-0.04}$	...	...	n
86	004316.10+411841.2	10.817115	41.311543	0.4	0.2	1.9	$0.35^{+0.06}_{-0.07}$	1180	⟨XRB⟩	p
88	004321.07+411750.2	10.837815	41.297389	0.4	0.1	1.7	$1.1^{+0.1}_{-0.1}$	1203	⟨hard⟩	p
87	004321.48+411556.5	10.839501	41.265805	0.7	0.4	3.4	$0.21^{+0.05}_{-0.06}$	...	...	p
89	004324.84+411726.9	10.853509	41.290917	0.4	0.2	1.8	$0.47^{+0.08}_{-0.07}$	1216	⟨hard⟩	n
90	004326.33+411911.4	10.859718	41.31994	0.4	0.1	0.11	$0.38^{+0.09}_{-0.07}$	1224	⟨AGN⟩	g
91	004332.38+411040.9	10.884951	41.178136	0.7	0.4	8.7	$15.0^{+0.5}_{-0.5}$	1253	⟨hard⟩^{a}	n
92	004334.33+411323.1	10.893064	41.223187	0.5	0.3	6.1	$5.4^{+0.3}_{-0.3}$	1261	⟨hard⟩	n
93	004335.91+411433.0	10.899635	41.2426	0.8	0.6	5.1	$0.41^{+0.09}_{-0.07}$	1262		p
94	004337.28+411443.1	10.905322	41.245424	0.4	0.2	5.0	$16.0^{+0.4}_{-0.4}$	1267	GlC	c
95	004339.06+412116.7	10.912737	41.354885	0.7	0.7	7.2	$0.73^{+0.07}_{-0.06}$	...	...	p
96	004345.83+411203.7	10.940976	41.201128	2.0	2.0	8.1	$0.39^{+0.11}_{-0.09}$	1298	⟨hard⟩	n
99	004350.76+412117.4	10.961516	41.355033	0.4	0.4	5.1	$0.65^{+0.06}_{-0.05}$	1319	⟨hard⟩	p
97	004353.65+411654.6	10.973526	41.282044	0.4	0.4	7.6	$6.6^{+0.2}_{-0.2}$	1327	⟨GlC⟩	n
98	004356.43+412202.3	10.985126	41.367503	0.4	0.4	3.8	$0.45^{+0.05}_{-0.05}$	1340	GlC	c
105	004402.72+411711.3	11.011322	41.28666	1.0	1.0	6.5	$0.18^{+0.04}_{-0.03}$	...	...	n
101	004404.75+412126.5	11.019799	41.35756	0.3	0.3	2.7	$0.75^{+0.06}_{-0.06}$	1373	⟨AGN⟩	p
102	004416.02+413057.3	11.066667	41.516147	0.4	0.4	4.3	$1.7^{+0.1}_{-0.1}$	1420	XRB	n
103	004425.73+412241.8	11.107221	41.378442	0.3	0.3	2.0	$0.22^{+0.03}_{-0.03}$	1450	⟨hard⟩	p
104	004429.57+412135.1	11.123203	41.359913	0.3	0.3	3.1	$18.0^{+0.3}_{-0.3}$	1463	GlC	c

NuSTAR ID	*Chandra* Catalog Name	*Chandra* RA	*Chandra* Dec.	*Chandra* RA err [$''$]	*Chandra* Dec. err [$''$]	Theta $'$	*Chandra* Flux (0.35-8.0 keV) $\times 10^{-13}\ erg\ cm^{-2}\ s^{-1}$	Stiele ID	Stiele Class.	PHAT Cpt.
105	004429.73+412257.4	11.123878	41.382771	0.5	0.5	2.6	$0.09^{+0.02}_{-0.02}$	···	···	n
109	004430.16+412301.1	11.125694	41.383802	0.6	0.6	2.7	$0.04^{+0.02}_{-0.01}$	···	···	g
105	004430.45+412310.1	11.126901	41.3863	0.4	0.4	2.8	$0.21^{+0.03}_{-0.03}$	1468	⟨hard⟩	n
106	004437.08+411951.1	11.154504	41.331024	0.5	0.5	5.3	$0.42^{+0.05}_{-0.05}$	1488	⟨hard⟩	g
100	004448.13+412247.4	11.200545	41.379973	0.7	0.7	6.1	$0.27^{+0.04}_{-0.04}$	1525	⟨hard⟩	p
110	004455.53+413440.3	11.231167	41.57808	0.3	0.3	2.7	$0.45^{+0.05}_{-0.04}$	1547	⟨AGN⟩	n
108	004457.39+412247.9	11.239115	41.380094	0.7	0.7	7.8	$1.0^{+0.1}_{-0.1}$	1553	⟨XRB⟩	n
111	004513.82+413806.4	11.307524	41.635323	0.8	0.8	6.1	$0.24^{+0.04}_{-0.04}$	1598	⟨hard⟩	g
112	004518.39+413936.0	11.326586	41.66018	0.5	0.5	4.4	$0.28^{+0.04}_{-0.04}$	1611	⟨hard⟩	p
113	004520.74+413932.1	11.336316	41.659109	0.6	0.6	4.3	$0.14^{+0.03}_{-0.03}$	···	···	g
117	004526.86+413216.8	11.361729	41.538161	0.6	0.6	5.2	$0.27^{+0.04}_{-0.03}$	1631	⟨AGN⟩	n
118	004527.34+413253.5	11.363743	41.548363	0.4	0.4	5.4	$2.2^{+0.1}_{-0.1}$	1634	⟨hard⟩	g
114	004527.89+413904.9	11.366179	41.651539	0.4	0.4	4.3	$0.43^{+0.05}_{-0.04}$	1635	⟨hard⟩	p
119	004528.29+412943.4	11.367681	41.495538	0.4	0.4	6.0	$1.9^{+0.1}_{-0.1}$	1636	⟨hard⟩	p
115	004529.35+413751.6	11.37223	41.631176	1.0	1.0	5.6	$0.06^{+0.02}_{-0.02}$	···	···	g
116	004530.65+413559.8	11.377557	41.600135	0.9	0.9	7.1	$0.38^{+0.06}_{-0.05}$	1643	⟨hard⟩	g
120	004545.57+413941.5	11.439867	41.661701	0.3	0.3	4.7	$71.0^{+0.6}_{-0.6}$	1692	GlC	c

[a] Sources have updated Stiele classifications from Stiele & Kong (2018).

Table 3.2: PHAT photometry for HMXB optical counterpart candidates

Catalog Name	*Chandra* RA	*Chandra* Dec.	PHAT RA	PHAT Dec.	F275W	F336W	F475W	F814W	F110W	F160W
004240.31+411845.3	10.667979	41.312682	10.667543	41.312546	22.03 ± 0.04	21.31 ± 0.01	20.940 ± 0.003	19.799 ± 0.003	$19.263^{\pm}0.003$	18.512 ± 0.003
004249.22+411815.5	10.70509	41.304395	10.705035	41.304478	...	25.2 ± 0.2	22.119 ± 0.006	19.314 ± 0.002	18.552 ± 0.002	17.586 ± 0.002
004308.62+411248.0	10.785948	41.213448	10.785837	41.213419	23.19 ± 0.07	22.97 ± 0.03	23.41 ± 0.01	23.09 ± 0.02	23.26 ± 0.04	22.63 ± 0.05
004316.10+411841.2	10.817115	41.311543	10.817102	41.31151	24.1 ± 0.1	23.15 ± 0.04	24.43 ± 0.02	22.15 ± 0.01	21.43 ± 0.01	19.906 ± 0.007
004321.07+411750.2	10.837815	41.297389	10.837831	41.297466	24.9 ± 0.2	24.04 ± 0.06	24.43 ± 0.02	24.48 ± 0.06	25.0 ± 0.2	...
004321.48+411556.5	10.839501	41.265805	10.839394	41.265853	23.8 ± 0.1	23.20 ± 0.05	23.79 ± 0.01	23.19 ± 0.02	22.90 ± 0.03	21.72 ± 0.02
004335.91+411433.0	10.899635	41.2426	10.899774	41.242598	22.62 ± 0.05	22.80 ± 0.03	24.04 ± 0.01	23.53 ± 0.02	22.97 ± 0.04	23.29 ± 0.09
004339.06+412116.7	10.912737	41.354885	10.912961	41.354867	23.8 ± 0.1	23.23 ± 0.04	23.87 ± 0.01	23.63 ± 0.03	23.60 ± 0.04	23.27 ± 0.06
004350.76+412117.4	10.961516	41.355033	10.961508	41.355045	22.78 ± 0.06	21.16 ± 0.01	21.694 ± 0.004	19.843 ± 0.002	19.129 ± 0.002	18.252 ± 0.002
004404.75+412126.5	11.019799	41.35756	11.019758	41.357577	23.51 ± 0.09	22.36 ± 0.02	22.150 ± 0.005	19.938 ± 0.003	18.735 ± 0.002	17.790 ± 0.002
004425.73+412241.8	11.107221	41.378442	11.107175	41.378477	26.1 ± 0.6	24.9 ± 0.1	24.65 ± 0.02	22.62 ± 0.01	21.880 ± 0.009	21.45 ± 0.01
004448.13+412247.4	11.200545	41.379973	11.200584	41.380057	23.48 ± 0.08	23.39 ± 0.04	24.59 ± 0.02	22.95 ± 0.01	21.851 ± 0.009	20.448 ± 0.006
004518.39+413936.0	11.326586	41.66018	11.326624	41.660177	25.6 ± 0.4	24.8 ± 0.1	25.28 ± 0.03	24.70 ± 0.04	24.10 ± 0.05	23.27 ± 0.05
004527.89+413904.9	11.366179	41.651539	11.36618	41.651542	24.3 ± 0.2	22.81 ± 0.03	23.405 ± 0.009	20.870 ± 0.004	19.971 ± 0.003	18.819 ± 0.002
004528.29+412943.4	11.367681	41.495538	11.367687	41.495535	19.76 ± 0.01	19.202 ± 0.005	20.231 ± 0.002	19.014 ± 0.002	18.526 ± 0.001	17.754 ± 0.001

PHAT photometry for all point source optical counterparts to NuSTAR hard X-ray sources. Sources are identified by their *Chandra* catalog name, which corresponds to the *Chandra* *Catalog Name* column in Table 3.1. Ellipses indicate that the source was not detected in that filter.

Table 3.3: Output best fit parameters for stellar optical counterparts from BEAST SED fitting code

Catalog Name	log(L) $L_\odot$	log(g) $cm\,s^{-2}$	log(T) K	A_V mag	Mass $M_\odot$	χ^2	Best-fit Spectral Type
004240.31+411845.6	$4.5^{+0.1}_{-0.1}$	$2.2^{+0.1}_{-0.1}$	$4.03^{+0.02}_{-0.02}$	$2.0^{+0.1}_{-0.1}$	13^{+1}_{-1}	49	χ^2 too high to trust fit
004249.22+411815.8	$3.8^{+0.1}_{-0.1}$	$0.7^{+0.2}_{-0.3}$	$3.61^{+0.02}_{-0.03}$	$0.7^{+0.3}_{-0.4}$	5^{+2}_{-3}	11	possible He burning star
004308.63+411248.4	$3.1^{+0.5}_{-0.3}$	$3.6^{+0.2}_{-0.1}$	$4.2^{+0.1}_{-0.1}$	$0.7^{+0.5}_{-0.3}$	5^{+2}_{-1}	1	B
004316.11+411841.5	$5.7^{+0.3}_{-1.1}$	$3.8^{+0.3}_{-0.8}$	$4.6^{+0.1}_{-0.4}$	$4.3^{+0.2}_{-0.3}$	45^{+34}_{-35}	50	high χ^2, flat SED
004321.08+411750.6	$3.0^{+0.5}_{-0.4}$	$4.1^{+0.2}_{-0.3}$	$4.2^{+0.1}_{-0.1}$	$1.2^{+0.4}_{-0.5}$	5^{+2}_{-1}	6	B
004321.48+411556.9	$3.6^{+0.5}_{-0.4}$	$4.1^{+0.3}_{-0.2}$	$4.4^{+0.1}_{-0.1}$	$1.2^{+0.2}_{-0.2}$	7^{+4}_{-3}	1	B
004335.91+411433.4	$4.0^{+0.3}_{-0.6}$	$4.2^{+0.2}_{-0.3}$	$4.5^{+0.1}_{-0.1}$	$1.7^{+0.2}_{-0.2}$	10^{+3}_{-4}	5	B
004339.06+412117.6	$3.4^{+0.4}_{-0.4}$	$4.1^{+0.2}_{-0.2}$	$4.3^{+0.1}_{-0.1}$	$1.0^{+0.2}_{-0.2}$	6^{+3}_{-2}	5	B
004350.76+412118.1	$6.5^{+0.1}_{-0.1}$	$3.8^{+0.1}_{-0.1}$	$4.72^{+0.02}_{-0.02}$	$3.2^{+0.1}_{-0.1}$	106^{+8}_{-7}	1756	χ^2 too high to trust fit
004404.75+412127.2	$5.2^{+0.1}_{-0.1}$	$1.9^{+0.1}_{-0.1}$	$4.06^{+0.02}_{-0.02}$	$4.4^{+0.1}_{-0.1}$	19^{+2}_{-2}	459	χ^2 too high to trust fit
004425.73+412242.4	$4.6^{+0.6}_{-0.7}$	$3.4^{+0.5}_{-0.3}$	$4.4^{+0.2}_{-0.2}$	$3.8^{+0.2}_{-0.2}$	14^{+11}_{-8}	8	B
004448.13+412247.9	$5.7^{+0.1}_{-0.1}$	$3.9^{+0.1}_{-0.1}$	$4.63^{+0.02}_{-0.02}$	$4.6^{+0.1}_{-0.1}$	49^{+4}_{-3}	940	high χ^2, flat SED
004518.38+413936.6	$2.8^{+0.5}_{-0.4}$	$4.1^{+0.2}_{-0.2}$	$4.2^{+0.1}_{-0.1}$	$1.4^{+0.6}_{-0.6}$	4^{+2}_{-1}	10	B
004527.88+413905.5	$6.5^{+0.1}_{-0.1}$	$3.8^{+0.1}_{-0.1}$	$4.70^{+0.03}_{-0.04}$	$5.2^{+0.1}_{-0.1}$	158^{+39}_{-25}	667	χ^2 too high to trust fit
004528.24+412943.	$5.4^{+0.1}_{-0.1}$	$2.5^{+0.1}_{-0.1}$	$4.28^{+0.02}_{-0.02}$	$2.8^{+0.1}_{-0.1}$	26^{+2}_{-2}	3409	χ^2 too high to trust fit

Output best fit parameters for stellar optical counterparts using the BEAST SED fitting code for all point sources listed in Table 3.2. Median values $\pm 33\%$ are listed. After the posterior distribution is complete, the BEAST code calculates the χ^2 value for the most likely model, listed here. Fits are considered robust for $\chi^2 < 12$. The *Best-fit Spectral Type* column lists the most likely spectral type of each source, based on its best fit physical properties. See Section 3.4.2 for a more detailed description of BEAST SED fitting.

Table 3.4: HMXB Candidate Classification Data

Catalog Name	Good BEAST Fit	SFH indicates young SF	*NuSTAR* classified HBH/pulsar/NS
004240.31+411845.6		···	✓ (hbh)
004249.22+411815.8	✓	···	
004308.63+411248.4	✓	···	✓ (pul)
004316.11+411841.5		···	✓ (hbh)
004321.08+411750.6	✓	···	✓ (ns)
004321.48+411556.9	✓	···	
004335.91+411433.4	✓	✓	
004339.06+412117.6	✓	···	✓ (pul)
004350.76+412118.1			✓ (ns)
004404.75+412127.2			✓ (hbh)
004425.73+412242.4	✓	✓	✓ (pul)
004448.13+412247.9		✓	✓ (ns)
004518.38+413936.6	✓	✓	
004527.88+413905.5		✓	✓ (pul)
004528.24+412943.9		✓	✓ (hbh)

Table evaluating likelihood of HMXB candidates based on BEAST fits, SFH, and *NuSTAR* classification of compact object. Check marks are given when a source is likely to be a HMXB using the given criteria: the source has a good BEAST SED fit to a stellar companion, the source is in a region with young (within the last 60 Myr) star formation, or the *NuSTAR* classification of the compact object is a pulsar, non-magenetized neutron star, or a pulsar. Ellipses in the SFH column indicate that no star formation history is available for the region around the source, due to crowding near the bulge of M31.

Chapter 4

MULTIWAVELENGTH CHARACTERIZATION OF THE HMXB POPULATION IN M31

Portions of this chapter were originally published in collaboration with Benjamin F. Williams, Meredith Durbin, Julianne Dalcanton, Vallia Antoniou, Breanna A. Binder, Michael Eracleous, Paul P. Plucinsky, Manami Sasaki, and Neven Vulic in the January 2021 edition of the Astrophysical Journal (Lazzarini et al., 2021, ApJ*, Vol. 906, 120; 2021 © American Astronomical Society, DOI: 10.3847/1538-4357/abccca), and are reproduced below with the permission of the American Astronomical Society.*

4.1 Introduction

Population studies of X-ray binaries (XRBs) in constrain models of their formation and evolution by tying their X-ray and optical properties to their parent stellar populations. Previous studies have tied the XRB population of a galaxy, in some cases including both low and high mass XRBs, to galactic properties such as the galaxy's total stellar mass (e.g., Lehmer et al., 2010), the stellar mass formed in a given star forming episode (e.g., Boroson et al., 2011; Zhang et al., 2012), the star formation rate (e.g., Ranalli et al., 2003; Gilfanov et al., 2004; Mineo et al., 2012; Antoniou et al., 2010; Antoniou & Zezas, 2016; Lehmer et al., 2019), and the galaxy metallicity (e.g., Basu-Zych et al., 2013, 2016; Brorby et al., 2016).

XRBs for which the secondary star is also massive enough to form a neutron star or black hole are high mass X-ray binaries (HMXBs). The HMXB phase is a key observable window in the evolution of massive binary stars, a phase of critical importance given their role as progenitors of compact object mergers detectable with gravitational waves (Tauris & van den Heuvel, 2006). The binary fraction of massive stars – those with M$> 8M_{\odot}$ that go on to form black holes and neutron stars at the end of their lives – is at least 60%, with the majority of these massive stellar binaries in close enough systems to interact during their lifetime (e.g.; Sana et al., 2012). This high binary fraction makes it clear that understanding massive stellar evolution as a whole requires understanding massive binary stellar evolution in particular.

While relatively rare compared to their low-mass counterparts, massive stars play a major role in their host galaxies, and have long been known to ionize, chemically enrich, and inject energy into the interstellar medium (e.g.; Dalgarno & McCray, 1972; Oey, 1999). More recently, how-

ever, HMXBs have emerged as another important source of feedback (e.g.; Garratt-Smithson et al., 2019), and as a likely contributor to cosmic reionization (e.g.; Mesinger et al., 2014; Madau & Fragos, 2017; Greig & Mesinger, 2018).

Progress in all of the above requires characterizing the HMXB production rate and understanding how the observed HMXB population depends on the age of the parent stellar population. These data, which are critical for constraining predictions of compact object merger rates (e.g.; Fragos et al., 2013; Andrews et al., 2018; Fragos et al., 2019), can best be collected in nearby galaxies, where both the XRB and stellar populations can be resolved.

Nearby galaxies are well-suited to detailed studies of XRB populations, as they can be observed in relatively few telescope pointings, and do not have the distance uncertainties and absorption issues that plague Galactic measurements. Local Group X-ray observations from *Chandra*, *XMM-Newton*, and *NuSTAR*, combined with optical observations from the *Hubble Space Telescope (HST)* have connected XRBs with their parent stellar populations (Williams et al., 2018; Lazzarini et al., 2018; Garofali et al., 2018). However, the existing data have not converged on a simple picture for the age and production rate of XRBs. For example, in the SMC, HMXBs are associated with star formation bursts between 25 and 60 Myr ago (Antoniou et al., 2010, 2019), while in the LMC they are associated with younger bursts between 6 and 25 Myr ago (Antoniou & Zezas, 2016). In M33, the HMXB population appears to contain an even younger component ($<$5 Myr; Garofali et al., 2018). Local measurements of the HMXB production rate also span nearly an order of magnitude, ranging from 60 ± 17 systems/($M_\odot$ yr^{-1}) in the Milky Way to 480^{+400}_{-240} systems/($M_\odot$ yr^{-1}) in the low metallicity Small Magellanic Cloud (Bodaghee et al., 2012; Licquia & Newman, 2015; Antoniou & Zezas, 2016; Politakis et al., 2020), possibly indicating a trend of increasing HMXB production rate with decreasing metallicity (e.g.; Linden et al., 2010; Fragos et al., 2013; Ponnada et al., 2020; Fornasini et al., 2020). Given that no clear picture has emerged from these studies, more data in different environments are needed to understand the dependence of the HMXB production rate on the properties of the parent stellar population.

An obvious next target is M31, which has both a higher metallicity and lower SFR intensity than both M33 and the Magellanic Clouds. M31 has existing high-quality optical and X-ray ob-

servations that make it possible to derive HMXB age distributions and production rates. In M31 we can pair optical observations from the Panchromatic *Hubble* Andromeda Treasury (PHAT) – a survey of one third of the star-forming disk of M31 with six band photometry for over 100 million individual stars (Dalcanton et al., 2012; Williams et al., 2014b) – with X-ray observations from the *Chandra*-PHAT survey, a *Chandra* survey consisting of seven pointings covering most of the PHAT survey footprint (Williams et al., 2018).

We leverage several PHAT data products to investigate the M31 X-ray source population, including the 6-band catalog of resolved stellar photometry (Williams et al., 2014b), the spatially resolved recent star formation history maps (Lewis et al., 2015), and the Bayesian Extinction and Stellar Tool (BEAST) (Gordon et al., 2016), a spectral energy distribution (SED) fitting tool which infers the physical parameters for optical point sources from broad-band photometry.

The HMXB population of M31 has only recently been examined using these datasets. The main challenge has been selecting a large enough sub-sample of high quality HMXB candidates to produce a statistically robust result. Through visual inspection and spatial correlation of the *Chandra*-PHAT survey, Williams et al. (2018) identified 57 X-ray sources with point source optical counterpart candidates, 8 of which were high quality HMXB candidates based on optical colors and surrounding populations. These HMXB candidates had an age distribution that peaked at 15-20 Myr and 40-50 Myr. Lazzarini et al. (2018) analyzed the subset of *Chandra*-PHAT X-ray sources that were also detected by *NuSTAR*. Selecting for sources in regions with recent star formation, companion stars with SED fit parameters consistent with B-type stars, and hard X-ray colors consistent with an accreting black hole or neutron star resulted in a sample of 15 HMXB candidates, 7 of which appear in the *Chandra*-PHAT "best sample". The Lazzarini et al. (2018) study included an additional *Chandra* field that is not part of the *Chandra*-PHAT survey, which provided additional sources. The age distribution of the *NuSTAR*-selected sources broadly agreed with the Williams et al. (2018) result, with one peak at about 10 Myr and another at 25-50 Myr.

In this work, we combine likely ages from the star formation history with best-fit physical parameters for the point source X-ray optical counterpart candidates from the BEAST SED fitting tool, allowing us to select a more reliable, better characterized, and larger sample of HMXB can-

didates in M31. We use this sample to determine the age distribution of HMXB candidates in M31 and calculate an HMXB production rate over the last 80 Myr, because we expect HMXBs to reside in young regions. In Section 4.2 we discuss the published *Chandra* and *HST* catalogs that were used in this study. We describe the SED fitting analysis and how we used spatially resolved star formation histories to determine the best ages for each source. We also describe how we combined the SED fits, star formation history information, and multiwavelength observations to determine our best sample of HMXB candidates. In Section 4.4 we discuss the distribution of HMXB ages, calculate the resulting HMXB production rate in M31, and put these findings in the context of other local galaxies. We summarize our results in Section 5.5.

We assume a distance to M31 of 776 kpc, or a distance modulus of 24.45 (Dalcanton et al., 2012). We assume this distance when converting from flux to luminosity and use this fixed distance in our BEAST SED fits (Gordon et al., 2016).

4.2 Data

We used X-ray and optical/near-UV catalogs of the northern disk of M31 to determine the best HMXB candidate sample. The optical/near-UV source catalog is from the PHAT survey (Williams et al., 2014b), and the X-ray source catalog comes from the *Chandra*-PHAT survey. The details of which, including detailed reduction techniques, counterpart candidate identification, and cross-correlations with other work, are discussed in (Williams et al., 2018). Finally, we include X-ray spectral information of the sources from the *XMM-Newton* study of Sasaki et al. (2018).

The optical, and near-UV photometry that we used in this analysis comes from the PHAT survey by Dalcanton et al. (2012), which covered roughly one third of the star forming disk of M31. The final source catalog (Williams et al., 2014b) contains six band photometry for over 100 million individual stars. The optical and near-UV *HST* bands from the PHAT survey used in this work are F814W, F475W, F336W, and F275W with central wavelengths of 8353 Å, 4750 Å, 3375 Å, and 2750 Å, respectively. We use the near-IR F110W and F160W bands (central wavelengths of 1.150 μ and 1.545 μ) to screen for potential foreground stars, which fall in a very narrow sequence of F110W-F160W color (see Figure 19 from Williams et al. (2014b)).

We select our sample of high mass X-ray binary candidates from the *Chandra*-PHAT survey, a series of seven ∼50 ks *Chandra* pointings that overlap the PHAT footprint in M31 (Williams et al., 2018). The *Chandra*-PHAT survey has a limiting luminosity of $\sim 2 \times 10^{35}$ erg s^{-1} in the 0.35−8.0 keV band and detected 373 X-ray sources in the disk of M31, 57 of which were spatially coincident with point source optical counterparts in the PHAT data. The false match probability between *Chandra*-PHAT X-ray sources and O or B type stars in M31 is $\sim 2\%$, so we expect 1-2 false matches (Lazzarini et al., 2018). This false match probability was determined using the spatial density of O and B type stars in the PHAT survey photometry catalog (Williams et al., 2014b) and the average size of the 1σ *Chandra* error circles that were used to identify optical counterparts (Williams et al., 2018). We use a combination of X-ray, optical, and IR properties to rule out foreground stars and background AGN from our sample, which is described in more detail in Section 4.3.3.

We also include *XMM-Newton* spectral fits and classifications in our analysis, which come from the Sasaki et al. (2018) survey of the northern disk of M31, which had a limiting luminosity of $\sim 7 \times 10^{34}$ erg s^{-1} in the 0.5−2.0 keV band. Sasaki et al. (2018) classified sources using their hardness ratios and performed spectral fitting for the sources with sufficient counts (>100) in the 0.5−2.0 keV band. The Sasaki et al. (2018) catalog included 389 X-ray sources. They cross-matched sources from their catalog with the *Chandra*-PHAT source catalog and found that 197 sources were detected in both surveys. The survey areas of the *Chandra*-PHAT survey and the XMM-*Newton* survey are similar but do not overlap perfectly. For sources in our sample with counterparts in the Sasaki et al. (2018) catalog, we list the identification number and classification from the *XMM-Newton* survey in Table 4.1.

In Figure 4.1 we show the location of the 57 *Chandra*-PHAT X-ray sources with point source optical counterpart candidates. We plot each point with a color and shape corresponding to its best-fit spectral type, as described in Section 4.3.1. Sources plotted as black crosses do not fit the expected range of effective temperature, luminosity, and radius for O or B type main sequence or supergiant stars. We also include the outline of the PHAT survey footprint, the Chandra-PHAT survey footprint, and the *XMM-Newton* survey of M31 by Sasaki et al. (2018).

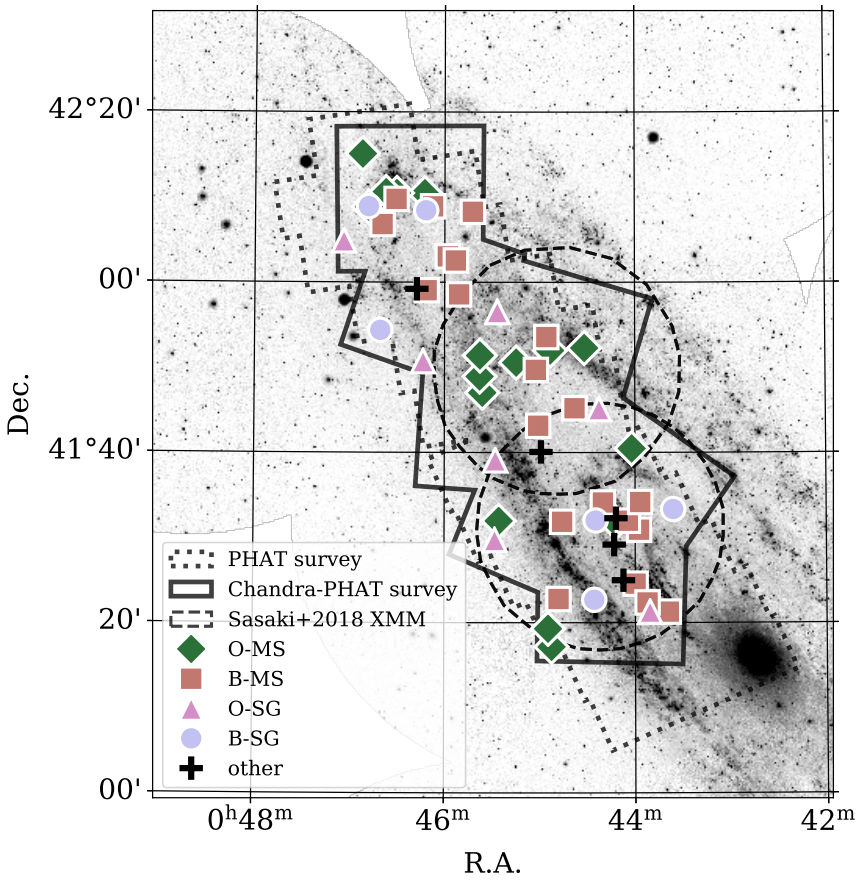

Figure 4.1 Near UV image of M31 from the *Galaxy Evolution Explorer* (*GALEX;* Gil de Paz et al., 2009a) with the footprint of the Panchromatic *Hubble* Andromeda Treasury survey outlined in the black dotted lines, the footprint of the Chandra-PHAT survey in the black solid lines, and the footprint of the *XMM-Newton* survey by Sasaki et al. (2018) outlined in the black dashed circles. We plot the position of each of the 57 *Chandra*-PHAT X-ray sources with point source optical counterparts. The color and shape of each point indicate the most likely spectral type of the companion star, based on its SED fit effective temperature, luminosity, and radius as described in Section 4.3.1. The quality of each HMXB candidate was evaluated using a series of flags, described in Section 4.3.3. Sources plotted as black crosses do not have an effective temperature, luminosity, and radius consistent with an O or B type main sequence or supergiant star. ©AAS. Reproduced with permission from Lazzarini et al. (2021).

4.3 Analysis

We identify the best optical counterpart candidates and best HMXB candidates using the method described briefly here and in more detail in Section 4.3.3. We start by fitting SED models to the PHAT photometry in the UV-optical for our initial sample of 57 UV-optical counterpart candidates from Williams et al. (2018). We then leverage the results to search for mismatches between the optical and X-ray properties that may indicate a chance superposition. We then further interpret these comparisons to better-distinguish background AGN and foreground stars from point sources more likely to lie in the disk of M31. Lastly, for the M31 sample, we combine the physical parameters inferred from the SED fits with age information from the surrounding stellar population (Lewis et al., 2015) to identify our sample of best HMXB candidates.

4.3.1 SED Fitting

We fit SEDs for the identified optical counterparts to HMXB candidates using the publicly available Bayesian Extinction and Stellar Tool (BEAST) (Gordon et al., 2016). The BEAST fits multi-band photometry with theoretical SEDs from the Padova/PARSEC single star stellar evolution models (Marigo et al., 2008; Bressan et al., 2012; Marigo et al., 2017). We use four-band photometry from the PHAT survey (F275W, F336W, F475W, and F814W) and assume a fixed distance in our SED fitting as all sources are assumed to be in the disk of M31. Photometric bias and uncertainty are applied from artificial star tests performed on the data.

The BEAST fits six stellar parameters using a combination of stellar models, dust models, and models of photometric bias: age, mass, metallicity, A_V, R_V, and f_A, a parameter used to describe the mixing of different types of dust observed in the Local Group. Luminosity, effective temperature, radius, and surface gravity are then derived using the best-fit stellar models. As detailed in Gordon et al. (2016), the BEAST uses a Kroupa IMF as a prior on stellar mass, a flat prior on A_V, a uniform prior on R_V and f_A, a uniform prior on age, and a flat prior on stellar metallicity. The BEAST then then maps the mass and age priors into Hertzsprung-Russell and stellar atmosphere effective temperature versus surface gravity diagrams to produce priors on the

other stellar physical parameters including luminosity, effective temperature, radius, and surface gravity.

Because the BEAST uses a probabilistic approach, any number of parameters may be fit and a probability distribution is returned for each parameter. If there are not enough data points being fit, the output distribution for each parameter will mirror the input priors. We report the parameters for the best-fit stellar models and dust models in Table 4.1, including 16th and 84th percentile errors for each model, which reflect the probability distribution for each measurement.

To analyze the high mass stars that dominate our sample, we limited our stellar model grid to ages from log(t/yr) of 6.6 to 7.9 with steps of 0.1, matching the grid used in the SFH maps (Lewis et al., 2015). We limit our metallicity grid to metallicities of $Z_{initial}$=0.001, 0.004, 0.008, 0.012, 0.019, 0.03 to cover the slightly super-solar to solar range of metallicities observed in M31 (Gregersen et al., 2015). We use the default range of dust extinction values, A_V of 0.0 to 10.6 magnitudes, but use the smaller step size of 0.2 mag to create a finer grid (Gordon et al., 2016).

We use the best-fit luminosity, effective temperature, and stellar radius of the companion star from its BEAST SED fit to determine its most likely spectral type. We expect the strongest HMXB candidates to have companion stars that are consistent with the expected properties of an O or B type main sequence or supergiant star. We plot the best-fit effective temperature and luminosity for all sources in the Hertzsprung-Russell diagram in Figure 4.2. We also include the ranges expected for O and B type main sequence and supergiant stars (Lamers & Levesque, 2017) and isochrones from the Padova stellar models at different ages (Marigo et al., 2008), at solar metallicity.

HMXB systems might host Be stars with cold disks. The H-α emission line does not lie within the filter set used by the PHAT survey (Dalcanton et al., 2012). In an emission line survey of M31 designed to overlap with the PHAT footprint by Peters et al. (2020), Be stars were identified using narrow-band photometry. They also included the surface temperature and surface gravity for all of the B and Be stars in their catalog using the BEAST tool. When controlling for spectral type, there was no difference between the distribution of effective temperatures fit by the BEAST for the group of B and Be stars in the sample. The effective temperature of Be stars is expected to be normal compared to non-emission line B stars (e.g., Porter & Rivinius, 2003), so the presence of a

decretion disk around the companion star should not affect our fits.

4.3.2 Age Determination with Spatially Resolved Star Formation Histories

In addition to SED fitting for each individual companion star, we used spatially resolved recent star formation histories from Lewis et al. (2015) to determine a most likely age for each source.

Lewis et al. (2015) derived the spatially resolved recent star formation history of M31 with the color magnitude diagram (CMD) fitting code, `MATCH` (Dolphin, 2002). They divided the PHAT survey footprint into roughly nine thousand 100 by 100 pc regions (1 pc = 3.76″ in M31). The PHAT survey is divided into 23 roughly equal sized regions, referred to as "bricks". The star formation history maps cover all bricks except bricks 1 and 3, which due to their location close to the galactic bulge have too high stellar density to do accurate CMD fitting. One of our HMXB candidates (004339.06+412117.6) falls within Brick 3 and so does not have an age determined via star formation history.

Each 100 by 100 pc region has a measured star formation rate from log(t/yr) of 6.6 to 10.15 with a step size of 0.1. The CMD fitting optimized fits for main sequence stars, focusing the fits on the recent (¡500 Myr) star formation history of M31. This range is not a limiting factor for us, as we are interested only in the star formation rate in the last 80 Myr to probe populations that could be the parent of an HMXB secondary star. The oldest of these are B-type stars, which typically have main sequence lifetimes of <50 Myr (Bressan et al., 2012).

The errors on the star formation rate measurements were generated by the `MATCH` software using hybridMC fitting. For each 100 by 100 pc region, the best fit SFR in each time bin was determined using maximum likelihood estimation. The errors represent the range of all viable star formation histories that could produce the population of stars in that region (Dolphin, 2013). Because the best fit star formation history often includes a best fit measurement of 0 star formation rate in some bins, the error bars are asymmetric, as the bins with 0 measured star formation rate only have upper errors. We present an example of a star formation rate measurement in the region surrounding one of our HMXB candidates, 004637.22+421034.5 in Figure 4.3. The SFH for this region shows a peak in the $40-50$ Myr time bin, and there are several bins with a best fit SFR of 0.0

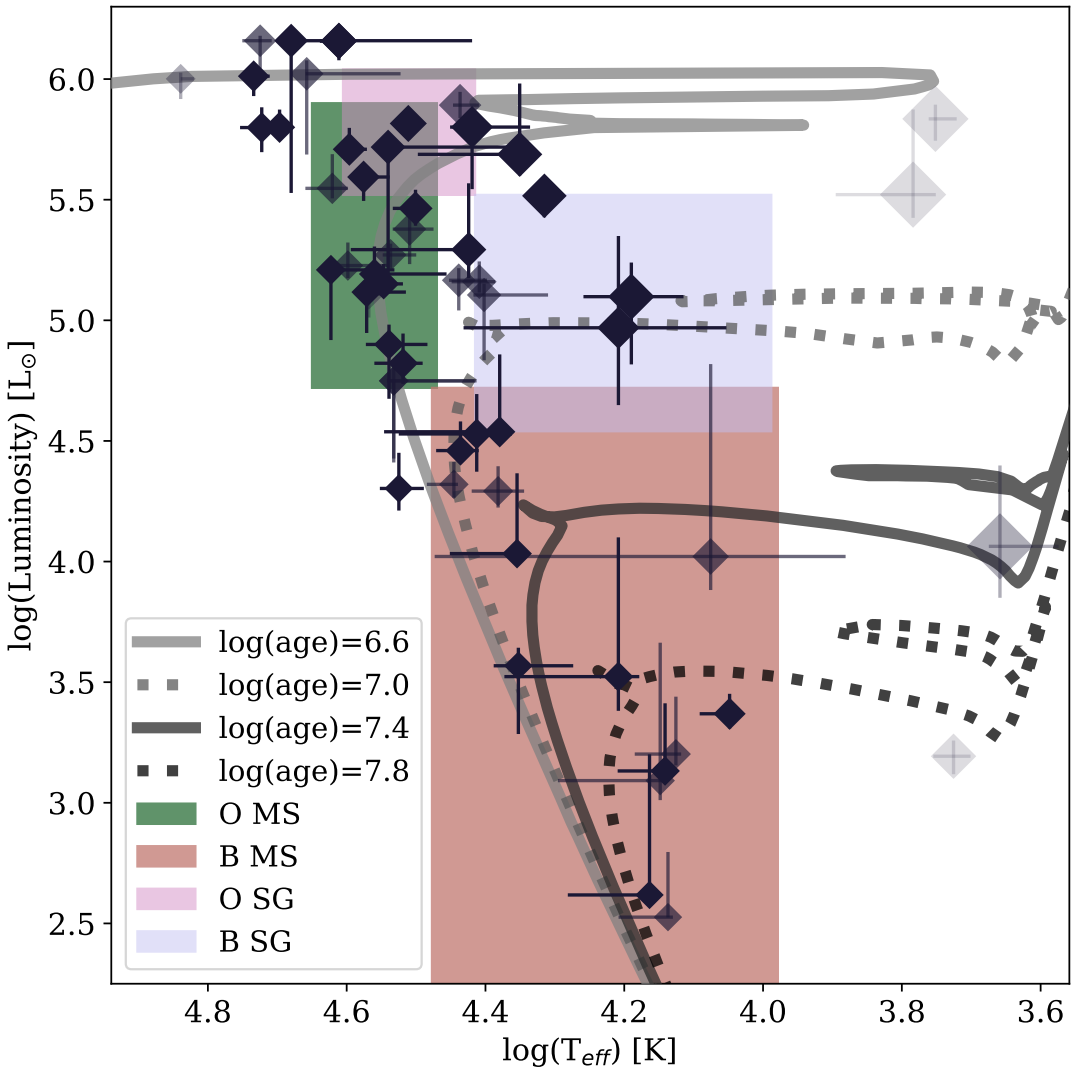

Figure 4.2 We present the best-fit effective temperature and luminosity for the optical counterpart candidates to the *Chandra*-PHAT X-ray sources with point source optical counterparts. The shaded regions represent the range of values expected for main sequence O and B type stars (O MS, B MS) and O and B type supergiants (O SG, B SG) (Lamers & Levesque, 2017). We also plot isochrones from the Padova stellar models (Marigo et al., 2008). The size of diamond points scales with the best-fit radius for the star from its BEAST SED fit. The opacity of the diamond points depends on how many "flags" were raised for the source, as described in Section 4.3.3. The darkest points represent our best sample of 33 HMXB candidates that raised zero flags and the lightest point represents the one source that raised 4 flags. See Table 4.1 for the effective temperatures, luminosities, and radii for all sources. We list the values used to evaluate the quality of each HMXB candidate in Table 4.3 and list the flags raised for each source in Table 4.4. ©AAS. Reproduced with permission from Lazzarini et al. (2021).

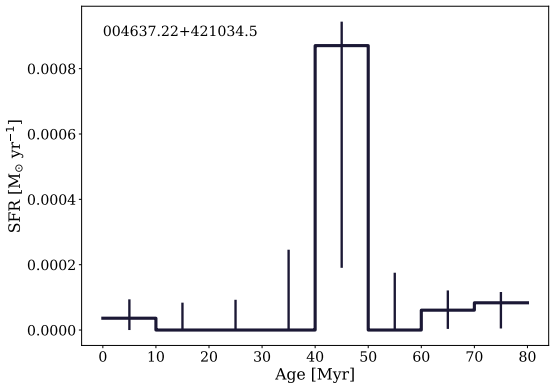

Figure 4.3 An example of the star formation history for one 100 by 100 pc region, produced by Lewis et al. (2015). This is the region surrounding the HMXB candidate in our sample, 004637.22+421034.5. ©AAS. Reproduced with permission from Lazzarini et al. (2021).

$M_\odot$ yr^{-1}. There is covariance in the measurements and errors for each bin, because there is a fixed amount of stellar mass in the region. The error bars are large to demonstrate this. For example, if the SFR in the 20−30 Myr bin was increased to the top of its upper limit, the SFR in other bins would need to be lower to conserve the total stellar mass in the region. Because the 40−50 Myr time bin is the only bin with significant star formation, it has a large lower error to accommodate the upper errors on all of the other bins.

We used the spatially resolved recent star formation history within the last 80 Myr in regions containing our HMXB candidates to determine their most likely ages. To do this, we calculated the total stellar mass formed in each age bin using its measured SFR and then divided this mass by the total mass formed in that region over the last 80 Myr. This measurement of the fraction of stellar mass formed in each time bin can be used as a probability distribution function (PDF), providing a measurement of the probability that the HMXB in that region has a given age. We then determine the most likely age as the age at which 50% of the cumulative stellar mass in that region was formed, with errors showing the ages at which 16% and 84% of the cumulative stellar mass had formed. We list these age measurements in the column labeled 'local SFH age' in Table 4.1. This method has been used to measure the ages of HMXBs in other galaxies including the Magellanic Clouds and M33 (e.g., Antoniou et al., 2010; Antoniou & Zezas, 2016; Williams et al.,

2018; Lazzarini et al., 2018; Garofali et al., 2018; Antoniou et al., 2019). Figure 10 in Williams et al. (2018) provides a particularly useful overview.

4.3.3 Determining the Best HMXB Candidate Sample

We created a series of flags that were used to evaluate which HMXB candidates from the *Chandra*-PHAT survey made up our best sample. We describe each flag in detail in the subsequent subsections.

We use the measured A_V from the PHAT dust maps (Dalcanton et al., 2015). The maps were created using near IR CMD fitting on red giant branch stars using the PHAT photometry. The maps are divided into 25 pc cells. We use the values from the map in the cell containing each HMXB candidate. The maps present the median A_V and the width of the log-normal distribution in each 25 pc cell. We use equations in Dalcanton et al. (2015) to convert these values to a mean A_V in each cell with the corresponding standard deviation.

We use some of the BEAST SED fit parameters to determine the best sample. We compare the BEAST SED fit A_V values with the measured A_V values from the PHAT dust maps and with the *XMM-Newton* N_H measurements. We also use the most likely spectral type which we determined with the BEAST SED fit effective temperature, luminosity, and radius as described in Section 4.3.1.

We use N_H values from the X-ray spectral fits by Sasaki et al. (2018) using the XMM survey of M31. Sources in the *XMM-Newton* catalog were matched with the *Chandra*-PHAT catalog (Williams et al., 2018), and not all of the *Chandra*-PHAT sources with point source optical counterpart candidates have counterparts in the *XMM-Newton* survey catalog. Sources in the *XMM-Newton* source catalog with more than 100 counts in the $0.2-12$ keV band have spectral fits. There are 32 matches between our sample of 57 X-ray sources with point source optical counterparts from the *Chandra*-PHAT catalog and the *XMM-Newton* catalog, 21 of which had enough counts for *XMM-Newton* spectral fits.

We use the *Chandra* hardness ratios for the *Chandra*-PHAT X-ray sources in our analysis as well. The two hardness ratios we use are HR1: (M-S)/(H+M+S) and HR2: (H-M)/(H+M+S) where H represents the net counts in the $2-8$ keV band, M represents the net counts in the $1-2$ keV bad,

and S represents the net counts in the $0.35-1$ keV band. Lastly, we used the near infrared color (F110W-F160W) of the optical counterpart candidates to flag potential foreground stars (Williams et al., 2014b). We list all of the values used to assess the quality of each HMXB candidate in Table 4.3. We include a summary of which sources fit which rejection criteria, referred to as "flags", in Table 4.4. We describe each flag in more detail below. Our best sample includes sources for which zero or one of the flags described below are raised.

Flag: A_V

Our first flag evaluates whether measurements of the source's A_V indicate that it is unlikely to be in the disk of M31, suggesting that it could be either a background galaxy or a foreground star. To raise this flag a source has to have disagreement between 1. its BEAST SED-fit A_V and the local measured A_V from the PHAT dust maps, 2. its BEAST SED-fit A_V and the Hydrogen column density, N_H, measured with its *XMM-Newton* spectrum, or 3. its local PHAT A_V and the Hydrogen column density, N_H, measured with its *XMM-Newton* spectrum. For a given source, if any of these three criteria are met, the A_V flag is raised. We provide more details on how we determined whether the preceding three criteria were met in this section.

Criteria 1: To determine whether the BEAST fit A_V agreed with measurements of A_V from the PHAT dust maps, we calculated the probability of measuring the BEAST SED fit A_V given the log normal distribution of the measured A_V from the PHAT dust maps. We include a flag value of 1 for sources with a probability of less than 6×10^{-7}, the 5σ limit, and a flag value of 0 for sources with higher probability. The distance to the source is fixed in the BEAST SED fits. If the fit A_V differs significantly from the A_V value measured using CMD fitting, it could indicate that our fit makes the incorrect assumption that the source is in the disk of M31 and could be a background galaxy or foreground star, both of which would make it a poor HMXB candidate. We note excess dust reddening could be intrinsic to the HMXB system itself due to the presence of stellar winds or a decretion disk, however it is difficult to distinguish between a source that is reddened because it is far behind the disk of M31 and a source that is reddened due to expected processes in an HMXB. If a source raises this flag, it does not mean that it is not a good HMXB candidate, which is why

we are using a system of flags and only ruling out sources that raise more than one flag.

Criteria 2: There is an observed correlation between optical dust extinction, A_V and the Hydrogen column density measured from the X-ray spectrum. Willingale et al. (2013) derived a function which relates the atomic and molecular Hydrogen column density to dust extinction, which is an improvement over previous, more simplistic, treatments of the dust-to-hydrogen ratio (Predehl & Schmitt, 1995; Güver & Özel, 2009).

In Figure 4.4, we plot the measured N_H (the sum of Galactic and intrinsic components) and the ratio of A_V to N_H for the sources that have counterparts in the Sasaki et al. (2018) catalog with enough counts (>100) for a spectral fit. The *XMM-Newton* spectra were fit with a power law model. Because the number of counts is low, the N_H values should not be strongly sensitive to the details of the extinction model, making the published N_H values suitable for our comparisons. We include lines representing the relationships measured by Willingale et al. (2013), Güver & Özel (2009), and Predehl & Schmitt (1995). We see a general agreement, with one obvious outlier, between the BEAST A_V and XMM N_H and the measured relationships.

If the A_V/N_H value using the BEAST SED-fit A_V plotted on the y-axis is more than a factor of two outside of the expected relationship from Willingale et al. (2013), we call that a disagreement between the BEAST SED fit A_V and the Hydrogen column density, N_H and raise the A_V flag. Only one source fails this test, 004412.04+413217.4, which is also an outlier compared to the PHAT A_V (see criteria 3).

Criteria 3: We use a similar method to set the criteria to determine whether the PHAT dust map A_V and XMM N_H values agree. We include the comparison between the PHAT A_V and XMM N_H in Figure 4.4 with the darker diamonds. The PHAT A_V and XMM N_H follow the expected correlation quite well.

If the ratio of the PHAT dust map A_V and XMM N_H differs from the expected value from Willingale et al. (2013) by more than a factor of two, as shown in Figure 4.4, we call that a disagreement between the PHAT dust map A_V and the *XMM-Newton* N_H. Only one source raises this flag, source 004412.04+413217.4, which also raises the flag comparing the BEAST SED fit A_V and *XMM-Newton* N_H.

A mis-match in the BEAST SED fit A_V or the PHAT dust map A_V and the *XMM-Newton* N_H could indicate that the X-ray source is not in the disk of M31 and could either be a foreground star or a background galaxy.

Flag: XMM Background Galaxy

Two of the sources in our *Chandra*-PHAT sample have counterparts in the Sasaki et al. (2018) *XMM-Newton* sample that are classified as background galaxies based on their spectral fit. Two sources fit these criteria: 004537.67+415124.4 and 004502.33+414943.1.

While we note that these sources are classified as background galaxies based on their *XMM-Newton* spectral fits, especially based on their high N_H values, we still only rule out a source as an HMXB candidate if it fails more than one test. This is because we expect HMXBs to form in regions with high column densities, so a high measured N_H could indicate that the HMXB is still within its natal cloud, rather than behind the disk of M31.

Flag: No Spectral Type

In Section 4.3.1 we discuss how we determined the spectral type for each source using the HR diagram presented in Figure 4.2.

Some sources had SED fit radii, luminosities, and effective temperatures that were not consistent with common HMXB secondary star types (O or B type main sequence or supergiant stars). These parameters suggest that their fluxes are unlikely to be dominated by a high-mass secondary star, making them less likely to be HMXBs. We set the no spectral type flag value to 1 for these sources.

Flag: Soft Chandra Hardness Ratios

We use the hardness ratios from the *Chandra*-PHAT catalog to examine whether a source is a good HMXB candidate. HMXBs are known to have hard X-ray spectra (e.g.; Tüllmann et al., 2011). To meet the criteria for the soft *Chandra* hardness ratios flag, a source must have HR1$<$-0.4 and

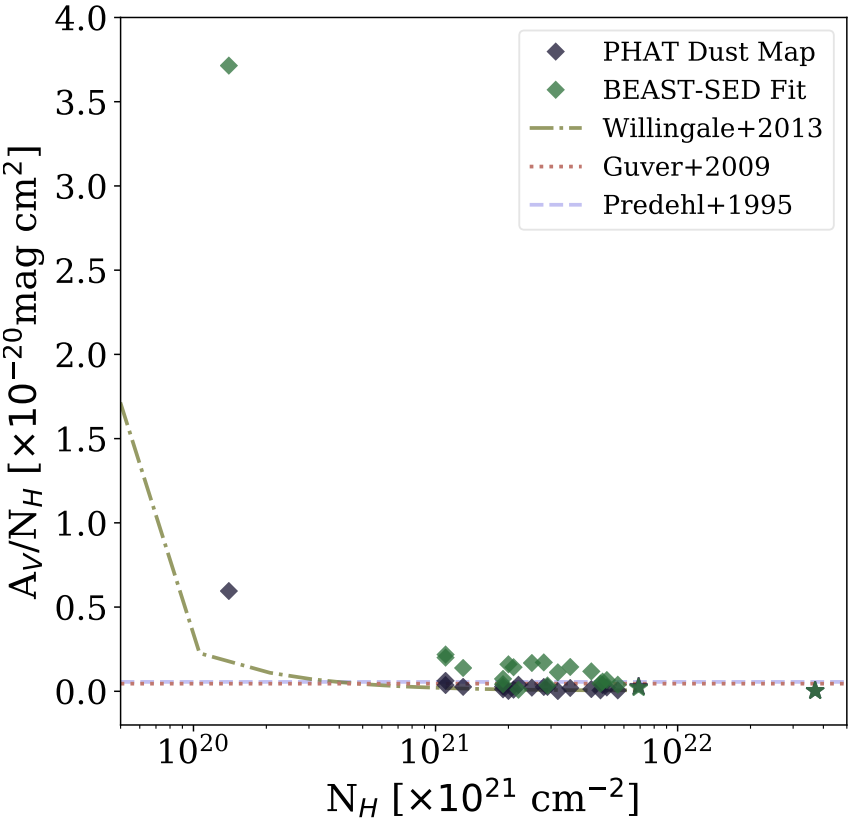

Figure 4.4 We compare the Hydrogen column density (N_H) for X-ray sources from the Sasaki et al. (2018) *XMM-Newton* catalog with the best-fit A_V from the BEAST SED fits (lighter diamonds) and the measured A_V from the PHAT dust maps (Dalcanton et al., 2015) (darker diamonds). We plot the N_H on the x-axis and the ratio of the A_V/N_H on the y-axis. We include the measured relationship between A_V and N_H by Willingale et al. (2013), Güver & Özel (2009), and Predehl & Schmitt (1995). The points plotted as stars indicate sources that are suggested to be behind the disk of M31 based on their *XMM-Newton* spectral fits. ©AAS. Reproduced with permission from Lazzarini et al. (2021).

HR2<0.1. These cutoff values were designed to flag potential foreground stars and supernova remnants using the hardness ratio diagram in Figure 8 of Williams et al. (2018) as a guide.

Only one source, 004407.44+412460.0 is softer than an HMXB. We suggest that this source is a foreground star given its soft hardness ratios and point source optical counterpart.

Flag: Foreground IR Colors

Foreground stars are known to populate a relatively narrow range of F110W-F160W color space, as shown in Figure 19 of Williams et al. (2014b). On the F160W vs. F110W-F160W color magnitude diagram, foreground stars create a nearly vertical sequence between 0.4<F110W-F160W<0.8.

We raise the foreground IR colors flag for 19 sources that have 0.4<F110W-F160W<0.8. We note that a foreground IR color is not a definite sign that the optical counterpart to one of our X-ray sources is a foreground star, which is why we only remove sources from our best sample if more than one flag is raised.

Best HMXB Candidate Sample Summary

We start with the 57 sources in the *Chandra*-PHAT sample of X-ray sources with point source optical counterparts. There are 33 sources which raise zero flags, 23 of which are found in regions with measured star formation in the last 80 Myr. There are 51 sources that raise one or zero flags, 35 of which are found in regions with measured star formation in the last 80 Myr. We only use sources that are found in regions with star formation in the last 80 Myr for our age analysis and HMXB production rate calculations because they have measured star formation rates in that time range. However, sources that raise one or fewer flags and are found in regions without recent star formation could still be good HMXB candidates that might be moving with a high enough velocity to have exited their birth regions.

4.4 Results & Discussion

We present the age distribution of a few sample selections of HMXB candidates. The ages are taken from their local star formation histories. By combining these ages with the known total

SFH of M31, we then infer the HMXB production rate for M31. HMXBs are known to exhibit significant variability, and only a fraction of systems are active at any given time. For this reason, our estimates on the production rate should be interpreted as lower limits.

4.4.1 Age Distribution of HMXBs in M31

As outlined in Section 4.3.2, we calculated a PDF for each source, indicating the probability that the HMXB has a given age using the star formation history of the 100 pc by 100 pc region immediately surrounding it. To understand the age distribution of the full population, we summed the PDFs for all of the best HMXB candidates to produce an age distribution, the number of HMXB candidates we expect to have formed in each time bin.

We determine the errors on the age distribution by first calculating the errors on the PDF for each source. To calculate the errors on the PDFs for each source, we sampled from within the 1σ errors on the star formation rate measurements and then generated the PDF for the region with the randomly sampled SFRs. We determined the maximum and minimum stellar mass that could be formed in each region by summing the SFR in all time bins and adding the upper and lower errors in quadrature. If a random draw of the SFR produced a total stellar mass outside these limits, we performed another random draw. We randomly sampled from the SFR errors for all HMXB candidates 10,000 times and summed the PDFs for all sources on each iteration to produce a randomly sampled overall age distribution. The errors on the age distribution represent the 16th and 84th percentile measurements.

We present the age distributions for a few possible catalog sub-samples with the dark histograms in Figure 4.5, first column. The first row includes all candidates that are in regions with measured star formation within the last 80 Myr, 40 sources. The second row includes only HMXB candidates that raised one or fewer flags, as described in Section 4.3.3 that reside in regions with star formation in the last 80 Myr, 35 sources. The bottom row includes only our best HMXB candidates, sources that raised zero flags and are in regions with recent star formation, totalling to 23 sources. The dark histogram represents the age distribution, with errors.

The lighter line represents the age distribution of an equal number of randomly selected regions

from within the PHAT survey area that is also covered by the Chandra-PHAT survey. In each row, we select a number of regions from the PHAT SFH map that matches the number of sources used to create the darker histogram. We calculated the PDF for each randomly selected region using its star formation rate measurements from the last 80 Myr, and then summed the PDFs from all regions to generate an overall age distribution. We performed this random selection 10,000 times and plot the median age distribution in Figure 4.5. Because the regions are randomly selected for each row, the shape is similar, but not identical.

We note that the error bars on our HMXB age distribution measurements are relatively large, and that some time bins only have upper errors. This is caused by the large covariance between time bins for a given SFH. Given the finite stellar mass within a region, if the best-fit SFH includes a high SFR in the 10-20 Myr bin, that will result in a lower SFR in another bin in order to conserve the total stellar mass formed. More simply, if the highest SFR allowed within errors is selected in one bin, a lower SFR within errors must be selected in another bin to maintain the same total stellar mass formed in that region in all time bins. The bins from 50 to 80 Myr show only upper errors bars, which happens when the best fit SFR is zeros, but with upper limits, so that the uncertainty only allows for the possibility of a higher mass fraction.

The high probability portions of the histogram represent ages with high rates in their best fit, making it unlikely for a Monte Carlo selection with a higher rate in that time bin to generate an total stellar mass within the acceptable range. Thus, these distributions suggest a clear signal in the age distribution, even if there is some chance that all of the covariances and upper limits could formally conspire to reduce that signal.

We quantify the significance of our observed HMXB age distributions for each sub-sample by comparing with the age distributions produced by the 10,000 iterations where we randomly selected an equal number of regions from the PHAT star formation history maps. We wanted to know what fraction of the 10,000 random iterations for each sub-sample produced greater than or equal to the same number of candidates in the time bins between 10 and 50 Myr, where our HMXB candidate age distribution shows the largest peak. We found that zero of the 10,000 random iterations, for all of the three sub-sample sizes, produced greater than or equal to the number of

candidates in our best observed HMXB age distributions for all sub-samples. This gives a $<0.01\%$ probability of measuring the observed peak in our age distribution with a random sample. If we assume the lowest end of the errors on our HMXB age distributions, we found that the random draws were able to reproduce the number of candidates in the 10 to 50 Myr time range 0.23%, 0.25% and 0.25% of the time, for each sub-sample respectively.

4.4.2 HMXB Production Rate

We present two measures of the HMXB production rate: the number of HMXB systems formed per unit of star formation rate (HMXB systems/($M_\odot$ yr^{-1}) and the number of HMXB systems formed per solar mass (HMXB systems/$M_\odot$). Our HMXB production rate measurements should be interpreted as a lower limit because we only observe the fraction of HMXBs that were active at the time of observation. The observed duty cycle, or fraction of time that the XRB is active, of XRBs covers a wide range. For example, the observed duty cycle for Galactic black hole XRBs ranges from 0.2% to 100% with a mean value of 10%, although these values were measured for a Galactic sample mostly consisting of low-mass XRBs (Tetarenko et al., 2016).

Single stellar evolution predicts that stars massive enough to form black holes and neutron stars should not be observed after $\sim$50 Myr. However, binary interaction may delay the onset of the supernova of the primary star because of mass transfer via binary interactions (e.g., Zapartas et al., 2017). Thus, we perform our calculation of HMXB production per unit SFR for both an assumed 50 Myr age range and an extended 80 Myr age range.

Calculation of HMXBs per Unit SFR

For direct comparison with measurements in other galaxies, we calculate the number of HMXBs produced as a function of star formation rate (HMXB systems/($M_\odot$ yr^{-1})). To do this, we must make several assumptions related to the timescales over which HMXBs form and survive. First, we must assume a steady state, such that the global star formation rate does not change significantly over the lifetimes of massive stars ($\sim$50-80 Myr). This should be a reasonable assumption for a massive galaxy such as M31. Second, we must assume that HMXBs only form and survive over the

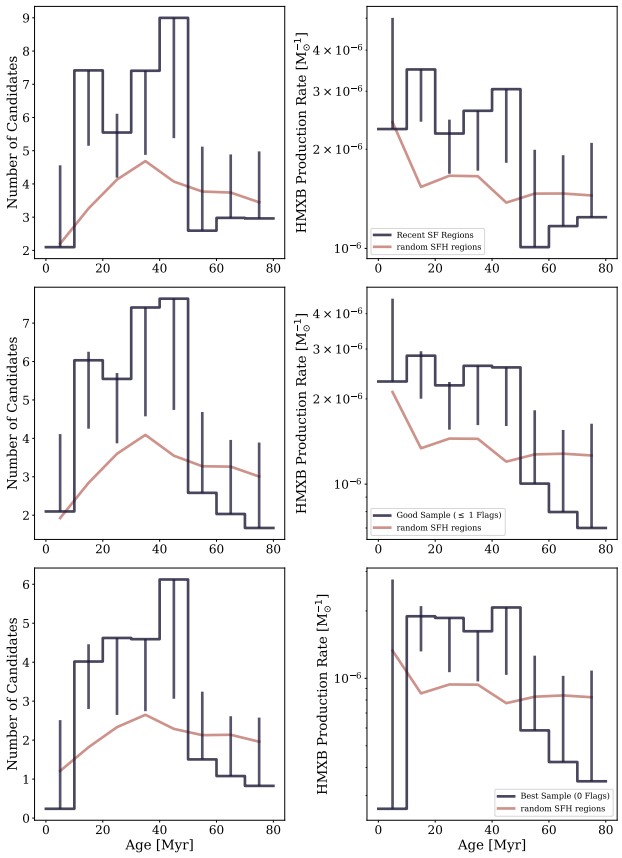

Figure 4.5 Likely age distribution and HMXB production rate using the HMXB candidates in our sample. **Top row:** The top row shows the distribution of likely ages and the production rate measurement for all of the *Chandra*-PHAT sources with point source optical counterparts that are in regions with measured star formation within the last 80 Myr. The left plot shows the age distribution for our HMXB candidates. The dark histogram represents the overall age distribution for the sample, produced using the star formation history for the 100 by 100 pc region surrounding each HMXB candidate. The error bars on the histogram come from sampling within the errors on the SFR measurements 10,000 times. The pink line represents the median age distribution for an equal number of randomly selected regions from the PHAT star formation history map covered by the Chandra-PHAT survey. This random selection was performed 10,000 times. The right plot shows the HMXB production rate in units of HMXB systems produced per $M_\odot$. The production rate was calculated by dividing the number of candidates in each time bin by the total stellar mass formed in the PHAT survey footprint that was covered by the Chandra-PHAT survey during the same time period. The black histogram represents the HMXB candidate sample and the pink line represents the median production rate for the random sample. **Middle row:** The middle row represents the same analysis for HMXB candidates that raised one or fewer flags as described in Section 4.3.3. This sample consists of 35 HMXB candidates. **Bottom row:** The bottom row represents the same analysis for HMXB candidates in our sample that raised zero flags, as described in Section 4.3.3. This is our best sample and comprises 23 HMXB candidates. ©AAS. Reproduced with permission from Lazzarini et al. (2021).

lifetime of massive stars so that their total number is constant under the condition of a steady state star formation rate. These assumptions allow us to estimate the number of HMXBs as a function of star formation rate.

We first find the total number of HMXB candidates in each time range (50 or 80 Myr). Our best sample, for sources that raise zero flags we find 19.6 candidates form within the last 50 Myr and 23 candidates form within the last 80 Myr. For sources that raise one or fewer flags, we find 28.7 candidates form within the last 50 Myr and 35 candidates form within the last 80 Myr. We then divide each total number of HMXB candidates by the mean total star formation rate within the PHAT footprint that is covered by the *Chandra*-PHAT survey over the time range (see Section 4.3.2). The mean SFR over the last 50 Myr is 0.226 ± 0.016 $M_\odot$ yr^{-1} and over the last 80 Myr is 0.235 ± 0.021 $M_\odot$ yr^{-1}.

For the sample of HMXB candidates that raised zero flags, we calculate an HMXB production rate of 89$-$107 HMXBs/($M_\odot$ yr^{-1}) in the last 80 Myr and an HMXB production rate of 80$-$93 HMXBs/($M_\odot$ yr^{-1}) in the last 50 Myr. For the equal sized random sample, the rate is 65$-$77 HMXBs/($M_\odot$ yr^{-1}) in the last 80 Myr and 43$-$49 HMXBs/($M_\odot$ yr^{-1}) in the last 50 Myr. For the sample of HMXB candidates that raised one or fewer flags, we calculate an HMXB production rate of 136$-$163 HMXBs/($M_\odot$ yr^{-1}) in the last 80 Myr and an HMXB production rate of 118$-$136 HMXBs/($M_\odot$ yr^{-1}) in the last 50 Myr. For the equal sized random sample, the rate is 100$-$119 HMXBs/($M_\odot$ yr^{-1}) in the last 80 Myr and 66$-$76 HMXBs/($M_\odot$ yr^{-1}) in the last 50 Myr.

Time Resolved HMXB Production Rate

Because we have measured an age distribution as well as a time resolved recent star formation history, we are also able to calculate a time resolved HMXB production rate. We start with the summed PDF for the stellar populations immediately surrounding each HMXB candidate in the sample (shown in the left column of Figure 4.5), which yields the number of HMXB candidates that likely formed in each 10 Myr time bin. We then divide the PDF in each time bin by the total star formation rate within the PHAT footprint that is covered by the *Chandra*-PHAT survey during that time bin. Lastly, we divide by the width of the time bin (10 Myr) to get the number of HMXB

candidates we expect to form per stellar mass.

We present the HMXB production rate in each time bin in units of HMXB systems/$M_{\odot}$ in the right column of Figure 4.5. The sample used to create the plots is described in Section 4.4.1. We also include the production rate for the random sample, shown in pink. In all three sub-samples, the HMXB production rate appears remarkably flat at early times, with a drop at 50 Myr. This relatively constant rate results in a simple conversion between these rates and our results from Section 4.4.2. By multiplying the constant rate here by the characteristic time scales assumed in Section 4.4.2 we recover the number of HMXBs formed per unit SFR. As in the age distribution plots in the left column of Figure 4.5, the errors on our HMXB production rates are large due to covariance between the measured SFR in each time bin.

Comparison with Other Measurements

We can compare our calculation of the HMXB production rate in units of HMXB systems/$M_{\odot}$ most directly with theoretical predictions. Linden et al. (2010) investigated how metallicity impacts the formation of bright (bolometric $L_X > 1 \times 10^{36}$ erg s^{-1}) XRBs. At solar metallicity, they predicted an HMXB production rate of $\sim$8 HMXB systems per starburst of 10^6 M$_{\odot}$, approximately 5 Myr after the starburst. Comparison between our observed population and this simulated one is difficult. The simulated population is selected using unabsorbed bolometric X-ray luminosity, and has a limiting X-ray luminosity of $\sim 7 \times 10^{34}$ erg s^{-1} in the 0.35$-$8.0 keV *Chandra* band, which is lower than the limiting luminosity of $\sim 2 \times 10^{35}$ erg s^{-1} in the 0.35$-$8.0 keV band for the *Chandra*-PHAT survey. However, our measurements agree within an order of magnitude.

We note that a direct comparison between empirical galaxy samples is difficult due to inconsistencies between how the HMXB samples were gathered in various studies. The limiting X-ray luminosity of each survey and number of X-ray observations used to gather each HMXB sample will influence the number detected because both the HMXB luminosity function and duty cycle will affect the number of sources detected. However, the X-ray luminosity function for HMXBs has a very sharp knee right around $\sim 10^{35}$ erg s^{-1} (Sturm et al., 2013a), attributed to the propeller effect, which can inhibit accretion at low accretion rates (e.g.; Shtykovskiy & Gilfanov, 2005).

The knee in the luminosity function suggests that as long as the limiting luminosity gets down to $\sim 10^{35}$ erg s^{-1}, the number of expected HMXBs should be comparable. Thus, as long as the duty cycles of various populations are similar, comparisons may be of interest.

A recent observational study of the HMXB population in NGC55 (Politakis et al., 2020) compared the HMXB production rate of that galaxy with those measured in other galaxies including the SMC, LMC, and Milky Way (Antoniou et al., 2010; Bodaghee et al., 2012; Antoniou & Zezas, 2016; Antoniou et al., 2019). In this section, we discuss the HMXB production rates of the SMC, LMC, and Milky Way that are presented in Table 5 of Politakis et al. (2020), which were calculated with the average SFR of each galaxy. They measured an HMXB production rate in NGC55 of 299^{+50}_{-46} HMXBs/(M$_\odot$ yr^{-1}), down to a limiting X-ray luminosity of 3×10^{35} erg s^{-1} in the *Chandra* 0.3$-$7 keV energy band. The HMXB production rate has also been measured in the LMC and SMC using the average SFR for each galaxy, down to a limiting luminosity of 3×10^{33} erg s^{-1} in the 2$-$8 keV energy band, with production rates of 160^{+96}_{-64} and 480^{+400}_{-240} HMXBs/(M$_\odot$ yr^{-1}), respectively (Antoniou & Zezas, 2016). The HMXB production rate of the Milky Way has also been measured at 69 ± 17 HMXBs/(M$_\odot$ yr^{-1}) (Bodaghee et al., 2012; Licquia & Newman, 2015). The Milky Way sample was hard X-ray selected (*INTEGRAL*; 20$-$40 keV) with a sensitivity limit of 3.78×10^{-11} erg cm^{-2} s^{-1} (Bodaghee et al., 2007), which translates to a limiting luminosity of a few $\times10^{33}$ to a few $\times10^{35}$ erg s^{-1}, depending on the distance to the HMXB. The agreement between our measurement of 80$-$136 HMXBs/(M$_\odot$ yr^{-1}) over the last 50 Myr and the measurement of 69 ± 17 HMXB systems/($M_\odot$ yr^{-1}) in the Milky Way suggests that the HMXB populations are comparable when scaled by star formation rate.

There is a known correlation between the number of HMXBs produced and the local SFR and metallicity. The number of HMXBs produced is expected to scale with the SFR (e.g.; Lehmer et al., 2010; Mineo et al., 2012; Antoniou et al., 2019), a galaxy with a higher SFR is expected to produce more HMXBs. The host galaxy metallicity also plays a role. Galaxies with lower metallicity have been predicted to produce HMXBs at a higher rate due to reduced mass loss in the late stages of stellar evolution via stellar winds (e.g.; Linden et al., 2010; Fragos et al., 2013; Ponnada et al., 2020; Fornasini et al., 2020). This correlation is evident in the sample of galaxies

discussed in Politakis et al. (2020), where the lowest metallicity galaxy, the SMC, has the highest HMXB production rate while the highest metallicity galaxy, the Milky Way, has the lowest HMXB production rate. We would expect M31, which has roughly solar metallicity in its disk (Gregersen et al., 2015), to have a production rate similar to that of the Milky Way, which is consistent with our measurement.

4.4.3 HMXB Velocities

Measuring the velocities of HMXB systems can be used to constrain the natal kick imparted on the compact object during its supernova. We present the methodology we used to calculate the average HMXB transverse velocity using correlations between HMXB positions and the positions of young star clusters in M31. In this section, we describe measurements made in other nearby galaxies and outline why we were unable to make this measurement for the HMXB population in M31.

This type of analysis has been done successfully in nearby galaxies and the Milky Way. Some studies distinguish the velocities of Be-XRBs (X-ray binaries with B−type emission line stars as the companion to the compact object), and SG-XRBs (X-ray binaries with supergiant companion stars). Antoniou & Zezas (2016) found that the mean transverse velocity of HMXBs in the SMC is 13.1 km s^{-1}. In the LMC, they estimated a transverse velocity of $\sim$ 12.4 ± 7.0 km s^{-1} for HMXBs, excluding black hole or white dwarf systems. The subset of the LMC HMXB population that are confirmed NS/Be-XRB systems travel with a velocity of $\sim$ 10.8 ± 7.3 km s^{-1}. van den Heuvel et al. (2000) measured the transverse velocities of Be-XRBs and SG-XRBs in the Milky Way using parallax and found a mean velocity of 42 ± 14 km s^{-1} for SG-XRBs and 15 ± 6 km s^{-1} for Be-XRBs.

We attempted to associate our HMXB candidates with nearby young star clusters using the cluster catalog from the PHAT survey by (Johnson et al., 2015) and the catalog of SED fit ages for the PHAT clusters from de Meulenaer et al. (2015). For each HMXB candidate in our best sample, we found the distance to the nearest cluster with an age that agreed with the local stellar population within the 1σ errors on the age of the population. The distribution of distances from the HMXB

sample was indistinguishable from a sample of random positions. Thus, we cannot constrain the precise birth places of our HMXB candidates, meaning we cannot measure their velocities. It is possible that the inclination of the M31 disk leads to a young cluster density that hinders our ability to reliably match objects to their birth clusters.

4.5 Conclusions

In this work we present a study of the HMXB population of M31. We use a combination of spatially resolved star formation histories, SED fits for the optical counterparts, *Chandra* and *XMM-Newton* X-ray observations, and dust maps of M31 to characterize the largest sample of high quality HMXB candidates in M31 to date. Our main conclusions follow:

- We have presented a new method that combines SED fits of the companion stars in HMXB candidates with ages of local stellar populations from spatially resolved star formation histories, and other multiwavelength observations to select a sample of high quality HMXB candidates.

- We found that the dominant ages of the HMXBs in our best sample are $10-50$ Myr. This is consistent with the studies of SMC, LMC, and M33, which show that the HMXB age depends on the star-formation history in a galaxy.

- We calculated that the HMXB production rate in M31 was $\sim 2 \times 10^{-6}$ HMXB systems/$M_{\odot}$ between 10 and 50 Myr ago before dropping below $\sim 1 \times 10^{-6}$ HMXB systems/$M_{\odot}$ after 50 Myr.

- We also calculate the number of HMXB systems formed over the last 50 and 80 Myr per unit SFR. For our best sample, 89-107 HMXBs/($M_{\odot}$ yr^{-1}) candidates were produced over the last 80 Myr and 80-93 HMXBs/($M_{\odot}$ yr^{-1}) candidates were produced over the last 50 Myr.

- We were not able to determine the transverse velocities of our HMXB candidates by associating them with nearby young clusters, which could be caused by the inclination of the disk

of M31.

This study still marks our early efforts to understand the HMXB populations in M31. Future work will include modeling the population with binary population synthesis. For systems that are bright enough, follow-up optical spectroscopy will allow us to confirm the nature of the companion stars and time-resolved optical spectroscopy will allow us to determine the orbital parameters of any true HMXB systems.

Table 4.1: SED fit parameters for point source optical counterparts to *Chandra*-PHAT X-ray sources

Chandra-PHAT Name	*Chandra* RA	*Chandra* Dec.	*PHAT Name*	0.35−8.0 keV Lum. $\times 10^{36}$ erg s^{-1}	log(T_{eff}) K	log(L) erg s^{-1}	R) $R_{\odot}$]	A_V mag	M $M_{\odot}$	SED Age log(yr)	Local SFH Age log(yr)	S18 ID	S18 Class.
004350.76+412118.1	10.961532	41.354841	J004350.76+412118.16	$3.18^{+0.28}_{-0.26}$	$4.6^{+0.1}_{-0.1}$	$6.2^{+0.1}_{-0.1}$	$23.9^{+2.0}_{-2.2}$	$3.2^{+0.2}_{-0.1}$	38^{+2}_{-1}	$6.6^{+0.1}_{-0.0}$	NA	60	<XRB>
004425.73+412242.4	11.107230	41.378284	J004425.72+412242.52	$1.08^{+0.17}_{-0.15}$	$4.1^{+0.4}_{-0.2}$	$4.0^{+0.8}_{-0.1}$	$24.1^{+8.2}_{-15.4}$	$4.0^{+0.1}_{-0.7}$	7^{+11}_{-3}	$7.7^{+0.3}_{-0.8}$	16^{+47}_{-47}		
004452.51+411710.7	11.218860	41.286154	J004452.52+411711.09	$2.49^{+0.29}_{-0.27}$	$4.7^{+0.1}_{-0.1}$	$6.0^{+0.1}_{-0.1}$	$11.5^{+0.9}_{-1.2}$	$1.4^{+0.2}_{-0.1}$	29^{+3}_{-1}	$6.6^{+0.1}_{-0.0}$	NA		
004448.13+412247.9	11.200555	41.379836	J004448.14+412248.21	$1.31^{+0.19}_{-0.17}$	$4.5^{+0.1}_{-0.1}$	$4.9^{+0.1}_{-0.2}$	$7.8^{+0.9}_{-1.2}$	$3.6^{+0.2}_{-0.2}$	19^{+3}_{-3}	$6.9^{+0.1}_{-0.3}$	15^{+3}_{-3}	229	<XRB>
004359.83+412435.6	10.999298	41.409707	J004359.79+412436.02	$0.35^{+0.15}_{-0.11}$	$4.5^{+0.1}_{-0.1}$	$4.7^{+0.1}_{-0.3}$	$6.8^{+1.5}_{-0.3}$	$2.2^{+0.2}_{-0.2}$	19^{+1}_{-6}	$6.7^{+0.4}_{-0.1}$	34^{+4}_{-4}	87	
004407.44+412460.0	11.030994	41.416487	J004407.45+412500.04	$0.13^{+0.07}_{-0.05}$	$3.8^{+0.1}_{-0.1}$	$5.8^{+0.1}_{-0.1}$	$864.9^{+109.2}_{-71.2}$	$5.0^{+0.2}_{-0.1}$	36^{+1}_{-2}	$6.7^{+0.1}_{-0.1}$	NA	115	
004454.75+411918.3	11.228091	41.321625	J004454.74+411917.97	$0.89^{+0.18}_{-0.16}$	$4.7^{+0.1}_{-0.1}$	$5.8^{+0.1}_{-0.1}$	$10.7^{+1.7}_{-0.4}$	$2.8^{+0.2}_{-0.1}$	22^{+1}_{-1}	$6.7^{+0.1}_{-0.1}$	NA	249	<XRB>
004339.06+412117.6	10.912759	41.354665	J004339.11+412117.52	$3.54^{+0.32}_{-0.29}$	$4.4^{+0.1}_{-0.1}$	$3.6^{+0.1}_{-0.3}$	$4.0^{+0.3}_{-0.4}$	$1.0^{+0.1}_{-0.3}$	8^{+1}_{-2}	$7.2^{+0.5}_{-0.2}$	28^{+8}_{-8}	37	
004352.37+412222.8	10.968206	41.372807	J004352.32+412223.18	$0.31^{+0.11}_{-0.08}$	$4.5^{+0.1}_{-0.1}$	$4.7^{+0.1}_{-0.3}$	$6.8^{+1.3}_{-0.4}$	$2.0^{+0.1}_{-0.2}$	19^{+1}_{-6}	$6.7^{+0.4}_{-0.1}$	NA		
004445.88+413152.2	11.191097	41.531045	J004445.85+413154.69	$0.44^{+0.17}_{-0.14}$	$4.5^{+0.1}_{-0.1}$	$4.8^{+0.1}_{-0.1}$	$7.9^{+1.0}_{-1.0}$	$1.6^{+0.2}_{-0.1}$	19^{+2}_{-1}	$6.8^{+0.1}_{-0.2}$	25^{+3}_{-3}	223	
004412.17+413148.4	11.050810	41.529889	J004412.16+413148.13	$1.91^{+0.23}_{-0.20}$	$4.5^{+0.1}_{-0.1}$	$5.3^{+0.1}_{-0.1}$	$12.1^{+1.3}_{-0.9}$	$1.8^{+0.2}_{-0.1}$	29^{+1}_{-6}	$6.6^{+0.3}_{-0.0}$	10^{+65}_{-65}	127	<XRB>
004424.80+413201.4	11.103437	41.533501	J004424.80+413201.30	$3.46^{+0.30}_{-0.27}$	$4.2^{+0.2}_{-0.2}$	$5.0^{+0.4}_{-0.3}$	$38.9^{+17.3}_{-17.2}$	$4.8^{+0.3}_{-0.4}$	16^{+12}_{-4}	$7.1^{+0.2}_{-0.4}$	15^{+3}_{-3}	157	<XRB>
004357.54+413055.8	10.989854	41.515274	J004357.53+413055.62	$0.89^{+0.16}_{-0.14}$	$4.5^{+0.1}_{-0.1}$	$4.3^{+0.1}_{-0.1}$	$4.2^{+0.8}_{-0.2}$	$1.4^{+0.2}_{-0.1}$	14^{+2}_{-1}	$6.8^{+0.2}_{-0.1}$	34^{+12}_{-12}	83	<XRB>
004404.55+413159.4	11.019069	41.532972	J004404.53+413159.41	$0.28^{+0.10}_{-0.08}$	$4.1^{+0.1}_{-0.1}$	$3.1^{+0.6}_{-0.1}$	$5.9^{+1.1}_{-0.7}$	$1.2^{+0.5}_{-0.1}$	5^{+2}_{-1}	$7.9^{+0.1}_{-0.4}$	NA	103	<hard>
004420.18+413408.2	11.084197	41.568733	J004420.17+413408.04	$0.32^{+0.10}_{-0.08}$	$4.4^{+0.1}_{-0.1}$	$4.0^{+0.3}_{-0.1}$	$6.8^{+0.6}_{-0.9}$	$1.0^{+0.3}_{-0.1}$	10^{+3}_{-1}	$7.2^{+0.1}_{-0.3}$	45^{+3}_{-3}	145	<XRB>
004356.78+413410.9	10.986712	41.569508	J004356.79+413410.67	$0.30^{+0.10}_{-0.08}$	$4.2^{+0.2}_{-0.1}$	$3.5^{+0.6}_{-0.1}$	$7.4^{+1.2}_{-1.5}$	$2.2^{+0.7}_{-0.2}$	7^{+4}_{-1}	$7.7^{+0.1}_{-0.5}$	NA	75	<XRB>
004413.18+412911.4	11.055003	41.486291	J004413.15+412910.92	$0.65^{+0.15}_{-0.12}$	$3.7^{+0.1}_{-0.1}$	$4.1^{+0.3}_{-0.2}$	$172.6^{+122.3}_{-19.5}$	$5.2^{+0.7}_{-1.3}$	8^{+3}_{-1}	$7.6^{+0.2}_{-0.2}$	45^{+3}_{-3}	131	<XRB>
004412.04+413217.4	11.050227	41.537919	J004412.06+413217.37	$0.30^{+0.18}_{-0.12}$	$3.8^{+0.1}_{-0.1}$	$5.5^{+0.4}_{-0.1}$	$519.5^{+69.1}_{-77.0}$	$5.2^{+0.8}_{-0.3}$	27^{+17}_{-2}	$6.8^{+0.1}_{-0.1}$	15^{+3}_{-3}	126	<XRB>
004336.08+413320.4	10.900448	41.555509	J004336.09+413320.61	$0.53^{+0.13}_{-0.11}$	$4.4^{+0.1}_{-0.1}$	$5.1^{+0.1}_{-0.3}$	$18.7^{+3.1}_{-1.7}$	$2.2^{+0.2}_{-0.1}$	21^{+1}_{-5}	$6.9^{+0.1}_{-0.1}$	30^{+29}_{-29}	33	<XRB>
004402.02+414028.8	11.008606	41.674477	J004402.06+414028.53	$0.53^{+0.14}_{-0.12}$	$4.7^{+0.1}_{-0.1}$	$6.2^{+0.1}_{-0.1}$	$14.2^{+1.9}_{-1.2}$	$3.0^{+0.2}_{-0.1}$	37^{+2}_{-2}	$6.6^{+0.1}_{-0.0}$	NA	93	<XRB>
004528.24+412943.9	11.367908	41.495416	J004528.24+412943.93	$9.23^{+0.48}_{-0.45}$	$4.4^{+0.1}_{-0.1}$	$5.9^{+0.1}_{-0.1}$	$39.4^{+3.2}_{-4.0}$	$2.4^{+0.2}_{-0.1}$	23^{+1}_{-1}	$6.6^{+0.1}_{-0.0}$	5^{+3}_{-3}	333	<XRB>
004525.67+413158.2	11.357166	41.532700	J004525.67+413158.26	$0.26^{+0.10}_{-0.07}$	$4.4^{+0.1}_{-0.1}$	$5.2^{+0.1}_{-0.1}$	$16.9^{+2.0}_{-1.3}$	$2.8^{+0.2}_{-0.1}$	23^{+1}_{-3}	$6.8^{+0.2}_{-0.1}$	NA		
004510.96+414559.2	11.295728	41.766228	J004510.96+414559.08	$2.34^{+0.25}_{-0.22}$	$4.7^{+0.1}_{-0.3}$	$6.2^{+0.1}_{-0.6}$	$17.5^{+12.5}_{-0.8}$	$4.2^{+0.5}_{-0.1}$	38^{+4}_{-11}	$6.6^{+0.1}_{-0.0}$	55^{+7}_{-7}	290	<XRB>
004527.88+413905.5	11.366238	41.651368	J004527.88+413905.55	$2.13^{+0.24}_{-0.22}$	$4.4^{+0.1}_{-0.1}$	$5.7^{+0.3}_{-0.1}$	$46.3^{+4.0}_{-12.7}$	$5.2^{+0.1}_{-0.2}$	26^{+24}_{-1}	$6.6^{+0.1}_{-0.0}$	39^{+7}_{-7}	331	<XRB>
004459.11+414005.1	11.246362	41.667904	J004459.09+414004.99	$1.18^{+0.20}_{-0.17}$	$3.7^{+0.1}_{-0.1}$	$3.2^{+0.1}_{-0.1}$	$46.6^{+3.6}_{-5.2}$	$0.2^{+0.2}_{-0.1}$	6^{+1}_{-1}	$7.9^{+0.0}_{-0.1}$	71^{+6}_{-6}	261	<XRB>
004500.89+414309.8	11.253781	41.719177	J004500.92+414309.93	$0.70^{+0.15}_{-0.12}$	$4.2^{+0.1}_{-0.1}$	$2.6^{+0.6}_{-0.1}$	$3.2^{+1.0}_{-0.3}$	$1.2^{+0.9}_{-0.1}$	4^{+2}_{-1}	$7.9^{+0.1}_{-0.5}$	45^{+3}_{-3}	268	<hard>
004536.13+414702.5	11.400541	41.783846	J004536.16+414702.64	$0.23^{+0.10}_{-0.07}$	$4.6^{+0.1}_{-0.1}$	$5.7^{+0.1}_{-0.1}$	$15.3^{+1.2}_{-1.7}$	$1.4^{+0.2}_{-0.1}$	44^{+3}_{-17}	$6.6^{+0.1}_{-0.0}$	54^{+7}_{-7}		
004537.84+414856.7	11.407659	41.815539	J004537.92+414856.53	$0.28^{+0.11}_{-0.08}$	$4.6^{+0.1}_{-0.1}$	$5.2^{+0.1}_{-0.1}$	$10.0^{+7.2}_{-0.4}$	$1.8^{+0.9}_{-0.1}$	28^{+1}_{-4}	$6.6^{+0.3}_{-0.1}$	45^{+3}_{-3}	360	galaxy
004537.67+415124.4	11.406884	41.856688	J004537.69+415122.88	$0.43^{+0.14}_{-0.12}$	$4.6^{+0.1}_{-0.1}$	$5.1^{+0.1}_{-0.1}$	$8.7^{+0.5}_{-1.1}$	$1.4^{+0.2}_{-0.1}$	25^{+2}_{-1}	$6.7^{+0.1}_{-0.1}$	64^{+11}_{-11}	358	galaxy
004453.33+415159.5	11.222383	41.866435	J004453.34+415159.45	$0.56^{+0.13}_{-0.11}$	$4.5^{+0.1}_{-0.1}$	$5.4^{+0.1}_{-0.1}$	$15.6^{+1.4}_{-2.0}$	$3.4^{+0.2}_{-0.1}$	28^{+3}_{-2}	$6.8^{+0.1}_{-0.2}$	34^{+4}_{-4}	247	<XRB>
004455.72+415334.6	11.232348	41.892823	J004455.72+415334.38	$0.30^{+0.11}_{-0.09}$	$4.4^{+0.1}_{-0.1}$	$4.3^{+0.1}_{-0.1}$	$8.0^{+1.3}_{-0.6}$	$1.8^{+0.2}_{-0.1}$	12^{+1}_{-1}	$7.1^{+0.2}_{-0.1}$	45^{+5}_{-5}	252	<hard>
004422.57+414506.5	11.094291	41.751726	J004422.58+414506.76	$5.73^{+0.41}_{-0.39}$	$4.5^{+0.1}_{-0.2}$	$5.7^{+0.1}_{-0.5}$	$20.0^{+6.9}_{-0.9}$	$2.2^{+0.1}_{-0.2}$	43^{+1}_{-22}	$6.6^{+0.3}_{-0.0}$	35^{+4}_{-4}	151	<XRB>
004437.96+414512.6	11.158345	41.753417	J004437.96+414512.56	$1.33^{+0.21}_{-0.19}$	$4.0^{+0.1}_{-0.1}$	$3.4^{+0.1}_{-0.1}$	$12.9^{+0.7}_{-2.4}$	$1.4^{+0.1}_{-0.2}$	6^{+1}_{-1}	$7.9^{+0.0}_{-0.1}$	NA	199	<AGB>
004502.33+414943.1	11.259843	41.828560	J004502.34+414943.56	$0.33^{+0.11}_{-0.08}$	$4.1^{+0.1}_{-0.1}$	$3.2^{+0.2}_{-0.1}$	$7.5^{+0.5}_{-0.9}$	$1.0^{+0.2}_{-0.1}$	5^{+1}_{-1}	$7.9^{+0.0}_{-0.1}$	35^{+3}_{-3}	272	galaxy
004514.76+415034.5	11.311624	41.842838	J004514.76+415034.35	$0.73^{+0.16}_{-0.13}$	$4.5^{+0.1}_{-0.1}$	$5.2^{+0.1}_{-0.1}$	$10.1^{+0.5}_{-1.4}$	$0.8^{+0.2}_{-0.1}$	26^{+1}_{-1}	$6.7^{+0.1}_{-0.1}$	15^{+3}_{-3}	303	<XRB>
004431.82+415217.2	11.132787	41.871348	J004431.81+415216.99	$0.32^{+0.11}_{-0.09}$	$4.5^{+0.1}_{-0.1}$	$5.5^{+0.1}_{-0.1}$	$17.9^{+1.2}_{-2.4}$	$2.6^{+0.2}_{-0.1}$	30^{+5}_{-2}	$6.8^{+0.1}_{-0.2}$	37^{+23}_{-23}	180	
004611.38+415903.9	11.547594	41.984285	J004611.39+415903.91	$1.52^{+0.22}_{-0.20}$	$4.4^{+0.2}_{-0.1}$	$4.5^{+0.3}_{-0.1}$	$10.8^{+0.5}_{-3.7}$	$3.8^{+0.3}_{-0.2}$	14^{+7}_{-1}	$7.1^{+0.1}_{-0.4}$	34^{+7}_{-7}		
004617.57+415913.6	11.573363	41.986986	J004617.57+415913.74	$0.52^{+0.13}_{-0.11}$	$4.8^{+0.0}_{-0.1}$	$6.0^{+0.1}_{-0.1}$	$7.0^{+1.3}_{-0.2}$	$2.2^{+0.2}_{-0.1}$	29^{+1}_{-3}	$6.6^{+0.1}_{-0.0}$	65^{+11}_{-11}		

Chandra-PHAT Name	*Chandra* RA	*Chandra* Dec.	*PHAT Name*	0.35−8.0 keV Lum. $\times 10^{36}$ erg s^{-1}	log(T_{eff}) K	log(L) erg s^{-1}	R) $R_\odot$]	A_V mag	M $M_\odot$	SED Age log(yr)	Local SFH Age log(yr)	S18 ID	S18 Class.
004613.49+415043.3	11.556365	41.845282	J004613.48+415043.48	$2.83^{+0.32}_{-0.29}$	$4.6^{+0.1}_{-0.1}$	$6.2^{+0.1}_{-0.1}$	$23.9^{+0.7}_{-3.5}$	$3.0^{+0.2}_{-0.1}$	38^{+1}_{-2}	$6.6^{+0.1}_{-0.0}$	26^{+36}_{-36}		
004640.59+415422.8	11.669246	41.906253	J004640.58+415423.14	$3.98^{+0.34}_{-0.32}$	$4.4^{+0.1}_{-0.1}$	$5.8^{+0.1}_{-0.3}$	$38.4^{+4.4}_{-4.1}$	$4.2^{+0.2}_{-0.2}$	45^{+1}_{-13}	$6.6^{+0.1}_{-0.0}$	NA		
004550.83+415835.1	11.462002	41.976310	J004550.84+415835.47	$0.40^{+0.12}_{-0.09}$	$4.6^{+0.1}_{-0.1}$	$5.2^{+0.1}_{-0.3}$	$7.6^{+1.6}_{-0.7}$	$2.6^{+0.2}_{-0.1}$	28^{+1}_{-7}	$6.6^{+0.1}_{-0.0}$	68^{+9}_{-9}		
004558.04+420302.9	11.492053	42.050671	J004558.05+420302.99	$2.24^{+0.35}_{-0.31}$	$4.6^{+0.1}_{-0.1}$	$5.1^{+0.1}_{-0.2}$	$8.7^{+0.9}_{-0.8}$	$1.6^{+0.2}_{-0.1}$	26^{+1}_{-5}	$6.6^{+0.2}_{-0.0}$	NA		
004543.15+415519.4	11.430069	41.922003	J004543.17+415519.30	$0.27^{+0.13}_{-0.09}$	$4.7^{+0.1}_{-0.1}$	$6.0^{+0.1}_{-0.3}$	$16.5^{+4.4}_{-0.2}$	$2.8^{+0.2}_{-0.1}$	29^{+14}_{-1}	$6.6^{+0.1}_{-0.0}$	15^{+3}_{-3}		
004552.94+420234.0	11.470802	42.042636	J004552.95+420233.98	$0.76^{+0.16}_{-0.14}$	$4.4^{+0.1}_{-0.1}$	$4.5^{+0.1}_{-0.1}$	$7.6^{+1.3}_{-0.6}$	$2.2^{+0.2}_{-0.1}$	14^{+1}_{-1}	$6.9^{+0.3}_{-0.1}$	NA		
004526.67+415631.0	11.361433	41.941835	J004526.66+415631.40	$1.06^{+0.22}_{-0.19}$	$4.4^{+0.2}_{-0.1}$	$5.3^{+0.3}_{-0.1}$	$20.9^{+1.2}_{-8.7}$	$3.4^{+0.1}_{-0.6}$	26^{+10}_{-3}	$6.8^{+0.1}_{-0.2}$	45^{+3}_{-3}	326	<hard>
004611.85+420827.9	11.549452	42.140872	J004611.85+420827.88	$5.15^{+0.36}_{-0.33}$	$4.2^{+0.1}_{-0.1}$	$5.1^{+0.1}_{-0.3}$	$49.2^{+6.4}_{-4.8}$	$4.4^{+0.3}_{-0.1}$	18^{+2}_{-5}	$7.0^{+0.2}_{-0.1}$	27^{+7}_{-7}		
004607.50+420855.7	11.531340	42.148604	J004607.50+420855.87	$0.68^{+0.16}_{-0.13}$	$4.4^{+0.1}_{-0.1}$	$4.5^{+0.2}_{-0.2}$	$9.2^{+0.9}_{-2.9}$	$3.8^{+0.2}_{-0.4}$	14^{+4}_{-2}	$7.1^{+0.1}_{-0.3}$	35^{+3}_{-3}		
004612.67+421027.8	11.552859	42.174164	J004612.67+421027.80	$0.54^{+0.14}_{-0.11}$	$4.6^{+0.1}_{-0.1}$	$5.5^{+0.1}_{-0.1}$	$11.3^{+1.2}_{-1.2}$	$3.0^{+0.2}_{-0.1}$	38^{+1}_{-12}	$6.6^{+0.1}_{-0.0}$	NA		
004630.46+421028.7	11.626957	42.174428	J004630.47+421028.71	$0.36^{+0.11}_{-0.09}$	$4.4^{+0.1}_{-0.1}$	$5.2^{+0.1}_{-0.1}$	$19.3^{+1.9}_{-2.2}$	$3.2^{+0.2}_{-0.1}$	22^{+2}_{-1}	$6.9^{+0.1}_{-0.2}$	65^{+10}_{-10}		
004703.82+420453.0	11.765938	42.081202	J004703.82+420452.95	$5.46^{+0.40}_{-0.37}$	$4.5^{+0.1}_{-0.1}$	$5.8^{+0.1}_{-0.1}$	$25.6^{+2.7}_{-2.1}$	$3.8^{+0.2}_{-0.1}$	25^{+2}_{-1}	$6.6^{+0.1}_{-0.0}$	NA		
004639.47+420649.2	11.664524	42.113468	J004639.52+420648.81	$0.26^{+0.10}_{-0.08}$	$4.1^{+0.1}_{-0.1}$	$2.5^{+0.3}_{-0.1}$	$3.2^{+0.3}_{-0.4}$	$0.4^{+0.3}_{-0.1}$	4^{+1}_{-1}	$7.9^{+0.0}_{-0.3}$	55^{+7}_{-7}		
004648.19+420855.4	11.700826	42.148515	J004648.19+420855.43	$4.14^{+0.32}_{-0.29}$	$4.3^{+0.1}_{-0.1}$	$5.5^{+0.1}_{-0.1}$	$44.7^{+4.2}_{-4.3}$	$3.6^{+0.2}_{-0.1}$	31^{+1}_{-2}	$6.7^{+0.1}_{-0.1}$	45^{+3}_{-3}		
004630.68+420947.0	11.627879	42.162824	J004630.68+420947.03	$0.52^{+0.14}_{-0.11}$	$4.1^{+0.1}_{-0.1}$	$3.1^{+0.3}_{-0.1}$	$6.4^{+0.8}_{-0.5}$	$3.0^{+0.3}_{-0.1}$	5^{+1}_{-1}	$7.9^{+0.0}_{-0.2}$	29^{+45}_{-45}		
004542.25+420817.9	11.426149	42.138102	J004542.28+420818.16	$0.83^{+0.18}_{-0.15}$	$4.4^{+0.1}_{-0.1}$	$4.3^{+0.1}_{-0.1}$	$6.2^{+0.7}_{-0.7}$	$1.8^{+0.2}_{-0.1}$	13^{+2}_{-1}	$7.0^{+0.1}_{-0.3}$	NA		
004637.22+421034.5	11.655142	42.176036	J004637.22+421034.26	$0.22^{+0.11}_{-0.07}$	$4.6^{+0.1}_{-0.1}$	$5.2^{+0.1}_{-0.1}$	$8.7^{+1.1}_{-0.9}$	$0.6^{+0.2}_{-0.1}$	27^{+1}_{-3}	$6.7^{+0.1}_{-0.1}$	46^{+4}_{-4}		
004652.18+421505.8	11.717429	42.251372	J004652.05+421505.73	$0.49^{+0.14}_{-0.12}$	$4.7^{+0.1}_{-0.1}$	$5.8^{+0.1}_{-0.1}$	$9.5^{+1.5}_{-0.4}$	$3.2^{+0.2}_{-0.1}$	22^{+4}_{-1}	$6.7^{+0.1}_{-0.1}$	NA		
004648.27+420851.1	11.701185	42.147349	J004648.25+420851.12	$1.49^{+0.21}_{-0.18}$	$4.6^{+0.1}_{-0.1}$	$5.6^{+0.1}_{-0.1}$	$14.7^{+1.6}_{-1.2}$	$2.8^{+0.2}_{-0.1}$	39^{+2}_{-8}	$6.6^{+0.1}_{-0.0}$	27^{+8}_{-8}		

SED fit parameters for HMXB candidate companion stars. We describe each column in the order they are presented in the table. We include the name and position of each source from the *Chandra*-PHAT catalog (Williams et al., 2018) and the name of the HMXB candidate's companion star in the PHAT catalog (Williams et al., 2014b), and its *Chandra* 0.35−8.0 keV luminosity. We include the best-fit parameters for each companion star with errors from the BEAST SED fit including the effective temperature, optical luminosity, radius, dust extinction (A_V), mass, and age. We include the age of the stellar population in the 100 by 100 pc region surrounding the HMXB candidate from the Lewis et al. (2015) star formation history maps. Sources with a local SFH age listed as "NA" lie in regions without measured star formation in the last 80 Myr. For sources that were also detected in the Sasaki et al. (2018) (S18) *XMM-Newton* survey of M31, we include the source ID and classification. Sources without a listed "S18" ID did not have a corresponding source in the S18 catalog.

Table 4.2. Physical Properties Used to Classify Companion Stars

Stellar Type	T_{eff} [K]	log(L) [$L_\odot$	Radius [$R_\odot$
O-SG	26,000−40,300	5.52−6.04	22−25
B-SG	9730−26,000	4.54−5.52	25−66
O-MS	29,000−42,500	5.04−6.00	13−18
B-MS	10,100−29,000	2.02−5.04	3.4−13

Note. — List of the ranges of effective temperatures, luminosities, and radii used to classify companion stars. For a visual representation of these ranges, see Figure 4.2. Values come from Appendix B of Lamers & Levesque (2017).

Table 4.3: Values used to determine best HMXB candidate sample

Chandra-PHAT Name	BEAST A_V mag	PHAT A_V mag	A_V PDF	XMM N_H cm^{-2}	S18 ID	XMM Comments	Spectral Type	Chandra HR1	Chandra HR2	F110W-F160W (IR Color)
004350.76+412118.1	$3.20^{+0.20}_{-0.07}$	0.04±1.45	4.63×10^{-4}	2.00×10^{21}	60	XMM spec	O-SG	-0.04	0.63	0.88
004425.73+412242.4	$4.00^{+0.12}_{-0.71}$	1.28±0.20	3.28×10^{-1}	N/A	N/A	no XMM match	B-SG	-0.02	0.81	0.43
004452.51+411710.7	$1.40^{+0.17}_{-0.11}$	0.04±1.48	5.71×10^{-1}	N/A	N/A	no XMM match	O-MS	0.03	0.58	0.94
004448.13+412247.9	$3.60^{+0.19}_{-0.24}$	0.04±1.43	2.93×10^{-5}	3.20×10^{21}	229	XMM spec	B-MS	0.12	0.63	1.40
004359.83+412435.6	$2.20^{+0.18}_{-0.17}$	0.06±1.30	3.54×10^{-2}	N/A	87	no XMM spec	B-MS	-0.10	0.58	0.61
004407.44+412460.0	$5.00^{+0.23}_{-0.09}$	0.31±0.69	1.91×10^{-5}	N/A	115	no XMM spec	none	-0.80	-0.15	0.71
004454.75+411918.3	$2.80^{+0.20}_{-0.08}$	1.81±0.17	2.88×10^{-2}	4.90×10^{21}	249	XMM spec	O-MS	-0.06	0.51	1.12
004339.06+412117.6	$1.00^{+0.11}_{-0.28}$	0.66±0.41	1.41×10^{-1}	N/A	37	no XMM spec	B-MS	0.02	0.83	0.33
004352.37+412222.8	$2.00^{+0.15}_{-0.17}$	0.53±0.47	5.69×10^{-1}	N/A	N/A	no XMM match	B-MS	0.26	0.56	0.60
004445.88+413152.2	$1.60^{+0.20}_{-0.10}$	0.94±0.35	3.45×10^{-1}	N/A	223	no XMM spec	B-MS	-0.37	0.50	0.17
004412.17+413148.4	$1.80^{+0.18}_{-0.10}$	0.34±0.69	4.95×10^{-1}	1.30×10^{21}	127	XMM spec	O-MS	0.00	0.49	0.54
004424.80+413201.4	$4.80^{+0.33}_{-0.40}$	0.72±0.41	5.55×10^{-3}	2.80×10^{21}	157	XMM spec	B-SG	0.04	0.60	0.84
004357.54+413055.8	$1.40^{+0.22}_{-0.09}$	0.23±0.84	8.47×10^{-1}	1.90×10^{21}	83	XMM spec	B-MS	-0.07	0.66	1.15
004404.55+413159.4	$1.20^{+0.51}_{-0.03}$	0.38±0.62	9.11×10^{-1}	N/A	103	no XMM spec	B-MS	-0.36	0.38	0.60
004420.18+413408.2	$1.00^{+0.33}_{-0.02}$	0.76±0.33	3.11×10^{-2}	2.90×10^{21}	145	XMM spec	B-MS	-0.33	0.33	0.22
004356.78+413410.9	$2.20^{+0.65}_{-0.21}$	0.28±0.74	1.36×10^{-1}	4.80×10^{21}	75	XMM spec	B-MS	-0.05	0.58	1.01
004413.18+412911.4	$5.20^{+0.70}_{-1.26}$	0.71±0.38	1.06×10^{-3}	3.60×10^{21}	131	XMM spec	none	0.00	0.76	0.75
004412.04+413217.4	$5.20^{+0.77}_{-0.28}$	0.83±0.39	1.01×10^{-2}	1.40×10^{20}	126	XMM spec	none	-0.30	0.11	0.74
004336.08+413320.4	$2.20^{+0.17}_{-0.13}$	0.31±0.66	1.38×10^{-1}	5.66×10^{21}	33	XMM spec	B-SG	-0.09	0.66	0.68
004402.02+414028.8	$3.00^{+0.19}_{-0.11}$	0.20±0.87	4.33×10^{-3}	2.10×10^{21}	93	XMM spec	O-MS	0.26	0.54	0.69
004528.24+412943.9	$2.40^{+0.19}_{-0.09}$	0.68±0.43	4.04×10^{-1}	1.10×10^{21}	333	XMM spec	O-SG	-0.14	0.51	0.77
004525.67+413158.2	$2.80^{+0.19}_{-0.10}$	0.27±0.74	1.41×10^{-2}	N/A	N/A	no XMM match	O-MS	-0.10	0.72	0.78
004510.96+414559.2	$4.20^{+0.52}_{-0.06}$	0.54±0.45	1.49×10^{-3}	2.50×10^{21}	290	XMM spec	O-MS, O-SG	-0.05	0.64	1.32
004527.88+413905.5	$5.20^{+0.05}_{-0.24}$	0.57±0.46	2.52×10^{-4}	4.40×10^{21}	331	XMM spec	O-SG	0.01	0.77	1.15
004459.11+414005.1	$0.20^{+0.18}_{-0.12}$	0.85±0.35	2.36×10^{-13}	2.20×10^{21}	261	XMM spec	none	-0.08	0.50	0.63
004500.89+414309.8	$1.20^{+0.91}_{-0.04}$	0.29±0.75	10.15×10^{-1}	N/A	268	no XMM spec	B-MS	-0.04	0.67	0.30
004536.13+414702.5	$1.40^{+0.17}_{-0.11}$	1.34±0.19	8.16×10^{-4}	N/A	N/A	no XMM match	O-MS	0.13	0.78	0.12

Chandra-PHAT Name	BEAST A_V mag	PHAT A_V mag	A_V PDF	XMM N_H cm^{-2}	S18 ID	XMM Comments	Spectral Type	Chandra HR1	Chandra HR2	F110W-F160W (IR Color)
004537.84+414856.7	$1.80^{+0.88}_{-0.06}$	1.74±0.26	3.65×10^{-2}	N/A	360	no XMM spec	O-MS	-0.10	0.79	0.30
004537.67+415124.4	$1.40^{+0.17}_{-0.11}$	1.87±0.13	3.28×10^{-9}	6.90×10^{21}	358	galaxy	O-MS	0.35	0.96	0.13
004453.33+415159.5	$3.40^{+0.21}_{-0.07}$	1.17±0.22	4.25×10^{-1}	5.10×10^{21}	247	XMM spec	O-MS	0.07	0.52	0.62
004455.72+415334.6	$1.80^{+0.19}_{-0.12}$	0.82±0.34	6.03×10^{-1}	N/A	252	no XMM spec	B-MS	-0.26	0.55	0.70
004422.57+414506.5	$2.20^{+0.13}_{-0.22}$	0.41±0.59	2.47×10^{-1}	1.10×10^{21}	151	XMM spec	O-SG	-0.13	0.54	0.88
004437.96+414512.6	$1.40^{+0.14}_{-0.20}$	0.40±0.64	8.50×10^{-1}	N/A	199	no XMM spec	B-MS	-0.03	0.53	1.01
004502.33+414943.1	$1.00^{+0.20}_{-0.10}$	1.14±0.29	7.28×10^{-3}	3.70×10^{22}	272	galaxy	B-MS	0.02	0.96	0.18
004514.76+415034.5	$0.80^{+0.16}_{-0.12}$	0.54±0.55	1.58×10^{-1}	1.90×10^{21}	303	XMM spec	O-MS	-0.05	0.59	0.00
004431.82+415217.2	$2.60^{+0.19}_{-0.09}$	2.23±0.12	1.08×10^{-5}	N/A	180	no XMM spec	O-MS	0.01	0.98	0.26
004611.38+415903.9	$3.80^{+0.29}_{-0.25}$	0.80±0.35	5.56×10^{-2}	N/A	N/A	no XMM match	B-MS	0.04	0.67	1.11
004617.57+415913.6	$2.20^{+0.19}_{-0.09}$	0.47±0.53	3.15×10^{-1}	N/A	N/A	no XMM match	none	-0.18	0.41	0.55
004613.49+415043.3	$3.00^{+0.20}_{-0.08}$	0.95±0.35	3.25×10^{-1}	N/A	N/A	no XMM match	O-SG	0.03	0.73	1.00
004640.59+415422.8	$4.20^{+0.17}_{-0.23}$	0.14±1.01	3.47×10^{-5}	N/A	N/A	no XMM match	B-SG	0.01	0.65	0.95
004550.83+415835.1	$2.60^{+0.19}_{-0.10}$	0.40±0.58	7.07×10^{-2}	N/A	N/A	no XMM match	B-MS	0.08	0.86	1.12
004558.04+420302.9	$1.60^{+0.17}_{-0.11}$	0.53±0.47	8.78×10^{-1}	N/A	N/A	no XMM match	B-MS	-0.25	0.43	0.83
004543.15+415519.4	$2.80^{+0.20}_{-0.08}$	2.25±0.09	3.04×10^{-8}	N/A	N/A	no XMM match	O-MS, O-SG	0.07	0.95	0.36
004552.94+420234.0	$2.20^{+0.18}_{-0.10}$	0.64±0.44	4.98×10^{-1}	N/A	N/A	no XMM match	B-MS	-0.13	0.70	0.85
004526.67+415631.0	$3.40^{+0.11}_{-0.56}$	1.09±0.28	3.21×10^{-1}	N/A	326	no XMM spec	O-SG	-0.01	0.35	1.16
004611.85+420827.9	$4.40^{+0.29}_{-0.14}$	0.65±0.36	1.19×10^{-3}	N/A	N/A	no XMM match	B-SG	-0.03	0.63	0.90
004607.50+420855.7	$3.80^{+0.20}_{-0.41}$	0.56±0.48	9.89×10^{-3}	N/A	N/A	no XMM match	B-MS	-0.21	0.54	0.82
004612.67+421027.8	$3.00^{+0.20}_{-0.08}$	0.85±0.29	2.92×10^{-1}	N/A	N/A	no XMM match	O-MS	0.17	0.67	0.67
004630.46+421028.7	$3.20^{+0.20}_{-0.08}$	1.44±0.21	3.28×10^{-1}	N/A	N/A	no XMM match	O-MS	-0.00	0.48	0.66
004703.82+420453.0	$3.80^{+0.22}_{-0.06}$	0.26±0.75	3.16×10^{-4}	N/A	N/A	no XMM match	O-SG	0.09	0.64	1.25
004639.47+420649.2	$0.40^{+0.27}_{-0.10}$	1.04±0.27	2.91×10^{-10}	N/A	N/A	no XMM match	B-MS	-0.11	0.69	0.21
004648.19+420855.4	$3.60^{+0.21}_{-0.07}$	1.18±0.29	2.90×10^{-1}	N/A	N/A	no XMM match	B-SG	0.02	0.67	0.99
004630.68+420947.0	$3.00^{+0.26}_{-0.05}$	1.09±0.32	3.72×10^{-1}	N/A	N/A	no XMM match	B-MS	0.11	0.19	1.20
004542.25+420817.9	$1.80^{+0.18}_{-0.10}$	0.89±0.37	4.90×10^{-1}	N/A	N/A	no XMM match	B-MS	0.10	0.60	0.63
004637.22+421034.5	$0.60^{+0.21}_{-0.10}$	1.46±0.15	1.14×10^{-16}	N/A	N/A	no XMM match	O-MS	-0.16	0.65	-0.00
004652.18+421505.8	$3.20^{+0.20}_{-0.07}$	1.59±0.20	2.09×10^{-1}	N/A	N/A	no XMM match	O-MS	-0.18	0.60	1.19

Chandra-PHAT Name	BEAST A_V mag	PHAT A_V mag	A_V PDF	XMM N_H cm^{-2}	S18 ID	XMM Comments	Spectral Type	Chandra HR1	Chandra HR2	F110W-F160W (IR Color)
004648.27+420851.1	$2.80^{+0.20}_{-0.08}$	1.59±0.20	1.36×10^{-1}	N/A	N/A	no XMM match	O-MS	-0.08	0.54	1.08

Multiwavelength measurements for each source. These values were used to determine which sources from the *Chandra*-PHAT catalog are the best HMXB candidates. BEAST A_V measurements come from the BEAST SED fits. PHAT A_V measurements come from the PHAT survey dust maps by Dalcanton et al. (2015). The A_V PDF value is the probability of the BEAST A_V value given the log-normal dust distribution from the PHAT dust maps at the position of the HMXB candidate. The S18 ID and N_H values come from the Sasaki et al. (2018) XMM survey of M31. The XMM comment column contains the following information: "no match" indicates that there is no match in the XMM source catalog for the *Chandra*-PHAT source and the S18 ID for that source is listed as "NA". The XMM comment "no spec" means that there is a match in the XMM source catalog but there are not enough counts (< 100) for a spectral fit. The comment "behind M31" indicates that the XMM spectral fit classifies the source as a galaxy behind the disk of M31. Lastly, the comment "XMM spec" indicates that the XMM source corresponding to the *Chandra*-PHAT source has sufficient counts (≥ 100) for a spectral fit. The Spectral Type column indicates the most likely spectral type for the HMXB candidate companion star based off of its BEAST SED fit radius, luminosity, and effective temperature. The *Chandra* hardness ratios from the *Chandra*-PHAT catalog are listed for each source. The hardness ratios listed are HR1=(M-S)/(H+M+S) and HR2=(H-M)/(H+M+S) where S=0.35-1.0 keV, M=1-2 keV and H=2-8 keV. The F110W-F160W (IR Color) column lists the F110W-F160W near infrared color for the optical counterpart candidate for each source from the PHAT photometry catalog.

Table 4.4: Flags used to determine best HMXB candidate sample

Chandra-PHAT Name	FLAG: A_V	FLAG: XMM BG	FLAG: No Spec. Type	FLAG: Soft Chandra HRs	FLAG: FG IR Color	FLAG SUM
004350.76+412118.1	0	0	0	0	0	0
004425.73+412242.4	0	0	0	0	1	1
004452.51+411710.7	0	0	0	0	0	0
004448.13+412247.9	0	0	0	0	0	0
004359.83+412435.6	0	0	0	0	1	1
004407.44+412460.0	0	0	1	1	1	3
004454.75+411918.3	0	0	0	0	0	0
004339.06+412117.6	0	0	0	0	0	0
004352.37+412222.8	0	0	0	0	1	1
004445.88+413152.2	0	0	0	0	0	0
004412.17+413148.4	0	0	0	0	1	1
004424.80+413201.4	0	0	0	0	0	0
004357.54+413055.8	0	0	0	0	0	0
004404.55+413159.4	0	0	0	0	1	1
004420.18+413408.2	0	0	0	0	0	0
004356.78+413410.9	0	0	0	0	0	0
004413.18+412911.4	0	0	1	0	1	2
004412.04+413217.4	1	0	1	0	1	3
004336.08+413320.4	0	0	0	0	1	1
004402.02+414028.8	0	0	0	0	1	1
004528.24+412943.9	0	0	0	0	1	1
004525.67+413158.2	0	0	0	0	1	1

Chandra-PHAT Name	FLAG: A_V	FLAG: XMM BG	FLAG: No Spec. Type	FLAG: Soft Chandra HRs	FLAG: FG IR Color	FLAG SUM
004510.96+414559.2	0	0	0	0	0	0
004527.88+413905.5	0	0	0	0	0	0
004459.11+414005.1	1	0	1	0	1	3
004500.89+414309.8	0	0	0	0	0	0
004536.13+414702.5	0	0	0	0	0	0
004537.84+414856.7	0	0	0	0	0	0
004537.67+415124.4	1	1	0	0	0	2
004453.33+415159.5	0	0	0	0	1	1
004455.72+415334.6	0	0	0	0	1	1
004422.57+414506.5	0	0	0	0	0	0
004437.96+414512.6	0	0	0	0	0	0
004502.33+414943.1	0	1	0	0	0	1
004514.76+415034.5	0	0	0	0	0	0
004431.82+415217.2	0	0	0	0	0	0
004611.38+415903.9	0	0	0	0	0	0
004617.57+415913.6	0	0	1	0	1	2
004613.49+415043.3	0	0	0	0	0	0
004640.59+415422.8	0	0	0	0	0	0
004550.83+415835.1	0	0	0	0	0	0
004558.04+420302.9	0	0	0	0	0	0
004543.15+415519.4	1	0	0	0	0	1
004552.94+420234.0	0	0	0	0	0	0
004526.67+415631.0	0	0	0	0	0	0

Chandra-PHAT Name	FLAG: A_V	FLAG: XMM BG	FLAG: No Spec. Type	FLAG: Soft Chandra HRs	FLAG: FG IR Color	FLAG SUM
004611.85+420827.9	0	0	0	0	0	0
004607.50+420855.7	0	0	0	0	0	0
004612.67+421027.8	0	0	0	0	1	1
004630.46+421028.7	0	0	0	0	1	1
004703.82+420453.0	0	0	0	0	0	0
004639.47+420649.2	1	0	0	0	0	1
004648.19+420855.4	0	0	0	0	0	0
004630.68+420947.0	0	0	0	0	0	0
004542.25+420817.9	0	0	0	0	1	1
004637.22+421034.5	1	0	0	0	0	1
004652.18+421505.8	0	0	0	0	0	0
004648.27+420851.1	0	0	0	0	0	0

List of flag values used to determine best HMXB candidate sample. The values used to determine the flags are listed in Table 4.3 and a discussion of how each cutoff was determined is in Section 4.3.3.

Chapter 5

NEUTRON STARS AND BLACK HOLES IN THE SMALL MAGELLANIC CLOUD

Portions of this chapter were originally published in collaboration with B. F. Williams, A. E. Hornschemeier, V. Antoniou, G. Vasilopoulos, F. Haberl, N. Vulic, A. Zezas, A. Bodaghee, B. D. Lehmer, T. J. Maccarone, A. Ptak, D. Wik, F. M. Fornasini, Jaesub Hong, J. A. Kennea, J. A. Tomsick, T. Venters, A. Udalski, and A. Cassity in the October 2019 edition of the Astrophysical Journal (Lazzarini et al., 2019, ApJ*, Vol. 884, 2; 2019 © American Astronomical Society, DOI: 10.3847/1538-4357/ab3f32), and are reproduced below with the permission of the American Astronomical Society.*

5.1 Introduction

Population studies of X-ray binaries (XRBs) probe how the local star forming environment affects the production of black holes (BH) and neutron stars (NS), the endpoints of evolution for massive stars. Nearby galaxies provide the opportunity to combine observations of accreting BH and NS, observable as XRBs, with detailed observations of their local star forming environments. The XRB population depends on the physical properties of their host galaxies including metallicity (e.g., Basu-Zych et al., 2013, 2016; Brorby et al., 2016), star formation rate (e.g., Ranalli et al., 2003; Gilfanov et al., 2004; Mineo et al., 2012; Antoniou et al., 2010; Antoniou & Zezas, 2016; Lehmer et al., 2019), and stellar mass (e.g., Boroson et al., 2011; Zhang et al., 2012; Lehmer et al., 2010, 2017; Antoniou et al., 2019). Stars with masses greater than $\sim$8 $M_{\odot}$ – those that go on to form NS and BH at the ends of their lives – have binary fractions of at least 60% (Sana et al., 2012; Duchêne & Kraus, 2013), making the XRB phase an important evolutionary stage for a large fraction of the massive stellar populations in galaxies.

Obtaining better constraints on the formation and evolution of XRBs is key to understanding binary star evolution, the creation of binary compact-object systems detectable with gravitational waves, and to understanding the heating of the primordial intergalactic medium (IGM) out of which the first galaxies formed (e.g., Mesinger et al., 2014; Madau & Fragos, 2017; Greig & Mesinger, 2018). These topics all require information on the demographics of a population of XRBs (fraction with BH and NS primaries) and their dependence on the metallicity and star formation of the surrounding stellar population.

Completing a full population study of XRBs in the Milky Way is challenging due to the wide range of distances to these systems and reddening because of dust in the Milky Way disk. There has been some successful work (e.g., Grimm et al., 2002; Bodaghee et al., 2012; Lutovinov et al., 2013; Sidoli & Paizis, 2018), but it is difficult to survey a whole population down to a low enough L_X to observe the quiescent population of XRBs. Recent surveys of the Galactic center and Norma arm with *NuSTAR* have added to our understanding of the Galactic XRB population at hard X-ray energies (Hong et al., 2016; Fornasini et al., 2017). In extragalactic XRB populations all sources are at the same distance, allowing for accurate measurement of source luminosities.

Previous studies of Local Group galaxies with X-ray missions such as *Chandra* and *XMM-Newton* have connected the XRB populations with the ages of the stellar populations hosting them (e.g., Antoniou et al., 2009, 2010, 2019; Antoniou & Zezas, 2016; Garofali et al., 2018; Lazzarini et al., 2018; Williams et al., 2018). However, the soft ($E < 10$ keV) X-ray band alone does not allow us to distinguish among the compact-object types for an entire population of XRBs.

With the launch of the *Nuclear Spectroscopic Telescope Array* (*NuSTAR*) in 2012 (Harrison et al., 2013), we are now able to use the 4–25 keV energy range to study extragalactic populations (e.g., Wik et al., 2014; Yukita et al., 2016; Vulic et al., 2018). An entire population of XRBs can be separated into groups according to compact-object type using *NuSTAR* because of spectral differences in the hard band ($E < 10$ keV). We can distinguish XRBs with BH and NS primaries by comparing their X-ray luminosities and colors with those of Galactic XRBs of known compact-object type (Zezas et al., in preparation).

BH and NS XRBs may be further subdivided into accretion states (BHs) and by magnetic field strength (NS). As the accretion rate of a BH XRB varies, it undergoes spectral state transitions, commonly referred to as accretion states. Its X-ray luminosity and hard colors vary due to shifts in the dominant emission mechanism (for more detailed overview see e.g., Remillard & McClintock, 2006; Done et al., 2007; Tetarenko et al., 2016). NS XRBs can also be classified as accreting pulsars (high magnetic field) or low magnetic field neutron stars (Z-type and atoll-type), with these two groups separated in the X-ray intensity/hardness space. Note that accreting pulsars have harder X-ray spectra than hard state BHs in the energy range we study in this paper (e.g., Reig, 2011).

An intriguing sub-class of XRBs are the ultra luminous X-ray sources (ULXs), bright systems with isotropic luminosities that exceed the Eddington limit for a stellar mass ($\sim$10$-$20 $M_{\odot}$) BH (Kaaret et al., 2017). It was initially suggested that these systems hosted intermediate-mass BHs accreting at sub-Eddington rates, but has now been established that at least a few of them host pulsating NSs (Bachetti et al., 2014; Carpano et al., 2018; Fürst et al., 2016; Israel et al., 2017). In addition, it has been shown that the spectral properties of pulsating and non pulsating ULXs share similarities and are consistent with theoretical predictions of super-Eddington accretion onto a NS (Koliopanos et al., 2017; Walton et al., 2018). Moreover, the recent discovery of Be-XRB pulsars that have gone through major outbursts (e.g. Swift J0243.6+6124 Wilson-Hodge et al., 2018) reaching luminosities near or above 10^{39} erg/s have enabled us to investigate the spectral changes of those systems and compare them with ULXs (e.g. Koliopanos & Vasilopoulos, 2018). These studies have demonstrated that XRB pulsars that are traditionally thought as some of the harder accreting systems, can become significant softer at high accretion rates, while exhibiting a thermal like cut-off in their X-ray spectra (Koliopanos et al., 2017). Thus ULXs can be classified using any diagnostic tool developed to classify systems based on their spectral properties.

A. Zezas et al. (in preparation) have developed a diagnostic for determining compact-object type in extragalactic XRB populations using a sample of Rossi X-ray Timing Explorer (*RXTE*) Proportional Counter Array (PCA) spectra from Galactic XRBs of known compact object type. The hard X-ray coverage of *RXTE* makes these observations comparable to *NuSTAR* observations in the 4–25 keV energy band, when adjustments are made for instrument response.

The diagnostic diagrams created with X-ray colors and luminosities have been used to classify compact-objects in nearby galaxies including M83 (Yukita et al., 2016), NGC 253 (Lehmer et al., 2013; Wik et al., 2014), M33 (West et al., 2018, Yang et al. 2019, in preparation), and M31 (Yukita et al., 2017; Stiele & Kong, 2018; Lazzarini et al., 2018, D. Wik et al., 2019, in preparation). Vulic et al. (2018) applied this method to a larger sample of 12 galaxies within 5 Mpc. Here we provide *NuSTAR*-based classifications of the XRB population in the Small Magellanic Cloud (SMC). Due to the proximity of the SMC ($D = 61.9 \pm 0.6$ kpc; de Grijs & Bono, 2015), we probe to lower point source luminosities in the 4–25 keV band than other *NuSTAR* observed galaxies.

The SMC is the second closest star-forming galaxy to the Milky Way (Hilditch et al., 2005) with a well-mapped star formation history (Harris & Zaritsky, 2004; Rubele et al., 2018). Beyond its proximity and depth of study, the SMC is an interesting environment for studying XRBs because it has a comparable number of confirmed and candidate high mass XRBs (HMXBs) to the Milky Way — ∼120 compared to ∼110 — (Haberl & Sturm, 2016; Liu et al., 2005, 2006; Krivonos et al., 2012).

The low metallicity of the SMC, $Z \sim 1/5\ Z_{\odot}$ (e.g., Luck et al., 1998; Antoniou & Zezas, 2016), makes it an interesting comparison point with the XRB populations observed with *NuSTAR* in other galaxies. Metallicity has been seen to cause variations in the XRB luminosity function (Basu-Zych et al., 2016; Lehmer et al., 2019), with low-metallicity galaxies hosting more luminous HMXBs. Douna et al. (2015) found that low metallicity galaxies hosted roughly 10 times the number of $L > 10^{39}$ erg s^{-1} HMXBs seen in solar metallicity galaxies.

Of the HMXBs in the SMC, all but possibly two of the confirmed HMXBs (Maravelias et al., 2014) are known to be Be/X-ray binaries (e.g., Haberl & Sturm, 2016), where the stellar companion is an Oe or Be star. Given the high number of known HMXB systems in the SMC, there is a noticeable absence of systems with confirmed BH accretors (Liu et al., 2005). Actually, there is only one Be/X-ray binary system with a confirmed BH accretor (Casares et al., 2014), and that system is in the Milky Way. Zhang et al. (2004) have proposed that the dearth in observed BH-HMXBs may be because Be/BH binaries are transient systems with a long quiescent state. Another possibility for the scarcity of Be/BH systems is that their formation is disfavored by binary evolution (Belczynski & Ziolkowski, 2009).

Distinguishing between BH and NS XRBs is a challenging problem to which there are currently limited solutions. A NS can be confirmed if a low-mass XRB (LMXB) has a Type IX-ray burst (Lewin et al., 1993) or if pulsations are observed. BHs can be classified if their companion star has a well measured orbital period, radial velocity amplitude and constrained inclination angle, al of which allow a constraint to be placed on the compact-object mass (Orosz & Bailyn, 1997). There is of course also the new prospect of precision mass measurements via gravitational waves that can give estimations of masses indicative of NS versus BH (e.g., Abbott et al., 2016, 2017; The LIGO

Scientific Collaboration & the Virgo Collaboration, 2018); however, gravitational waves can only be detected by the LIGO detectors after the XRB phase has ended.

In this paper we present deep *NuSTAR* observations (1 Ms in total) of three fields along the SMC bar chosen to maximize the number of observed HMXBs. We present source classifications for selected sources with well constrained X-ray luminosities and hardness ratios. In Section 5.2, we describe the *NuSTAR* observations used in this work and we describe the data reduction methods used. In Section 5.3, we discuss how compact-objects were classified using their X-ray luminosities and hardness ratios. In Section 5.4, we present our results and discuss individual sources of interest. In Section 5.5, we present a brief summary of our results.

Throughout this chapter we assume a Galactic neutral hydrogen column density of 6.65×10^{20} cm^{-2} for Field 1, 4.53×10^{20} cm^{-2} for Field 2, and 6.90×10^{20} cm^{-2} for Field 3 (Dickey & Lockman, 1990, see Table 5.1 and Figure 5.1 for field locations) for converting *NuSTAR* count rates to fluxes. We assume a distance of 61.9$\pm$0.6 kpc to the SMC (de Grijs & Bono, 2015) to convert fluxes to luminosities.

5.2 NuSTAR Data & Analysis

The *NuSTAR* data were collected over three separate $15' \times 15'$ fields (see Figure 5.1) from 2017 March 12 to 2017 August 12. Fields 1 and 3 were observed in two epochs and field 2 was observed in three epochs. Observations were planned so that each field had a total exposure time of roughly 200 ks, for both focal plane modules A and B (FPMA, FPMB). Table 5.1 provides an overview of all individual observations and exposure times for each field.

The three fields that comprise this survey were chosen because of their large HMXB populations and potential for hosting elusive BH XRBs. All three fields host young stellar populations that are rich in accreting pulsars. The young stellar populations are likely to host BH XRBs, and there are two HMXBs without detected pulsations, potential BH candidates.

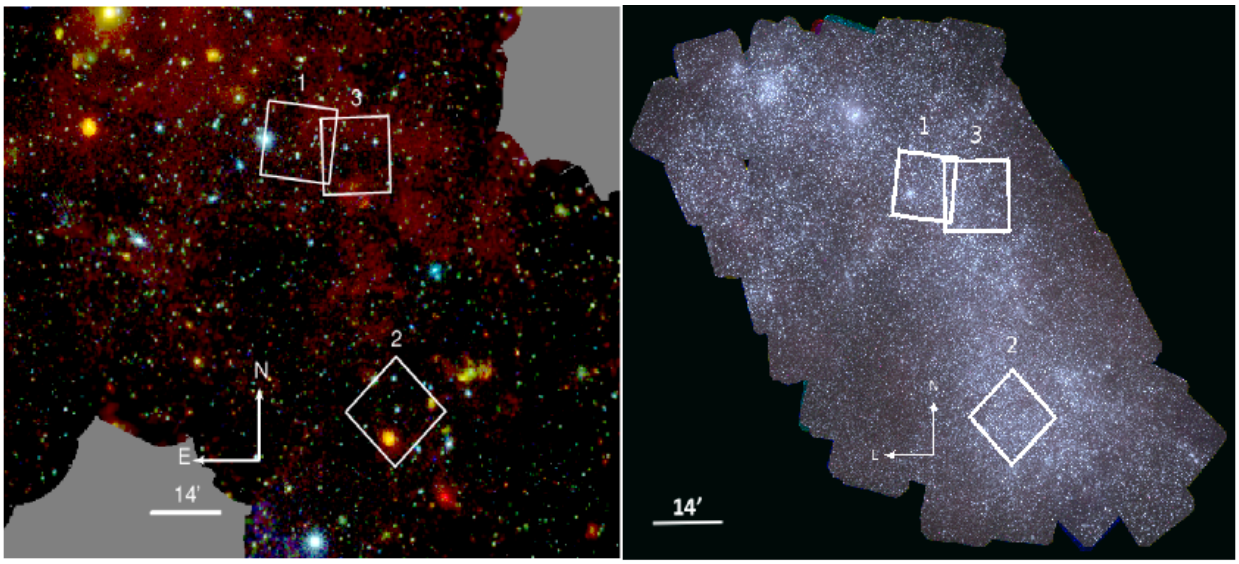

Figure 5.1 *XMM-Newton* X-ray mosaic image (left) and UV-optical mosaic image (right) of the SMC with the three fields observed by *NuSTAR* presented in this work marked. Left: The image was created by combining *XMM-Newton* observations in the direction of the nearby star-forming galaxy, available until April 2017 (Maitra et al., 2019) and following the procedure described by Haberl et al. (2012). The RGB color is composed of three energy bands 0.2-1.0 keV (red), 1.0-2.0 keV (green) and 2.0-4.5 keV (blue). Colors of point sources are characteristic of their nature, with orange being mostly SNRs, green galaxy clusters or background AGNs and blue HMXBs. Right: *Swift* ultraviolet optical telescope (UVOT) mosaic image of the Small Magellanic Cloud with the three fields observed by *NuSTAR* labeled. This RGB image was created using the following filters: blue = *uvw2*, green = *uvm2*, red = *uvw1*. The three *Swift* filters have the following central wavelengths, respectively: 1928, 2246, 2600 Å (Hagen et al., 2017). ©AAS. Reproduced with permission from Lazzarini et al. (2019).

Table 5.1. Log of *NuSTAR* Observations

Obs. ID	R.A. (J2000)	Dec. (J2000)	Field ID	Exposure Time [ks]	Date (start) yyyy mon. dd	Notes
50311001002	13.92740	–72.43900	1	137	2017 Apr 24	Stray light in FPMB
50311001004	13.82720	–72.43990	1	137	2017 Aug 12	
Field 1 Total				274		
50311002002	12.71280	–73.25750	2	284	2017 Mar 12	
50311002004	12.67640	–73.28180	2	129	2017 Jul 19	
50311002006	12.62280	–73.27560	2	46	2017 Aug 09	
Field 2 Total				459		
50311003002	13.26350	–72.48780	3	146	2017 May 03	Stray light in FPMB
50311003004	13.17230	–72.48070	3	147	2017 Aug 07	
Field 3 Total				293		

Note. — Log of *NuSTAR* observations used in this analysis. More information on stray light contamination can be found in Section 5.2.2. Listed exposure times are combined for FPMA and FPMB telescopes and contain data from good time intervals (see Section 5.2.1 for more details). The total exposure time for the two observations that had stray light contamination in the FPMB images only include the exposure time for FPMA, as the contaminated FPMB images were not included in data analysis.

5.2.1 *Initial Processing*

We reduced the *NuSTAR* observations using `HEASOFT v6.24` along with `CALDB v4.7.9`. We reprocessed Level 1 event files using the `nupipeline` tool, stopping at Level 2 and using the parameters `SAAMODE=strict` and `TENTACLE=yes` to filter out time intervals with high background due to passage through the South Atlantic Anomaly. We used the `nuproducts` tool to generate light curves for the FPMA and FPMB telescope for each observation. We inspected the light curves to confirm that the observations did not include any flares. We generated images with data from good time intervals (GTIs) in the 4-6, 6-12, 12-25 and full 4–25 keV bands using the `heasoft` tool `xselect`.

5.2.2 *Stray Light*

We inspected images for stray light contamination. The FPMB telescope images from Field 1 (obsid 50311001002) and Field 3 (obsid 50311003002) both had visible stray light contamination due to the nearby X-ray bright binary SMC X-1. We confirmed the stray light contamination using the publicly available `nustar_stray_light`[1] tool. Stray light contamination resulted in a loss of $\sim$45% of the detector area in obsid 50311001002 and $\sim$40% of the detector area in obsid 50311003002. Due to the large area lost to stray light contamination and the potential for stray light contamination beyond the regions where stray light is immediately visible by eye, the FPMB images for observations 50311001002 and 50311003002 were omitted from further analysis (background fitting, simultaneous PSF fitting) and are not included in the total exposure times listed in Table 5.1.

5.2.3 *Background Fitting*

Background fitting was done using the `nuskybgd` tool (Wik et al., 2014), which is publicly available[2]. The background emission in *NuSTAR* images comes from a combination of stray light from

[1] https://github.com/bwgref/nustar_stray_light

[2] https://github.com/NuSTAR/nuskybgd

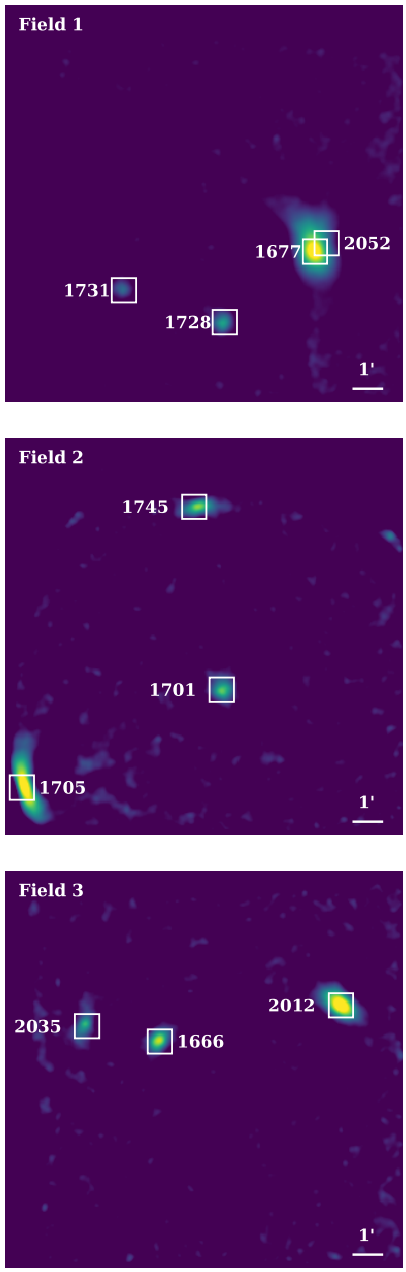

Figure 5.2 Images of the three *NuSTAR* fields 1 (top), 2 (center), and 3 (bottom) with sources that are detected above 3σ in the 4–25 keV band, marked with white boxes. These images are for display purpose only, not analysis. Images were generated by stacking the 4–25 keV images from each observation for each field. Images were then deconvolved with the *NuSTAR* PSF from CALDB v4.7.9, using publicly available code by Brian Grefenstette; https://github.com/bwgref/m51_deconvolution. ©AAS. Reproduced with permission from Lazzarini et al. (2019).

sources outside the field of view (FOV), as well as the cosmic X-ray background, instrumental background, and reflected solar X-rays. The `nuskybgd` tool fits combinations of models of the aforementioned types of emission to extracted background spectra from source-free regions in *NuSTAR* images, with the aim to model the position and energy dependent background emission to improve our source characterization. Because stray light regions were masked out of our images prior to background fitting, we only fit possible leftover stray light with the background fitting tool.

We fit the background emission in the full 4–25 keV band for each observation and separately for each FPMA and FPMB telescope image, omitting FPMB images for observations 50311001002 and 50311003002. For each module, the *NuSTAR* FOV is divided between four CCDs (0-3). To account for spatial variation in the background emission across the FOV, we fit each detector separately. We fit individual background models for each observation and the FPMA/FPMB images, which are then applied when fitting for count rates, as described in Section 5.2.4. We follow the methodology used in Vulic et al. (2018), while for a more detailed overview of the `nuskybgd` tool, see Wik et al. (2014).

5.2.4 Point Source Detection with PSF Fitting

Characterizing point source emission in crowded regions is challenging with *NuSTAR*, especially given its relatively broad point spread function (PSF) in comparison to $E < 10$ keV imaging telescopes such as *XMM-Newton* and *Chandra*. *NuSTAR*'s PSF core has a full width at half maximum of 18 and a half-power diameter of 58 (Harrison et al., 2013). In crowded regions, emission from point sources can be contaminated by the PSF wings of other nearby sources. To account for this, we fit point source count rates and hardness ratios using simultaneous PSF fitting for an input source catalog, using the method presented in Wik et al. (2014) and following the methodology outlined in Vulic et al. (2018). The steps of this PSF fitting analysis are described below.

PSF and Response File Correction

The *NuSTAR* telescope distorts the PSF into a banana shape for sources that are off axis ($\theta > 3'$) (Harrison et al., 2013; Wik et al., 2014). We use the library of *NuSTAR* PSFs as a function of

off-axis angle from the CALDB to correct for the shape distortion of source PSFs toward the edges of the FOV.

To account for energy-dependent vignetting, we generated an energy weighted vignetting function by weighting the *NuSTAR* vignetting function by a typical XRB power law spectrum. The *NuSTAR* vignetting function is highly energy-dependent (Harrison et al., 2013), with higher levels of vignetting at high energies. We used this weighted function to generate ancillary response files (ARFs) and created RMFs using the appropriate response file from the *NuSTAR* CALDB.

Astrometric Alignment

Astrometric alignment was done via PSF fitting with the input SMC *Chandra* X-ray Visionary Program (XVP) survey source catalog of Antoniou et al. (2019). The *Chandra* XVP survey observed 11 fields, identified for their young stellar populations, with 3 additional observations from the archive all to a limiting luminosity of $\sim 1.3 \times 10^{32}$ erg s^{-1} in the full (0.5–8.0 keV) band. We chose the brightest 3–4 sources in each field in the 4–25 keV band to calculate the x and y shifts between the *NuSTAR* and *Chandra* images. We performed this astrometric alignment independently for each observation and field in our sample with a mean x shift of ~ 1.1 pixels ($\sim$2.7) and mean y shift of ~ -0.5 pixels ($\sim$1.2). The shifts were then applied when performing PSF fitting in order to estimate the source count rates.

Count Rate Extraction with Simultaneous PSF Fitting

PSF fitting was performed within user-defined rectangular regions. We ensured that the edge of each fitting rectangle extended at least $1'$ on either side of the input source position to ensure that we exceeded twice the half power diameter of the *NuSTAR* PSF. When possible, we used one rectangular region to encompass the observation's FOV, but due to the roll angle of certain observations, we used multiple rectangles so that we would eliminate regions outside the FOV from the extraction regions.

For each rectangular region, we generated the axis-corrected PSFs and vignetting-corrected response files. We generated a background image using the background model produced with

`nuskybgd`. Then, a model image was produced by combining the PSFs with the background image. This model image was then fit to the data to extract count rates for each source. For a more detailed discussion of the model fitting procedure, see Section 4.3.2 from Vulic et al. (2018).

The count rates were fit in soft (S; $4-6$ keV), medium (M; $6-12$ keV), hard (H; $12-25$ keV), and full (F; $4-25$ keV) energy bands. These bands were chosen as they provide the most robust separation between types of sources on the diagnostic diagrams (Zezas et al., in preparation; Vulic et al., 2018). We calculated the significance of each source detection using the source count rate, background count rate, and exposure time. The background rate used for each source was determined with the simultaneous PSF fitting code, taking the background model (§5.2.3) into account.

We only use sources with a significance greater than 3σ in the 4–25 keV band for our source classification analysis, although we report all sources whose positions were input into our PSF fitting routine that returned lower significance measurements as upper limits. We chose the 3σ detection threshold because all sources have multi-wavelength counterparts. Specifically, we use the *Chandra* source positions for all sources from the Antoniou et al. (2019) catalog as priors on our PSF count rate fitting, so we know that all sources have previously been detected at X-ray wavelengths.

The PSF fitting code by Wik et al. (2014) assumes a default photon index of 2. To test the impact of the chosen photon index on our analysis, we ran our analysis with a photon index of 0.9 for sources associated with known pulsars and 1.7 for other sources for a subset of our 3σ sample. We found a $\ll 1\%$ difference in the output count rates and hardness ratios when compared to the output with the default photon index, which is expected as the hardness ratios are calculated using count rates rather than fluxes. Given this negligible difference in output, the count rates and hardness ratios reported in this work were all obtained with the default photon index, which allowed for more efficient data analysis. The relatively weak dependence of PSF on energy for *NuSTAR* may play an important role in this result (Madsen et al., 2015).

In addition to fitting count rates, we used the simultaneous PSF fitting routine to fit the hardness ratios for our sources. We use the technique developed by Wik et al., (in preparation) and described

in detail in Vulic et al. (2018). The hardness ratios we fit were HR1 $= (M - S)/(M + S)$ and HR2 $= (H - M)/(H + M)$. We performed simultaneous PSF fitting with the hardness ratios as free parameters. This reduces the errors associated with the hardness ratios because instead of propagating the error on the count rate measurements the HR errors are calculated independently.

We input 50 *Chandra* source positions for simultaneous PSF fitting with 0.5–8.0 keV luminosities down to $\sim 5 \times 10^{33}$ erg s^{-1} (Antoniou et al., 2019). The luminosity limit for the input *Chandra* sources was determined by iterating the PSF fitting routine and adding in $\sim$3 *Chandra* sources in descending luminosity order each time the code was run. We first input only the brightest few *Chandra* sources that were easily visible in the 4–25 keV *NuSTAR* images (see Figure 5.2, and then added about 3–5 sources at a time until additional sources were not detected. We list the positions, count rate in each band, hardness ratios, exposure time, and background count rate for all 50 sources for which we attempted to fit count rates in Table 5.2. These measurements merge all the observations for each field.

We also ran the PSF fitting routine for each individual observation in order to determine source variability and compare with the quasi-simultaneous *Swift-XRT* observations. We list the count rates and hardness ratios for each source with greater than 3σ significance from each observation in Table 5.3.

5.2.5 Using Simultaneous Swift-XRT Observations to Test PSF Fitting in Crowded Regions

As part of the SMC *NuSTAR* Legacy observation program, deep observations of the *NuSTAR* fields presented in this paper were taken with the Neil Gehrels *Swift-XRT* Observatory (*Swift-XRT* , Gehrels et al., 2004) X-ray Telescope (XRT, Burrows et al., 2005) (PI: V. Antoniou). The *Swift-XRT* observations were quasi-simultaneous with our *NuSTAR* observations, taken between 0 and 7 days apart (see Figure 5.6). Data were retrieved from the *Swift-XRT* data center[3], and were analyzed using standard procedures as outlined in Evans et al. (2007, 2009), and briefly summarized below.

[3] http://www.swift.ac.uk/

Swift-XRT data were reduced using the `xrtpipeline` (v0.13.4), that can be found in HEASoft 6.23 software[4]. Clean events were extracted with the HEASoft FTOOLS (Blackburn, 1995), by using the command line interface `xselect`. Source detection was performed using the command line interface `ximage`. Only sources with significance above 3 σ were selected. The complete observing log can be found in Table 5.4. We present the count rates for each source by observation in Table 5.5.

We used the quasi-simultaneous *Swift-XRT* observations to determine how effective our simultaneous PSF fitting code was in extracting count rates for sources in crowded regions. We selected two crowded regions within Field 1 (the regions surrounding sources 1677 and 1728; see Figure 5.3), and performed simultaneous PSF fitting for all *Chandra* sources with 0.5-8.0 keV flux above 5×10^{33} erg s^{-1} within $\sim$0.5′ of the brightest central source. Then we performed PSF fitting again, only including *Chandra* sources that had also been detected in the *Swift-XRT* observations.

We found that the measured count rate and hardness ratios for source 1677 did not shift drastically when surrounding sources within 30″ that were not detected by *Swift-XRT* were removed from the input *Chandra* source list used in PSF fitting. Source 1677 was detected with $\sim 342\sigma$ significance in the full 4–25 keV *NuSTAR* band. Source 2052 was detected by *NuSTAR* with ~ 11 σ confidence in the full 4–25 keV band, but not detected by *Swift-XRT*. When we removed source 2052 from our input source list and re-performed PSF fitting to extract the count rate for source 1677, we found that the 4–25 keV count rate measured for source 1677 increased by only $\sim 2\%$. Similarly, when we re-fit for the hardness ratios of source 1677 when source 2052 was removed, we found that both HR1 and HR2 decreased by $\sim 1\%$ and $\sim 2\%$, respectively.

We performed the same experiment with source 1728, which was detected by *NuSTAR* with $\sim$11σ significance in the 4–25 keV band, and in the *Swift-XRT* observations. Source 1726 is located roughly 30″ away from source 1728, and was not detected in the *Swift-XRT* observations. Source 1726 was not detected with a $\sim$1σ upper limit in the 4–25 keV band by *NuSTAR*. When we removed source 1726 from our input source list and re-fit for the count rate and hardness ratios for

[4](Blackburn et al., 1999) `https://heasarc.nasa.gov/lheasoft/`

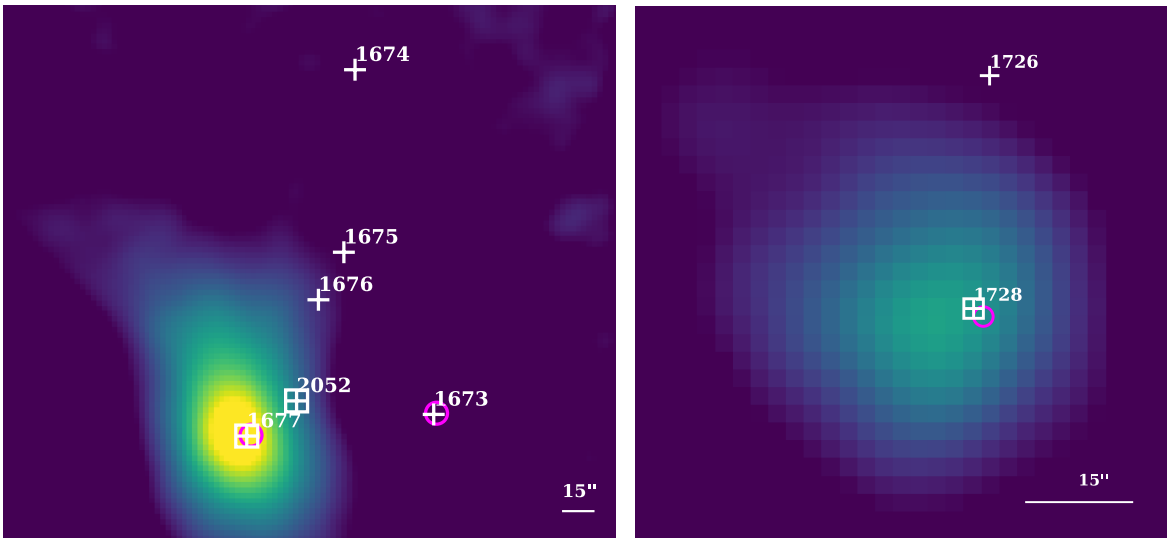

Figure 5.3 Zoom in of 4–25 keV band deconvolved image of Field 1 shown in Figure 5.2. Sources for which we obtain upper limits with our *NuSTAR* observations are marked with white crosses. Sources that were detected by *NuSTAR* above 3σ significance in the 4–25 keV band are marked with a white box and white cross. Magenta circles indicate source detections by *Swift-XRT*. Each circle indicates the average position of the *Swift-XRT*-detected source, weighted by exposure time for each observation. To test how well our PSF fitting code retrieved source count rates and hardness ratios in crowded regions, we first fit for all sources in our input *Chandra* source catalog with 0.5-8.0 keV luminosities above 5×10^{33} erg s^{-1}. Next, we only fit for sources that were also detected by *Swift-XRT* (marked with magenta circles) and compared the output count rates and hardness ratios. We found that the difference in the measured count rates and hardness ratios for the brightest sources in each region (1677 in the left panel and 1728 in the right panel) shifted by 7% or less.

source 1728, we found that the measured 4–25 keV count rate for source 1728 increased by $\sim 7\%$, while HR1 increased by $\sim 3\%$ and HR2 decreased by $\sim 4\%$.

We found that 4–25 keV count rates and hardness ratios for the brightest sources in the two crowded regions we tested changed by 7% or less when we omitted input sources that were not detected in the *Swift-XRT* observations. We conclude that the PSF-fitting routine was not significantly overfitting the bright sources, and therefore we included all *Chandra* sources with 0.5-8.0 keV luminosity above $\sim 5 \times 10^{33}$ erg s^{-1} in our input source list to allow the PSF-fitting routine to deconvolve confused sources to the maximum extent possible.

5.2.6 NuSTAR Timing Analysis

We looked for pulsations in the observations of our 10 sources that were detected above 3σ significance. We performed analysis for each source using the cleaned combined FPMA and FPMB event list for all observations of each source's field (see Table 5.1). For each source we produced a trimmed event file, including all counts within a 20 pixel ($\sim 50''$) radius of the source position and selected event corresponding to 4–25 keV photon energies. For the period search we used barycenter corrected event times (barycenter correction was done with the `barycorr` tool from `FTOOLS`). We performed an epoch folding (Leahy et al., 1983) test to search for pulsations of each detected system. The test was implemented through `python` by using `stingray` and `HENDRICS` (Huppenkothen et al., 2019). We initially searched all event files for a periodic signal over a broad range of frequencies from 0.001 - 1 Hz. This was done using the HENzsearch tool. Once a candidate periodic signal was determined, we performed another search within a smaller range around the candidate frequency to get a more precise value, while also fitting a Gaussian curve to the best-fit frequency in order to estimate uncertainties. Upon determining a periodic signal we folded the events using the best fit period in order to obtain pulse profiles with 16 bins over a complete pulse phase. We then determined the maximum ($R_{\rm M}$) and minimum ($R_{\rm m}$) values of the pulse profiles and calculated the pulsed fraction as $PF = (R_{\rm M} - R_{\rm m})/(R_{\rm M} + R_{\rm m})$. For systems where no significant period was detected we determined a upper limit for the PF that would have resulted in a 3σ detection.

We were able to confirm pulse periods for all six pulsars in our sample at an above 3σ significance level. Moreover, we detected a pulse period from a candidate HMXB, thus confirming the nature of the compact object. All period detections had a significance above 3σ. Given the long baseline of the *NuSTAR* observations we have also performed an accelerated epoch folding test to search for period derivative (e.g. see Vasilopoulos et al., 2018); all period derivatives were consistent with zero ($|\dot{\nu}| < 10^{-11}$). We note that for source 2052, we were not able to measure a pulse period due to high background emission from the nearby and much brighter source 1677.

We list the results of our timing analysis for each source in their individual subsections in Section 5.4. We present a summary of the pulse periods we measured for each pulsar during each observation along with their published pulse periods in Table 5.6.

5.3 Source classification

We classify XRBs in the SMC by comparing their X-ray luminosities and hardness ratios with those of Galactic XRBs with known compact-object types. The diagnostic diagrams that were used to classify each source are presented in Figures 5.10–5.18, which plot the position of each source on the hardness-intensity and hardness ratio diagrams during each epoch of observation. For a more general overview of our sample, we also present a set of diagnostic diagrams where we plot count rate and hardness ratios for each source when all epochs of observation are combined in Figure 5.4. We note that due to variability between observations, we do not use the combined diagram (Figure 5.4) for our source classification.

The Galactic XRBs used in the diagnostic diagrams were observed with RXTE, not *NuSTAR*, and their count rates were corrected for the different responses of the two missions. This method was developed by Zezas et al. (in preparation) and has been used previously to classify compact-objects in NGC 253 (Wik et al., 2014), M83 (Yukita et al., 2016), M31 (Chapter 3, Lazzarini et al., 2018), Holmberg II, IC 342, M82, M81, NGC 4945, Holmberg IX, Circinus, NGC 1313, and NGC 5204 (Vulic et al., 2018). With better statistics, we can use the full spectra to gain even more information, separating black holes and neutron stars effectively (Maccarone et al., 2016).

Beyond classifying an XRB as having a black hole or neutron star primary, we can further

classify black holes by accretion state (soft, intermediate, hard). The difference in spectrum can be used to infer changes in the dominant emission mechanism in each state. For black holes in the hard state, emission is dominated by a power law component from the optically thin region inside of and around the optically thick accretion disk. In the soft state, softer thermal blackbody emission from the optically thick disk dominates. The intermediate state is a shorter-lived transient state between the soft and hard states during which the luminosity remains fairly constant while the hardness ratio shifts. These differences in emission spectra allow hardness ratios, in combination with full band luminosities, to be used to discriminate between different black hole accretion states (e.g., Remillard & McClintock, 2006)

Pulsars and Z-track NS XRBs are also included in the hardness-intensity diagnostic diagram. Low magnetic field neutron stars inhabit a narrow region of the hardness-intensity diagram, varying mostly in luminosity rather than X-ray color. Accreting pulsars generally exhibit harder X-ray spectra than even hard state black holes – with a power law index of approximately 1 – allowing for their separation from accreting black holes in hardness ratio parameter space (White et al., 1983). Low magnetic field neutron stars sources have softer X-ray spectra than pulsars (Hasinger & van der Klis, 1989).

The differences in hardness and luminosity in different black hole accretion states and neutron star types allows us to use these parameters to classify XRBs of unknown compact-object type. To create a diagnostic tool that can be used for *NuSTAR* sources, A. Zezas et al. (in preparation) completed spectral fitting for 6 BH-XRBs and 9 accreting pulsars using over 2500 RXTE PCA observations (Sobolewska et al., 2009; Reig, 2011). Different spectral models were applied to these spectra depending on their accretion state (i.e. the contribution of the thermal and power law components). These spectral models were then used to predict each source count rate in the S, M, H, and F *NuSTAR* bands. The 4–25 keV energy range used in our *NuSTAR* observations falls within the energy range of the RXTE-PCA spectra, ensuring that the spectral models can adequately predict the *NuSTAR* count rate in this energy range.

To classify the sources in the SMC, and thus determine the compact-object type, we examine their position on the diagnostic diagrams (Figures 5.10–5.18), taking their error bars into account.

For sources with error bars spanning multiple compact-object types, we list all possible compact-object types/states. All sources have two or three epochs of observation, which we plot separately on the diagrams to account for variability in both count rate and hardness ratios between observations. For sources with significant variability, we list source classifications consistent with all epochs of observation. We summarize our classifications in Table 5.7.

We note that because the field of view covered for this survey is much larger than for previous extragalactic *NuSTAR* surveys, the rate of background AGN in our observations is likely to increase. We discuss one likely background AGN in our sample in §5.4.5.

5.4 Results & Discussion

The deep *NuSTAR* observations of 3 fields along the Small Magellanic Cloud Bar, resulted in a catalog of 10 sources with greater than 3σ significance (4–25 keV) and 40 additional sources with upper limits on the count rate. Table 5.7 provides our tentative classifications of the source compact-object types based on their hardness ratios and hard X-ray luminosities. We plot sources on the diagnostic diagram using their count rates and add the luminosity axis assuming a power law model with a photon index of 1.7 and the mean Galactic column density from all three fields (see §5.1).

5.4.1 Comparison with Archival XMM-Newton Observations

When performing PSF fitting to measure *NuSTAR* count rates for sources in our observed fields, we used as priors the *Chandra* source catalog from Antoniou et al. (2019) for initial source positions. We used input sources down to $\sim 5 \times 10^{33}$ erg s^{-1} in the 0.5-8.0 keV *Chandra* band, which corresponds to $\sim$ 15 times below our *NuSTAR* detection limit, correcting for bandpass differences. Of the 50 source positions we input into our PSF fitting routine, 10 sources had measured count rates above the 3σ detection limit, while 40 sources were non-detections and are presented as upper limits.

We investigated whether the sources that were not detected in our *NuSTAR* observations would have expected 4–25 keV fluxes below our detection limit based on their independent flux mea-

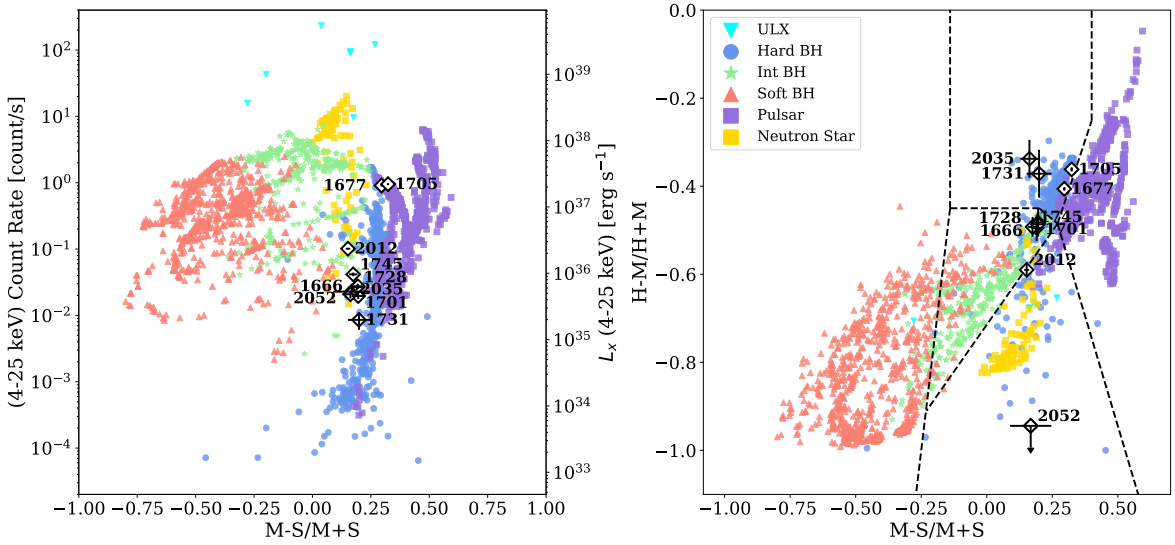

Figure 5.4 Hardness-intensity diagram and hardness ratio plots for *NuSTAR* sources combining all epochs of observation for each field. This figure is used to give an overview of the sources in our sample. To classify our sources we used diagnostic diagrams with each epoch of observation plotted separately for each source in order to account for variability between observations (see Figures 5.10-5.18). Colored points are Galactic *RXTE-PCA* observations of accreting black holes, pulsars and low-magnetic field neutron stars (Zezas et al., in preparation). White diamonds with black outlines and error bars indicate SMC sources with $\geq 3\sigma$ detection in the full 4–25 keV *NuSTAR* band. Black dotted lines show empirical boundaries between different compact-object types in color-color space, following Vulic et al. (2018). We note the small error bars on the sources in our sample due to the large number of source counts. The lowest luminosity source in our 3σ significance sample has $\sim$1500 net counts in the 4–25 keV band while the brightest sources have over 100,000 net counts. The error bars plotted represent 0.4 to 10% errors in the 4–25 keV count rates. Note that source 1705 is a combination of two pulsars: previously confirmed SXP15.3 and the newly confirmed pulsar SXP305, which is presented in this paper. See §5.4.6 for more details.

surements in other energy bands with another telescope. In order to determine whether we would expect non-detections for these sources, we cross matched our *NuSTAR* source catalog with the *XMM-Newton* survey of the SMC (Sturm et al., 2013a). We positionally cross matched sources within 5″. We find 38 matches between the Sturm et al. (2013a) catalog and our full *NuSTAR* catalog, including sources with upper limits on *NuSTAR* flux. In Figure 5.5 we plot the 0.2-12 keV flux measured by *XMM-Newton* (Sturm et al., 2013a) against our measured 4–25 keV flux (or upper limits on flux, where applicable).

Black points in Figure 5.5 are our 3σ detections and sources plotted in red are 1 σ upper limits on flux from our *NuSTAR* observations. We plot a horizontal blue line that indicates the flux limit for a 3σ detection. The gray region on our diagram indicates the upper limits on flux that are consistent with measurements of zero counts from a source. We perform PSF fitting at the location of all input *Chandra* sources, so we obtain either a measured or a zero count rate detection for each source, with errors. The upper limits within the gray region show the upper errors on a zero count rate measurement. We note that sources within the gray region correspond to non-detections, while red sources outside of the gray region may potentially be detected at very low significance. The scatter in the upper limit values for the low signal to noise detections is expected scatter in these measurements.

We also include lines indicating the relationship between 0.2-12 keV flux and 4–25 keV flux for various spectral models by using `XSPEC v. 12.10.0c`. The first four lines in the legend assume a simple power law model with a hard power law index (0.9) and softer power law index (1.7) and high Galactic absorption (4×10^{21} cm^{-2}) and low Galactic absorption (6×10^{20} cm^{-2}). The fifth line indicates the predicted 4–25 keV flux assuming the `compmag` model in `XSPEC`. The `compmag` model is used by Ballhausen et al. (2017) to fit the 4–25 keV *NuSTAR* spectrum of a low luminosity pulsar observed with *NuSTAR*, A 0535+26. The model is cited as a more physical, rather than empirical, fit to a low luminosity pulsar spectrum. It includes cylindrical accretion onto a magnetized neutron star, including different velocity profiles and the second-order bulk Comptonization term in scattering calculations. We list the conversion factors that were used to generate the lines for each spectral model shown in Figure 5.5 in Table 5.8.

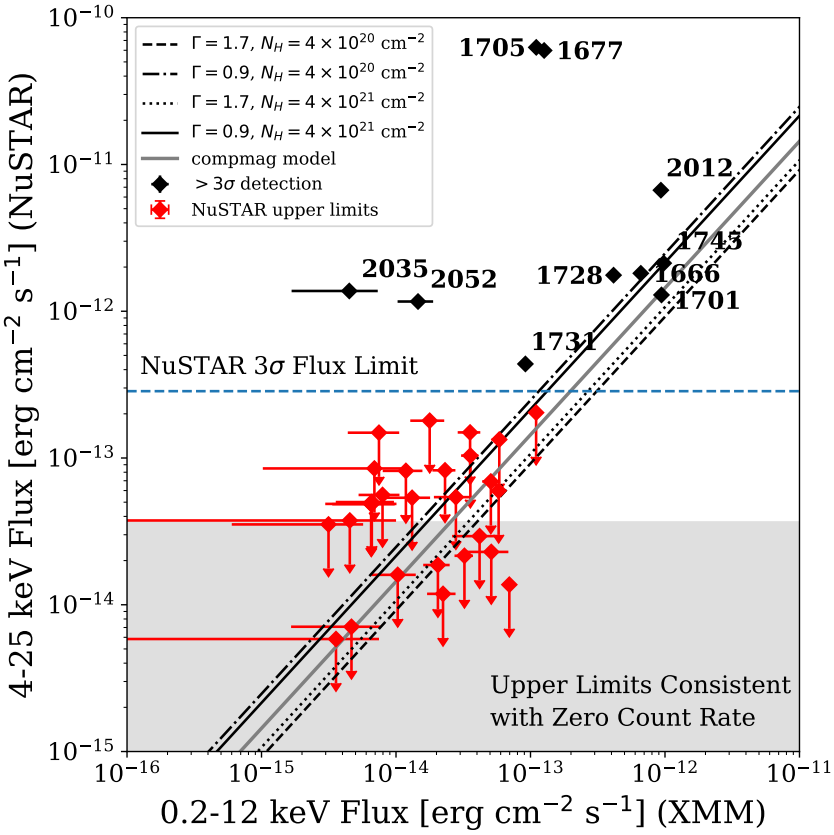

Figure 5.5 We compare measured 4–25 keV *NuSTAR* source fluxes (combining all observations FMPA + FPMB data, omitting FPMB telescope for observations with stray light noted in Table 5.1) and source flux upper limits with their 0.2-12 keV fluxes measured by *XMM-Newton* (Sturm et al., 2013a). Black points indicate sources with greater than 3σ significance for their 4–25 keV count rates. Red points indicate the 1σ upper limits for sources below the 3σ detection limit. The horizontal blue line indicates the 3σ flux limit for our observations. The gray shaded region indicates upper limits corresponding to zero measured count rate. We note that the spread in the upper limits of the red points corresponds to the expected scatter of low signal to noise measurements for these sources. The diagonal lines represent the relationship between 4–25 keV and 0.2-12 keV flux for various spectral models. The first four models in the legend assume a simple power law with the given photon index and Galactic column density. The fifth model represents a more physically motivated model for a low luminosity pulsar observed with *NuSTAR* by Ballhausen et al. (2017). For more details on the comparison between *NuSTAR* and *XMM-Newton* flux measurements, see §5.4.1. Note that source 1705 is a combination of two pulsars: previously confirmed SXP15.3 and the newly confirmed pulsar SXP305, which is presented in this paper. See §5.4.6 for more details.

We expect non-detections for all red sources in Figure 5.5 in the 4–25 keV *NuSTAR* band because their 0.2-12 keV fluxes measured by Sturm et al. (2013a) suggest that their 4–25 keV fluxes are below our detection limit for all spectral models. We note that several of our $>3\sigma$ sources have higher than expected 4–25 keV *NuSTAR* fluxes, for all spectral models. This difference is likely due to source variability.

5.4.2 Classifying Low Luminosity HMXBs

Many of the hard X-ray sources we detected in this sample are spatially coincident with confirmed pulsars within 5″. In our classifications listed in Table 5.7, many of our sources have luminosities and hardness ratios consistent with multiple compact-object types, including accreting black hole primaries. Sources 1728, 1701, 1666, 2012, and 2035 are found in regions of the diagnostic diagrams (Figures 5.14, 5.12, 5.10, 5.17, 5.18) consistent with multiple compact-object types - yet all of these XRBs are associated with known X-ray pulsars (Haberl & Sturm, 2016). Hereafter, we refer to these sources as inconsistent pulsars, as relates to the *NuSTAR* hardness-intensity diagram.

The SMC presents a unique opportunity to observe low-luminosity accreting pulsars. Given its proximity, we are attempting to classify XRBs in the SMC at lower luminosities than has been possible in previous extragalactic *NuSTAR* studies. Previous work in M31 had a 4–25 keV luminosity limit of $\sim 3 \times 10^{36}$ erg s^{-1} (Wik et al., in prep.; Lazzarini et al., 2018) and more distant galaxies surveyed by Vulic et al. (2018) had 4–25 keV luminosity limits of at least 1×10^{37} erg s^{-1}.

The low-luminosity ($L_{4-25keV} < 1 \times 10^{37}$ erg s^{-1}) pulsars we observe tend to have softer $(M-S)/(M+S)$ hardness ratios than the Galactic accreting pulsars used to generate the diagram. There are many proposed differences between the HMXB populations at solar (Galactic) and sub-solar metallicity (SMC). Population synthesis studies predict that metallicity may affect HMXB populations in different ways. It has been suggested that at lower metallicity, HMXB populations may be more luminous due to hosting more massive compact objects (Dray, 2006; Fragos et al., 2013), have a higher fraction of Roche lobe overflow systems, and a different ratio of Be versus supergiant stellar companions (Linden et al., 2010). The underlying cause of these predicted differences between solar (Galactic) and sub-solar metallicity (SMC) HMXBs is the fact

that lower-metallicity stars exhibit weaker radiatively driven winds.

Looking at the hardness ratio diagram (Figure 5.4, right panel), the $(H-M)/(H+M)$ colors of sources 1728, 1666, 1701, 2012, and 2035 all fall within roughly -0.3 and -0.6, a range that matches the Galactic pulsars used in the diagnostic diagram. The only difference appears in the $(M-S)/(M+S)$ hardness ratio. All of our inconsistent low-luminosity pulsars have a $(M-S)/(M+S)$ hardness ratio of ~ 0.2, while the Galactic accreting pulsars have slightly higher hardness ratios ranging from ∼0.3-0.5. As we describe in the next two sections, we cannot explain this inconsistency with X-ray variability. We also discuss in more detail the HMXB candidates that were detected above 3σ significance that do not have confirmed pulsations in §5.4.4. We have also thoroughly investigated whether source confusion or mis-matching might give rise to these differences. The overall good matching of *XMM-Newton*, *NuSTAR*, and *Swift-XRT* flux indicates we have identified the correct source matches.

5.4.3 Highly Variable Sources

Several of our high significance *NuSTAR* sources have higher 4–25 keV fluxes than extrapolated from their 0.2-12 keV fluxes measured with *XMM-Newton* by Sturm et al. (2013a), as shown in Figure 5.5. The *XMM-Newton* and *NuSTAR* observations were not simultaneous. *XMM-Newton* observations were taken between 2000 and 2009 while *NuSTAR* observations presented in this paper were taken in 2017.

To confirm that these flux differences are due to variability, we compare our *NuSTAR* measurements with the quasi-simultaneously measured 0.2-10 keV count rates from *Swift-XRT*. We positionally matched sources detected in each *NuSTAR* observation with sources detected in each *Swift-XRT* observation within $10''$.

Nine of our ten 3σ sources were detected in the quasi-simultaneous *Swift-XRT* observations. For more details on the *Swift-XRT* observations and data reduction, see §5.2.5. Only one of our 3σ *NuSTAR* sources was not detected by *Swift-XRT*, source 2052. Source 2052 is a likely background AGN (see §5.4.5), so it is likely more luminous at the higher energy range probed by *NuSTAR* (4–25 keV) than *Swift-XRT* (0.2-10 keV) due to photoelectric absorption.

In Figure 5.6, each point indicates a pair of quasi-simultaneous measurements of a source's count rate by *NuSTAR* (4–25 keV) and *Swift-XRT* (0.2-10 keV). Each point is labeled with the source number and is color coded by the time separation between the *NuSTAR* and *Swift-XRT* observations. We list the count rates and hardness ratios measured for our 3σ sources during each *NuSTAR* observation in Table 5.3. We list the 0.2-10 keV count rates for each source detected by *Swift-XRT* in Table 5.5. In Figure 5.6 we also include lines that show the relationship between *NuSTAR* 4–25 keV count rates and *Swift-XRT* 0.2-10 keV count rates for sources assuming various spectral models. Most of our sources fall along the two lines for $\Gamma = 0.9$, expected for accreting pulsars.

We note that some of the *Swift-XRT* and *NuSTAR* observations that we compare in this figure were taken up to 7 days apart, with a median time separation of 1 day. This quasi-simultaneity makes it harder to directly compare the 0.2-10 keV count rates measured by *Swift-XRT* and the 4-25 keV count rates measured by *NuSTAR*. Differences in the measured count rates could be due to source variability if the observations are not truly simultaneous.

Figures 5.10–5.18 show hardness-intensity and hardness ratio diagrams indicating the location of each source on the diagram during each observing epoch to investigate spectral shifts and variability between epochs. We include one diagram for all of our 3σ sources except source 2052, which was not detected with high enough significance in each individual observation to produce good hardness ratio measurements.

In the following sections we describe several sources that demonstrated significant variability when we compare their *NuSTAR* and *Swift-XRT* fluxes to those measured with *XMM-Newton* in the Sturm et al. (2013a) catalog.

Source 1705 - Detection of two Be-XRBs

Source 1705 falls along the boundary between the hard state black hole and pulsar loci on our diagnostic diagrams (Figure 5.13) during each epoch of observation. Source 1705 is $0.5''$ away from CXO J005215.4–731915, listed as source 93 in Haberl & Sturm (2016), and $7.5''$ away from the known pulsar SXP15.3. Based on the results of our timing analysis (see §5.4.6) we suggest

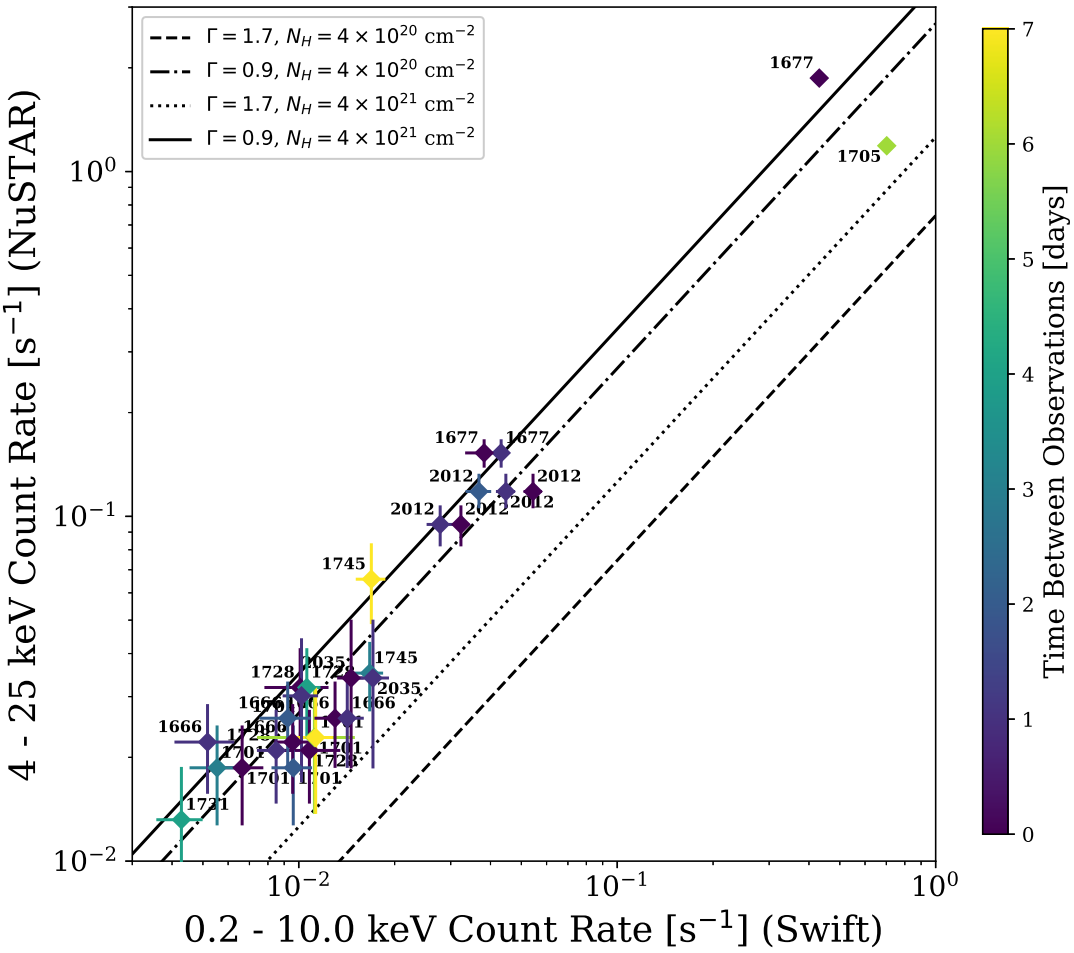

Figure 5.6 We compare measured 4–25 keV *NuSTAR* source count rates (combining FMPA and FPMB data, omitting FPMB telescope for observations with stray light noted in Table 5.1) and quasi-simultaneously measured 0.2-10 keV count rates from *Swift-XRT*. Each point represents a pair of roughly simultaneous observations, color coded by the time between observations in days. Sources are labeled with their Source IDs as listed in Table 5.2. Note that most sources are plotted more than once. Each point represents an individual observation. The count rates for each individual observation used to create this diagram are listed in Table 5.3. Lines on the plot represent the relationship between the *NuSTAR* 4–25 keV count rate and the *Swift-XRT* 0.2-10 keV count rate assuming different power law spectral models, as described in the legend. Only sources that were detected by *Swift-XRT* are plotted here. Note that source 1705 is a combination of two pulsars: previously confirmed SXP15.3 and the newly confirmed pulsar SXP305, which is presented in this paper. See §5.4.6 for more details.

that during the first observation of source 1705 in March 2017 we detected flux predominantly from CXO J005215.4–731915 and during the next two observations in July and August 2017 we detected flux mostly from SXP15.3.

SXP15.3 was found in outburst starting in July 2017 as part of the S-CUBED survey with *Swift-XRT* (Kennea et al., 2018). In November 2017 Ducci et al. (2017) observed the source in outburst. Maitra et al. (2018) observed the source in late 2017 with both *NuSTAR* and *Swift-XRT* simultaneously and measured a 3–80 keV luminosity of $\sim 10^{38}$ erg s^{-1}. We obtained three *NuSTAR* observations of this source in March, July, and August 2017, respectively (see Table 5.3).

The outburst evolution of SXP15.3 found in the literature matches the flux variations seen in our observations. During the first epoch of our observations in March 2017, the 4–25 keV luminosity of source 1705 was $\sim 1 \times 10^{36}$ erg s^{-1}. By the second and third epochs in July and August 2017, source 1705's $4 - 25$ keV luminosity had increased to $3 - 4 \times 10^{37}$ erg s^{-1}. Our observations did not continue through the end of 2017, when SXP15.3 reached the peak of its outburst.

We note that CXO J005215.4–731915, located within $0.5''$ of the *NuSTAR* position, was in outburst during the first epoch of our observations in March 2017. CXO J005215.4–731915 is a high confidence Be-XRB with a typical X-ray spectrum and an early-type optical counterpart (Haberl & Sturm, 2016).

Our timing analysis of source 1705 revealed interesting results, depending on the epoch analyzed. During the first observation (obsid 50311002002) taken in March 2017, we detected pulsations with a period of $\sim$305 seconds. We suggest that during this first observation, what we were observing is associated with CXO J005215.4–731915 and that we are able to confirm it as Be-XRB pulsar. During the second and third observation epochs (obsids 50311002004, 50311002006) in July and August 2017 we detected a period of 15.3 seconds, which matches SXP15.3. We can not exclude that we were detecting flux from both Be-XRBs, CXO J005215.4–731915 and SXP15.3, with the flux from SXP15.3 dominating during the second two epochs when that source was known to be in outburst.

Source 1677 - Detection of SXP59.0

Source 1677 is associated with known pulsar SXP59.0 (RX J0054.9−7226), with noted X-ray variability in the literature (Haberl & Sturm, 2016). We measured a pulse period of 58.8 seconds using an averaged power spectrum (see Section 5.2.6 for more details on pulse fitting).

Source 1677 has a 4–25 keV flux roughly two orders of magnitude greater than would be expected given its 0.2-12 keV flux measured with *XMM-Newton*, as shown in Figure 5.5. Its 4–25 keV luminosity also decreased by roughly one order of magnitude between our two epochs of observation, April and August 2017.

Source 1677 lies in regions of the diagnostic diagram that overlap with pulsars, hard state black holes, intermediate state black holes, and non-magnetized neutron stars. Between the first observing epoch in April 2017 and August 2017, source 1677 became less luminous, and its spectrum became softer in both the $(M-S)/(M+S)$ and $(H-M)/(H+M)$ colors.

Source 1677 matches to source 63 in Sturm et al. (2013a) within 0.8″. Sturm et al. (2013a) note that this source demonstrates significant short-term variability in the 0.2-12 keV band. Haberl & Sturm (2016) cite that SXP59.0 has a ratio of 840 between its maximum and minimum X-ray flux presented in the literature. This extreme variability would account for the excess flux we see in our *NuSTAR* observations compared to the *XMM-Newton* observations from Sturm et al. (2013a).

Source 1677 was also detected in two *Swift-XRT* observations within one day of the *NuSTAR* observations. Both 0.2-10 keV count rate measurements by *Swift-XRT* agree with the 4–25 keV count rate measured simultaneously by *NuSTAR* assuming a hard ($\Gamma \sim 0.9$) power law model. Kennea et al. (2017, 2018) discovered that SXP59.0 was in outburst in April 2017 with *Swift-XRT* observations, part of the S-CUBED survey. The 4–25 keV luminosity we measure with *NuSTAR* also shows this source in outburst(4–25 keV $L_X \sim 10^{38}$ erg s^{-1}).

Source 2035 - Detection of SXP46.6

Source 2035 is associated with known pulsar SXP46.6 (XTE J0053−724) noted in Haberl & Sturm (2016). It also presents a higher measured 4–25 keV flux with *NuSTAR* than we would expect given

its 0.2-12 keV flux measured with *XMM-Newton* by roughly a factor of 100.

Source 2035 matches to source 1828 in Sturm et al. (2013a) within 1.5″. Sturm et al. (2013a) do not note this source as having significant short-term X-ray variability. However, Haberl & Sturm (2016) give a ratio between the maximum and minimum 0.2-10 keV flux in the literature for this source of 1300, suggesting that it is highly variable.

The system had a luminosity of a few $\times 10^{35}$ erg s^{-1} during the first observation (obsid 50311003002) in May 2017 but reached a luminosity of close to 10^{36} erg s^{-1} in August 2017. We were able to confirm pulsations with a pulse period of 45.98 seconds only in the second *NuSTAR* observation. During the first observation a periodic signal of ∼58.8 s was derived from the extracted event files. We interpret that this signal is due to contamination from the nearby pulsar SXP 59 that is only ∼4.5away from the center of the extraction region. We note that SXP46.6 did not have detected pulsations in the *Chandra* X-ray Visionary Program survey (Hong et al., 2017) when it was observed in 2006.

Source 2035 was detected in our *Swift-XRT* observations (see Figure 5.6) taken within one day of the *NuSTAR* observations. The *Swift-XRT* flux measured for this source agrees with our measured *NuSTAR* flux assuming a power law model with a photon index of 0.9. Given that both its soft X-ray flux measured with *Swift-XRT* and hard X-ray flux measured with *NuSTAR* are higher than would be expected from the soft X-ray flux measured with *XMM-Newton* in Sturm et al. (2013a), this highly variable source was likely caught in an outburst during the *NuSTAR* observations.

Source 2035's position on the diagnostic diagrams (Figure 5.18) changes between its two epochs of observation. In May 2017 its position on the hardness-intensity diagram straddles the loci associated with pulsars and hard state black holes, in a low-luminosity region of the diagram with few points associated with pulsars. In August 2017 its luminosity was higher and it moved to a region consistent with hard state black holes. Its position in the hardness ratio diagrams favors a hard state black hole classification but does not rule out a pulsar classification, particularly in the hardness-intensity diagram.

5.4.4 Sources without Confirmed Pulsations

Source 1731 - HMXB

Source 1731 is located within $\sim 1''$ of source 117 in the Haberl catalog (Haberl & Sturm, 2016); XMMU J005618.8−722802. XMMU J005618.8−722802 was observed by Sturm et al. (2013a) where it is identified as a HMXB candidate. Haberl & Sturm (2016) note that the source has measured Balmer (Hα) emission from its specturm. Shtykovskiy & Gilfanov (2005) first observed this source with *XMM-Newton* and noted that it lies inside of the star cluster NGC 330.

The position of source 1731 changes on the diagnostic hardness-intensity and hardness ratio diagrams between epochs of observation (Figure 5.15). During the first observation (April 2017) source 1731 occupies a region of the hardness-intensity diagram that has significant overlap between the hard state black hole locus and the pulsar locus. Its $(M-S)/(M+S)$ hardness ratio is softer than the pulsar locus of the diagram. During its second observation in August 2017, source 1731's luminosity is almost 10 times lower and its position on both the hardness-intensity and hardness ratio diagrams is consistent with pulsars and hard state black holes, within errors. We did not observe pulsations for source 1731 using an averaged power spectrum.

Source 1745 - Low luminosity Be-XRB

Source 1745 [source 84 in Haberl & Sturm (2016)] lies in the overlapping region between hard and intermediate state accreting black holes and accreting pulsars on the diagnostic diagrams. Thus far source 1745 has been identified as a Be-XRB (Meyssonnier & Azzopardi, 1993; Haberl & Sasaki, 2000; Antoniou et al., 2009; Haberl & Sturm, 2016) with a clear emission-line star as its optical counterpart. Its X-ray spectrum is typical of an X-ray binary with $\Gamma < 1.3$ (Haberl & Sturm, 2016). This source does not have published variability information and does not have a detected pulse period in the literature. We did not observe pulsations for source 1745 using an averaged power spectrum.

5.4.5 Pulsars

Source 1728 - Detection of SXP 645

Source 1728 is associated with known pulsar SXP 645 (XMMU J005535.2−722906). We measured a pulse period of 625.0 seconds using an averaged power spectrum. This measured period is slightly shorter than the value from the literature, 645 seconds (Haberl et al., 2008). Source 1728 is difficult to classify with our diagnostic diagrams because it lies in a region that overlaps between hard state black holes and pulsars. It matches within 1.13″ to source 55 in Haberl & Sturm (2016), where it is listed as a Be-XRB with an accreting pulsar primary.

Source 1666 - Detection of SXP 138

Source 1666 is associated with known pulsar SXP 138 (CXOU J005323.8−72271). We measured a pulse period of 138.9 seconds using an averaged power spectrum. This measured period agrees with the 138.04 ± 0.61 second period observed by Edge et al. (2004b). On our diagnostic diagrams, source 1666 lies in a region with overlap between hard state black holes and pulsars. It matches to source 30 in the Haberl & Sturm (2016) catalog within 0.6″, where it is identified as a Be-XRB with measured X-ray pulsations. Its companion star is a Be star (Coe et al., 2005; Harris & Zaritsky, 2004).

Source 1701 - Detection of SXP323

Source 1701 is associated with known pulsar SXP323 (RX J0050.8−7316). We measured a pulse period of 312.5 seconds using an averaged power spectrum. This measured period is slightly shorter than the published period of 323 seconds (Imanishi et al., 1999). Similarly to the other pulsars in our sample with $L_{4-25keV} < 1 \times 10^{37}$ erg s^{-1}, it lies in a region of our diagnostic diagram with overlap between accreting pulsars and hard state black holes. Source 1701 matches within 0.5″ to source 47 in Haberl & Sturm (2016), which is identified as RX J0050.8−7316 (SXP323).

Source 2012 - Detection of SXP7.77

Source 2012 is associated with the known pulsar SMC X-3 (SXP 7.77). We measured a pulse period of 7.76 seconds using an averaged power spectrum, which agrees with the published period of 7.77 seconds (Edge et al., 2004a). On our diagnostic diagrams, source 2012 lies at the intersection of hard state black hole, pulsar, and intermediate state black holes on the hardness-intensity diagram. On the hardness ratio diagram, source 2012 lies at the soft (lower-left) corner of the pulsar locus.

Source 2012 matches to SMC X-3, listed as source 9 in Haberl & Sturm (2016), within 0.44″. SMC X-3 is a well documented accreting pulsar (Li et al., 1977) with a Be optical counterpart (Evans et al., 2004). SMC X-3 was observed in a likely Type II outburst starting in 2016 and ending in February 2017, although it continued to be detected after the end of its outburst (Kennea et al., 2016b,a, 2018; Koliopanos & Vasilopoulos, 2018). SMC X-3 has a well measured orbital period ($\sim$ 45 days) and measured X-ray variability that is consistent with Type I outbursts that peak at the XRB's orbital periastron (Townsend et al., 2017). We note that its hardness ratios and luminosity did not vary significantly between our two observations with *NuSTAR* in May and August 2017 (see Fig. 5.17).

Source 2052 - Likely AGN

Source 2052 is likely a background AGN. It matches within 1.7″ to source 661 in Sturm et al. (2013a) where it was classified as a likely AGN. Sturm et al. (2013a) classify it as a likely background AGN because of its hard X-ray colors and the ratio of its X-ray to optical flux ($log(f_X/f_o)$) is greater than -1, typical for an AGN (Maccacaro et al., 1988). However, this source does not appear in the Sturm et al. (2013b) catalog of background AGN in the SMC, which was based on identifications with radio sources. This source also does not appear in the catalog of newly identified AGN behind the SMC (Maitra et al., 2019), which on the other hand was X-ray/NIR selected.

Source 2052 is roughly 100 times brighter in the 4–25 keV bandpass than its 0.2-12 keV flux

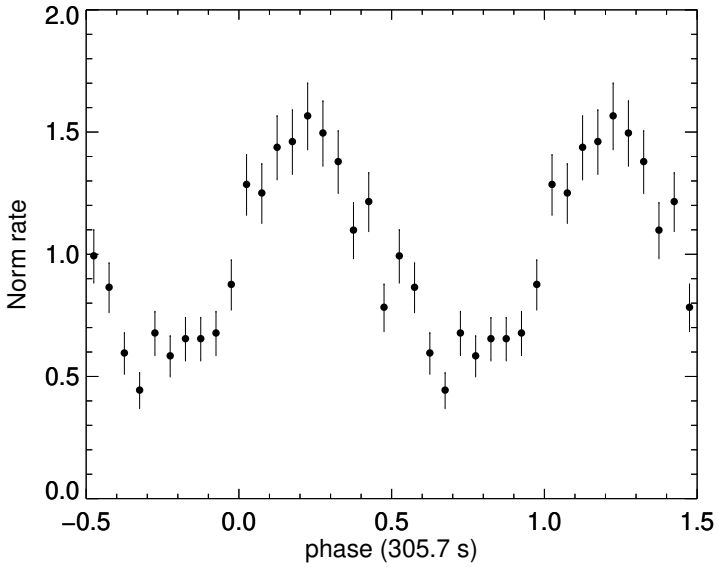

Figure 5.7 Pulse profile of the newly discovered pulsar SXP 305. The profile was fit for the full 4-25 keV *NuSTAR* band and is background subtracted. ©AAS. Reproduced with permission from Lazzarini et al. (2019).

measured by *XMM-Newton* would indicate, assuming a power law model with a photon index of 1.7. Source 2052 was not detected in our quasi-simultaneous *Swift-XRT* observations. This is likely due to photoelectic absorption which would preferentially affect softer (E$<$ 10 keV) X-ray photons detected by *Swift-XRT* over harder (E$>$ 10 keV) X-ray photons detected by *NuSTAR*.

5.4.6 Detection of Pulsations from CXO J005215.4–731915 and its likely orbital period

The small angular distance of CXO J005215.4–731915 to SXP 15.3 led to initial confusion about the correct optical counterpart for SXP 15.3 (see the discussion on SXP 15.3 in Schurch et al., 2011). Only after the detection of both X-ray sources in a Chandra observation (Laycock et al., 2010), it became clear that there are two Be-XRBs only 7.5″ apart. A Swift observation nearly simultaneous to the first *NuSTAR* observation shows that CXO J005215.4–731915 was active during

the March 2017 observation. The pulse profile for our NuSTAR observations of CXO J005215.4-731915 is shown in Figure 5.7.

The optical counterpart of CXO J005215.4–731915 was observed by the Optical Gravitational Lensing Experiment (OGLE), which started observations in 1992 (Udalski et al., 1992). The star was monitored during phases II (smc_sc6.99991), III (smc100.1.43700) and IV (smc720.26.531) until today (for OGLE-IV see Udalski et al., 2015). Observations are performed with the 1.3 m Warsaw telescope at Las Campanas Observatory, Chile. Images are taken in the V and I filter pass-bands and photometric magnitudes are calibrated to the standard VI system.

The OGLE II and III I-band light curve of the optical counterpart of CXO J005215.4–731915 was presented by Schurch et al. (2011) revealing regular outbursts by up to 0.5 mag. Figure 5.8 shows an updated light curve including the OGLE IV data. Seven outbursts are now recorded over more than 22 years. A Lomb-Scargle periodogram of the full light curve reveals a broad peak around $\sim$1163 days. A grid of intervals with this period (indicated by thin vertical lines in Fig. 5.8) anchored on the peak of the fifth outburst (the only one with a fully covered peak) shows that the outbursts do not occur strictly periodically. A period of more than 1000 days is very long for the orbital period of a Be-XRB and Schurch et al. (2011) proposed that the outbursts are caused by changes in the structure and size of the circum-stellar disk. After detrending the OGLE light curve they suggest an orbital period of 21.68 days, detected in their Lomb-Scargle periodogram.

We followed a similar approach by smoothing the data, subtracted the smoothed curve in order to remove the long-term trends, and created a periodogram using the Lomb-Scargle algorithm (Fig. 5.9). The periodogram between 0.5 and 30 days shows a series of peaks near 20–21 days and around 1 day. The six highest peaks of similar strength are at 0.953, 1.049, 20.133, 20.481, 21.314 and 21.705 days. The periods of all these peaks can be related to each other as aliases with periods of $\sim$364 days or $\sim$1180 days, the latter being caused by the outburst period. Short periods around one day are believed to be caused by non-radial pulsations (NRPs), a phenomenon commonly observed in Be stars (see e.g. Rivinius et al., 2013). Therefore, we interpret the 21.68 day period reported by Schurch et al. (2011) (consistent with our peak at 21.705 days) as likely being an alias of an NRP period close to one day.

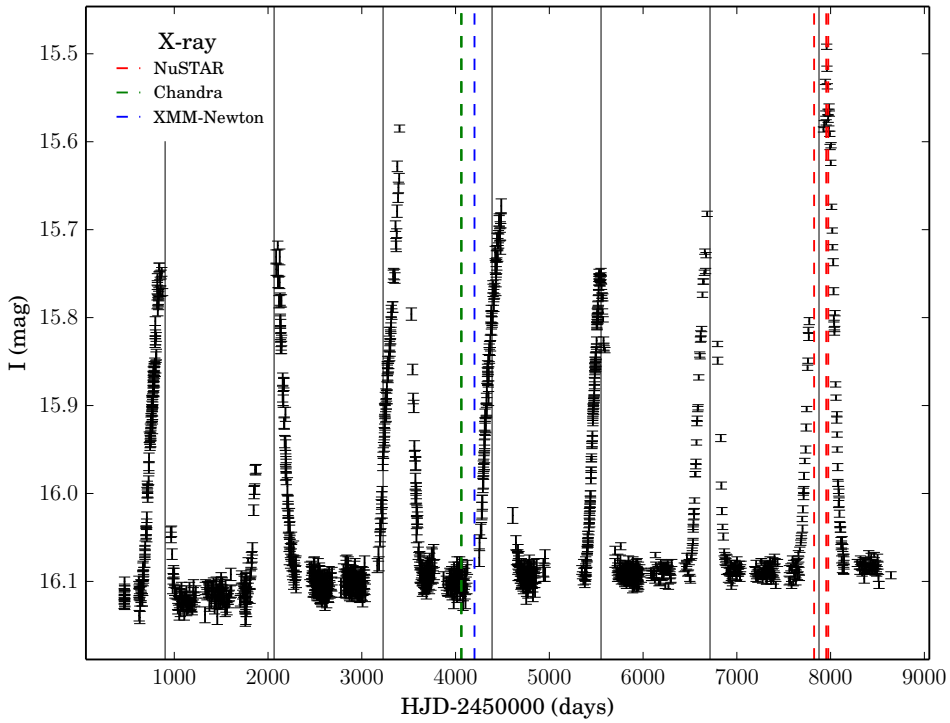

Figure 5.8 OGLE I-band light curve of the optical counterpart of CXO J005215.4–731915. The colored vertical dashed lines mark the times of X-ray observations and the full black lines are separated by 1163 days. ©AAS. Reproduced with permission from Lazzarini et al. (2019).

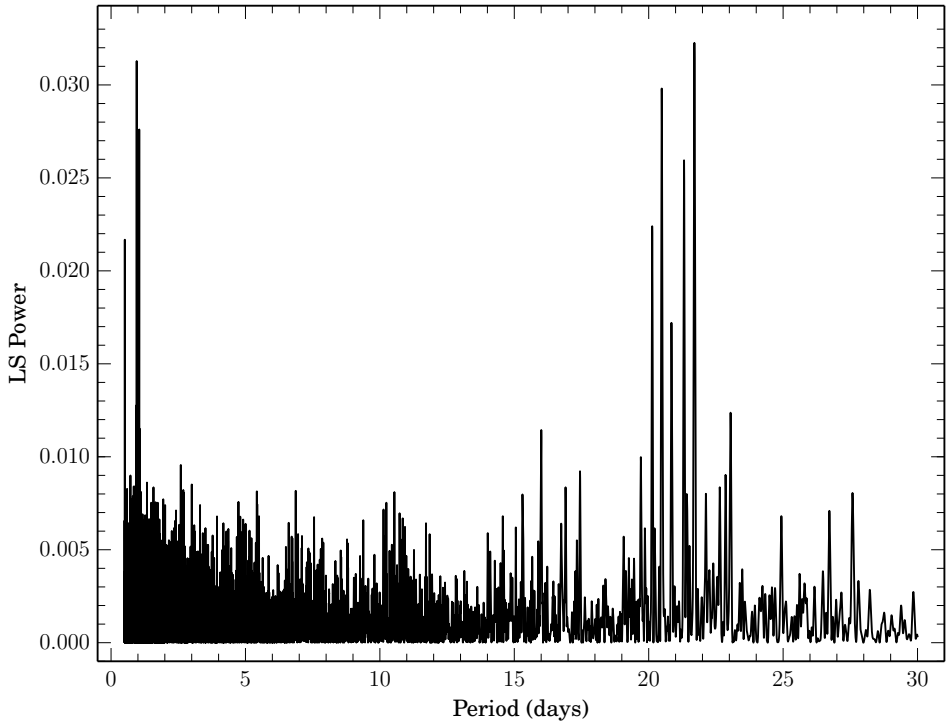

Figure 5.9 Lomb-Scargle periodogram between 0.5 and 30 days inferred from the smoothed OGLE I-band light curve shown in Fig. 5.8. ©AAS. Reproduced with permission from Lazzarini et al. (2019).

Maggi et al. (2014) suggested an orbital period of 1180 days for Swift J010745.0−722740, based on two strong outbursts seen in the OGLE light curve of this Be/X-ray binary in the SMC. No further optical outburst could be seen so far, but an X-ray detection in April 2017 at the time expected for the next outburst (Vasilopoulos et al., 2017) confirmed the outburst period. 3XMM J051259.8−682640 in the Large Magellanic Cloud showed three remarkable dips in its 15 year OGLE light curve, suggesting a possible 1350 day orbital period (Haberl et al., 2017). The seven regular outbursts observed every ∼1163 days and the aliasing effects of a shorter period and ∼1180 days seen from CXO J005215.4–731915 might indicate the orbital period (∼1160–1180 days) of the system after all and it could be the third Be-XRB with an orbital period longer than 1000 days. The outbursts would be caused by the perigee passage of the neutron star and are not expected to be strictly periodic due to long-term variations of the circum-stellar disc around the Be star. Finally, we note that the largest orbital period in an Be-XRB systems is measured in PSR J2032+4127/MT91 213, where the orbital period is ∼50 yr (Lyne et al., 2015), and its last periastron passage was in 2017 (Petropoulou et al., 2018; Ho et al., 2017). Although, no major outburst was observed during the 2017 periastron passage of PSR J2032+4127, the discovery of the system demonstrates the existence of more Be-XRBs with very high orbital periods.

5.5 Conclusions

In this chapter we present 1 Ms of new *NuSTAR* observations of three fields in the Small Magellanic Cloud, including a catalog with 10 sources with greater than a 3σ significance and 40 sources with upper limits on the source count rate.

We detected point sources down to a 3σ luminosity limit of 10^{35} erg s^{-1} in the 4–25 keV band, the lowest point source luminosity limit of any nearby galaxy observed with *NuSTAR*. This detection sensitivity allowed us to analyze lower luminosity XRBs in the Small Magellanic Cloud than has been possible in other nearby galaxies.

We used X-ray colors and luminosities to classify XRBs by compact-object type, black hole or neutron star, and to further subdivide black holes by accretion state and neutron stars as pulsars or low magnetic field neutron stars. We identified four sources as strongly variable both when

we compare our *NuSTAR* observations to archival *XMM-Newton* observations as well as between epochs of our observations.

We confirmed pulse periods for the seven known pulsars in our 3σ sample (1728, 1677, 1701, 1705, 1666, 2012, 2035) using epoch folding for each source during each individual observation. We did not observe pulsations for the two HMXBs in our 3σ sample that do not have confirmed pulse periods in the literature (1731, 1745).

We also present the first observations of periodic pulsations from SXP305 (CXO J005215.4–731915), a Be-XRB. We measured an X-ray pulse period of 305.69 ± 0.16 seconds. CXO J005215.4–731915 is located 0.5 from the measured position of source 1705 and was observed in outburst during the first observation of Field 2 (50311002002). We did not detect pulsations during the second two observations of Field 2 (50311002004, 50311002006) because the nearby pulsar SXP15.3 was in outburst and dominated the flux detected at the location of 1705. The likely orbital period for this system is $\sim$1160-1180 days, which we measured using optical light curves from OGLE.

We note that several low luminosity sources that are associated with confirmed pulsars fall in regions of the diagnostic diagrams consistent with multiple compact-object types. We raise questions about the apparent spectral differences of SMC pulsars as compared to the Milky Way pulsars that were used to create the diagnostics. Further work on *NuSTAR* spectroscopic analysis for the sources in this catalog will be presented in V. Antoniou, et al., in preparation. More detailed pulse timing analysis for bright accreting pulsars will be presented in future work.

Table 5.2: *NuSTAR* SMC Legacy Survey Source Catalog

Source ID	R.A.	Dec.	F Count Rate $\times 10^{-3}\ s^{-1}$	S Count Rate $\times 10^{-3}\ s^{-1}$	M Count Rate $\times 10^{-3}\ s^{-1}$	H Count Rate $\times 10^{-3}\ s^{-1}$	$\frac{(M-S)}{(M+S)}$	$\frac{(H-M)}{(H+M)}$	Exp. Time	Bgd. Rate s^{-1}	Field	Haberl ID
1701	12.686279	–73.268131	$19.57^{0.49}_{0.48}$	$6.34^{0.30}_{0.29}$	$9.62^{0.32}_{0.31}$	$3.18^{0.20}_{0.19}$	$0.20^{0.03}_{0.03}$	$-0.48^{0.03}_{0.03}$	309	1.20	2	47
1745	12.738000	–73.168813	$41.60^{0.71}_{0.70}$	$14.21^{0.43}_{0.41}$	$20.60^{0.46}_{0.45}$	$6.89^{0.33}_{0.32}$	$0.17^{0.02}_{0.02}$	$-0.49^{0.02}_{0.02}$	207	1.40	2	84
2012	13.023879	–72.434562	$101.21^{0.89}_{0.91}$	$38.00^{0.60}_{0.59}$	$51.60^{0.64}_{0.61}$	$12.07^{0.34}_{0.33}$	$0.15^{0.01}_{0.01}$	$-0.59^{0.01}_{0.01}$	259	1.20	3	9
1705[b]	13.064458	–73.320945	$951.58^{3.70}_{3.60}$	$244.96^{2.00}_{1.90}$	$482.76^{2.60}_{2.50}$	$221.40^{1.90}_{1.90}$	$0.32^{0.00}_{0.00}$	$-0.36^{0.00}_{0.00}$	107	1.20	2	93/16
1666	13.349638	–72.454316	$27.47^{0.58}_{0.56}$	$8.95^{0.32}_{0.30}$	$13.63^{0.37}_{0.36}$	$4.39^{0.26}_{0.26}$	$0.19^{0.02}_{0.02}$	$-0.49^{0.02}_{0.02}$	192	1.20	3	30
2035	13.480736	–72.445979	$20.82^{0.71}_{0.68}$	$7.00^{0.40}_{0.38}$	$9.44^{0.44}_{0.42}$	$4.24^{0.39}_{0.36}$	$0.16^{0.03}_{0.03}$	$-0.34^{0.04}_{0.04}$	151	1.20	3	22
2052	13.713261	–72.442148	$22.79^{2.20}_{2.20}$	$10.24^{1.30}_{1.20}$	$14.92^{1.50}_{1.50}$	$0.00^{0.84}_{--}$	$0.17^{0.08}_{0.08}$	$-0.94^{0.10}_{--}$	260	1.10	1	–
1677	13.734407	–72.446681	$906.22^{3.10}_{3.00}$	$242.76^{1.70}_{1.70}$	$449.76^{2.10}_{2.00}$	$190.81^{1.10}_{1.10}$	$0.30^{0.00}_{0.00}$	$-0.41^{0.00}_{0.00}$	285	1.10	1	23
1728	13.896565	–72.485134	$26.68^{0.63}_{0.61}$	$9.02^{0.39}_{0.29}$	$13.12^{0.42}_{0.40}$	$4.30^{0.26}_{0.25}$	$0.19^{0.03}_{0.03}$	$-0.49^{0.03}_{0.03}$	185	1.10	1	55
1731	14.078402	–72.467787	$8.56^{0.39}_{0.37}$	$2.60^{0.22}_{0.21}$	$4.14^{0.24}_{0.23}$	$1.76^{0.20}_{0.19}$	$0.20^{0.04}_{0.04}$	$-0.37^{0.05}_{0.05}$	176	1.10	1	117
1695	12.294759	–73.288091	<2.0	<0.7	<0.9	<0.6	$0.06^{0.17}_{0.18}$	$-0.47^{0.25}_{--}$	144	1.20	2	–
2111	12.338442	–73.294647	<0.6	<0.4	<0.2	<0.2	$-0.38^{0.37}_{--}$	$-1.00^{1.10}_{--}$	220	1.20	2	–
2115	12.488716	–73.282034	<0.0	<0.2	<0.0	<0.0	$--^{--}_{--}$	$--^{--}_{--}$	307	1.20	2	–
2118	12.522018	–73.196036	<0.5	<0.1	<0.2	<0.2	$0.22^{0.23}_{0.22}$	$-0.30^{0.24}_{--}$	247	1.70	2	–
2119	12.527318	–73.263826	<0.0	<0.1	<0.0	<0.0	-0.02^{--}_{--}	$-1.00^{1.60}_{--}$	323	1.20	2	–
2121	12.598875	–73.305656	<0.7	<0.4	<0.4	<0.1	$0.13^{0.12}_{0.12}$	$-0.44^{0.15}_{0.17}$	330	1.20	2	–
2123	12.675824	–73.360578	<0.1	<0.3	<0.0	<0.1	$--^{--}_{--}$	$--^{--}_{--}$	272	1.10	2	–
1702	12.687766	–73.261037	<4.5	<2.0	<2.2	<0.6	$0.06^{0.09}_{0.09}$	$-0.51^{0.10}_{0.10}$	322	1.20	2	–
2124	12.687912	–73.255423	<0.3	<0.1	<0.3	<0.2	$--^{--}_{--}$	$--^{--}_{--}$	302	1.20	2	–
2125	12.699929	–73.304988	<1.2	<0.7	<0.5	<0.2	$-0.04^{0.11}_{0.11}$	$-0.29^{0.14}_{0.15}$	343	1.20	2	45
2127	12.731243	–73.343496	<1.4	<0.5	<0.8	<0.3	$0.15^{0.17}_{0.16}$	$-0.38^{0.19}_{0.24}$	298	1.10	2	–
2129	12.746321	–73.348747	<1.4	<0.3	<0.4	<0.8	$-0.07^{0.37}_{--}$	$0.44^{0.23}_{0.23}$	288	1.10	2	–
1864	12.762729	–73.357891	<0.6	<0.1	<0.2	<0.6	0.53^{--}_{--}	0.67^{--}_{--}	274	1.10	2	–
1865	12.763887	–73.360729	<0.5	<0.0	<0.2	<0.5	$--^{--}_{--}$	$0.31^{1.30}_{--}$	269	1.10	2	–
2134	12.915870	–73.300610	<0.7	<0.4	<0.4	<0.2	$0.52^{0.09}_{0.13}$	$0.27^{0.03}_{0.09}$	298	1.20	2	–
1662	12.972087	–72.530245	<0.3	<0.2	<0.3	<0.1	$0.18^{0.30}_{0.29}$	$-0.15^{0.29}_{0.32}$	275	1.20	3	11
2137	13.008025	–73.234996	<0.1	<0.2	<0.2	<0.0	$0.20^{0.15}_{0.15}$	$0.00^{0.15}_{0.14}$	239	1.00	2	–

Source ID	R.A.	Dec.	F Count Rate $\times 10^{-3}\ s^{-1}$	S Count Rate $\times 10^{-3}\ s^{-1}$	M Count Rate $\times 10^{-3}\ s^{-1}$	H Count Rate $\times 10^{-3}\ s^{-1}$	$\frac{(M-S)}{(M+S)}$	$\frac{(H-M)}{(H+M)}$	Exp. Time	Bgd. Rate s^{-1}	Field	Haberl ID
94	13.038505	–72.431364	<0.2	<0.2	<0.2	<0.2	0.95^{--}_{--}	-0.99^{--}_{--}	260	1.20	3	–
96	13.066980	–72.433882	<0.2	<0.2	<0.1	<0.1	-0.97^{--}_{--}	0.97^{--}_{--}	271	1.20	3	–
1663	13.140267	–72.410466	<0.8	<0.6	<0.6	<0.1	$0.13^{0.25}_{0.23}$	$-0.52^{0.29}_{--}$	244	1.20	3	–
1664	13.146238	–72.421389	<0.5	<0.3	<0.3	<0.1	$-0.07^{0.67}_{--}$	$0.16^{0.43}_{0.42}$	265	1.20	3	94
2017	13.243471	–72.435198	<0.1	<0.1	<0.2	<0.0	$--^{--}_{--}$	$--^{--}_{--}$	278	1.20	3	–
2024	13.382805	–72.446137	<0.7	<0.2	<0.3	<0.6	0.61^{--}_{--}	$0.56^{--}_{0.34}$	178	1.20	3	–
1668	13.407895	–72.402495	<0.6	<0.2	<0.7	<0.1	$0.51^{--}_{0.28}$	$-0.33^{0.26}_{--}$	137	1.20	3	–
1670	13.468735	–72.533149	<2.3	<0.7	<0.9	<0.9	$0.08^{0.13}_{0.13}$	$0.10^{0.12}_{0.13}$	166	1.20	3	–
1403	13.478602	–72.456238	<3.9	<0.8	<1.6	<1.9	$0.27^{0.17}_{0.16}$	$0.15^{0.12}_{0.11}$	155	1.20	3	–
2047	13.619948	–72.511644	<0.2	<0.3	<0.1	<0.1	-0.99^{--}_{--}	-1.00^{--}_{--}	227	1.10	1	–
1722	13.621017	–72.518590	<0.2	<0.2	<0.1	<0.2	$-0.04^{0.33}_{0.33}$	$-0.08^{0.43}_{--}$	219	1.10	1	–
1673	13.654902	–72.443810	<0.1	<0.1	<0.2	<0.0	$--^{--}_{--}$	$--^{--}_{--}$	264	1.10	1	–
1674	13.688963	–72.399620	<1.0	<0.4	<0.7	<0.2	$--^{--}_{--}$	$-0.33^{0.58}_{--}$	259	1.10	1	–
1675	13.693395	–72.423048	<0.7	<1.1	<0.3	<0.2	-0.99^{--}_{--}	-0.97^{--}_{--}	279	1.10	1	63
1676	13.704129	–72.429160	<1.8	<0.7	<0.9	<0.6	0.11^{--}_{--}	-0.20^{--}_{--}	273	1.10	1	–
1678	13.738063	–72.506046	<1.2	<0.3	<0.8	<0.4	$0.86^{--}_{0.28}$	$-0.36^{0.21}_{0.24}$	268	1.10	1	–
1679	13.768155	–72.375208	<0.2	<0.3	<0.4	<0.0	$0.21^{0.76}_{0.40}$	$-1.00^{0.26}_{--}$	247	1.10	1	–
1680	13.782369	–72.378083	<0.1	<0.3	<0.1	<0.0	$-0.09^{0.78}_{--}$	$-1.00^{0.81}_{--}$	253	1.10	1	111
1724	13.826634	–72.523471	<2.3	<0.7	<0.8	<1.0	$0.14^{0.13}_{0.13}$	$0.05^{0.12}_{0.12}$	172	1.10	1	–
1726	13.894533	–72.476154	<3.0	<1.3	<1.8	<0.3	$0.33^{0.21}_{0.18}$	$-0.72^{0.18}_{--}$	198	1.10	1	–
1760	13.923780	–72.448851	<0.1	<0.1	<0.1	<0.1	1.00^{--}_{--}	$0.17^{--}_{2.90}$	203	1.10	1	–
2232	13.985326	–72.492418	<0.6	<0.3	<0.2	<0.3	-0.19^{--}_{--}	$0.34^{0.59}_{0.46}$	187	1.10	1	–
2237	14.094049	–72.507746	<0.6	<0.2	<0.2	<0.5	$-0.64^{0.99}_{--}$	$0.79^{0.65}_{--}$	156	1.10	1	–

NuSTAR source catalog with count rates and hardness ratios from combining all observations of each field. Bands used are as follows: $S = 4-6$ keV, $M = 6-12$ keV, $H = 12-25$ keV, $F = 4-25$ keV. Sources listed above the horizontal line were detected at a 3σ significance level, all sources listed after the horizontal line are upper limits. Entries listed as "–" indicate missing values. Haberl ID indicates listed identification number in Haberl & Sturm (2016). Background count rate was fit using the methods described in Section 5.2.3. Exposure times

listed include both FPMA and FPMB telescope images, with the exception of the two FPMB telescope images that were omitted from source extraction due to stray light contamination in Fields 1 and 3.

[a] We use source IDs are from Antoniou et al. (2019) as the source positions from that catalog were used as the priors on source positions in our PSF fitting routine to extract count rates and hardness ratios.

[b] *NuSTAR* source 1705 is a combination of two sources, SXP15.3 and the newly confirmed pulsar SXP305. See §5.4.6 for more details.

Table 5.3: Count Rate and Hardness Ratios By Observation

Source ID	R.A.	Dec.	F Count Rate $\times 10^{-3}\ s^{-1}$	S Count Rate $\times 10^{-3}\ s^{-1}$	M Count Rate $\times 10^{-3}\ s^{-1}$	H Count Rate $\times 10^{-3}\ s^{-1}$	$\frac{(M-S)}{(M+S)}$	$\frac{(H-M)}{(H+M)}$	Obs. ID	Date yyyy-mm-dd
1701	12.686279	–73.268131	$18.65^{0.61}_{0.60}$	$6.08^{0.37}_{0.36}$	$8.95^{0.39}_{0.39}$	$3.22^{0.26}_{0.25}$	$0.18^{0.04}_{0.04}$	$-0.45^{0.03}_{0.03}$	50311002002	2017-03-12
1701	12.686279	–73.268131	$22.83^{0.91}_{0.91}$	$7.85^{0.62}_{0.57}$	$11.74^{0.50}_{0.49}$	$3.03^{0.32}_{0.29}$	$0.20^{0.04}_{0.04}$	$-0.54^{0.04}_{0.04}$	50311002004	2017-07-19
1701	12.686279	–73.268131	$30.15^{1.40}_{1.30}$	$9.49^{0.86}_{0.78}$	$14.44^{0.90}_{0.84}$	$5.11^{0.75}_{0.68}$	$0.19^{0.05}_{0.05}$	$-0.44^{0.05}_{0.04}$	50311002006	2017-08-09
1745	12.738000	–73.168813	$35.10^{0.81}_{0.79}$	$12.24^{0.49}_{0.47}$	$17.57^{0.53}_{0.52}$	$5.47^{0.38}_{0.36}$	$0.17^{0.02}_{0.02}$	$-0.51^{0.02}_{0.02}$	50311002002	2017-03-12
1745	12.738000	–73.168813	$65.72^{1.80}_{1.70}$	$21.71^{1.10}_{1.00}$	$32.30^{1.20}_{1.10}$	$11.99^{0.86}_{0.81}$	$0.18^{0.03}_{0.03}$	$-0.46^{0.03}_{0.03}$	50311002004	2017-07-19
1745	12.738000	–73.168813	$32.84^{3.70}_{3.30}$	$11.72^{2.20}_{1.90}$	$15.57^{2.50}_{2.20}$	$5.98^{1.80}_{1.40}$	$0.16^{0.09}_{0.09}$	$-0.58^{0.11}_{0.10}$	50311002006	2017-08-09
2012	13.023879	–72.434562	$118.05^{1.50}_{1.20}$	$42.47^{0.95}_{0.94}$	$59.76^{1.10}_{1.00}$	$15.88^{0.64}_{0.45}$	$0.17^{0.01}_{0.01}$	$-0.58^{0.01}_{0.01}$	50311003002	2017-05-03
2012	13.023879	–72.434562	$94.74^{1.30}_{1.30}$	$35.54^{0.85}_{0.79}$	$48.33^{0.88}_{0.86}$	$11.29^{0.51}_{0.50}$	$0.14^{0.01}_{0.01}$	$-0.58^{0.01}_{0.01}$	50311003004	2017-08-07
1705[a]	13.064458	–73.320945	$60.71^{1.60}_{1.50}$	$18.89^{0.90}_{0.86}$	$32.01^{1.10}_{1.00}$	$9.54^{0.76}_{0.71}$	$0.26^{0.03}_{0.03}$	$-0.52^{0.03}_{0.03}$	50311002002	2017-03-12
1705[a]	13.064458	–73.320945	$1188.09^{5.30}_{5.00}$	$313.94^{2.80}_{2.70}$	$595.60^{3.50}_{3.50}$	$268.75^{2.60}_{2.60}$	0.31^{--}_{--}	-0.35^{--}_{--}	50311002004	2017-07-19
1705[a]	13.064458	–73.320945	$1749.18^{20.00}_{15.00}$	$466.64^{14.00}_{6.60}$	$889.38^{15.00}_{9.50}$	$383.44^{8.60}_{8.40}$	$0.31^{0.01}_{0.01}$	$-0.39^{0.01}_{0.01}$	50311002006	2017-08-09
1666	13.349638	–72.454316	$25.97^{0.72}_{0.73}$	$8.13^{0.42}_{0.40}$	$13.06^{0.48}_{0.46}$	$4.11^{0.33}_{0.32}$	$0.20^{0.03}_{0.03}$	$-0.54^{0.03}_{0.03}$	50311003002	2017-05-03
1666	13.349638	–72.454316	$22.15^{0.64}_{0.65}$	$7.36^{0.43}_{0.42}$	$10.71^{0.43}_{0.11}$	$4.26^{0.38}_{0.37}$	$0.18^{0.03}_{0.03}$	$-0.40^{0.03}_{0.03}$	50311003004	2017-08-07
2035	13.480736	–72.445979	$6.32^{0.66}_{0.59}$	$1.50^{0.34}_{0.31}$	$2.50^{0.40}_{0.35}$	$2.27^{0.40}_{0.36}$	$0.21^{0.07}_{0.07}$	$-0.18^{0.08}_{0.08}$	50311003002	2017-05-03
2035	13.480736	–72.445979	$33.97^{1.60}_{1.50}$	$11.60^{1.00}_{0.85}$	$15.75^{0.99}_{1.20}$	$8.41^{1.00}_{0.85}$	$0.16^{0.03}_{0.03}$	$-0.29^{0.03}_{0.03}$	50311003004	2017-08-07
2052	13.713261	–72.442148	< 0.32	< 0.61	< 0.44	< 0.17	0.97^{--}_{--}	0.38^{--}_{--}	50311001002	2017-04-24
2052	13.713261	–72.442148	< 0.15	< 0.25	< 0.12	< 0.10	0.95^{--}_{--}	1.00^{--}_{--}	50311001004	2017-08-12
1677	13.734407	–72.446681	$1867.01^{5.00}_{5.00}$	$495.88^{2.80}_{2.70}$	$929.93^{3.40}_{3.40}$	$403.31^{2.30}_{2.30}$	0.30^{--}_{--}	-0.40^{--}_{--}	50311001002	2017-04-24
1677	13.734407	–72.446681	$152.74^{1.50}_{1.40}$	$51.39^{0.91}_{0.87}$	$76.33^{0.99}_{0.96}$	$23.57^{0.58}_{0.56}$	$0.19^{0.01}_{0.01}$	$-0.52^{0.01}_{0.01}$	50311001004	2017-08-12
1728	13.896565	–72.485134	$31.89^{0.96}_{0.90}$	$10.68^{0.60}_{0.57}$	$16.14^{0.63}_{0.61}$	$4.74^{0.35}_{0.34}$	$0.22^{0.03}_{0.03}$	$-0.53^{0.03}_{0.03}$	50311001002	2017-04-24
1728	13.896565	–72.485134	$20.94^{0.65}_{0.63}$	$7.43^{0.41}_{0.39}$	$9.86^{0.47}_{0.46}$	$3.22^{0.28}_{0.26}$	$0.15^{0.03}_{0.03}$	$-0.51^{0.03}_{0.03}$	50311001004	2017-08-12
1731	14.078402	–72.467787	$13.19^{0.56}_{0.54}$	$3.94^{0.32}_{0.30}$	$6.12^{0.35}_{0.34}$	$2.86^{0.28}_{0.26}$	$0.22^{0.04}_{0.04}$	$-0.38^{0.04}_{0.04}$	50311001002	2017-04-24
1731	14.078402	–72.467787	$2.08^{0.42}_{0.39}$	$0.57^{0.25}_{0.21}$	$1.33^{0.27}_{0.23}$	$0.22^{0.21}_{--}$	$0.16^{0.15}_{0.14}$	$-0.45^{0.17}_{0.20}$	50311001004	2017-08-12

Catalog of count rates and hardness ratio for 3σ sources broken down by observation. Bands used are as follows: $S = 4 - 6$ keV, $M = 6 - 12$ keV, $H = 12 - 25$ keV, $F = 4 - 25$ keV. We note that source 2052 was not detected when each observation was reduced separately, but the count rates and hardness ratios from the combined observations can be found in Table

5.2.

[a] We use source IDs are from Antoniou et al. (2019) as the source positions from that catalog were used as the priors on source positions in our PSF fitting routine to extract count rates and hardness ratios.

[a] *NuSTAR* source 1705 is a combination of two sources, SXP15.3 and the newly confirmed pulsar SXP305. The new pulsar, SXP305, was in outburst during the first observation and the previously known pulsar SXP15.3 was in outburst during the second two observations. See §5.4.6 for more details.

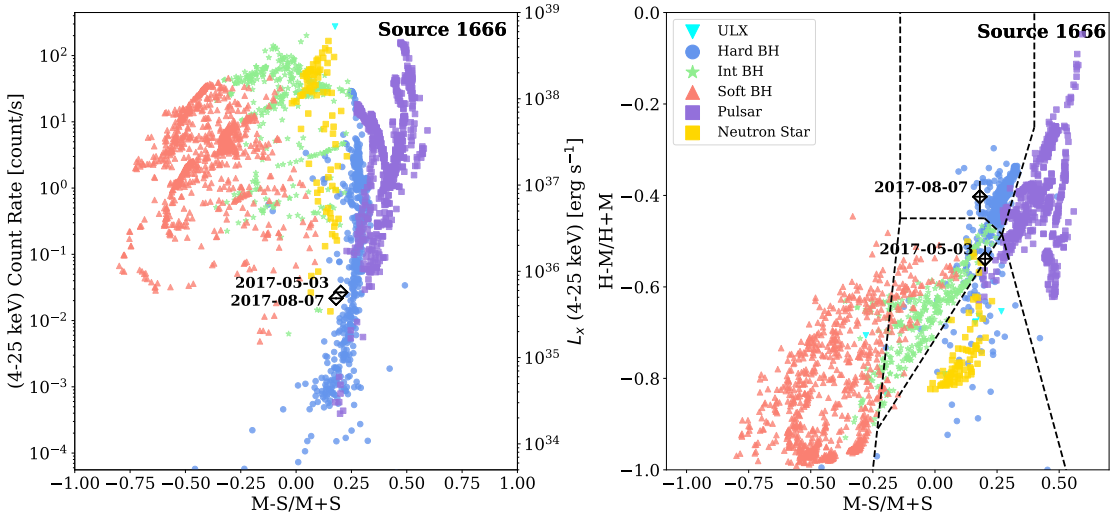

Figure 5.10 Hardness intensity and hardness ratio diagrams showing Source 1666 (source number indicated in upper right corner of each panel) at each observing epoch. The date of each observation is included as a label on the plot in yyyy-mm-dd format. For more information on background points, see caption of Figure 5.4. Source count rates and hardness ratios for each observation are listed in Table 5.3. ©AAS. Reproduced with permission from Lazzarini et al. (2019).

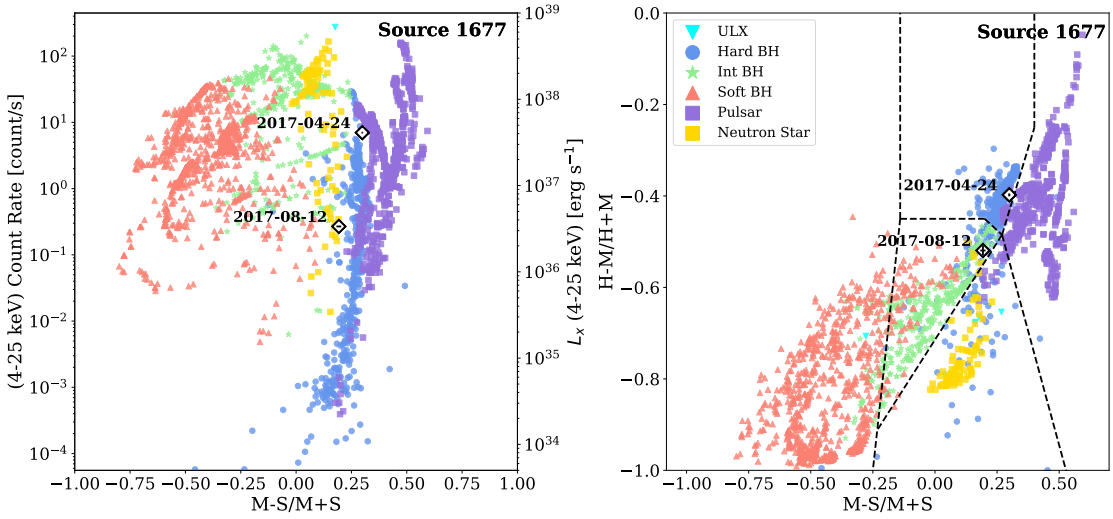

Figure 5.11 Hardness-intensity and hardness ratio diagrams for source 1677 at each observing epoch. See caption of Figure 5.4 for more information on background points. Count rates and hardness ratios for this source during each observation are listed in Table 5.3. ©AAS. Reproduced with permission from Lazzarini et al. (2019).

Table 5.4. *Swift-XRT* Observations List

Obs. ID	R.A. (J2000)	Dec. (J2000)	Field ID	Exp. Time [s]	Date (start) MJD
00088082001	13.87418	-72.4405	1	2419.87	57867.79688
00088082002	13.87418	-72.4405	1	12089.4	57871.25364
00088082003	13.93822	-72.4248	1	9322.35	57976.09448
00088082004	13.92335	-72.4361	1	1882.95	57977.53664
00088083001	12.69375	-73.2741	2	7202.19	57824.08328
00088083002	12.69375	-73.2741	2	7272.09	57826.00306
00088083003	12.69375	-73.2741	2	7272.09	57827.06391
00088083004	12.89389	-73.2506	2	983.931	57959.94944
00088083005	12.74704	-73.2501	2	6692.72	57960.28014
00088083006	12.71321	-73.2655	2	9324.84	57975.61163
00088032001	13.21749	-72.4804	3	5034.55	57876.30592
00088032002	13.21749	-72.4804	3	5651.39	57877.11145
00088032003	13.21749	-72.4804	3	4247.88	57878.02015
00088032004	13.25689	-72.5004	3	10076.5	57972.10376
00088032005	13.24207	-72.4562	3	5526.52	57973.02310

Note. — Observation IDs, positions, corresponding *NuSTAR* field, exposure time, and observation date for *Swift-XRT* observations.

Table 5.5. *Swift-XRT* 0.2-10 keV Count Rates For Each *Swift* Observation

Source ID	Count Rate [s^{-1}]	Obs. ID	Date [yyyy-mm-dd]
1701	0.007 ± 0.001	88083001	2017-03-12
1701	0.010 ± 0.001	88083002	2017-03-14
1701	0.006 ± 0.001	88083003	2017-03-15
1701	0.011 ± 0.004	88083004	2017-07-25
1701	0.011 ± 0.002	88083005	2017-07-26
1701	0.010 ± 0.001	88083006	2017-08-10
1745	0.017 ± 0.002	88083003	2017-03-15
1745	0.017 ± 0.002	88083005	2017-07-26
2012	0.054 ± 0.004	88032001	2017-05-03
2012	0.045 ± 0.003	88032002	2017-05-04
2012	0.037 ± 0.003	88032003	2017-05-05
2012	0.032 ± 0.002	88032004	2017-08-07
2012	0.028 ± 0.003	88032005	2017-08-08
1705[a]	0.702 ± 0.028	88083004	2017-07-25
1666	0.013 ± 0.002	88032001	2017-05-03
1666	0.014 ± 0.002	88032002	2017-05-04
1666	0.009 ± 0.002	88032003	2017-05-05
1666	0.010 ± 0.001	88032004	2017-08-07
1666	0.005 ± 0.001	88032005	2017-08-08
2035	0.015 ± 0.001	88032004	2017-08-07
2035	0.017 ± 0.002	88032005	2017-08-08
1673	0.002 ± 0.001	88082003	2017-08-11
1677	0.431 ± 0.014	88082001	2017-04-24
1677	0.043 ± 0.002	88082003	2017-08-11
1677	0.038 ± 0.005	88082004	2017-08-12
1728	0.010 ± 0.002	88082001	2017-04-24
1728	0.011 ± 0.001	88082002	2017-04-28
1728	0.008 ± 0.001	88082003	2017-08-11
1728	0.011 ± 0.003	88082004	2017-08-12
1731	0.004 ± 0.001	88082002	2017-04-28

Note. — Source count rates for quasi-simultaneous *Swift-XRT* observations that were used to create Figure 5.6. *Swift-XRT* count rates are for the full 0.2-10 keV energy band. Sources are listed by their source IDs in Table 5.2. For more information on *Swift-XRT* count rate fitting, see §5.2.5. For exposure times for each *Swift-XRT* observation, see Table 5.4.

[a] *NuSTAR* source 1705 is a combination of two sources, SXP15.3 and the newly confirmed pulsar SXP305. See §5.4.6 for more details.

Table 5.6. Pulsation Periods

Source ID	Measured Pulse Period [s]	Pulsed Fraction	Observation Start [MJD]
1666A (SXP138)	140.73±0.04	0.44±0.04	57876.12
1666B (SXP138)	140.85±0.05	0.49±0.06	57972.12
1677A (SXP59.0)	58.863±0.007	0.562±0.005	57867.07
1677B (SXP59.0)	58.799±0.010	0.38±0.03	57977.09
1701A (SXP323)	316.19±0.16	0.5±0.05	57824.07
1701B (SXP323)	316.26±0.24	0.47±0.06	57953.59
1701C (SXP323)	316.1±0.9	0.58±0.09	57974.96
1705A (SXP305)	305.69±0.15 (new pulsar)	0.55±0.05	57824.07
1705B (SXP15.3)	15.2822±0.0005	0.251±0.013	57953.60
1705C (SXP15.3)	15.2738±0.0016	0.32±0.03	57974.96
1728A (SXP645)	647.2±0.8	0.24±0.04	57867.07
1728B (SXP645)	–	¡0.32	57977.09
2012A (SXP7.77)	7.76923±0.00011	0.45±0.02	57876.12
2012B (SXP7.77)	7.76903±0.00014	0.47±0.04	57972.12
2035A (SXP46.6)	58.826±0.006*	0.31±0.06	57876.12
2035B (SXP46.6)	45.981±0.005	0.32±0.06	57972.12

Note. — Measured pulse periods for pulsars in 3σ source sample. Pulse periods were measured using epoch folding method, see §5.2.6 for an overview of methodology. The measured pulse period for each source during each observation are listed separately. Pulsed Fractions are given for detections, based on a folded pulse profile with 16 phase bins, upper limits are given for non detections. The suffix A, B, C correspond to the first, second, and third observations of the field containing that source. See Table 5.1 for an overview of observations.
*Source 2035 is 4.6 arcmin away from 1677 (SXP 59). During the first observation of Field 3, no point source (i.e. SXP 46.6) was visible in NuSTAR image, we only see background contamination. The fit pulse period reflects background contamination from source SXP 59.

Table 5.7. *NuSTAR* SMC Source Classifications

NuSTAR ID	$L_{4-25keV}$ $[\times 10^{35}\ erg\ s^{-1}]$	Diagnostic Diagram Classification	Haberl ID	Sep. [″]	Simbad Name	Properties from Haberl & Sturm (2016)
1728	5.86	PUL, HBH, IBH, NS	55	1.14	SXP645, XMMU J005535.2−722906	confirmed pulsar
1677	199	PUL, IBH, HBH, NS	23	1.07	SXP59.0, RX J0054.9−7226	confirmed pulsar
2052	5.01	HBH[a]	–	1.71	XMMU J005451.2−722630	likely AGN[b]
1731	1.88	HBH, PUL, IBH	117	1.10	XMMU J005618.8−722802	emission-line star optical cpt. within positional errors
1701	4.30	HBH, IBH, PUL	47	0.54	SXP323, RX J0050.8−7316	confirmed pulsar
1745	9.14	PUL, HBH, IBH, NS	84	0.83	RX J0050.9−7310	hard Be-XRB spectrum
1705[c]	209	PUL, HBH	93/16	0.50	SXP15.3 and SXP305	confirmed pulsar, newly confirmed pulsar
1666	6.04	HBH, PUL, IBH, NS	30	0.61	SXP138, CXOU J005323.8−722715	confirmed pulsar
2012	22.2	NS, PUL, HBH, IBH	9	0.45	SXP7.77, SMC X-3	confirmed pulsar
2035	4.58	HBH, PUL	22	0.93	SXP46.6, XTE J0053−724	confirmed pulsar

Note. — Table including *NuSTAR* source ID, 4–25 keV luminosities, our classification of each source using the diagnostic diagrams (figures 5.10–5.18), and ID, Simbad names and source properties listed in the Haberl & Sturm (2016) catalog. The column labeled "Sep." indicates the separation between our source position and the position listed in Haberl & Sturm (2016) in arcseconds. Source classifications were determined by inspecting the source positions on the diagnostic hardness-intensity and hardness ratio diagrams during each individual epoch of observation (Figs. 5.10-5.18). We did not use the hardness ratios and count rates from the merged observations because most sources changed full band luminosity and/or hardness ratios between epochs. For sources that lie in overlapping regions between compact-object types on the diagnostic diagrams, we list all possible classifications. We note that SMC *NuSTAR* source 2052 did not match to any source in the Haberl & Sturm (2016) catalog within 5 because it is a likely background AGN, not a HMXB. All sources with $L_{4-25keV} < 1.0 \times 10^{36}\ erg\ s^{-1}$ are considered low luminosity sources, when compared with XRB populations studied in other nearby galaxies.

[a] Source 2052 is classified using the diagnostic diagram created by combining all epochs of observation shown in Figure 5.4 because it did not have count rate and hardness ratio measurements with well defined errors in each individual observation.

[b] Likely AGN classification from Sturm et al. (2013a)

[c] Source 1705 is a combination of two sources, SXP15.3 and the newly confirmed pulsar SXP305. See §5.4.6 for more details.

Table 5.8. Flux Conversion Factors For Figure 5.5

Model	Conversion Factor
$\Gamma = 1.7$; $N_H = 4 \times 10^{20}$ cm^{-2}	0.917
$\Gamma = 0.9$; $N_H = 4 \times 10^{20}$ cm^{-2}	2.473
$\Gamma = 1.7$; $N_H = 4 \times 10^{21}$ cm^{-2}	2.148
$\Gamma = 0.9$; $N_H = 4 \times 10^{21}$ cm^{-2}	1.068
`compmag` (Ballhausen et al., 2017)	1.44

Note. — Conversion factors used to create lines for each spectral model in Figure 5.5. To create the lines, an array of 0.2-12.0 keV fluxes spanning the range of values shown in the figure were multiplied by the conversion factor to get the corresponding 4–25 keV flux for that model.

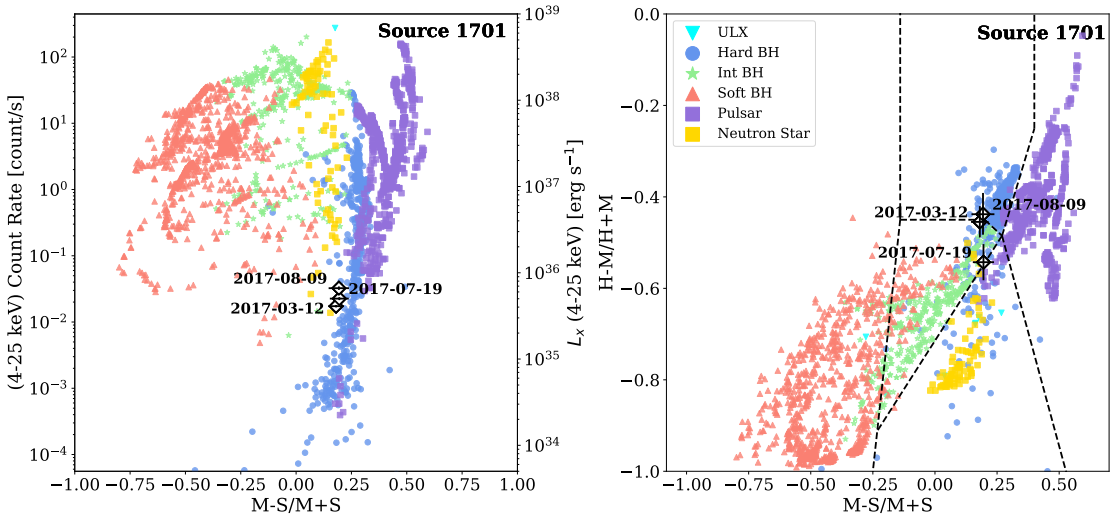

Figure 5.12 Hardness-intensity and hardness ratio diagrams for source 1701 at each observing epoch. See caption of Figure 5.4 for more information on background points. Count rates and hardness ratios for this source during each observation are listed in Table 5.3. ©AAS. Reproduced with permission from Lazzarini et al. (2019).

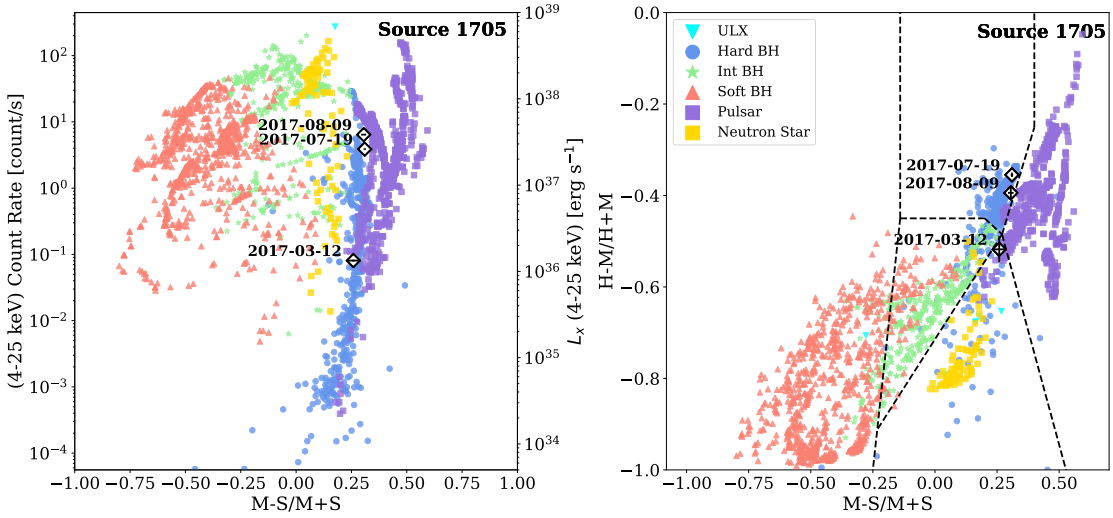

Figure 5.13 Hardness-intensity and hardness ratio diagrams for source 1705 at each observing epoch. See caption of Figure 5.4 for more information on background points. Count rates and hardness ratios for this source during each observation are listed in Table 5.3. We note that source 1705 is actually two sources - SXP 15.3 and the new pulsar presented in §5.4.6, SXP305. SXP305 is active during the first observation of Field 2 (2017-03-12) and SXP15.3 is active during the second two observations (2017-07-19, 2017-08-09). ©AAS. Reproduced with permission from Lazzarini et al. (2019).

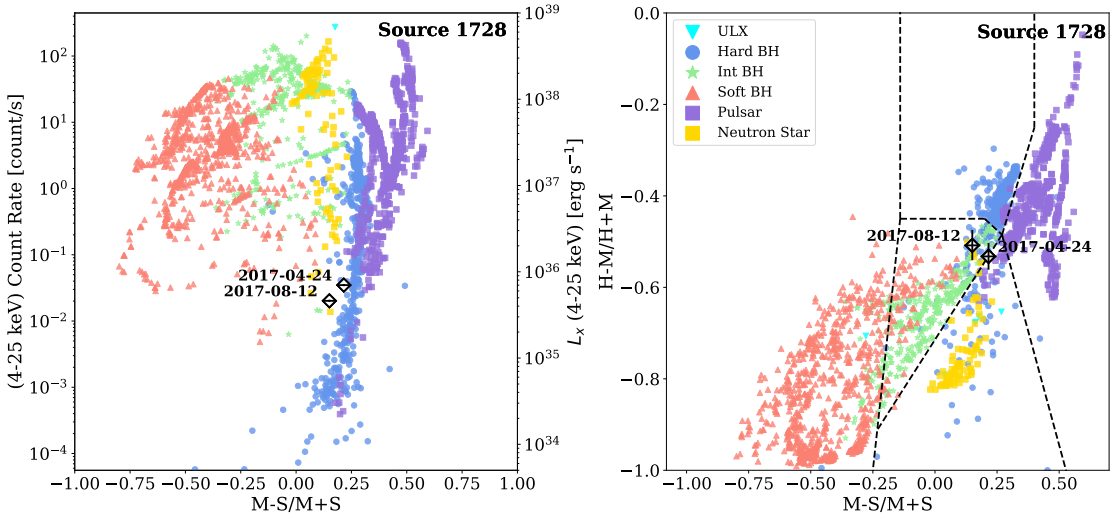

Figure 5.14 Hardness-intensity and hardness ratio diagrams for source 1728 at each observing epoch. See caption of Figure 5.4 for more information on background points. Count rates and hardness ratios for this source during each observation are listed in Table 5.3. ©AAS. Reproduced with permission from Lazzarini et al. (2019).

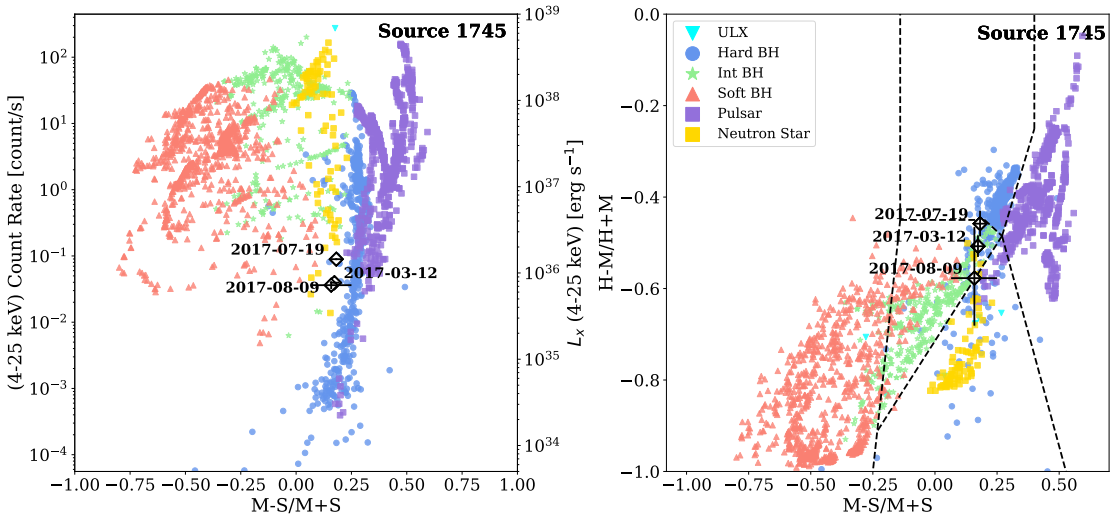

Figure 5.15 Hardness-intensity and hardness ratio diagrams for source 1731 at each observing epoch. See caption of Figure 5.4 for more information on background points. Count rates and hardness ratios for this source during each observation are listed in Table 5.3. ©AAS. Reproduced with permission from Lazzarini et al. (2019).

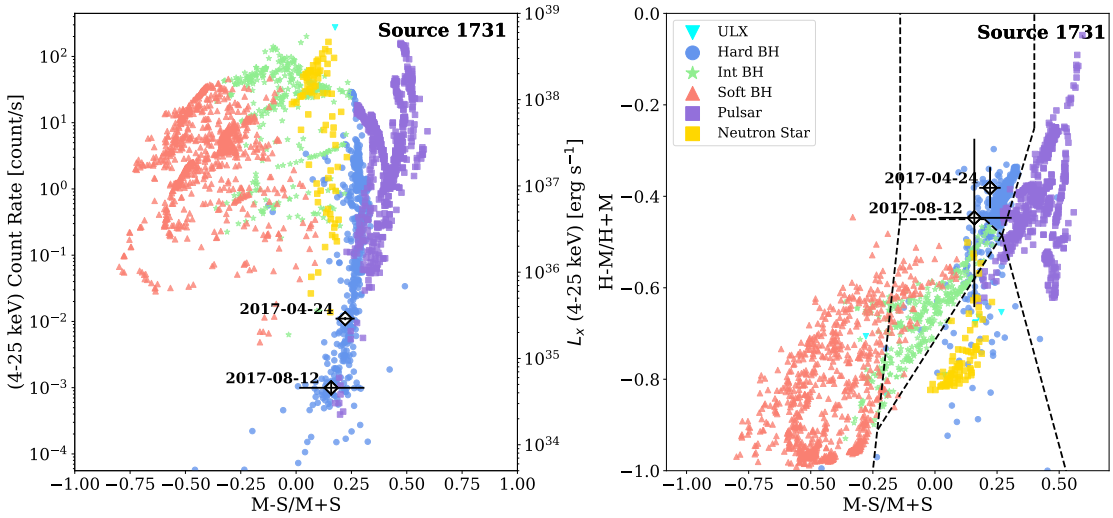

Figure 5.16 Hardness-intensity and hardness ratio diagrams for source 1745 at each observing epoch. See caption of Figure 5.4 for more information on background points. Count rates and hardness ratios for this source during each observation are listed in Table 5.3. ©AAS. Reproduced with permission from Lazzarini et al. (2019).

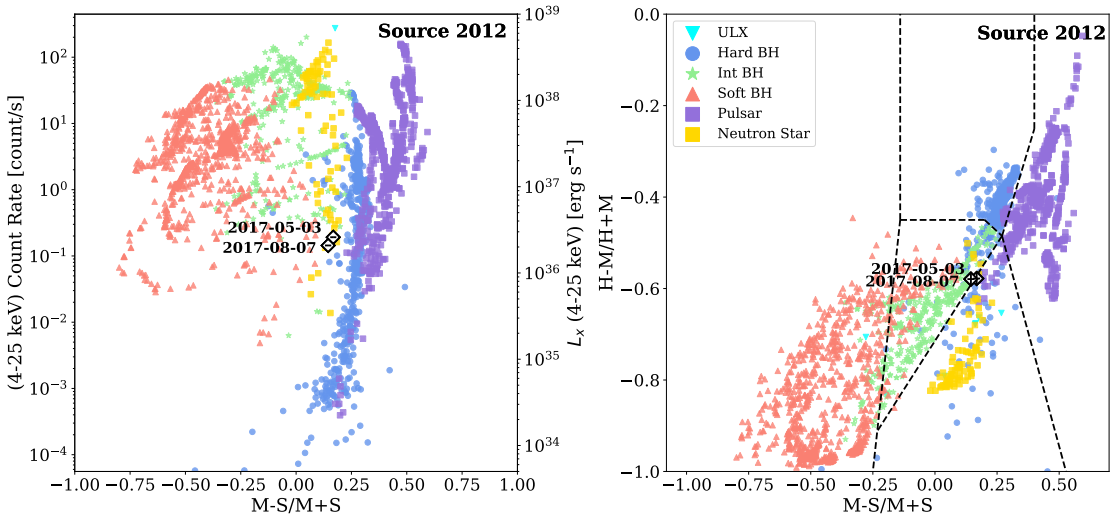

Figure 5.17 Hardness-intensity and hardness ratio diagrams for source 2012 at each observing epoch. See caption of Figure 5.4 for more information on background points. Count rates and hardness ratios for this source during each observation are listed in Table 5.3. ©AAS. Reproduced with permission from Lazzarini et al. (2019).

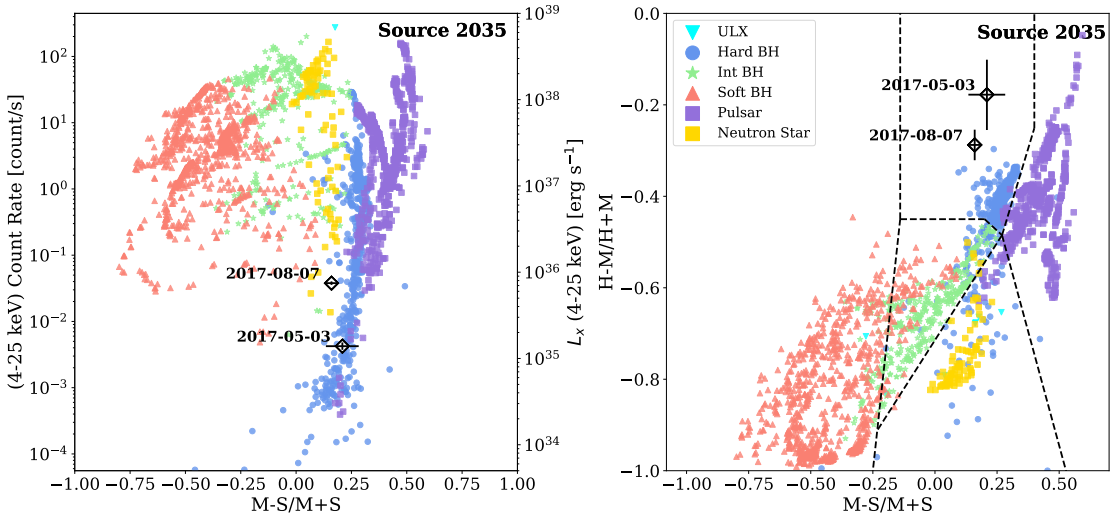

Figure 5.18 Hardness-intensity and hardness ratio diagrams for source 2035 at each observing epoch. See caption of Figure 5.4 for more information on background points. Count rates and hardness ratios for this source during each observation are listed in Table 5.3. ©AAS. Reproduced with permission from Lazzarini et al. (2019).

Chapter 6

THE SPATIALLY RESOLVED RECENT STAR FORMATION HISTORY OF M33

6.1 Introduction

The recent star formation history (SFH) of a galaxy allows us to look backwards in time to see the effects of the astrophysical phenomena that have influenced its evolution. If this recent SFH can also be spatially resolved, we can see the impact of the astrophysics that controls the structure of the galaxy including the formation and evolution of spiral arms and the connection between local star formation events and the dust and gas from which new stars form.

There are several methods for deriving the recent star formation history of a galaxy. For studies of distant galaxies, integrated light can relate a galaxy's current star formation rate to other galaxy-scale properties such as its mass, luminosity, and color. While these studies are useful for obtaining statistically significant results with large samples of galaxies, they do not allow us to study the physics surrounding star formation within each galaxy in detail. For this, we must turn to the more local universe where we can resolve star formation across individual galaxies rather than approximating their physical properties with a handful of parameters.

Most methods for measuring the recent star formation history of local galaxies rely on star formation rate (SFR) indicators, which trace the presence of young, newly formed stars through a variety of signatures, both direct and indirect each with a characteristic time scale. Ultraviolet (UV) emission from young massive stars traces star formation within the last $100-200$ Myr, corresponding to these stars lifetimes (Kennicutt & Evans, 2012). As a direct tracer of star formation, UV emission has been widely used to measure star formation rates in nearby galaxies, especially after the launch of GALEX (e.g. Gil de Paz et al., 2009b). However the UV flux is attenuated by interstellar dust, making it more of a lower limit on the SFR. Hα emission from gas ionized by young O-stars traces very recent star formation within the last 10 Myr. Hα is thus an indirect tracer of young, massive stars ($>$15 M$_{\odot}$), but is the best available measure of the instantaneous SFR in external galaxies. Dust attenuation is also a source of systematic uncertainty in Hα measurements (Kennicutt & Evans, 2012).

A more direct method for measuring the star formation rate is to not just confirm the presence of young, massive stars, but instead to actually count the number of stars of various masses directly

and use this distribution to infer time-resolved star formation rate that would produce the observed population. This method requires deep, high resolution observations to resolve individual stars for a full population. Resolved stellar populations provide the information necessary to produce a spatially resolved and time-resolved star formation history. We can use resolved stars to construct color-magnitude diagrams (CMDs) for specific spatial regions within galaxies. The distribution of stars on the CMD is a product of the galaxy's history of star formation, the evolution of the galaxy's metallicity, and the initial mass function (IMF) observed through the distribution of dust. Like all SFH measurement techniques, modelling the CMD relies on assumptions about the IMF, stellar evolution and atmospheric models, binary fraction and the dust will influence the results. CMD fitting is the only method we currently have to produce a time-resolved SFR measurement.

Much of the early work using CMD fitting on galaxies in the local universe focused on low mass galaxies and smaller portions of large galaxies. Dwarf galaxies are an excellent target for resolved stellar populations work because of their abundance in the Local Volume, making them close enough to resolve their individual stars (e.g., Harris & Zaritsky, 2004, 2009; McQuinn et al., 2010; Weisz et al., 2011, 2014; Geha et al., 2015; Cignoni et al., 2019). Other studies focused on larger galaxies have often relied on small fields across the disk to answer questions about galaxy evolution, such as inside-out growth, but these small fields make resolving the temporal evolution of large scale structures such as spiral arms or bars difficult (e.g., Williams, 2002, 2003; Brown et al., 2006, 2007, 2008; Williams et al., 2009, 2010; Bernard et al., 2012, 2015).

CMD modelling has successfully derived spatially resolved SFHs for well-resolved galaxies. There have been several significant applications of this SFH measurement technique in nearby galaxies including M31 (Lewis et al., 2015; Williams et al., 2017), M33 (Williams et al., 2009), M81 (Choi et al., 2015), NGC 300 (Gogarten et al., 2010), and NGC 2403 (Williams et al., 2013b).

Lewis et al. (2015) provided the first spatially resolved star formation history of a significant portion of an L_* galaxy, M31, using photometry from the Panchromatic Hubble Andromeda Treasury (PHAT). Their fits were optimized for main sequence stars, providing a recent star formation history for roughly 9000 100 pc by 100 pc regions across the northern third of the star forming disk within the last $\sim$500 Myr. Williams et al. (2017) provided an analogous measurement of

the spatially resolved ancient star formation history of M31 by focusing their fits on older stellar populations. Both studies capitalized on the rich dataset from PHAT, which provided six-band photometry from the near-infrared through near-UV for over 100 million individual stars in M31 (Dalcanton et al., 2012; Williams et al., 2014b).

The spatially resolved SFH maps derived via CMD-modelling have had several significant applications in subsequent work. By comparing the spatially resolved SFH maps derived via CMD-modelling with SFRs derived from various indicators, Lewis et al. (2017) found that the SFR indicators in M31 were under-estimating the total amount of star formation. Díaz-Rodríguez et al. (2018) used SFH maps to measure the progenitor mass distribution for core collapse supernovae in M31 and M33 using the SFH maps of Lewis et al. (2015) and Jennings et al. (2014). The Lewis et al. (2015) SFH maps in M31 have also been used to measure the age distribution of high mass X-ray binaries in M31 (Lazzarini et al., 2018, 2021).

The M31 results have been important, but it is only one system, moreover, one that is recovering from a major merger. In this chapter, we derive the spatially resolved recent SFH of M33. M33 is the third most massive galaxy in the Local Group after M31 and the Milky Way, making it an obvious next target for CMD-fitting based SFH measurements. Its proximity allows us to resolve stars down to the ancient main sequence (Williams et al., 2009). In fact, we can resolve its stellar populations better than we can in M31 due to its similar distance but lower stellar surface density.

The contrasts between M33 and M31 and the Milky Way make it an excellent target to study star formation. The star formation rate intensity of M33 is higher than M31 (Verley et al., 2009; Lewis et al., 2015), allowing us to study high intensity star formation regions. M33 also has a well known metallicity gradient (Magrini et al., 2009, 2010; Toribio San Cipriano et al., 2016; Lin et al., 2017), which allows it to fill in the gap in metallicity-space of the Local Group galaxies between M31 and the Large Magellanic Cloud. Unlike M31, M33 has a quiescent merger history (i.e. has not undergone a significant merger event), which is supported by observations of inside-out growth of its disk (Williams et al., 2009). It does not have a significant bulge component (Kormendy & McClure, 1993; McLean & Liu, 1996) and has been observed to host a weak bar (Elmegreen et al., 1992; Regan & Vogel, 1994; Block et al., 2004; Hernández-López et al., 2009; Corbelli &

Walterbos, 2007), both of which reduce confusion between bulge and disk stellar populations.

There has been significant previous work to measure the spatially-resolved recent SFH of M33 using star formation indicators across the electromagnetic spectrum and resolved stellar populations. In the following paragraphs we will discuss what is already known about the spatially resolved recent SFH from SFR indicators before discussing previous work measuring the spatially resolved recent SFH via CMD-modelling.

The spatially resolved recent SFH has been previously studied using broadband fluxes. Verley et al. (2009) measured the global SFH of M33 using extinction corrected FUV and Hα flux and detected a radial decline in SFR. Verley et al. (2007) measured the global and local SFR of M33 using 24 μm emission from HII regions. Boquien et al. (2015) found that SFR indicators are unreliable on scales smaller than 1 kpc by comparing the emission in bands with various SFR estimators at different resolutions. This highlights the importance of CMD modelling, which can resolve SFHs on a finer spatial scale.

CMD-fitting has been used to measure the recent SFH of M33 in targeted regions of the disk. Barker et al. (2007) presented the first application of CMD-fitting to measure the SFH of M33 . They analyzed three fields 4−6 optical scale lengths from the center of the nucleus and found that the mean age and metallicity of M33 decrease with radius. Williams et al. (2009) used CMD-fitting of resolved stellar populations to measure the SFH for four fields across the disk of M33. They found that the age of the majority of stars decreases with radius, suggesting inside-out growth of the disk of M33. Barker et al. (2011) applied CMD-fitting to two regions in the far outer disk of M33 and confirmed that the previously observed inside-out growth extends to the far outer disk. Jennings et al. (2014) used CMD-based SFH measurements to study star formation around supernova remnants in M33 and M31 in order to measure the progenitor masses. Their findings suggest that the most massive stars do not explode as supernovae, although they do not rule out the possibility of bias in their supernova sample. These CMD-based SFH measurements were targeted and did not cover the full disk, or a large contiguous area of the disk of M33. For that reason, the work presented in this chapter is a significant improvement, allowing us study temporal evolution in morphological features that is only possible with a survey covering a large area of M33.

We generate maps of SFH within the last ∼500 Myr in M33 using optical photometry from the Panchromatic Hubble Andromeda Treasury: Triangulum Extended Region (PHATTER) survey (Williams et al., 2021). Our approach mirrors that in Lewis et al. (2015)'s analysis of PHAT, allowing the two measurements to be compared. This presents a significant improvement over previous efforts to measure the spatially-resolved recent SFH of M33. While others have used CMD-fitting to derive SFHs in M33 (Williams et al., 2009), this will be the first application of this technique with such a fine spatial grid, across such a large area of M33, and with such high quality photometry. This chapter is one of the first projects using the rich PHATTER dataset to study the star formation, dust, morphology and more with six-band photometry for over 22 million individual stars in M33.

In this chapter we use optical photometry from the PHATTER survey (Williams et al., 2021) to derive the spatially resolved recent star formation history of M33. In Section 6.2 we present the optical photometry used as well as our method for creating artificial stars to measure photometric errors. In Section 6.3 we present our method for deriving the spatially resolved recent SFH of M33. In Section 6.4 we present the resulting SFH maps and in Section 6.5 we discuss our results. In Section 6.6 we summarize our findings.

6.2 PHATTER Data

We derive the spatially-resolved recent star formation history of M33 using photometry from the PHATTER survey[1]. The PHATTER survey covered a 14 kpc^2 region in the center of the star forming disk of M33, as shown in Figure 6.1. The PHATTER photometry catalog contains over 22 million individual stars and includes six filter photometry from the near-infrared to near-ultraviolet, as discussed in detail in Williams et al. (2021). The data we use in our analysis comes from the ACS (optical; F475W and F814W) data alone. The use of the optical-only catalog was critical for creating the artificial star tests (ASTs) in a reasonable time and creating a catalog of homogeneous exposure times across the survey footprint. We compute the SFH for all of the area within the

[1] https://archive.stsci.edu/hlsp/phatter

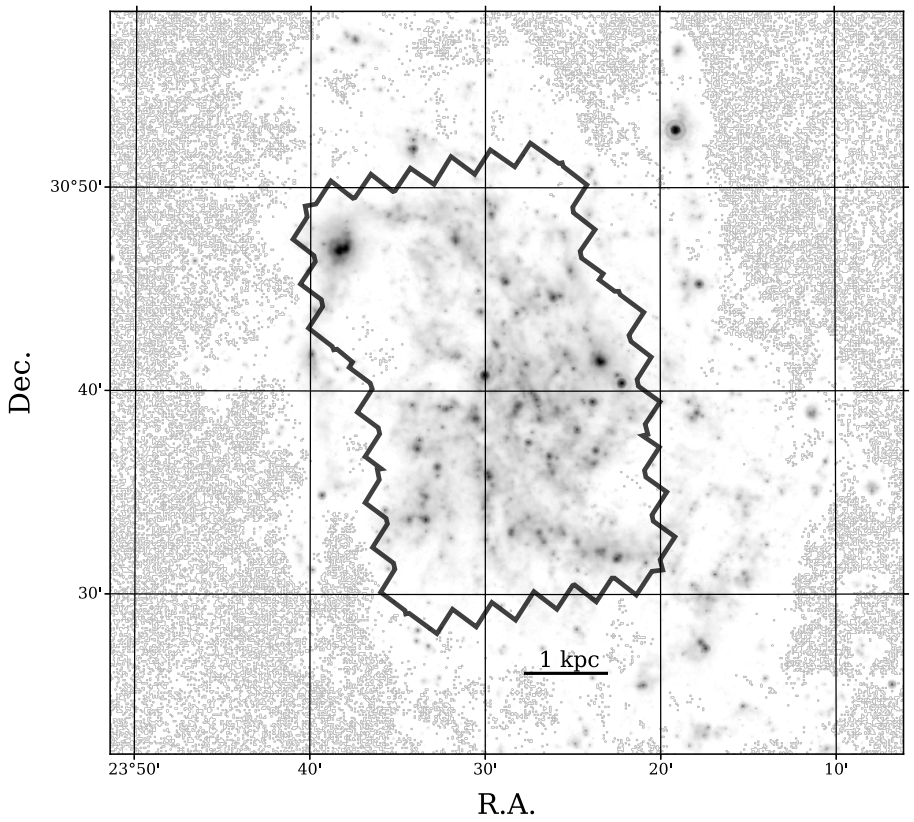

Figure 6.1 The PHATTER survey footprint overlaid on a 24μm image of M33 (Tabatabaei et al., 2007). The outline was generated with the ACS exposure map from the PHATTER survey and includes all regions for which star formation histories were calculated for this paper. The full survey outline was divided into 2005 individual regions that measure 100 pc on a side, using a grid of constant R.A. and Dec.

PHATTER survey outline indicated in Figure 6.1.

6.2.1 Photometry and Catalogs

We use optical photometry in the F475W and F814W bands for our measurements. We use the "gst" catalogs, which contain "good stars" that pass cuts related to their signal to noise, crowding, and sharpness. Specifically, all stars in the "gst" catalog have S/N>4, sharpness^2 <0.2, and crowding<2.25. These cuts are designed to leave only the stars with the highest quality photometry for our measurements. For our analysis, we divided the "gst" photometric catalog into 100 pc

by 100 pc regions along lines of constant R.A. and Dec., producing roughly 2000 regions across the survey area.

6.2.2 Artificial Star Tests

It can be challenging to accurately measure the magnitudes of stars in crowded regions. Faint stars can blend together, biasing the measured flux from other stars within the same region, such that magnitudes of stars in regions of high stellar density will have more biased, noisier measured flux. We quantify the degree of bias, noise and completeness in our photometric measurements using ASTs.

We repeatedly insert artificial stars into an image and then run the image through our standard photometric pipeline, as described in Williams et al. (2021). The measured difference between the input and recovered magnitude of these stars to quantify the effect of crowding in that region. The same test can be used to set the completeness. We calculate the magnitude at which 50% of the artificial stars are recovered and use this as our limiting magnitude when we measure the SFH in each region. Because these effects are sensitive to both stellar flux and stellar density, we want to repeat this process for stars across the CMD for for a range of local stellar densities.

Rather than fully populating each pixel with the required number of artificial stars, we take advantage of fact that because the photometric effects of crowding are primarily density-dependent, we can combine ASTs from across the galaxy, as long as the background stellar density is similar. We quantify local density using the number of stars in the "gst" catalog per square arcsecond, as listed in Table 6.1. We grouped artificial star tests by stellar density to increase the number of tests that can be used for each of the SFH regions. For each of the $\sim$2000 regions in our SFH analysis, we used a set of ASTs for a region of similar stellar density. The number of ASTs used for each stellar density bin are listed in Table 6.1.

When we solve for the SFH for each of the $\sim$2000 regions used in our analysis, we adopt the magnitude at which 50% of the stars are recovered as our limiting magnitude. We list these 50% completeness limits in Table 6.1. The 50% completeness limits listed in Table 6.1 correspond to a main sequence turn off (MSTO) age of about 9.5 log(year) at the faint end and about 9.2 log(year)

at the bright end. This suggests that our recent (<500 Myr) SFH maps should be complete, even in the most crowded regions.

6.3 Derivation of the SFHs

We use the CMD-fitting code MATCH to derive the SFHs (Dolphin, 2002). MATCH finds the combination of stellar ages and metallicities that best reproduces the observed CMD. MATCH incorporates photometric errors and completeness that are measured in the ASTs (see Section 6.2.2) and fits for dust extinction. The best fit SFH is then determined by MATCH using a Poisson maximum likelihood technique. For more details, see Dolphin (2002) and Lewis et al. (2015).

Because our focus is on the recent SFH only, we exclude regions of the CMD occupied by older, redder stars. The atmospheres and evolution of main sequence stars are generally better understood than later evolutionary stages, making the SFH recovery for young ages reasonably secure. In our fits, we only include stars with a F475W magnitude between 16 and 27 and an F814W magnitude between 15 and 26. We exclude stars that fall within the reddest, faintest region of our CMDs: stars with both F475W magnitudes greater than 21 and F475W-F814W color greater than 1.25.

The average number of stars we fit on the CMD for a given 100 pc by 100 pc analysis region is ∼8000, with a standard deviation of 3000 stars. The MATCH fitting of this region is essentially finding the intrinsic distribution of young stars and dust that reproduces the luminosity function and color distribution of the MS, given photometric selection, noise, and biases from the ASTs.

MATCH requires the user to input the age bins, metallicity, distance, extinction, binary fraction, and choice of initial mass function (IMF). Where possible, we adopt the same model parameters that Lewis et al. (2015) used to fit the SFHs in M31 using the PHAT data. We set a fixed distance modulus of 24.67 (de Grijs & Bono, 2014), use a binary fraction of 0.35, and draw the mass of the secondary from a uniform distribution and Kroupa IMF (Kroupa, 2001). We use the same set of age bins as Lewis et al. (2015), which span from 6.6 to 10.15 log(years) with a spacing of 0.1 dex, with the last bin spanning from log(time)=9.9−10.15. The Padova isochrones used in our fits do not contain tracks for stars younger than 4 Myr. We calculate the stellar mass formed in the youngest time bin (between 6.6 and 6.7 log(years)) for each spatial region, and then derive

Table 6.1. 50% Completeness Limits

Stellar Density [stars arcsec^{-2}]	m_{F475W} [mag]	m_{F814W} [mag]	Number of ASTs used	Mean Dist. from Center of M33 [kpc]
0−10	27.6	26.7	53031	2.6
10−12	27.6	26.7	39977	2.7
12−14	27.6	26.7	57711	2.6
14−16	27.5	26.6	59811	2.4
16−18	27.5	26.6	88746	2.3
18−20	27.5	26.6	102572	2.1
20−22	27.5	26.5	163183	2.0
22−24	27.4	26.4	194591	1.8
24−26	27.4	26.4	169226	1.7
26−28	27.3	26.3	142455	1.6
28−30	27.2	26.2	152861	1.3
30−32	27.2	26.1	145009	1.1
32−34	27.1	26.0	108324	0.9
34−45	26.7	25.4	144051	0.5

Note. — Table listing 50% completeness limits used in our SFH calculations, grouped by stellar density. Column 1 indicates the range of stellar densities for which the given 50% completeness limits apply. Columns 2 and 3 list the 50% completeness limits in F475W and F814W, respectively. In column 4 we include the number of ASTs used for each stellar density bin. In column 5 we list the mean distance from the center of M33 for analysis regions of the given density bin. We adopt the center of M33 from the FUV D25 ellipse from Gil de Paz et al. (2009b).

the SFR that extends to the present day by dividing that stellar mass by the total time between the upper bin edge (log(time)=6.7) and the present day (0 Myr).

Although MS evolutionary models are better understood than other phases the observational property of the MS does depend somewhat on the choice of isochrone model. We adopt the Padova (Marigo et al., 2008) isochrones with updated AGB tracks (Girardi et al., 2010) as our fiducial models for the SFHs reported in this chapter. The Padova models have a [M/H] range of [-2.3,0.1] with a resolution of 0.1 dex. We set limits on the allowed metallicity, [M/H], values for the oldest and youngest time bins, allowing ranges of [-2.3,-0.9] and [-0.4,0.1], respectively. To assess systematic uncertainties that come from choice of stellar models, we also derive SFHs using the MIST isochrones (Dotter, 2016). The MIST models have an allowed metallicity, [M/H], range of [-2.0,0.5] and we use the same metallicity limits for the oldest and youngest time bins when running MATCH with the MIST models as we do with the Padova models.

To generate our SFHs, we must generate synthetic CMDs with stars of various ages and metallicities distributed over a two dimensional parameter space of age and metallicity. While age-metallicity degeneracy is not as strong for main sequence stars, the metallicity will strongly effect the color of the MS (e.g., Gallart et al., 2005). M33 has a well-established metallicity gradient (Magrini et al., 2009, 2010; Toribio San Cipriano et al., 2016; Lin et al., 2017). We want to confirm that we recover this metallicity gradient to confirm that our fits are reliable. Generally, we find that our best-fit metallicity decreases with radius as expected.

To check the sensitivity of our fits to the metallicity gradient, we binned the SFH regions into annuli with a width of 1 kpc from the D25 ellipse center of M33 (Gil de Paz et al., 2009b) and measured the mean metallicity in each radial bin. We find a radial gradient of the metallicity of approximately 0.1 dex from the center of the PHATTER survey area out to the furthest regions, which are between 3 and 4 kpc from the center. This slope agrees with previous measurements of the slope of the metallicity gradient of M33 from observations of H II regions and planetary nebulae (e.g. Magrini et al., 2010). We did not observe a metallicity gradient when repeating this exercise wit the MIST models, suggesting that they are not as sensitive to metallicity for main sequence and He-burning stars that dominate the CMD. While our methodology is not optimized

for measuring the metallicity of M33, it is encouraging that our fits recover the metallicity gradient of M33 and this suggests that our SFH measurements are not systematically affected by metallicity.

6.3.1 Choice of Region Size

To generate the spatially resolved recent star formation history of M33, we use a region size that is approximately 100 pc on a side (projected $\sim 24''$). This is the same region size that was used to generate the spatially resolved recent star formation history of M31, and we chose to use the same region to make our results directly comparable. As described by Lewis et al. (2015), the 100 pc region size was chosen because it bridges the gap between previous work on Galactic pc scale star formation and star formation in more distant galaxies on kpc scales. In addition to scientific interest, the region size was chosen to provide a similar number of stars for the CMD for each individual region and to fit within the computational constraints of our analysis. Given the comparable distance of M33 to M31 and the analogous survey design, we chose to use the same region size for our analysis, which also eases comparison between the M33 and M31 results.

6.3.2 Extinction

M33 is lower metallicity than M31 and thus has only moderate dust extinction (Corbelli, 2003). It does, however, have enough dust that it needs to be accounted for when modeling the CMD. we account for dust in our CMD fitting by fitting for two parameters that describe the dust in each SFH region: foreground extinction (A_V), which reddens all the stars uniformly, and differential extinction in star forming regions (dA_V), which affects a subset of stars. We briefly describe the method we use for fitting A_V and dA_V below, but for a more in depth discussion, see Section 3.1 of Lewis et al. (2015).

We determine the best A_V and dA_V values by running our SFH calculations multiple times over a grid of A_V and dA_V values, subject to constant $A_V + dA_V \leq 2.5$ in order to avoid our SFH fits applying arbitrarily high dA_V at high extinction. First, we run the SFH calculations over a grid of A_V and dA_V values with a spacing of 0.3 over the range of A_V=[0.0,1.0]. We then choose the best (A_V,dA_V) pair using a maximum likelihood technique. Then we create a finer grid with 0.1

spacing in both values within 2σ of the best (A_V,dA_V) pair and repeat our maximum likelihood technique to identify the best fit (A_V,dA_V) for the region. This method is described in more detail in Appendix B of Lewis et al. (2015).

6.3.3 Uncertainties

Uncertainties in our measurement of the SFH of M33 come from a combination of random and systematic uncertainties, and dust. We quantify our random uncertainties and uncertainties due to dust using the same methods as Lewis et al. (2015).

The random uncertainties were calculated using a hybrid Monte Carlo process (Duane et al., 1987) implemented as part of the `MATCH` software package (Dolphin, 2013). These random uncertainties scale with the number of stars on the CMD for a given region, with more sparsely populated CMDs resulting in higher random uncertainties. The MCMC routine generates 10,000 possible SFHs for the CMD from a given analysis region. Each SFH has an associated likelihood value and the best SFH is the one with the highest likelihood value. The density of SFHs is then turned into a probability density to identify $\pm1\sigma$ errors on the SFR measured for each time bin. This method accounts for cases where the maximum likelihood SFH has zero star formation in individual time bins, allowing the uncertainties of the SFR on those time bins to be estimated.

To assess systematic uncertainties, we ran our full set of SFH calculations with two sets of stellar models: the Padova models that we use as our fiducial model set and the MIST stellar models. Differences between stellar models mainly stem from how they model different aspects of stellar evolution including mass loss, convection, and rotation (Conroy, 2013). These differences tend to be greater in post-main sequence phases of stellar evolution and for the most massive stars. We show the SFH for the full M33 PHATTER survey footprint for both sets of models in Figure 6.4. The dark histogram represents the Padova models and the lighter pink histogram represents the MIST models.

The Padova and MIST models agree quite well for ages where main sequence stars dominate. The two models agree within their random uncertainties for most time bins older than about 15 Myr, showing that random uncertainties dominate the errors on the SFH at these ages. The largest

systematic uncertainty in our SFR measurements are in the youngest time bins, where models for the most massive stars generate most of the uncertainty. At the youngest ages (<15 Myr), the model sets differ by up to a factor of two in the measured SFR, as expected.

Finally, we consider uncertainties presented by the dust content in each individual SFH region. To quantify the uncertainty presented by dust in our SFH fits, we first select the best fit A_V, dA_V pair for each region estimated via maximum likelihood, as described in more detail in Section 6.3.2. Because we only refine our A_V, dA_V grid down to 0.1, we note that we might have determined a slightly different value for A_V, dA_V if we had used a finer grid. We determine the uncertainties due to dust by combining all SFHs with different A_V, dA_V values, weighted by their likelihood values to determine $\pm 1\sigma$ uncertainties. These dust uncertainties are incorporated into our uncertainties reported in Table 6.2.

Lastly, we acknowledge that our choice of binary fraction could present some uncertainty in our SFH calculations. For consistency, we adopt the same binary fraction used by Lewis et al. (2015) in deriving the recent SFH for M31 using the PHAT data. Lewis et al. (2015) tested various binary fractions in two SFH regions in their analysis and found that the choice of binary fraction did not have a significant impact on the SFH. They found that while the inclusion of binaries could impact the CMD for a given region, this effect was overpowered by the uncertainties due to dust, and so the choice of binary fraction did not have a measurable impact on the best fit. To keep our analysis as similar to theirs as possible for optimal comparison between surveys, we chose to adopt the same binary fraction in our work.

6.3.4 Reliability of SFHs as a Function of Lookback Time

Our SFH measurements are not sensitive to the older stellar populations that were excluded from the red side of the CMD in our fits. Our SFHs are therefore only reliable back to the ages of the oldest MS stars analyzed in each region. Due to crowding and dust extinction, this age can vary by region.

Based on analysis by Lewis et al. (2015), we only perform scientific analysis on our SFH measurements back to 400 Myr, which is a conservative limit. We briefly summarize their analysis

below.

Lewis et al. (2015) created artificial CMDs with MATCH to examine the sensitivity of their SFH measurements as a function of lookback time. They created artificial CMDs with constant SFR and solar metallicity and varied the stellar density and dust extinction. They use ASTs from regions of the PHAT survey with higher and lower crowding due to high stellar density and then created the SFHs with those ASTs using three different levels of dust extinction (unreddened, median reddening, maximum reddening). They found that in the least crowded and unreddened regions, their SFH measurements were reliable back to $\sim$1 Gyr. However, in the most crowded and dusty regions, their SFH measurements were only reliable up to no more than 500 Myr ago. As a result, they adopted the conservative limit of 400 Myr for their scientific analysis, which we also adopt in this work, although we will sometimes display maps for older ages when reliable.

6.4 Results

In this section we present the integrated and spatially-resolved SFHs for the PHATTER survey in M33. When combined, the SFH measurements for all of the sub-regions reveal the integrated recent SFH of M33 within the PHATTER footprint. In order to produce the integrated SFH, we add up the stellar mass formed within each spatial bin in the same time bin. In Figure 6.2, we show the spatially-resolved SFH, plotting the SFR measured in each spatial bin within the time ranges specified in the upper left corner of each panel. At the youngest ages, we have grouped the time bins together into bins of roughly 25 Myr to create smoother maps for our analysis. Each spatial bin is represented as a pixel, with the color of the pixel corresponding to the best-fit SFR during the time span specified. Regions plotted in black have a measured SFR of below 10^{-5} $M_{\odot}$ yr^{-1}, comparable to the typical uncertainty in low SFR regions. We note that towards the older bins, the central region of the galaxy does not have measured star formation. We are still in the process of understanding the reason for this. It does not seem to be due to crowding given our completeness limits in the highest stellar density regions (see Table 6.1), but we cannot yet fully rule out this explanation.

We also present the integrated SFH over the last 630 Myr in Figure 6.3. To generate this figure,

we summed the total stellar mass formed in each sub-region over all time bins back to 631 Myr. We also present the total SFH of M33 within the PHATTER footprint in Table 6.2. We list the start and end of each time bin, using the full resolution of our SFH fits, 0.1 log(years). We also include uncertainties on our full SFR measurements which include both random and dust uncertainties.

The average SFR over the last 100 Myr within the PHATTER survey outline is 0.33 ± 0.02 $M_\odot$ yr^{-1}. To compare this number with previously measured values, we account for the fact that our survey does not cover the full D25 area of M33. We adopt the FUV D25 ellipse from Gil de Paz et al. (2009b). We then measure the total FUV flux within this D25 ellipse and determine the fraction of the flux contained within the PHATTER survey footprint. We find that the fraction of total flux within our survey footprint is $\sim$45%, meaning we need to multiply our total SFR measurement by a factor of $\sim$2.3 to compare with global FUV SFR measurements.

When we scale up our SFR by this factor, we get a total SFR of $\sim$0.75 $M_\odot$ yr^{-1}. This value can be compared to FUV SFR measurements, which also trace star formation within 100 Myr. Verley et al. (2009) measured the global SFR of M33 using a combination of Hα and FUV flux measurements, using IR luminosities to correct for dust extinction. Their extinction corrected value for the global SFR in M33 over the last 100 Myr is 0.45 ± 0.10 $M_\odot$ yr^{-1}. This measurement is lower than our scaled-up global SFR and does not agree within errors, suggesting that the integrated light measurements may be missing some star formation that the resolved stars are able to capture. This underestimation agrees with findings by Lewis et al. (2017), who found that the 24 μm corrected FUV flux underestimated the SFR by a factor of $2.3-2.5$ when compared to CMD-based SFHs in M31.

6.5 Discussion

The SFH maps reveal multiple structures in the disk of M33 including spiral arms and a central bar. We discuss both the spiral and bar structures of M33 in the following subsections.

Table 6.2. Total PHATTER SFH

Age Range [log(years)]	Age Range [Myr]	Star Formation Rate [$M_\odot$ yr^{-1}]
6.6−6.7	4 − 5	$0.12^{+0.04}_{-0.04}$
6.7−6.8	5 − 6	$0.39^{+0.04}_{-0.03}$
6.8−6.9	6 − 8	$0.30^{+0.03}_{-0.02}$
6.9−7.0	8 − 10	$0.25^{+0.02}_{-0.02}$
7.0−7.1	10 − 13	$0.33^{+0.02}_{-0.02}$
7.1−7.2	13 − 16	$0.30^{+0.02}_{-0.02}$
7.2−7.3	16 − 20	$0.31^{+0.02}_{-0.02}$
7.3−7.4	20 − 25	$0.28^{+0.02}_{-0.02}$
7.4−7.5	25 − 32	$0.33^{+0.02}_{-0.02}$
7.5−7.6	32 − 40	$0.38^{+0.02}_{-0.02}$
7.6−7.7	40 − 50	$0.28^{+0.02}_{-0.01}$
7.7−7.8	50 − 63	$0.32^{+0.02}_{-0.02}$
7.8−7.9	63 − 79	$0.38^{+0.02}_{-0.02}$
7.9−8.0	79 − 100	$0.38^{+0.02}_{-0.01}$
8.0−8.1	100 − 126	$0.31^{+0.02}_{-0.01}$
8.1−8.2	126 − 158	$0.29^{+0.01}_{-0.01}$
8.2−8.3	158 − 200	$0.26^{+0.01}_{-0.01}$
8.3−8.4	200 − 251	$0.27^{+0.01}_{-0.01}$
8.4−8.5	251 − 316	$0.25^{+0.01}_{-0.01}$
8.5−8.6	316 − 398	$0.32^{+0.01}_{-0.01}$
8.6−8.7	398 − 501	$0.36^{+0.01}_{-0.01}$
8.7−8.8	501 − 631	$0.37^{+0.01}_{-0.01}$

Note. — The total SFH of the PHATTER survey in M33, summed across all spatial regions. The first column lists the start of each time bin in log(years) and the second column lists the end of each time bin in log(years). The third column lists the SFR for that time bin with uncertainties. The listed uncertainties incorporates both random and dust uncertainties. For more information on how these uncertainties were derived, see Section 6.3.3.

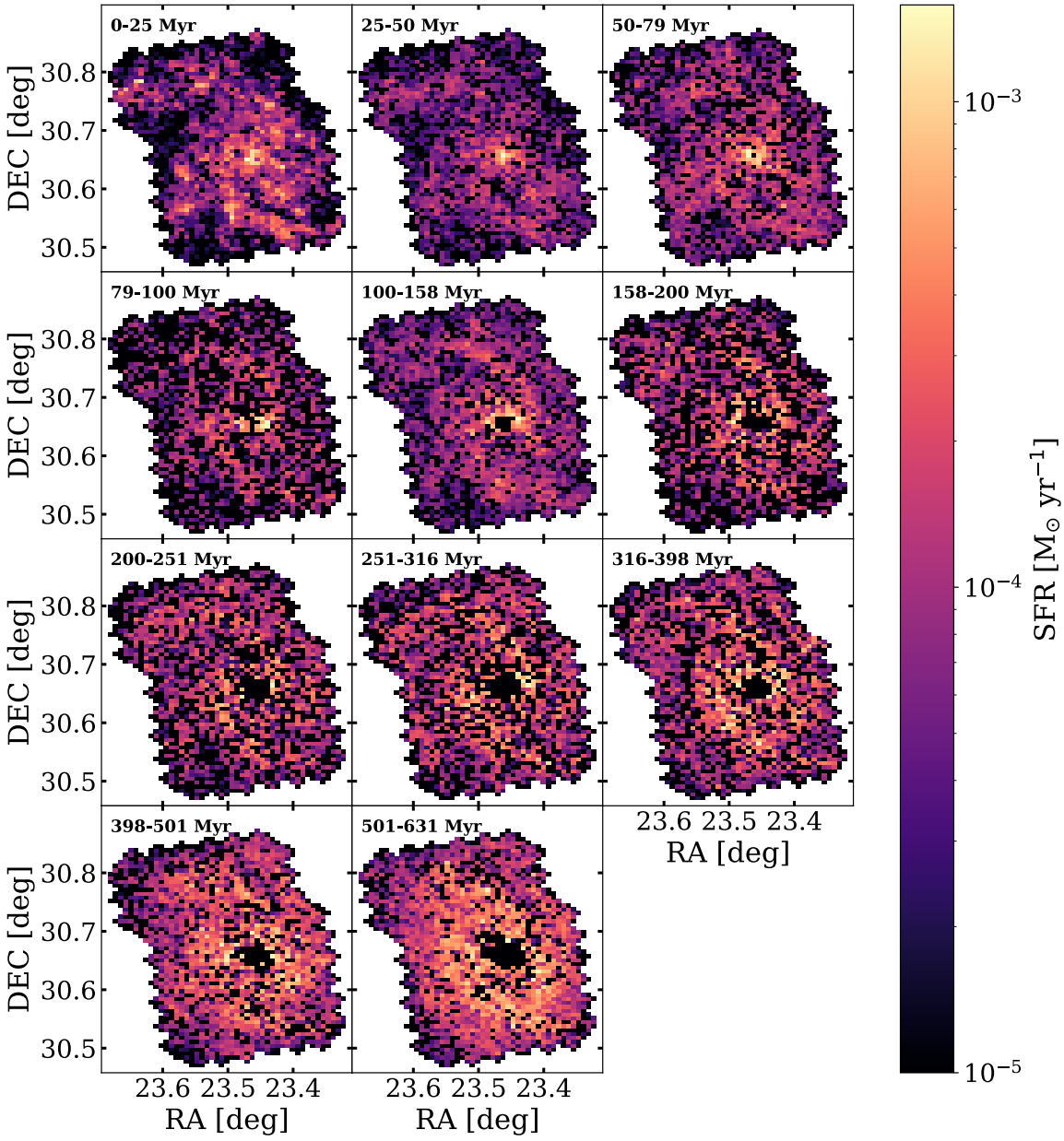

Figure 6.2 SFH maps of M33 within the PHATTER footprint area over indicated timescales. These time bins do not reflect the full 0.1 log(year) resolution of our SFH fits, but we group the SFH up to 100 Myr ago into 25 Myr bins to more clearly show the structure of the spiral arms. The SFR values shown are the best-fit values from our fits. Each pixel represents a 100 pc by 100 pc region for which we derived the SFH using CMD-fitting.

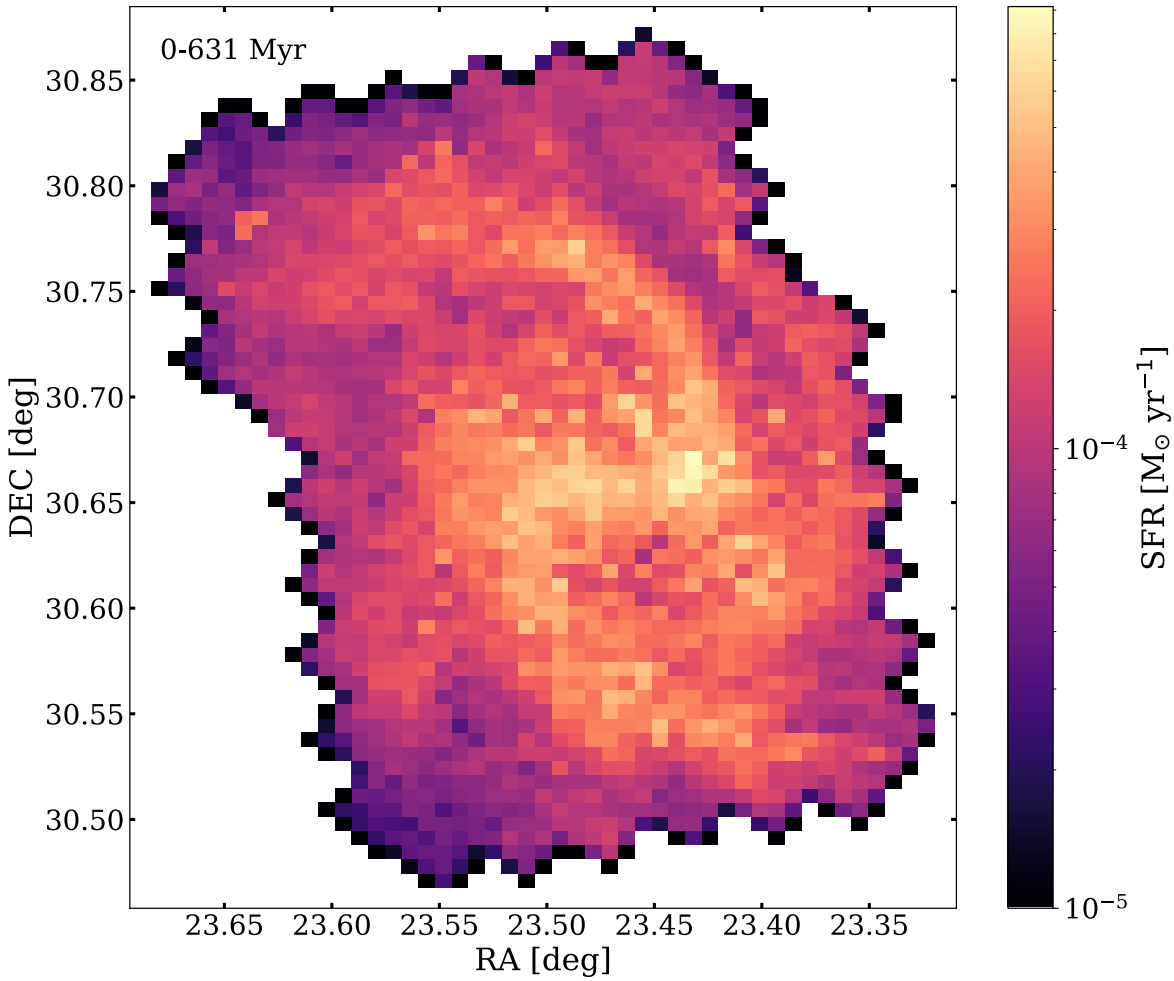

Figure 6.3 The spatially resolved star formation rate of M33 between 0 and 631 Myr ago. This map is essentially a combination of the multiple SFH maps shown in Figure 6.2 across temporal bins. The SFR value in each bin was calculated by summing the stellar mass formed in that spatial bin over all time bins between 0 and 631 Myr ago and then dividing by the total elapsed time. Each pixel represents a 100 pc by 100 pc region for which we derived the SFH using CMD-fitting. We note that the central pixels in the later time bins (older than 100 Myr) show 0 SFR, as noted in Section 6.4. The cause for this is not yet clear, but could be due to incompleteness.

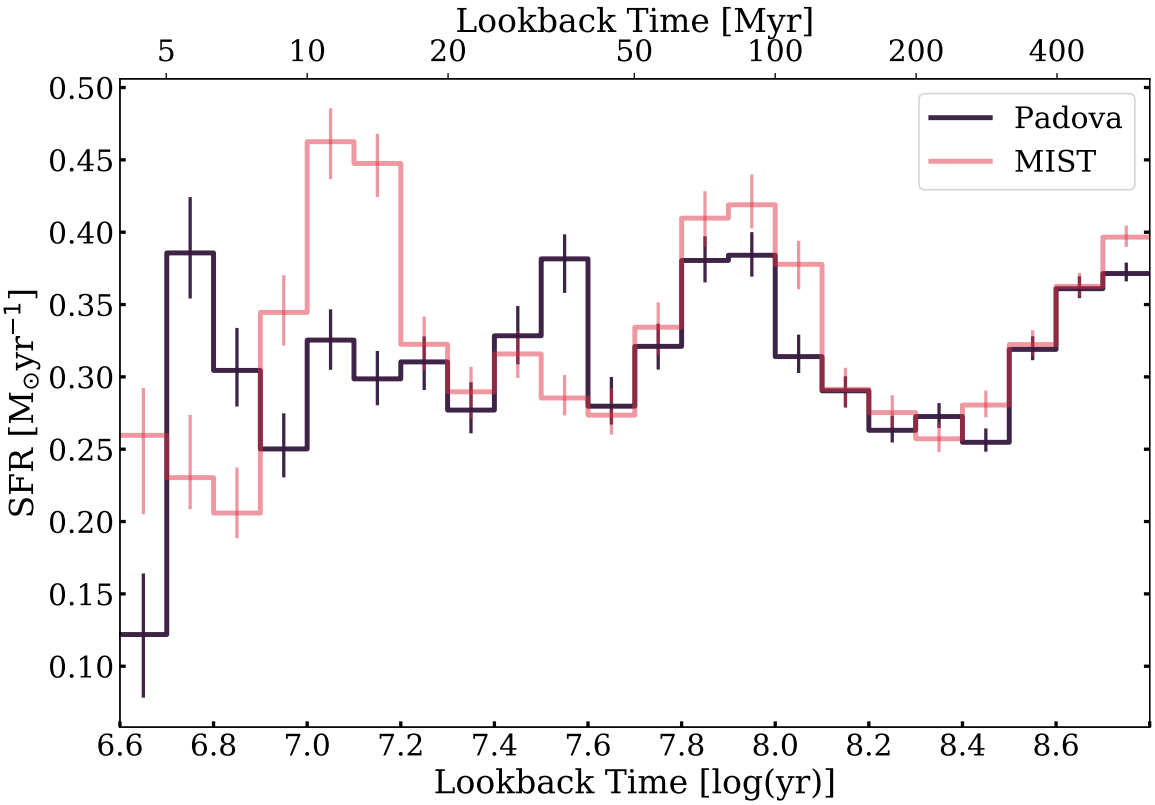

Figure 6.4 The total SFH for the PHATTER survey area, which covers ∼14 square kpc. This figure combines spatial bins in each 0.1 log(year) time bin, using the full time resolution of our fits. The error bars represent the random and dust uncertainties. The black histogram represents the SFH when we use the Padova stellar models in our CMD fitting, which we adopt as our fiducial stellar models. The pink histogram shows the SFH when we use the MIST stellar models. The two SFH fits illustrate systematic uncertainties in our measurements. The models agree very well up to about 20 Myr ago. Differences at younger ages reflect differences between how the two model sets treat the most massive, young stars. For a full discussion of the differences between these two SFH measurements and systematic uncertainties in our SFH measurements, see Section 6.3.3. The SFR values and error bars plotted for the Padova stellar models are listed in Table 6.2. Due to the extent of our survey area, we expect to have measured roughly 45% of the SF in M33, which we determined by comparing to the fraction of total FUV flux within the PHATTER survey footprint.

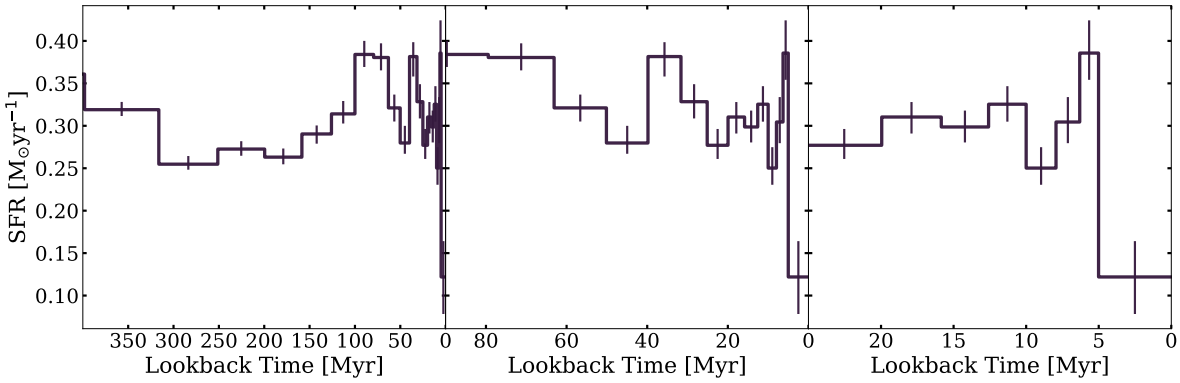

Figure 6.5 The total SFH for the PHATTER survey area from the Padova stellar models. These figures use a linear time scale on the x-axis to illustrate the resolution of our fits at different time scales. The left panel shows the SFH back to 400 Myr ago, the middle panel shows the SFH back to 90 Myr ago, and the right panel shows the SFH back to 25 Myr ago. The SFR values and error bars plotted are listed in Table 6.2.

6.5.1 Evolution of Spiral Structure

We observe evolution in the spiral arm structure of M33 within the PHATTER survey footprint. The earliest time bins for which we measure the spatially resolved SFH, we observe a flocculant spiral structure. In Figure 6.2, we observe the flocculant spiral structure in the first three time bins, between the present day and $\sim$ 79 Myr ago. Starting in the fourth time bin, 79$-$100 Myr ago, we begin to see the emergence of a strong two armed spiral structure, which is evident in all of the time bins $>$100 Myr.

To better visualize the evolution in spiral structure, we combined the SFR measurements for all bins younger than 79 Myr (which are somewhat noisy due to the stochastic nature of SF over short time intervals) and all bins older than 79 Myr. We present this time-combined SFH map in Figure 6.6, where the difference between the recent and older structure of the M33 spiral arms is more pronounced.

M33 has been characterized as a flocculant spiral galaxy with a number of weaker spiral arms, rather than the strong arms seen in grand design spirals (e.g. Humphreys & Sandage, 1980; Dobbs et al., 2018). The spiral structure in the left panel of Figure 6.6 (0$-$79 Myr ago) shows multiple,

weak spiral arms, in agreement with the morphology that M33 shows in optical images. This correspondence suggests that the optical morphology is strongly shaped by the very low mass-to-light (M/L) ratio populations of the youngest stars. M33's lack of optically visible strong spiral arms has led to some debate in the literature about whether the spiral structure of M33 is a result of tidal interactions with M31 (e.g. Semczuk et al., 2018) or if this spiral structure arose without interaction, as a result of gravitational instabilities in the stars and gas in M33 (Dobbs et al., 2018). Near infrared (NIR) observations have revealed a stronger two-arm spiral structure within the inner disk of M33 (Jarrett et al., 2003), which would be more consistent with a tidally induced spiral structure. The two-arm structure seen in the NIR agrees with our map of the SFH of M33 between 79 and 631 Myr ago. On the surface, this agreement may be surprising given the differing timescales of the two tracers. The NIR is typically presumed to be dominated by older red giant branch (RGB) and asymptotic giant branch (AGB) stars, far older than 500 Myr. However, there are two possible explanations. First, the NIR is in fact sensitive to red core Helium burning stars, which appear for ages $\lesssim$300 Myr (Melbourne et al., 2012). Second, a strong spiral pattern in the stellar mass (as traced by the RGB stars that dominate the disk mass) can act as a gravitational perturbation that helps confine the younger stars. Thus, while the gravitational instability driven flocculant structure imposed at birth dissipates over $\sim$50 Myr, older stars are swept into the larger tidally-driven gravitational perturbation.

We have used the maps in Figure 6.3 to test for propagation of one of the major spiral arms seen at older ages. We do so by comparing the ages of the stellar populations above and below the upper major spiral arm, which is visible in Figure 6.3. The arm starts in the center of M33 and spirals to the upper left of the image. For spiral arms supported by quasi-static density waves, we would expect an age gradient across the spiral arm. As gas enters into the spiral arm, it is shocked, which results in the formation of molecular clouds where star formation can occur (Roberts, 1969). Not observing an age gradient could suggest that the arm is instead supported by a tidally induced instability.

We traced out the spiral arm using an Hα map of M33 from Hoopes et al. (2001) and then selected SFH regions inside and outside of the spiral arm compared their SFHs. When scaled for

the total area selected, the regions outside of the spiral arm show statistically significant higher SFR within the last ∼30 Myr compared to the regions inside the arm. Our findings suggest that M33's major spiral arms are likely supported by stationary density waves rather than being induced tidally by kinematic interactions with companion galaxies. Our results differ from those by Choi et al. (2015) in M81, where they did not detect an age gradient across a major spiral arm using resolved stellar populations.

A more detailed study of the spiral structure of M33 with the new PHATTER data is forthcoming (A. Smercina, et al., in preparation).

6.5.2 Detection and Formation of M33 Bar

There has been some debate in the literature about whether M33 hosts a central bar. A weak central bar has been observed via photometric measurements at infrared (Regan & Vogel, 1994; Block et al., 2004; Hernández-López et al., 2009) and blue wavelengths (Elmegreen et al., 1992), and via measurements of gas dynamics (Corbelli & Walterbos, 2007).

We observe a bar structure within the center of the disk of M33 that emerges at ages older than roughly 79 Myr. The bar is clearly visible in the total SFH map (Figure 6.3). We wanted to explore the SFH periods where this bar appears in the data. When we look at the time-resolved SFH maps (Figure 6.2), the central regions are difficult to observe because crowding makes it difficult to measure the SFR at in the most central regions of the galaxy. We can use the maps in Figure 6.6 to visualize the timescale on which the bar structure emerges. We created a version of this image where we chose various break-points between the left and right panel. Most notably, when we created a similar figure where the left panel showed the SFH maps from $0-100$ Myr ago and the right panel showed the SFH maps $100-631$ Myr ago, the bar was visible in the left-hand panel. However, when we chose to set the break-point at 79 Myr ago or more recently, the left panel did not show evidence of a bar. This suggests that the gas does not trace the structure of the stellar bar. This is evident in the structure of the youngest stars (age$<$79 Myr), which follow the structure of the gas out of which they recently formed.

More detailed analysis is required to fully characterize our observations of the bar in M33, but

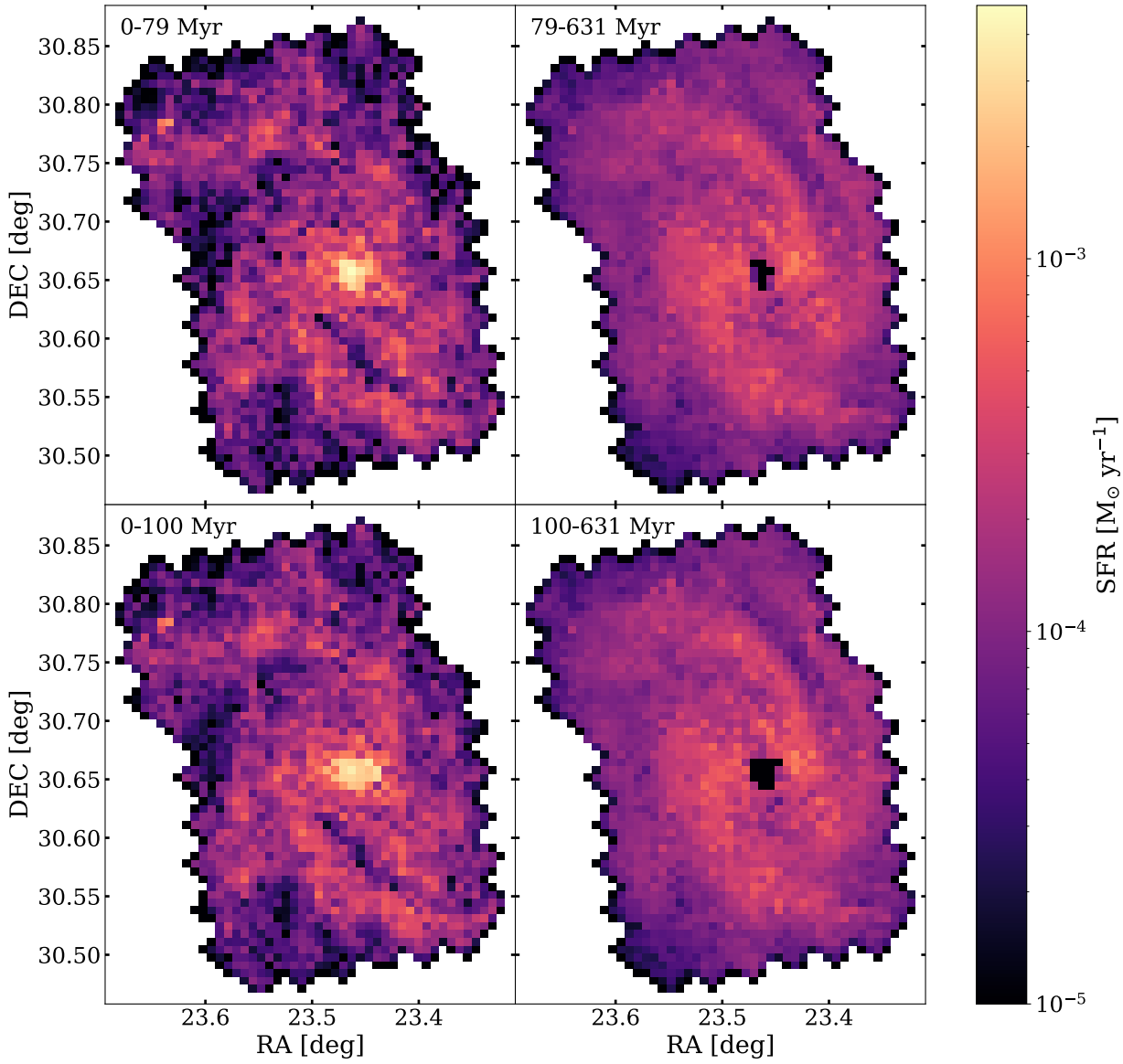

Figure 6.6 Star formation history map for the PHATTER survey footprint in M33. The left panels shows the SFR for each spatial bin, combining all time bins between 0 and 79 Myr ago. The right panel shows the SFR for each spatial bin, combining all time bins between 79 and 631 Myr ago. There is a clear difference between the spiral structure in the left and right panel, indicating a transition in the spiral structure of M33 around 79 Myr ago from a two armed spiral structure (right) to the more flocculant spiral structure we observe today.

its appearance in the star formation history maps helps us estimate a timescale on which large-scale morphological evolution has occurred within the disk of M33. We note that both the shift from a multi- to two-armed spiral and the emergence of the central bar occur on roughly the dynamical timescale of M33.

6.6 Conclusions

We have measured the SFH of M33 within the PHATTER survey footprint, which covers 14 kpc^2 and extends to 3.5 kpc, $1-2$ scale lengths, from the center of M33 (Williams et al., 2021). To measure the spatially resolved recent star formation history, we divided the survey area into roughly 2000 100 pc by 100 pc regions and measured the SFH for each region using color-magnitude diagram fitting. We summarize our main findings below.

1. We find that the SFR of M33 is relatively consistent over the survey area over the past 400 Myr.

2. We measure the mean SFR over the last 100 Myr within the PHATTER survey area to be 0.33 ± 0.02 M$_\odot$ yr^{-1}. When we scale up our measurement to account for the full D25 area of M33, we measure a mean SFR over the last 100 Myr of $\sim$0.75 M$_\odot$ yr^{-1}, which is higher than previous FUV 100 Myr SFR measurements.

3. We measure the current SFR (within the past 10 Myr) within the PHATTER survey area of M33 to be 0.21 ± 0.03 M$_\odot$ yr^{-1}.

4. We observe evolution in the spiral arm structure of M33 over time. The most recent SFH maps of M33 show a flocculant multi-armed structure, while the maps older than ~ 79 Myr ago show a more distinct two-armed structure.

5. We observe a bar in the center of M33, which is observed at ages older than ~ 79 Myr ago. Younger stellar populations formed in more recent star formation episodes do not appear to follow the bar structure.

Chapter 7

CONCLUSIONS & FUTURE WORK

In Chapter 2 I presented the results of the *Chandra*-PHAT survey. We produced a catalog of *Chandra*-detected X-ray sources in M31 within the footprint of the PHAT survey. We used X-ray and optical properties of detected sources to characterize them. We found that most of the optical counterparts of X-ray sources are background galaxies, viewed through the disk of M31. We identified 58 sources with point source optical counterparts, which serves as the basis sample of HMXB candidates in M31 in Chapters 3 and 4. We used color-color diagrams to identify bright, blue point source optical counterparts and found that eight of the point source optical counterparts in our sample had colors typical of massive main sequence stars. We found that the age distribution of HMXBs in our sample peaks between $15-20$ Myr and $40-50$ Myr, in agreement with age measurements in lower metallicity nearby galaxies.

In Chapter 3 I presented analysis of a sub-set of HMXB candidates in M31 for which overlapping *Hubble*, *Chandra*, and *NuSTAR* observations are available. We investigated the correlation between the hard X-ray determined compact object classification made with *NuSTAR* observations and the compact object determined from the *Hubble* imaging from the PHAT survey. We found that nine *NuSTAR* classified non-magnetized neutron stars are associated with star clusters. We also did not find any pulsars or hard accretion state black holes coincident with star clusters. There was not an observed preference for pulsars or hard accretion state black holes associated with UV-bright point source optical counterparts. None of the sources in our sample that are classified as hard accretion state black holes were associated with B-type companion stars, determined via SED-fitting. We found that an equal number of pulsars have point source optical counterparts and do not have point source optical counterparts, which are likely low mass X-ray binaries. We used the spatially resolved recent star formation history of M31 to determine the likely ages of HMXB systems in our sample. We found that three of the HMXBs in our sample are between 25 and 50 Myr old, while two or three are younger. The younger HMXBs are associated with stellar populations that are $\sim$4 and $\sim$10 Myr old. These ages agree with observed HMXB populations in other galaxies, and previous work presented in Chapter 2. This work demonstrates our ability to characterize the full HMXB system – both accreting compact object and companion star – with high resolution, multi-wavelength observations spanning from the nIR/optical/nUV to hard X-rays.

In Chapter 4 I presented analysis of the full *Chandra*-PHAT sample of HMXB candidates using multi-wavelength observations from the PHAT survey, *Chandra*-PHAT, and published *XMM-Newton* spectral fits. In this Chapter, I presented a new method for selecting a high quality sample of HMXBs by combining SED fits of the HMXB companion stars with spatially resolved star formation history maps. We found that the dominant ages of HMXBs in our sample are $10-50$ Myr, in agreement with measurements in other galaxies. We also calculated the HMXB production rate of M31. We calculated that the HMXB production rate between 10 and 50 Myr ago was $\sim 2 \times 10^{-6}$ HMXB systems/$M_{\odot}$, before dropping off. I also presented the number of HMXB systems formed in the last 50 and 80 Myr per unit SFR. For our best sample of HMXBs, $89-107$ HMXBS/($M_{\odot}$ yr^{-1}) were formed over the last 80 Myr and $80-93$ HMXBS/($M_{\odot}$ yr^{-1}) were formed over the last 50 Myr. We attempted to determine the velocities of HMXBs in our sample by associating them with young star clusters from the PHAT catalog, but were not able to make this measurement, likely due to the inclination of the disk of M31.

In Chapter 5 I presented the first results from the SMC NuSTAR Legacy Survey, 1 Ms of *NuSTAR* observations across three fields in the SMC. The source catalog contains 10 sources detected above a 3σ significance level in the $4-25$ keV band and 40 sources with upper limits on the source count rate. Due to the proximity of the SMC, the limiting source luminosity of 10^{35} erg s^{-1} is the lowest point-source luminosity limit of any nearby galaxy previously observed with *NuSTAR*, which allowed us to characterize lower luminosity XRBs than has been possible in previous work. We used hard X-ray colors and luminosities to classify XRBs by their compact object type. We confirmed the pulse periods of seven known pulsars in our 3σ sample. We did not observe pulsations from two HMXBs in our 3σ sample that do not have confirmed pulsations in the literature. We presented the first detection of pulsations from SXP 305 (CXO J005215.4$-$731915), a Be-HMXB with a pulse period of 305.69 ± 0.16 s. The likely orbital period for this Be-HMXB system is $\sim$1160-1180 days. We observed spectral differences between low-luminosity accreting pulsars in the SMC and the Galactic pulsars that were used to create the classification diagrams.

In Chapter 6 I presented the results of the spatially resolved recent star formation history of M33, measured with new photometry from the Panchromatic Hubble Andromeda Treasury: Trian-

gulum Extended Region (PHATTER) survey. I divided the stars in the PHATTER source catalog into roughly 2000 100 pc by 100 pc spatial regions. Using color-magnitude diagram fitting with the optical (F475W and F814W) photometry, I measured the SFR for each region in log-spaced age bins. I combined SFR measurements across spatial bins to measure the overall SFH of M33. I also calculated the mean SFR over the last 100 Myr and the current SFR of M33. We observe the morphological evolution of M33 in the maps of the spatially resolved star formation history over time. The spiral structure of M33 looks flocculent at recent times, but the older populations (¿100 Myr) show a simpler, two-arm structure. We also observe a bar in the center of M33, which is visible at ages older than around 80 Myr, which corresponds with the dynamical timescale of M33.

Over the next few years, I plan to build upon the work presented in this thesis as a postdoctoral fellow. In Chapters 2, 3 and 4 I presented detailed characterization of the HMXB population of M31 using observations from *Hubble*, *Chandra*, and NuSTAR. As a postdoctoral fellow, I plan to expand this type of HMXB characterization to M33 using existent *Chandra* and *NuSTAR* observations and the new PHATTER dataset including the spatially resolved recent star formation history presented in Chapter 6. With a large sample of well-characterized HMXBs, I can directly compare with theoretical HMXB populations created with binary population synthesis models. Through this comparison, we will be able to constrain parameters that describe some of the intermediate phases of massive binary stellar evolution that are difficult to directly constrain observationally. These constraints will be a powerful way to predict the fraction of compact binary mergers we observe with gravitational waves that come from the isolated binary stellar evolution formation channel.

BIBLIOGRAPHY

Abbott, B. P., Abbott, R., Abbott, T. D., et al. 2016, ApJ, 818, L22, doi: 10.3847/2041-8205/818/2/L22

—. 2017, ApJ, 848, L12, doi: 10.3847/2041-8213/aa91c9

Andrews, J. J., Zezas, A., & Fragos, T. 2018, ApJS, 237, 1, doi: 10.3847/1538-4365/aaca30

Antonini, F., & Gieles, M. 2020, MNRAS, 492, 2936, doi: 10.1093/mnras/stz3584

Antoniou, V., Hatzidimitriou, D., Zezas, A., & Reig, P. 2009, ApJ, 707, 1080, doi: 10.1088/0004-637X/707/2/1080

Antoniou, V., & Zezas, A. 2016, MNRAS, 459, 528, doi: 10.1093/mnras/stw167

Antoniou, V., Zezas, A., Hatzidimitriou, D., & Kalogera, V. 2010, ApJ, 716, L140, doi: 10.1088/2041-8205/716/2/L140

Antoniou, V., Zezas, A., Drake, J. J., et al. 2019, ApJ, 887, 20, doi: 10.3847/1538-4357/ab4a7a

Bachetti, M., Harrison, F. A., Walton, D. J., et al. 2014, Nature, 514, 202, doi: 10.1038/nature13791

Ballhausen, R., Pottschmidt, K., Fürst, F., et al. 2017, A&A, 608, A105, doi: 10.1051/0004-6361/201730845

Barker, M. K., Ferguson, A. M. N., Cole, A. A., et al. 2011, MNRAS, 410, 504, doi: 10.1111/j.1365-2966.2010.17458.x

Barker, M. K., Sarajedini, A., Geisler, D., Harding, P., & Schommer, R. 2007, AJ, 133, 1138, doi: 10.1086/511186

Basu-Zych, A. R., Lehmer, B., Fragos, T., et al. 2016, ApJ, 818, 140, doi: 10.3847/0004-637X/818/2/140

Basu-Zych, A. R., Lehmer, B. D., Hornschemeier, A. E., et al. 2013, ApJ, 774, 152, doi: 10.1088/0004-637X/774/2/152

Baumgardt, H., Makino, J., Hut, P., McMillan, S., & Portegies Zwart, S. 2003, ApJ, 589, L25, doi: 10.1086/375802

Belczynski, K., Holz, D. E., Bulik, T., & O'Shaughnessy, R. 2016, Nature, 534, 512, doi: 10.1038/nature18322

Belczynski, K., Kalogera, V., Rasio, F. A., et al. 2008, ApJS, 174, 223, doi: 10.1086/521026

Belczynski, K., & Ziolkowski, J. 2009, ApJ, 707, 870, doi: 10.1088/0004-637X/707/2/870

Bernard, E. J., Ferguson, A. M. N., Chapman, S. C., et al. 2015, MNRAS, 453, L113, doi: 10.1093/mnrasl/slv116

Bernard, E. J., Ferguson, A. M. N., Barker, M. K., et al. 2012, MNRAS, 420, 2625, doi: 10.1111/j.1365-2966.2011.20234.x

Binder, B., Gross, J., Williams, B. F., et al. 2017, ApJ, 834, 128, doi: 10.3847/1538-4357/834/2/128

Binder, B., Williams, B. F., Eracleous, M., et al. 2013, ApJ, 763, 128, doi: 10.1088/0004-637X/763/2/128

—. 2012, ApJ, 758, 15, doi: 10.1088/0004-637X/758/1/15

—. 2015, AJ, 150, 94, doi: 10.1088/0004-6256/150/3/94

Blackburn, J. K. 1995, in Astronomical Society of the Pacific Conference Series, Vol. 77, Astronomical Data Analysis Software and Systems IV, ed. R. A. Shaw, H. E. Payne, & J. J. E. Hayes, 367. http://adsabs.harvard.edu/abs/1995ASPC...77..367B

Blackburn, J. K., Shaw, R. A., Payne, H. E., Hayes, J. J. E., & HEASARC. 1999, FTOOLS: A general package of software to manipulate FITS files. http://ascl.net/9912.002

Block, D. L., Freeman, K. C., Jarrett, T. H., et al. 2004, A&A, 425, L37, doi: 10.1051/0004-6361:200400031

Bodaghee, A., Tomsick, J. A., Rodriguez, J., & James, J. B. 2012, ApJ, 744, 108, doi: 10.1088/0004-637X/744/2/108

Bodaghee, A., Courvoisier, T. J. L., Rodriguez, J., et al. 2007, A&A, 467, 585, doi: 10.1051/0004-6361:20077091

Boquien, M., Calzetti, D., Aalto, S., et al. 2015, A&A, 578, A8, doi: 10.1051/0004-6361/201423518

Boroson, B., Kim, D.-W., & Fabbiano, G. 2011, ApJ, 729, 12, doi: 10.1088/0004-637X/729/1/12

Braun, R. 1990, ApJS, 72, 761, doi: 10.1086/191432

Bressan, A., Marigo, P., Girardi, L., et al. 2012, MNRAS, 427, 127, doi: 10.1111/j.1365-2966.2012.21948.x

Broos, P. S., Townsley, L. K., Feigelson, E. D., et al. 2010, ApJ, 714, 1582, doi: 10.1088/0004-637X/714/2/1582

Brorby, M., Kaaret, P., Prestwich, A., & Mirabel, I. F. 2016, MNRAS, 457, 4081, doi: 10.1093/mnras/stw284

Brown, T. M., Smith, E., Ferguson, H. C., et al. 2006, ApJ, 652, 323, doi: 10.1086/508015

—. 2007, ApJ, 658, L95, doi: 10.1086/515395

Brown, T. M., Beaton, R., Chiba, M., et al. 2008, ApJ, 685, L121, doi: 10.1086/592686

Burrows, D. N., Hill, J. E., Nousek, J. A., et al. 2005, Space Sci. Rev., 120, 165, doi: 10.1007/s11214-005-5097-2

Carpano, S., Haberl, F., Maitra, C., & Vasilopoulos, G. 2018, MNRAS, 476, L45, doi: 10.1093/mnrasl/sly030

Casares, J., Negueruela, I., Ribó, M., et al. 2014, Nature, 505, 378, doi: 10.1038/nature12916

Chaty, S. 2013, Advances in Space Research, 52, 2132, doi: 10.1016/j.asr.2013.09.010

Choi, Y., Dalcanton, J. J., Williams, B. F., et al. 2015, ApJ, 810, 9, doi: 10.1088/0004-637X/810/1/9

Chomiuk, L., Strader, J., Maccarone, T. J., et al. 2013, ApJ, 777, 69, doi: 10.1088/0004-637X/777/1/69

Cignoni, M., Sacchi, E., Tosi, M., et al. 2019, ApJ, 887, 112, doi: 10.3847/1538-4357/ab53d5

Coe, M. J. 2000, in Astronomical Society of the Pacific Conference Series, Vol. 214, IAU Colloq. 175: The Be Phenomenon in Early-Type Stars, ed. M. A. Smith, H. F. Henrichs, & J. Fabregat, 656

Coe, M. J., Edge, W. R. T., Galache, J. L., & McBride, V. A. 2005, MNRAS, 356, 502, doi: 10.1111/j.1365-2966.2004.08467.x

Conroy, C. 2013, ARA&A, 51, 393, doi: 10.1146/annurev-astro-082812-141017

Corbelli, E. 2003, MNRAS, 342, 199, doi: 10.1046/j.1365-8711.2003.06531.x

Corbelli, E., & Walterbos, R. A. M. 2007, ApJ, 669, 315, doi: 10.1086/521618

Dalcanton, J. J., Williams, B. F., Seth, A. C., et al. 2009, ApJS, 183, 67, doi: 10.1088/0067-0049/183/1/67

Dalcanton, J. J., Williams, B. F., Lang, D., et al. 2012, ApJS, 200, 18, doi: 10.1088/0067-0049/200/2/18

Dalcanton, J. J., Fouesneau, M., Hogg, D. W., et al. 2015, ApJ, 814, 3, doi: 10.1088/0004-637X/814/1/3

Dalgarno, A., & McCray, R. A. 1972, ARA&A, 10, 375, doi: 10.1146/annurev.aa.10.090172.002111

Davidson, K., & Ostriker, J. P. 1973, ApJ, 179, 585, doi: 10.1086/151897

de Grijs, R., & Bono, G. 2014, AJ, 148, 17, doi: 10.1088/0004-6256/148/1/17

—. 2015, AJ, 149, 179, doi: 10.1088/0004-6256/149/6/179

de Meulenaer, P., Narbutis, D., Mineikis, T., & Vansevičius, V. 2015, A&A, 574, A66, doi: 10.1051/0004-6361/201425121

de Mink, S. E., Langer, N., Izzard, R. G., Sana, H., & de Koter, A. 2013, ApJ, 764, 166, doi: 10.1088/0004-637X/764/2/166

Di Stefano, R., Kong, A. K. H., Greiner, J., et al. 2004, ApJ, 610, 247, doi: 10.1086/421696

Díaz-Rodríguez, M., Murphy, J. W., Rubin, D. A., et al. 2018, ApJ, 861, 92, doi: 10.3847/1538-4357/aac6e1

Dickey, J. M., & Lockman, F. J. 1990, ARA&A, 28, 215, doi: 10.1146/annurev.aa.28.090190.001243

Dobbs, C. L., Pettitt, A. R., Corbelli, E., & Pringle, J. E. 2018, MNRAS, 478, 3793, doi: 10.1093/mnras/sty1231

Dolphin, A. E. 2002, MNRAS, 332, 91, doi: 10.1046/j.1365-8711.2002.05271.x

—. 2013, ApJ, 775, 76, doi: 10.1088/0004-637X/775/1/76

Done, C., Gierliński, M., & Kubota, A. 2007, A&A Rev., 15, 1, doi: 10.1007/s00159-007-0006-1

Done, C., Wardziński, G., & Gierliński, M. 2004, MNRAS, 349, 393, doi: 10.1111/j.1365-2966.2004.07545.x

Dorn-Wallenstein, T., Levesque, E. M., & Ruan, J. J. 2017, ApJ, 850, 86, doi: 10.3847/1538-4357/aa9329

Dotter, A. 2016, ApJS, 222, 8, doi: 10.3847/0067-0049/222/1/8

Douna, V. M., Pellizza, L. J., Mirabel, I. F., & Pedrosa, S. E. 2015, A&A, 579, A44, doi: 10.1051/0004-6361/201525617

Dray, L. M. 2006, MNRAS, 370, 2079, doi: 10.1111/j.1365-2966.2006.10635.x

Duane, S., Kennedy, A., Pendleton, B. J., & Roweth, D. 1987, Physics Letters B, 195, 216, doi: https://doi.org/10.1016/0370-2693(87)91197-X

Ducci, L., Romano, P., Kennea, J. A., et al. 2017, The Astronomer's Telegram, 11030

Duchêne, G., & Kraus, A. 2013, ARA&A, 51, 269, doi: 10.1146/annurev-astro-081710-102602

Edge, W. R. T., Coe, M. J., Corbet, R. H. D., Markwardt, C. B., & Laycock, S. 2004a, The Astronomer's Telegram, 225, 1

Edge, W. R. T., Coe, M. J., & McBride, V. A. 2004b, The Astronomer's Telegram, 220

Eldridge, J. J., & Stanway, E. R. 2016, MNRAS, 462, 3302, doi: 10.1093/mnras/stw1772

Elmegreen, B. G., Elmegreen, D. M., & Montenegro, L. 1992, ApJS, 79, 37, doi: 10.1086/191643

Esposito, P., Israel, G. L., Belfiore, A., et al. 2016, MNRAS, 457, L5, doi: 10.1093/mnrasl/slv194

Evans, C. J., Howarth, I. D., Irwin, M. J., Burnley, A. W., & Harries, T. J. 2004, MNRAS, 353, 601, doi: 10.1111/j.1365-2966.2004.08096.x

Evans, P. A., Beardmore, A. P., Page, K. L., et al. 2007, A&A, 469, 379, doi: 10.1051/0004-6361:20077530

—. 2009, MNRAS, 397, 1177, doi: 10.1111/j.1365-2966.2009.14913.x

Fornasini, F. M., Civano, F., & Suh, H. 2020, MNRAS, 495, 771, doi: 10.1093/mnras/staa1211

Fornasini, F. M., Tomsick, J. A., Hong, J., et al. 2017, ApJS, 229, 33, doi: 10.3847/1538-4365/aa61fc

Fragos, T., Andrews, J. J., Ramirez-Ruiz, E., et al. 2019, ApJ, 883, L45, doi: 10.3847/2041-8213/ab40d1

Fragos, T., Lehmer, B., Tremmel, M., et al. 2013, ApJ, 764, 41, doi: 10.1088/0004-637X/764/1/41

Fruscione, A., McDowell, J. C., Allen, G. E., et al. 2006, in Proc. SPIE, Vol. 6270, Society of Photo-Optical Instrumentation Engineers (SPIE) Conference Series, 62701V

Fürst, F., Walton, D. J., Harrison, F. A., et al. 2016, ApJ, 831, L14, doi: 10.3847/2041-8205/831/2/L14

Gallart, C., Zoccali, M., & Aparicio, A. 2005, ARA&A, 43, 387, doi: 10.1146/annurev.astro.43.072103.150608

Galleti, S., Federici, L., Bellazzini, M., Fusi Pecci, F., & Macrina, S. 2003, VizieR Online Data Catalog, 341

Galvin, T. J., & Filipovic, M. D. 2014, Serbian Astronomical Journal, 189, 15, doi: 10.2298/SAJ140505002G

Garcia, M. R., Hextall, R., Baganoff, F. K., et al. 2010, ApJ, 710, 755, doi: 10.1088/0004-637X/710/1/755

Garofali, K., Williams, B. F., Hillis, T., et al. 2018, MNRAS, doi: 10.1093/mnras/sty1612

Garratt-Smithson, L., Wynn, G. A., Power, C., & Nixon, C. J. 2019, MNRAS, 489, 4278, doi: 10.1093/mnras/stz2406

Gebhardt, K., Rich, R. M., & Ho, L. C. 2002, ApJ, 578, L41, doi: 10.1086/342980

Geha, M., Weisz, D., Grocholski, A., et al. 2015, ApJ, 811, 114, doi: 10.1088/0004-637X/811/2/114

Gehrels, N., Chincarini, G., Giommi, P., et al. 2004, ApJ, 611, 1005, doi: 10.1086/422091

Giesers, B., Dreizler, S., Husser, T.-O., et al. 2018, MNRAS, 475, L15, doi: 10.1093/mnrasl/slx203

Gil de Paz, A., Boissier, S., Madore, B. F., et al. 2009a, VizieR Online Data Catalog, 217

—. 2009b, VizieR Online Data Catalog, 217

Gilfanov, M., Grimm, H.-J., & Sunyaev, R. 2004, MNRAS, 351, 1365, doi: 10.1111/j.1365-2966.2004.07874.x

Girardi, L., Williams, B. F., Gilbert, K. M., et al. 2010, ApJ, 724, 1030, doi: 10.1088/0004-637X/724/2/1030

Glebbeek, E., Gaburov, E., Portegies Zwart, S., & Pols, O. R. 2013, MNRAS, 434, 3497, doi: 10.1093/mnras/stt1268

Gogarten, S. M., Dalcanton, J. J., Williams, B. F., et al. 2010, ApJ, 712, 858, doi: 10.1088/0004-637X/712/2/858

Gordon, K. D., Fouesneau, M., Arab, H., et al. 2016, ApJ, 826, 104, doi: 10.3847/0004-637X/826/2/104

Gregersen, D., Seth, A. C., Williams, B. F., et al. 2015, AJ, 150, 189, doi: 10.1088/0004-6256/150/6/189

Greig, B., & Mesinger, A. 2018, MNRAS, 477, 3217, doi: 10.1093/mnras/sty796

Grimm, H.-J., Gilfanov, M., & Sunyaev, R. 2002, A&A, 391, 923, doi: 10.1051/0004-6361:20020826

—. 2003, MNRAS, 339, 793, doi: 10.1046/j.1365-8711.2003.06224.x

Güver, T., & Özel, F. 2009, MNRAS, 400, 2050, doi: 10.1111/j.1365-2966.2009.15598.x

Haberl, F., Eger, P., & Pietsch, W. 2008, A&A, 489, 327, doi: 10.1051/0004-6361:200810100

Haberl, F., & Sasaki, M. 2000, A&A, 359, 573

Haberl, F., & Sturm, R. 2016, A&A, 586, A81, doi: 10.1051/0004-6361/201527326

Haberl, F., Sturm, R., Ballet, J., et al. 2012, A&A, 545, A128, doi: 10.1051/0004-6361/201219758

Haberl, F., Israel, G. L., Rodriguez Castillo, G. A., et al. 2017, A&A, 598, A69, doi: 10.1051/0004-6361/201629744

Hagen, L. M. Z., Siegel, M. H., Hoversten, E. A., et al. 2017, MNRAS, 466, 4540, doi: 10.1093/mnras/stw2954

Harris, J., & Zaritsky, D. 2004, AJ, 127, 1531, doi: 10.1086/381953

—. 2009, AJ, 138, 1243, doi: 10.1088/0004-6256/138/5/1243

Harrison, F. A., Craig, W. W., Christensen, F. E., et al. 2013, ApJ, 770, 103, doi: 10.1088/0004-637X/770/2/103

Harrison, F. A., Aird, J., Civano, F., et al. 2016, ApJ, 831, 185, doi: 10.3847/0004-637X/831/2/185

Hasinger, G., & van der Klis, M. 1989, A&A, 225, 79

Hatzidimitriou, D., Pietsch, W., Misanovic, Z., Reig, P., & Haberl, F. 2006, A&A, 451, 835, doi: 10.1051/0004-6361:20054402

Henze, M., Sasaki, M., Haberl, F., & Hatzidimitriou, D. 2015, The Astronomer's Telegram, 8227

Hernández-López, I., Athanassoula, E., Mújica, R., & Bosma, A. 2009, in Revista Mexicana de Astronomia y Astrofisica Conference Series, Vol. 37, Revista Mexicana de Astronomia y Astrofisica Conference Series, 160–162

Hilditch, R. W., Howarth, I. D., & Harries, T. J. 2005, MNRAS, 357, 304, doi: 10.1111/j.1365-2966.2005.08653.x

Ho, W. C. G., Ng, C.-Y., Lyne, A. G., et al. 2017, MNRAS, 464, 1211, doi: 10.1093/mnras/stw2420

Hong, J., Antoniou, V., Zezas, A., et al. 2017, ApJ, 847, 26, doi: 10.3847/1538-4357/aa8953

Hong, J., van den Berg, M., Schlegel, E. M., et al. 2005, ApJ, 635, 907, doi: 10.1086/496966

Hong, J., Mori, K., Hailey, C. J., et al. 2016, ApJ, 825, 132, doi: 10.3847/0004-637X/825/2/132

Hoopes, C. G., Walterbos, R. A. M., & Bothun, G. D. 2001, ApJ, 559, 878, doi: 10.1086/322422

Humphreys, R. M., & Sandage, A. 1980, ApJS, 44, 319, doi: 10.1086/190696

Huppenkothen, D., Bachetti, M., Stevens, A. L., et al. 2019, arXiv e-prints, arXiv:1901.07681. https://arxiv.org/abs/1901.07681

Imanishi, K., Yokogawa, J., Tsujimoto, M., & Koyama, K. 1999, PASJ, 51, L15, doi: 10.1093/pasj/51.6.L15

Israel, G. L., Papitto, A., Esposito, P., et al. 2017, MNRAS, 466, L48, doi: 10.1093/mnrasl/slw218

Ivanova, N., Justham, S., Chen, X., et al. 2013, A&A Rev., 21, 59, doi: 10.1007/s00159-013-0059-2

Jarrett, T. H., Chester, T., Cutri, R., Schneider, S. E., & Huchra, J. P. 2003, AJ, 125, 525, doi: 10.1086/345794

Jennings, Z. G., Williams, B. F., Murphy, J. W., et al. 2014, ApJ, 795, 170, doi: 10.1088/0004-637X/795/2/170

Johnson, L. C., Seth, A. C., Dalcanton, J. J., et al. 2015, ApJ, 802, 127, doi: 10.1088/0004-637X/802/2/127

Joss, P. C., & Rappaport, S. A. 1984, ARA&A, 22, 537, doi: 10.1146/annurev.aa.22.090184.002541

Justham, S., & Schawinski, K. 2012, MNRAS, 423, 1641, doi: 10.1111/j.1365-2966.2012.20985.x

Kaaret, P. 2002, ApJ, 578, 114, doi: 10.1086/342475

Kaaret, P., Feng, H., & Roberts, T. P. 2017, Annual Review of Astronomy and Astrophysics, 55, 303, doi: 10.1146/annurev-astro-091916-055259

Kennea, J. A., Coe, M. J., & Evans, P. A. 2016a, The Astronomer's Telegram, 9370

Kennea, J. A., Coe, M. J., Evans, P. A., Waters, J., & Jasko, R. E. 2018, ApJ, 868, 47, doi: 10.3847/1538-4357/aae839

Kennea, J. A., Evans, P. A., & Coe, M. J. 2017, The Astronomer's Telegram, 10250

Kennea, J. A., Coe, M. J., Evans, P. A., et al. 2016b, The Astronomer's Telegram, 9362

Kennicutt, R. C., & Evans, N. J. 2012, ARA&A, 50, 531, doi: 10.1146/annurev-astro-081811-125610

Kim, D.-W., Cameron, R. A., Drake, J. J., et al. 2004, ApJS, 150, 19, doi: 10.1086/379819

Kiminki, D. C., & Kobulnicky, H. A. 2012, ApJ, 751, 4, doi: 10.1088/0004-637X/751/1/4

Koliopanos, F., & Vasilopoulos, G. 2018, A&A, 614, A23, doi: 10.1051/0004-6361/201731623

Koliopanos, F., Vasilopoulos, G., Godet, O., et al. 2017, A&A, 608, A47, doi: 10.1051/0004-6361/201730922

Kong, A. K. H., Garcia, M. R., Primini, F. A., et al. 2002, ApJ, 577, 738, doi: 10.1086/342116

Kong, A. K. H., Heinke, C. O., di Stefano, R., et al. 2010, MNRAS, 407, L84, doi: 10.1111/j.1745-3933.2010.00910.x

Kong, A. K. H., Sjouwerman, L. O., Williams, B. F., Garcia, M. R., & Dickel, J. R. 2003, ApJ, 590, L21, doi: 10.1086/376687

Kormendy, J., & McClure, R. D. 1993, AJ, 105, 1793, doi: 10.1086/116555

Kotze, M. M., & Charles, P. A. 2012, MNRAS, 420, 1575, doi: 10.1111/j.1365-2966.2011.20146.x

Krivonos, R., Tsygankov, S., Lutovinov, A., et al. 2012, A&A, 545, A27, doi: 10.1051/0004-6361/201219617

Kroupa, P. 2001, MNRAS, 322, 231, doi: 10.1046/j.1365-8711.2001.04022.x

Kulkarni, S. R., Hut, P., & McMillan, S. 1993, Nature, 364, 421, doi: 10.1038/364421a0

Lamers, H. J. G. L. M., & Levesque, E. M. 2017, Understanding Stellar Evolution, doi: 10.1088/978-0-7503-1278-3

Laycock, S., Zezas, A., Hong, J., Drake, J. J., & Antoniou, V. 2010, ApJ, 716, 1217, doi: 10.1088/0004-637X/716/2/1217

Lazzarini, M., Hornschemeier, A. E., Williams, B. F., et al. 2018, ApJ, 862, 28, doi: 10.3847/1538-4357/aacb2a

Lazzarini, M., Williams, B. F., Hornschemeier, A. E., et al. 2019, ApJ, 884, 2, doi: 10.3847/1538-4357/ab3f32

Lazzarini, M., Williams, B. F., Durbin, M., et al. 2021, ApJ, 906, 120, doi: 10.3847/1538-4357/abccca

Leahy, D. A., Elsner, R. F., & Weisskopf, M. C. 1983, ApJ, 272, 256, doi: 10.1086/161288

Lee, J. H., & Lee, M. G. 2014, ApJ, 786, 130, doi: 10.1088/0004-637X/786/2/130

Lehmer, B. D., Alexander, D. M., Bauer, F. E., et al. 2010, ApJ, 724, 559, doi: 10.1088/0004-637X/724/1/559

Lehmer, B. D., Wik, D. R., Hornschemeier, A. E., et al. 2013, ApJ, 771, 134, doi: 10.1088/0004-637X/771/2/134

Lehmer, B. D., Berkeley, M., Zezas, A., et al. 2014, ApJ, 789, 52, doi: 10.1088/0004-637X/789/1/52

Lehmer, B. D., Eufrasio, R. T., Markwardt, L., et al. 2017, ApJ, 851, 11, doi: 10.3847/1538-4357/aa9578

Lehmer, B. D., Eufrasio, R. T., Tzanavaris, P., et al. 2019, arXiv e-prints, arXiv:1905.05197. https://arxiv.org/abs/1905.05197

Lewin, W. H. G., van Paradijs, J., & Taam, R. E. 1993, Space Sci. Rev., 62, 223, doi: 10.1007/BF00196124

Lewis, A. R., Dolphin, A. E., Dalcanton, J. J., et al. 2015, ApJ, 805, 183, doi: 10.1088/0004-637X/805/2/183

Lewis, A. R., Simones, J. E., Johnson, B. D., et al. 2017, ApJ, 834, 70, doi: 10.3847/1538-4357/834/1/70

Li, F., Jernigan, G., & Clark, G. 1977, IAU Circ., 3125

Li, K. L., Hu, C.-P., Lin, L. C. C., & Kong, A. K. H. 2016, ApJ, 828, 74, doi: 10.3847/0004-637X/828/2/74

Li, Z., Garcia, M. R., Forman, W. R., et al. 2011, ApJ, 728, L10, doi: 10.1088/2041-8205/728/1/L10

Licquia, T. C., & Newman, J. A. 2015, ApJ, 806, 96, doi: 10.1088/0004-637X/806/1/96

Lin, Z., Hu, N., Kong, X., et al. 2017, ApJ, 842, 97, doi: 10.3847/1538-4357/aa6f14

Linden, T., Kalogera, V., Sepinsky, J. F., et al. 2010, ApJ, 725, 1984, doi: 10.1088/0004-637X/725/2/1984

Liu, Q. Z., van Paradijs, J., & van den Heuvel, E. P. J. 2005, A&A, 442, 1135, doi: 10.1051/0004-6361:20053718

—. 2006, A&A, 455, 1165, doi: 10.1051/0004-6361:20064987

Luck, R. E., Moffett, T. J., Barnes, III, T. G., & Gieren, W. P. 1998, AJ, 115, 605, doi: 10.1086/300227

Luo, B., Brandt, W. N., Xue, Y. Q., et al. 2017, ApJS, 228, 2, doi: 10.3847/1538-4365/228/1/2

Lutovinov, A. A., Revnivtsev, M. G., Tsygankov, S. S., & Krivonos, R. A. 2013, MNRAS, 431, 327, doi: 10.1093/mnras/stt168

Lyne, A. G., Stappers, B. W., Keith, M. J., et al. 2015, MNRAS, 451, 581, doi: 10.1093/mnras/stv236

Maccacaro, T., Gioia, I. M., Wolter, A., Zamorani, G., & Stocke, J. T. 1988, ApJ, 326, 680, doi: 10.1086/166127

Maccarone, T. J., Kundu, A., Zepf, S. E., & Rhode, K. L. 2007, Nature, 445, 183, doi: 10.1038/nature05434

Maccarone, T. J., Yukita, M., Hornschemeier, A., et al. 2016, MNRAS, 458, 3633, doi: 10.1093/mnras/stw530

Mackey, A. D., Wilkinson, M. I., Davies, M. B., & Gilmore, G. F. 2008, MNRAS, 386, 65, doi: 10.1111/j.1365-2966.2008.13052.x

Madau, P., & Fragos, T. 2017, ApJ, 840, 39, doi: 10.3847/1538-4357/aa6af9

Madsen, K. K., Harrison, F. A., Markwardt, C. B., et al. 2015, ApJS, 220, 8, doi: 10.1088/0067-0049/220/1/8

Maggi, P., Sturm, R., Haberl, F., Vasilopoulos, G., & Udalski, A. 2014, The Astronomer's Telegram, 5778

Magrini, L., Stanghellini, L., Corbelli, E., Galli, D., & Villaver, E. 2010, A&A, 512, A63, doi: 10.1051/0004-6361/200913564

Magrini, L., Stanghellini, L., & Villaver, E. 2009, ApJ, 696, 729, doi: 10.1088/0004-637X/696/1/729

Maitra, C., Haberl, F., Ivanov, V. D., Cioni, M.-R. L., & van Loon, J. T. 2019, A&A, 622, A29, doi: 10.1051/0004-6361/201833663

Maitra, C., Paul, B., Haberl, F., & Vasilopoulos, G. 2018, MNRAS, 480, L136, doi: 10.1093/mnrasl/sly141

Mapelli, M., & Giacobbo, N. 2018, MNRAS, 479, 4391, doi: 10.1093/mnras/sty1613

Maravelias, G., Zezas, A., Antoniou, V., & Hatzidimitriou, D. 2014, MNRAS, 438, 2005, doi: 10.1093/mnras/stt2302

Marigo, P., Girardi, L., Bressan, A., et al. 2008, A&A, 482, 883, doi: 10.1051/0004-6361:20078467

—. 2017, ApJ, 835, 77, doi: 10.3847/1538-4357/835/1/77

McBride, V. A., Coe, M. J., Negueruela, I., Schurch, M. P. E., & McGowan, K. E. 2008, MNRAS, 388, 1198, doi: 10.1111/j.1365-2966.2008.13410.x

McConnachie, A. W., Irwin, M. J., Ferguson, A. M. N., et al. 2005, MNRAS, 356, 979, doi: 10.1111/j.1365-2966.2004.08514.x

McHardy, I. M., Gunn, K. F., Uttley, P., & Goad, M. R. 2005, MNRAS, 359, 1469, doi: 10.1111/j.1365-2966.2005.08992.x

McLean, I. S., & Liu, T. 1996, ApJ, 456, 499, doi: 10.1086/176674

McQuinn, K. B. W., Skillman, E. D., Cannon, J. M., et al. 2010, ApJ, 721, 297, doi: 10.1088/0004-637X/721/1/297

Melbourne, J., Williams, B. F., Dalcanton, J. J., et al. 2012, ApJ, 748, 47, doi: 10.1088/0004-637X/748/1/47

Mesinger, A., Ewall-Wice, A., & Hewitt, J. 2014, MNRAS, 439, 3262, doi: 10.1093/mnras/stu125

Meyssonnier, N., & Azzopardi, M. 1993, A&AS, 102, 451

Miller-Jones, J. C. A., Wrobel, J. M., Sivakoff, G. R., et al. 2012, ApJ, 755, L1, doi: 10.1088/2041-8205/755/1/L1

Mineo, S., Gilfanov, M., & Sunyaev, R. 2012, MNRAS, 419, 2095, doi: 10.1111/j.1365-2966.2011.19862.x

Moe, M., & Di Stefano, R. 2017, ApJS, 230, 15, doi: 10.3847/1538-4365/aa6fb6

Morscher, M., Pattabiraman, B., Rodriguez, C., Rasio, F. A., & Umbreit, S. 2015, ApJ, 800, 9, doi: 10.1088/0004-637X/800/1/9

Mushotzky, R. F., Done, C., & Pounds, K. A. 1993, ARA&A, 31, 717, doi: 10.1146/annurev.aa.31.090193.003441

O'Dell, S. L., Brissenden, R. J., Davis, W. N., et al. 2010, in Society of Photo-Optical Instrumentation Engineers (SPIE) Conference Series, Vol. 7803, Adaptive X-Ray Optics, ed. A. M. Khounsary, S. L. O'Dell, & S. R. Restaino, 78030H

Oey, M. S. 1999, in IAU Symposium, Vol. 193, Wolf-Rayet Phenomena in Massive Stars and Starburst Galaxies, ed. K. A. van der Hucht, G. Koenigsberger, & P. R. J. Eenens, 627

Okazaki, A. T., & Negueruela, I. 2001, A&A, 377, 161, doi: 10.1051/0004-6361:20011083

Orosz, J. A., & Bailyn, C. D. 1997, ApJ, 477, 876, doi: 10.1086/303741

Peters, M., Wisniewski, J. P., Williams, B. F., et al. 2020, AJ, 159, 119, doi: 10.3847/1538-3881/ab6d74

Petropoulou, M., Vasilopoulos, G., Christie, I. M., Giannios, D., & Coe, M. J. 2018, MNRAS, 474, L22, doi: 10.1093/mnrasl/slx185

Phillips, S. N., & Podsiadlowski, P. 2002, MNRAS, 337, 431, doi: 10.1046/j.1365-8711.2002.05886.x

Pietsch, W., Freyberg, M., & Haberl, F. 2005, A&A, 434, 483, doi: 10.1051/0004-6361:20041990

Podsiadlowski, P., Joss, P. C., & Hsu, J. J. L. 1992, ApJ, 391, 246, doi: 10.1086/171341

Podsiadlowski, P., Langer, N., Poelarends, A. J. T., et al. 2004, ApJ, 612, 1044, doi: 10.1086/421713

Politakis, B., Zezas, A., Andrews, J. J., & Williams, S. J. 2020, MNRAS, 493, 5369, doi: 10.1093/mnras/staa561

Ponnada, S., Brorby, M., & Kaaret, P. 2020, MNRAS, 491, 3606, doi: 10.1093/mnras/stz2929

Pooley, D., & Rappaport, S. 2006, ApJ, 644, L45, doi: 10.1086/505344

Portegies Zwart, S. F. 1995, A&A, 296, 691

Portegies Zwart, S. F., & McMillan, S. L. W. 2000, ApJ, 528, L17, doi: 10.1086/312422

Porter, J. M., & Rivinius, T. 2003, PASP, 115, 1153, doi: 10.1086/378307

Predehl, P., & Schmitt, J. H. M. M. 1995, A&A, 500, 459

Ranalli, P., Comastri, A., & Setti, G. 2003, A&A, 399, 39, doi: 10.1051/0004-6361:20021600

Rappaport, S. A., Podsiadlowski, P., & Pfahl, E. 2005, MNRAS, 356, 401, doi: 10.1111/j.1365-2966.2004.08489.x

Regan, M. W., & Vogel, S. N. 1994, ApJ, 434, 536, doi: 10.1086/174755

Reig, P. 2011, Ap&SS, 332, 1, doi: 10.1007/s10509-010-0575-8

Remillard, R. A., & McClintock, J. E. 2006, ARA&A, 44, 49, doi: 10.1146/annurev.astro.44.051905.092532

Rivinius, T., Carciofi, A. C., & Martayan, C. 2013, A&A Rev., 21, 69, doi: 10.1007/s00159-013-0069-0

Roberts, W. W. 1969, ApJ, 158, 123, doi: 10.1086/150177

Rodriguez, C. L., & Loeb, A. 2018, ApJ, 866, L5, doi: 10.3847/2041-8213/aae377

Rubele, S., Pastorelli, G., Girardi, L., et al. 2018, MNRAS, 478, 5017, doi: 10.1093/mnras/sty1279

Sana, H., de Mink, S. E., de Koter, A., et al. 2012, Science, 337, 444, doi: 10.1126/science.1223344

Sasaki, M., Haberl, F., Henze, M., et al. 2018, A&A, 620, A28, doi: 10.1051/0004-6361/201833588

Schaller, G., Schaerer, D., Meynet, G., & Maeder, A. 1992, A&AS, 96, 269

Schurch, M. P. E., Coe, M. J., McBride, V. A., et al. 2011, MNRAS, 412, 391, doi: 10.1111/j.1365-2966.2010.17914.x

Semczuk, M., Łokas, E. L., Salomon, J.-B., Athanassoula, E., & D'Onghia, E. 2018, ApJ, 864, 34, doi: 10.3847/1538-4357/aad4ae

Shakura, N. I., & Sunyaev, R. A. 1973, A&A, 500, 33

Shaw Greening, L., Barnard, R., Kolb, U., Tonkin, C., & Osborne, J. P. 2009, A&A, 495, 733, doi: 10.1051/0004-6361/200809864

Shtykovskiy, P., & Gilfanov, M. 2005, MNRAS, 362, 879, doi: 10.1111/j.1365-2966.2005.09320.x

Sidoli, L., & Paizis, A. 2018, MNRAS, 481, 2779, doi: 10.1093/mnras/sty2428

Sigurdsson, S., & Hernquist, L. 1993, Nature, 364, 423, doi: 10.1038/364423a0

Silaj, J., Jones, C. E., Tycner, C., Sigut, T. A. A., & Smith, A. D. 2010, ApJS, 187, 228, doi: 10.1088/0067-0049/187/1/228

Sippel, A. C., & Hurley, J. R. 2013, MNRAS, 430, L30, doi: 10.1093/mnrasl/sls044

Sobolewska, M. A., Gierliński, M., & Siemiginowska, A. 2009, MNRAS, 394, 1640, doi: 10.1111/j.1365-2966.2009.14436.x

Sota, A., Maíz Apellániz, J., Morrell, N. I., et al. 2014, ApJS, 211, 10, doi: 10.1088/0067-0049/211/1/10

Spitzer, Jr., L. 1969, ApJ, 158, L139, doi: 10.1086/180451

Stiele, H., & Kong, A. K. H. 2018, MNRAS, doi: 10.1093/mnras/sty106

Stiele, H., Pietsch, W., Haberl, F., et al. 2011, A&A, 534, A55, doi: 10.1051/0004-6361/201015270

Strader, J., Chomiuk, L., Maccarone, T. J., Miller-Jones, J. C. A., & Seth, A. C. 2012, Nature, 490, 71, doi: 10.1038/nature11490

Sturm, R., Haberl, F., Pietsch, W., et al. 2013a, A&A, 558, A3, doi: 10.1051/0004-6361/201219935

Sturm, R., Drašković, D., Filipović, M. D., et al. 2013b, A&A, 558, A101, doi: 10.1051/0004-6361/201220564

Supper, R., Hasinger, G., Lewin, W. H. G., et al. 2001, A&A, 373, 63, doi: 10.1051/0004-6361:20010495

Supper, R., Hasinger, G., Pietsch, W., et al. 1997, A&A, 317, 328

Tabatabaei, F. S., Beck, R., Krause, M., et al. 2007, A&A, 466, 509, doi: 10.1051/0004-6361:20066731

Tauris, T. M., & van den Heuvel, E. P. J. 2006, Formation and evolution of compact stellar X-ray sources, ed. W. H. G. Lewin & M. van der Klis, 623–665

Tauris, T. M., Kramer, M., Freire, P. C. C., et al. 2017, ApJ, 846, 170, doi: 10.3847/1538-4357/aa7e89

Tetarenko, B. E., Sivakoff, G. R., Heinke, C. O., & Gladstone, J. C. 2016, ApJS, 222, 15, doi: 10.3847/0067-0049/222/2/15

The LIGO Scientific Collaboration, & the Virgo Collaboration. 2018, ArXiv e-prints. https://arxiv.org/abs/1811.12907

Toribio San Cipriano, L., García-Rojas, J., Esteban, C., Bresolin, F., & Peimbert, M. 2016, MNRAS, 458, 1866, doi: 10.1093/mnras/stw397

Townsend, L. J., Kennea, J. A., Coe, M. J., et al. 2017, MNRAS, 471, 3878, doi: 10.1093/mnras/stx1865

Tozzi, P., Gilli, R., Mainieri, V., et al. 2006, A&A, 451, 457, doi: 10.1051/0004-6361:20042592

Tüllmann, R., Gaetz, T. J., Plucinsky, P. P., et al. 2011, ApJS, 193, 31, doi: 10.1088/0067-0049/193/2/31

Udalski, A., Szymanski, M., Kaluzny, J., Kubiak, M., & Mateo, M. 1992, Acta Astron., 42, 253

Udalski, A., Szymański, M. K., & Szymański, G. 2015, Acta Astron., 65, 1. https://arxiv.org/abs/1504.05966

Ulvestad, J. S., Greene, J. E., & Ho, L. C. 2007, ApJ, 661, L151, doi: 10.1086/518784

van den Heuvel, E. P. J., Portegies Zwart, S. F., Bhattacharya, D., & Kaper, L. 2000, A&A, 364, 563. https://arxiv.org/abs/astro-ph/0005245

van Speybroeck, L., Epstein, A., Forman, W., et al. 1979, ApJ, 234, L45, doi: 10.1086/183106

Vasilopoulos, G., Haberl, F., Carpano, S., & Maitra, C. 2018, A&A, 620, L12, doi: 10.1051/0004-6361/201833442

Vasilopoulos, G., Haberl, F., & Maggi, P. 2017, The Astronomer's Telegram, 10253

Venn, K. A., McCarthy, J. K., Lennon, D. J., et al. 2000, ApJ, 541, 610, doi: 10.1086/309491

Verley, S., Corbelli, E., Giovanardi, C., & Hunt, L. K. 2009, A&A, 493, 453, doi: 10.1051/0004-6361:200810566

Verley, S., Hunt, L. K., Corbelli, E., & Giovanardi, C. 2007, A&A, 476, 1161, doi: 10.1051/0004-6361:20078179

Vulic, N., Gallagher, S. C., & Barmby, P. 2014, ApJ, 790, 136, doi: 10.1088/0004-637X/790/2/136

—. 2016, MNRAS, 461, 3443, doi: 10.1093/mnras/stw1523

Vulic, N., Hornschemeier, A. E., Wik, D. R., et al. 2018, ApJ, 864, 150, doi: 10.3847/1538-4357/aad500

Walter, R., Lutovinov, A. A., Bozzo, E., & Tsygankov, S. S. 2015, A&A Rev., 23, 2, doi: 10.1007/s00159-015-0082-6

Walton, D. J., Fürst, F., Heida, M., et al. 2018, ApJ, 856, 128, doi: 10.3847/1538-4357/aab610

Weisskopf, M. C., Tananbaum, H. D., Van Speybroeck, L. P., & O'Dell, S. L. 2000, in Society of Photo-Optical Instrumentation Engineers (SPIE) Conference Series, Vol. 4012, X-Ray Optics, Instruments, and Missions III, ed. J. E. Truemper & B. Aschenbach, 2–16

Weisz, D. R., Dolphin, A. E., Skillman, E. D., et al. 2014, ApJ, 789, 147, doi: 10.1088/0004-637X/789/2/147

Weisz, D. R., Dalcanton, J. J., Williams, B. F., et al. 2011, ApJ, 739, 5, doi: 10.1088/0004-637X/739/1/5

West, L. A., Lehmer, B. D., Wik, D., et al. 2018, ApJ, 869, 111, doi: 10.3847/1538-4357/aaec6b

White, N. E., Swank, J. H., & Holt, S. S. 1983, ApJ, 270, 711, doi: 10.1086/161162

Wik, D. R., Lehmer, B. D., Hornschemeier, A. E., et al. 2014, ApJ, 797, 79, doi: 10.1088/0004-637X/797/2/79

Wik, D. R., Hornschemeier, A. E., Yukita, M., et al. 2016a, in AAS/High Energy Astrophysics Division, Vol. 15, AAS/High Energy Astrophysics Division #15, 402.02

Wik, D. R., Hornschemeier, A. E., Yukita, M., et al. 2016b, in American Astronomical Society Meeting Abstracts, Vol. 227, American Astronomical Society Meeting Abstracts #227, 126.04

Williams, B. F. 2002, MNRAS, 331, 293, doi: 10.1046/j.1365-8711.2002.05088.x

—. 2003, AJ, 126, 1312, doi: 10.1086/377347

Williams, B. F., Binder, B. A., Dalcanton, J. J., Eracleous, M., & Dolphin, A. 2013a, ApJ, 772, 12, doi: 10.1088/0004-637X/772/1/12

Williams, B. F., Dalcanton, J. J., Dolphin, A. E., Holtzman, J., & Sarajedini, A. 2009, ApJ, 695, L15, doi: 10.1088/0004-637X/695/1/L15

Williams, B. F., Dalcanton, J. J., Stilp, A., et al. 2013b, ApJ, 765, 120, doi: 10.1088/0004-637X/765/2/120

Williams, B. F., Garcia, M. R., Kong, A. K. H., et al. 2004a, ApJ, 609, 735, doi: 10.1086/421315

Williams, B. F., Garcia, M. R., McClintock, J. E., et al. 2005a, ApJ, 628, 382, doi: 10.1086/430876

Williams, B. F., Garcia, M. R., McClintock, J. E., Primini, F. A., & Murray, S. S. 2005b, ApJ, 632, 1086, doi: 10.1086/444369

Williams, B. F., Garcia, M. R., Primini, F. A., McClintock, J. E., & Murray, S. S. 2005c, ApJ, 631, 832, doi: 10.1086/432597

Williams, B. F., Sjouwerman, L. O., Kong, A. K. H., et al. 2004b, ApJ, 615, 720, doi: 10.1086/424589

Williams, B. F., Dalcanton, J. J., Stilp, A., et al. 2010, ApJ, 709, 135, doi: 10.1088/0004-637X/709/1/135

Williams, B. F., Hatzidimitriou, D., Green, J., et al. 2014a, MNRAS, 443, 2499, doi: 10.1093/mnras/stu1252

Williams, B. F., Lang, D., Dalcanton, J. J., et al. 2014b, ApJS, 215, 9, doi: 10.1088/0067-0049/215/1/9

Williams, B. F., Dolphin, A. E., Dalcanton, J. J., et al. 2017, ApJ, 846, 145, doi: 10.3847/1538-4357/aa862a

Williams, B. F., Lazzarini, M., Plucinsky, P. P., et al. 2018, ApJS, 239, 13, doi: 10.3847/1538-4365/aae37d

Williams, B. F., Durbin, M. J., Dalcanton, J. J., et al. 2021, arXiv e-prints, arXiv:2101.01293. https://arxiv.org/abs/2101.01293

Willingale, R., Starling, R. L. C., Beardmore, A. P., Tanvir, N. R., & O'Brien, P. T. 2013, MNRAS, 431, 394, doi: 10.1093/mnras/stt175

Wilson-Hodge, C. A., Malacaria, C., Jenke, P. A., et al. 2018, ApJ, 863, 9, doi: 10.3847/1538-4357/aace60

Yukita, M., Hornschemeier, A. E., Lehmer, B. D., et al. 2016, ApJ, 824, 107, doi: 10.3847/0004-637X/824/2/107

Yukita, M., Ptak, A., Hornschemeier, A. E., et al. 2017, ApJ, 838, 47, doi: 10.3847/1538-4357/aa62a3

Zapartas, E., de Mink, S. E., Izzard, R. G., et al. 2017, A&A, 601, A29, doi: 10.1051/0004-6361/201629685

Zezas, A., Kyanidis, S., Sobolewska, M., et al. 2014, in AAS/High Energy Astrophysics Division, Vol. 14, AAS/High Energy Astrophysics Division #14, 110.06

Zhang, F., Li, X.-D., & Wang, Z.-R. 2004, ApJ, 603, 663, doi: 10.1086/381540

Zhang, Z., Gilfanov, M., & Bogdán, Á. 2012, A&A, 546, A36, doi: 10.1051/0004-6361/201219015

Vita

Margaret Lazzarini grew up in the Pasadena area in Southern California. She attended Yale University and received a B.S. in Astronomy & Physics in 2013. After graduating, she taught high school physics and astronomy in Los Angeles as a Teach for America corps member. She began graduate study at the University of Washington in 2015 and received her Ph.D. in Astronomy in June 2021. Margaret will start as a National Science Foundation Astronomy & Astrophysics postdoctoral fellow at Caltech in September 2021.